City, University of London Institutional Repository

COMPUTATIONAL MODELLING OF VORTEX SHEDDING FLOWS

Vlado Pržulj

Thesis submitted for the

Degree of Doctor of Philosophy

in the School of Engineering

City University

Department of Civil Engineering

City University

London EC1V 0HB

July 1998

Contents

List of Tables

List of Figures

Acknowledgements

Abstract

This study describes the development and application of a two–dimensional CFD method for vortex shedding flows past square and circular cylinders. The overall approach can be regarded as a compromise between the accuracy and computational costs, especially for high–Reynolds number flows. The latter are modelled by variants of the $k - \epsilon$ eddy-viscosity model which is used in conjunction with wall functions.

The governing equations, expressed through Cartesian vector and tensor components, are discretised using the finite volume method with a colocated storage arrangement for all variables. Body–fitted (non–orthogonal) structured or block–structured numerical grids can be used. Fully-implicit, first–order accurate time discretisation is adopted, while the space discretisation is formally second–order accurate. In order to ensure a bounded solution, the high–resolution MINMOD and SMART schemes are implemented.

The numerical method is validated against experimental data for various laminar flow situations: (i) single square and circular cylinders in a uniform flow, (ii) two circular cylinders in tandem submerged in a uniform flow and (iii) a circular cylinder in oscillatory flows. In the case of the uniform flow over single cylinders, the issues affecting the accuracy and reliability of two–dimensional numerical solutions are addressed. It is shown that numerical uncertainties caused by a choice of the solution domain width (the blockage) very often cancel time and space discretisation errors. Further, advantages of high–resolution bounded schemes such as the MINMOD and SMART are confirmed. Variations of the mean drag coefficient and Strouhal number with Reynolds number are accurately predicted for the Reynolds number below 200, i.e. for two–dimensional flow conditions. For these conditions, some physical features of vortex shedding are emphasized. For other flow configurations, parametric studies are conducted to investigate effects of additional factors on the integral vortex shedding parameters and flow regimes. In all cases, the present results compare well to the published experimental and numerical data.

Various versions of the $k - \epsilon$ model are considered for turbulent flow predictions. A new model, with an unsteady modification related to the production of the dissipation rate, is proposed. This model and the RNG model are validated against data for vortex shedding from single square and circular cylinders. In the case of a square cylinder ($Re = 20,000$), both models yield satisfactory results for the integral parameters and most of the time–averaged and phase–averaged flow variables. These results stand comparison with those obtained by other models or LES methods. For a circular cylinder, the boundary layers are laminar before flow separation over a wide range of Reynolds numbers, up to 1×10^6. On the other hand, the tested $k - \epsilon$ models are based on the principal assumption that the flow is turbulent everywhere. Consequently, the flow separation is predicted wrongly which leads to unsuccessful predictions of other vortex shedding results. Better results are obtained for the postcritical regime ($Re > 10^6$), where the boundary layers are turbulent before separation.

Nomenclature

Latin Characters

a_P, a_j	Coefficients of the discretised governing equation corresponding to the central node P and the neighbouring node N_j
$\mathbf{A}$	Outward surface vector
$\mathcal{A}$	Cell–face area
B_f	Blockage factor, $H/(2Y_s)$
C_D, C_L	Drag and lift coefficients, $2F_{D,L}/(\rho U_0^2 DL)$
C_P	Pressure coefficient, $2(P - P_0)/(\rho U_0^2)$
C_{dm}, C_m	Morison's drag and inertia force coefficients, Eqs. (4.21) and (4.23)
C_F'	Morison's root–mean–square drag coefficient, Equation (4.25)
C_μ	Eddy–viscosity model constant, Table 2.1
$C_{\epsilon 1}$, $C_{\epsilon 1}^*$, $C_{\epsilon 2}$	Closure coefficients in the ϵ–equation, Table 2.1
$C_{\epsilon 1}'$, $C_{\epsilon 3}$	Closure coefficients in the PDM modification
C_t	Model constant for the unsteady modification of production of ϵ
$\mathcal{C}$	Net flux by convection
D	Diameter of a circular cylinder
$\mathcal{D}$	Net flux by diffusion
$\mathcal{D}_\phi^M$, $\mathcal{D}_\phi^T$	Rates of viscous and turbulent diffusion for ϕ ($\phi = \langle u_i u_j \rangle$, k, ϵ)
e_{ijk}	Permutation tensor: equal to +1 for any even number of indices permutations (123, 231, and 312), -1 for any uneven number of permutations (321, 213, and 132), and 0 if two arbitrary indices are equal
E	Logarithmic law constant
E_1	Estimated fractional error for the fine numerical solution, Eq. (B.5)
f	Vortex shedding frequency
$\mathbf{f}_b$, f_{bi}	Body force per unit mass
$f_{e,P}$, f_e	Linear interpolation factors, Equations (3.23) and (3.25)

$f_{ex},\ f_{ey},\ f_e$	Grid expansion factors
$f_D,\ f_U$	Downstream and upstream interpolation factors, Equations (3.56) and (3.57)
$\mathbf{F}$	Total force exerted on a cylinder (pressure + viscous)
$F_D,\ F_L$	Drag and lift components of the total force
$F_j^c,\ F_j^d$	Convective and diffusion fluxes through the cell–face j
$g_D,\ g_U$	Downstream and upstream geometric factors, Equation (3.60)
$G_D,\ G_U$	Downstream and upstream geometric factors, Equation (3.59)
h	Characteristic discretisation parameter (mesh size, time–step size)
H	Height of a square cylinder
$\mathbf{i},\ \mathbf{j},\ \mathbf{k}$	Unit vectors in x, y, z Cartesian directions
j	cell face, $j = e,\ w,\ s,\ n$
k	Kinetic energy of turbulent fluctuations per unit mass, $0.5\ \langle u_i u_i\rangle$
k_f	Kinetic energy of total fluctuations (periodic + turbulent) per unit mass, $0.5\ \widetilde{u}_i\widetilde{u}_i + k$
Kc	Keulegan–Carpenter number, $U_m T_{os}/D$
$\ell_k,\ \ell_m,\ \ell_t$	Kolmogorov, mixing and turbulent length scales
L	Length; distance between two cylinders in tandem
L_r	Length of the recirculation zone
$L_x,\ L_\epsilon$	Integral and dissipation rate length scales
$\dot{m}_j$	Mass flux through the cell–face j
$\mathbf{n}$	Outward unit face area vector, $\mathbf{A}/\mathcal{A}$
NI, NJ	Total number of cells (active + boundary) in local coordinate directions I and J, i.e. ξ and η
p	Fluctuating pressure
P	Pressure (ensemble–averaged value)
$\mathcal{P}_\phi$	Rates of production of ϕ ($\phi = \langle u_i u_j\rangle,\ k,\ \epsilon$)
q	Kinetic energy per unit mass of ensemble-mean flow, $0.5 U_i^2$
$\widetilde{q}$	Periodic component of the mean-flow kinetic energy, $0.5\widetilde{u}_i^2$
r	Grid or time–step refinement ratio
r_e	Ratio of consecutive gradients of variable ϕ, $(\phi_C - \phi_U)/(\phi_D - \phi_C)$
$\mathbf{r}$	Position vector
Re	Reynolds number, $U_0 D/\nu$

Re_m	Reynolds number for oscillatory flows, $U_m D/\nu$
$Re_c^i,\ Re_c^{3D}$	Critical Reynolds numbers for the onset of vortex shedding and three–dimensionality
Re_c^t	Critical Reynolds number for the onset of turbulence
R_{ij}	Reynolds stress tensor, $-\rho \langle u_i u_j \rangle$
Re_t	Turbulence Reynolds number, $k^2/(\nu\epsilon)$
$\mathcal{R}$	Rate of change term
s_ϕ	Specific (volumetric) source of ϕ
S	Strain–rate tensor invariant, $\sqrt{2S_{ij}S_{ij}}$
S^*	Dimensionless strain parameter, Sk/ϵ
S_{ij}	Mean strain–rate tensor invariant
$S_{\phi P}$	Source term of ϕ for the cell P
$S_\phi',\ S_\phi''$	Constant and linear part of the source term, Table 3.2
$\mathcal{S}$	Net sources
St	Strouhal number, $f D/U_0$
t	Time
t^*	Dimensionless time, $t U_0/D$
$\mathbf{t}$	Unit vector parallel to the wall
T	Vortex shedding period or averaging time interval
T_{os}	Period of oscillations
$T_k,\ T_t$	Kolmogorov and turbulent time scales, $\sqrt{\nu/\epsilon}$ and k/ϵ, respectively
T_p	Time scale of periodic motion, Equation (2.57)
T_ω	Combined time scale, $T_k + T_t\Omega/S$
T_u	Turbulence intensity
$u,\ v,\ w$	Fluctuating velocity components in x, y, z directions
u_i	Fluctuating velocity (turbulent fluctuations) in tensor notation
$\tilde{u}_i$	Periodic velocity in tensor notation
u_i'	Global fluctuating velocity in tensor notation, $\tilde{u}_i + u_i$
$\langle u_i u_j \rangle$	Kinematic Reynolds stresses
$\overline{u_i' u_j'}$	Time average of global fluctuating velocities (apparent Reynolds stresses)
$U,\ V,\ W$	Ensemble-mean velocity components in x, y, z directions

U_0, U_{in}	Uniform and time–dependent inlet velocity
U_m	Maximum oscillating velocity
U_r	Relative velocity, U_0/U_m
U_τ	Friction velocity, $\sqrt{|\tau_w|/\rho}$
U_*	Near–wall turbulence velocity scale, $C_\mu^{1/4} k^{1/2}$
U^+	Dimensionless near-wall velocity, U/U_τ
U	Mean velocity in vector notation
V	Volume
W_{ij}	Mean rotation (vorticity) tensor
x, y, z	Cartesian coordinates
x_i	Position vector in tensor notation
X_i, X_o	Position of inlet and outlet boundaries relative to the cylinder's centre
$2Y_s$	Solution domain width
y^+	Non-dimensional distance from the wall, $U_\tau\, y/\nu$
Y_P^*	Non-dimensional wall distance, $U_*\, y_P/\nu$ or $U_*\, \Delta n_P/\nu$

Greek Characters

α_e	Parameter defining a family of high–order convective schemes
α_ϕ	Under-relaxation factor for variable ϕ
β	High–order scheme factor; Stokes parameter, $D^2/(\nu\, T_{os})$
γ_t, γ_ϕ	Blending factors between the first–order and high–order accurate time and convective schemes, respectively
Γ_ϕ	Diffusion coefficient
δ_{ij}	Kronecker delta ($\delta_{ij} = 1$ if $i = j$ and $\delta_{ij} = 0$ otherwise)
Δn_c, Δn_P	Normal distance from the centre of the near–wall cell to the wall
Δt	Time-step size
Δt^*	Dimensionless time-step size, $\Delta t\, U_0/D$
ΔV_P	Volume of the cell P
$\Delta \phi$	Incremental change in ϕ
ϵ	Dissipation of k per unit mass
η	Local (curvilinear) coordinate

θ	Angle
θ_s	Angle of separation
ϑ	Phase; phase angle $2\pi t / T_{os}$
κ	Von Karman constant
μ	Molecular viscosity
μ_t	Turbulent (eddy) viscosity
μ_w	Effective near–wall viscosity, Equation (3.102)
ν	Kinematic molecular viscosity, μ/ρ
ν_t	Kinematic turbulent viscosity, μ_t/ρ
ξ	Local (curvilinear) coordinate
ϖ	Order of accuracy
ρ	Density
σ_k, σ_ϵ	Coefficients of turbulent diffusion for k and ϵ
τ_{ij}	Mean viscous stress tensor
τ_w	Wall shear stress
ϕ	General (ensemble–mean) dependent variable
$\tilde{\phi}$	Normalized general variable, $(\phi - \phi_U)/(\phi_D - \phi_U)$
φ_e	Flux limiter for bounded convective schemes
$\tilde{\varphi}$, φ	Periodic and turbulent fluctuations of variable Φ
φ'	Global fluctuations of Φ, $\tilde{\varphi} + \varphi$
$\widehat{\Phi}$, Φ, $\overline{\Phi}$	Instantaneous, ensemble–averaged and time–averaged flow variable
χ	Relative difference between two numerical results, $(\Phi_2 - \Phi_1)/\Phi_1$
ψ	Streamfunction
ω	Vorticity (in 2D)
ω_i	Random part of instantaneous vorticity vector $\widehat{\Omega}_i$ (tensor notation)
Ω_i	Mean vorticity vector in tensor notation, $e_{ijk}\,\partial U_k/\partial x_j$
Ω	Mean vorticity tensor invariant, $\sqrt{2W_{ij}W_{ij}}$

Subscripts

0	Inlet; initial; reference value
b	Boundary
C	Central
D	Drag; downstream
L	Lift
max	Maximum
min	Minimum
n	Normal direction; time step
out	Outlet
p	Pressure
P	At cell P
sym	Symmetry
t	Tangential (parallel to the wall); turbulent
U	Upstream
v	Viscous
w	Wall
w, e, s, n'	West, east, south and north cell–face, respectively
W, E, S, N	West, east, south and north neighbouring cell, respectively

Superscripts

$\hat{}$	Instantaneous value
$-$	Long time–averaged
$\sim$	Periodic component; peak–to–peak value; normalized variable
$'$	Root–mean–square value; fluctuating around the time–mean value
c	Convection
d	Diffusion
(k)	Outer iteration
(l)	Inner iteration
n	Time level

Mathematical Operators

$\overline{}$	Linear interpolation; time averaging
$\langle\ \rangle$	Ensemble averaging
∇	Vector operator 'nabla', $\mathbf{i}_i\ \partial/\partial x_i$
$\cdot$	Scalar product

Abbreviations

ASM	Algebraic Reynolds Stress Model
CBC	Convective Boundedness Criterion
CDS	Central Differencing Scheme
CFD	Computational Fluid Dynamics
CFL	Courant–Friedrichs–Lewy condition
CV	Control Volume
2D	Two–Dimensional
3D	Three–Dimensional
D	Domain
DNS	Direct Numerical Simulation
DSM	Differential Reynolds Stress Model
EVM	Eddy–Viscosity Model
LES	Large–Eddy Simulation
LUDS	Linear Upwind Differencing Scheme
NVD	Normalized Variable Diagram
PDM	Preferential Dissipation Modification
QUICK	Quadratic Upstream Interpolation for Convective Kinematics
RANS	Reynolds Averaged Navier–Stokes method
RNG	Renormalization Group
SIMPLE	Semi–Implicit Method for Pressure–Linked Equations
SKE	Standard $k - \epsilon$ model
SMART	Sharp and Monotonic Algorithm for Realistic Transport
TVD	Total Variation Diminishing
UDS	Upwind Differencing Scheme
UKE	Unsteady $k - \epsilon$ model

Chapter 1

INTRODUCTION

1.1 The Vortex Shedding Phenomenon

This thesis is concerned with the computation of (nominally) two-dimensional unsteady flows around square and circular cylinders normal to an unbounded stream. These simple geometries are examples of the wider category of *bluff bodies* which includes such structures as buildings, bridges, towers and offshore pipelines and platforms. A characteristic feature of the flows around such geometries is the periodic or quasi–periodic alternate separation of fluid from the surfaces. This is the well–known phenomenon of *vortex shedding*. In non–mathematical terms, Lugt (1983) defines the vortex as "*the rotating motion of a multitude of material particles around a common center.*" Of course, there is no vortex without *vorticity* which is "*the angular velocity of matter at a point in continuum space.*" The bluff body creates separated flow over a part of its surface and this is a precondition for the generation of vortices at the walls. Whether vortices will remain attached to the body, or will be separated (shed) from it, depends on the Reynolds number, Re. For a circular cylinder with the diameter D (Figure 1.1) placed in a moving fluid of viscosity μ and density ρ and uniform velocity U_0, the Reynolds number is defined as:

$$Re = \frac{\rho U_0 D}{\mu} .$$

(1.1)

An overall impression of the vortex–shedding phenomenon can be gained from Figure 4.12 which shows numerical (present work) and experimental visualizations of vortex shedding from a circular cylinder at $Re = 105$.

Vortex shedding is a time–dependent process and is one which is usually strongly dependent on the Reynolds number. Briefly, as the moving fluid approaches the cylinder (Figure 1.1), the pressure reaches a maximum at the stagnation point and boundary layers develop along the cylinder sides. At Reynolds number values in excess of 4.5, the boundary layers separate from each side under the influence of adverse pressure gradi-
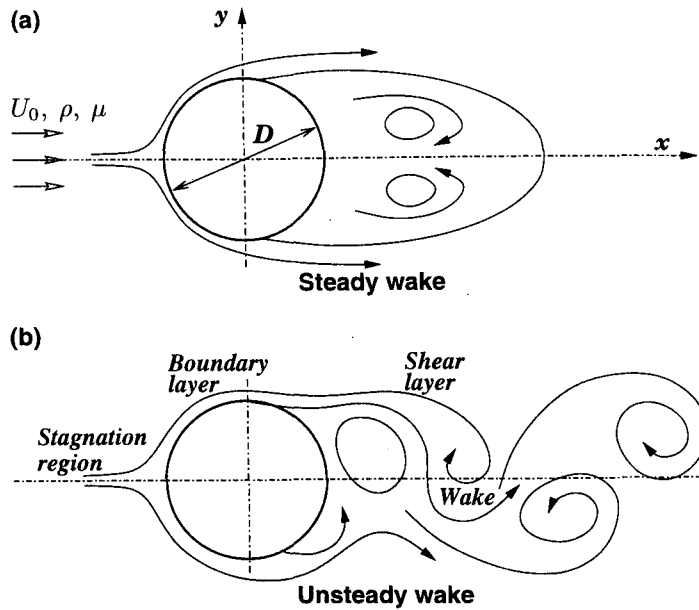
Figure 1.1: Characteristic flow regions for a circular cylinder: (a) steady separation, (b) vortex shedding.

ents and form two free shear layers that enclose a pair of recirculation regions behind the cylinder (i.e. two attached vortices). According to Coutanceau and Defaye (1991), the flow remains steady, two–dimensional and laminar at Re below $Re_c^i \approx 40$ which marks the onset of the *primary wake instability* which introduces a vortex shedding regime. The laminar periodic wake of staggered vortices of opposite sign –the "von Karman vortex street"– characterizes vortex shedding for Re below a certain value of the Reynolds number ($Re_c^{3D} \approx 190$ for a circular cylinder). Above this number, the two–dimensional wake undergoes a transition to a three–dimensional state and, later, to a turbulent state. For a circular cylinder, this occurs at $Re_c^t \approx 1000$. A change from the two–dimensional to the three–dimensional self–sustained flow is associated with a *secondary wake instability* of the vortex street. The wake transition regime is surprisingly rich in the three–dimensional vortex dynamics phenomena, as discussed recently by Williamson (1996). At $Re > Re_c^t$ the fundamental *shear flow instabilities* induce turbulence, first in the separated shear layers and then in the boundary layers. Depending on the Reynolds number, different flow regimes can be identified, some of which do not exhibit regular vortex shedding.

The alternate shedding of vortices from a bluff body alters the pressure field around it and causes fluctuations of surface pressure forces. These forces can be sufficient to cause flexible and lightly damped structures to oscillate. These oscillations may, in turn, interact with the flow leading to an aeroelastic response. If the vortex shedding frequency is close to the structure's natural frequency, self-induced oscillations may occur, with disastrous consequences to the stability of bridges, stacks, tall buildings, cooling towers, etc. The failure of the original Tacoma Narrows Bridge (USA) in 1940 (McCroskey, 1977) is a well

known example. Many other important parameters (e.g. the aerodynamic performance in terms of lift and drag, and the heat transfer coefficient) are influenced by vortex shedding. The phenomenon is therefore of interest to designers :of road vehicles, ships, aircrafts and their power plants, and heat exchange devices.

The study of vortex shedding has attracted researchers since the sixteenth century when Leonardo da Vinci drew the movement of water around an obstacle in a stream (MacCurdy, 1954). It has also been observed for long that telegraphic wires in the wind vibrate and 'sing'. Clearly, the unsteady lift and drag forces, induced by vortex shedding, excite an oscillatory motion of the elastic wires which, in turn, produce acoustical tones due to the periodic fluctuation in density and pressure. In his experiments on sound, Strouhal (1878) (see, e.g. Sarpkaya, 1979) found that the product of the vortex shedding frequency f and the wire diameter D, divided by the wind velocity U_0, was nearly constant for a range of values. This combination of variables is now known as the *Strouhal number*:

$$St = \frac{f\,D}{U_0}\,. \tag{1.2}$$

In 1915, Lord Rayleigh normalized Strouhal frequency data using the St-number versus Re-number. Williamson (1996) compared these original data with modern measurements and found them to be in remarkable agreement. Benard (1908) (see Coutanceau and Defaye, 1991) appears to have been the first to visualize a regular pattern of two rows of staggered vortices behind a circular cylinder. This pattern is usually called the "Karman vortex street". Using inviscid–flow theory, von Karman (1911) (see, for example, Lamb, 1932, p. 228) analysed the stability of two infinite parallel rows of equidistant vortices. Von Karman's analysis described the vortex patterns observed in the wake of bluff bodies and attracted many researches concerned with instability of vortex arrays.

Over the years, the two complementary approaches of experimentation and computation were used to analyse vortex shedding flow problems. The sections that follow review some of the results obtained by these two approaches.

1.2   Experimental Background

Several review articles, including those of Lienhard (1966), Berger and Wille (1972), Mc-Croskey (1977), Sarpkaya (1979), Bearman (1984), Basu (1985, 1986), Sarpkaya (1992), and Williamson (1996), report on the measurements of various vortex shedding parameters. This section defines the parameters that are commonly used and briefly presents the various flow regimes observed for fixed circular and square cylinders.

Vortex shedding parameters

The forces acting on a cylinder, and the dimensionless vortex shedding frequency, are a function of the Reynolds number. The total, time-dependent force exerted on the cylinder consists of the pressure force $\mathbf{F}_p$ and viscous or friction force $\mathbf{F}_v$:

$$\mathbf{F} = \oint_{cyl} P\, \mathbf{n}\, d\mathcal{A} - \oint_{cyl} \tau_{ij}\, n_j\, d\mathcal{A} = \mathbf{F}_p + \mathbf{F}_v \ . \tag{1.3}$$

Here P is the pressure, τ_{ij} is the viscous stress tensor, $d\mathcal{A}$ and $\mathbf{n} = \{n_j\}$ denote differential surface area and its outward unit vector, respectively. The total force is usually decomposed into two components: one in the direction parallel to the oncoming stream (the drag force $\mathbf{F}_D$) and another in the direction normal to it (the lift force $\mathbf{F}_L$). The corresponding non–dimensional forces, namely total drag and lift coefficients are defined as:

$$C_D = \frac{2F_D}{\rho U_0^2 D L} \ , \quad C_L = \frac{2F_L}{\rho U_0^2 D L} \ , \tag{1.4}$$

where L is the cylinder length. Obviously, these coefficients also depend on time, and may thus be treated as the sum of a time–averaged and a fluctuating component. These quantities will hereafter be denoted by an over-bar $-$ and a tilde $\sim$, respectively. Thus, for example, the drag coefficient is assembled as:

$$C_D = \overline{C}_D + \tilde{C}_D \ , \quad \overline{C}_D = \frac{1}{T} \int_{t_0}^{t_0+T} C_D(t)\, dt \ . \tag{1.5}$$

The time–averaged effect of the fluctuating forces is represented by the root–mean–square (r.m.s.) values of the drag and lift coefficients. Thus, for example, the r.m.s. lift coefficient C_L' reads:

$$C_L' = \left(\overline{\tilde{C}_L^2} \right)^{1/2} = \left[\frac{1}{T} \int_{t_0}^{t_0+T} \tilde{C}_L^2(t)\, dt \right]^{1/2} \ . \tag{1.6}$$

The static pressure is often made dimensionless through the definition of the pressure coefficient C_p:

$$C_p = \frac{P - P_0}{0.5\,\rho\, U_0^2} \ . \tag{1.7}$$

The power spectra of time-dependent quantities, such as the force coefficients or the velocity in the wake, can be used to determine the frequency of the shedding process. In the literature, the vortex shedding frequency f is generally associated with the dominant frequency in the power spectra of the lift fluctuations. Strouhal introduced the dimensionless vortex shedding frequency, Equation (1.2).

Flow regimes

Circular cylinder. In the case of a circular cylinder, the flow regimes were first defined by Roshko in 1954 (see Williamson, 1996) and recently by Williamson (1996). Coutanceau and Defaye (1991) gave an extensive description of the flow from the near wake to the far wake based on the flow visualizations. In Figure 1.2, the results from different sources are assembled to show the variation of $\overline{C}_D$, C_L', and St with the Reynolds number. Note that data from other sources, obtained for Re beyond 10^4, are considerably more scattered. This is evident when comparing the present figures with ones compiled by Lienhard (1966), Ericsson (1980), James et al. (1980), Cantwell and Coles (1983), - all for $\overline{C}_D$ and St, and by Basu (1985) and West and Apelt (1993) for C_L'. In practice, the lift
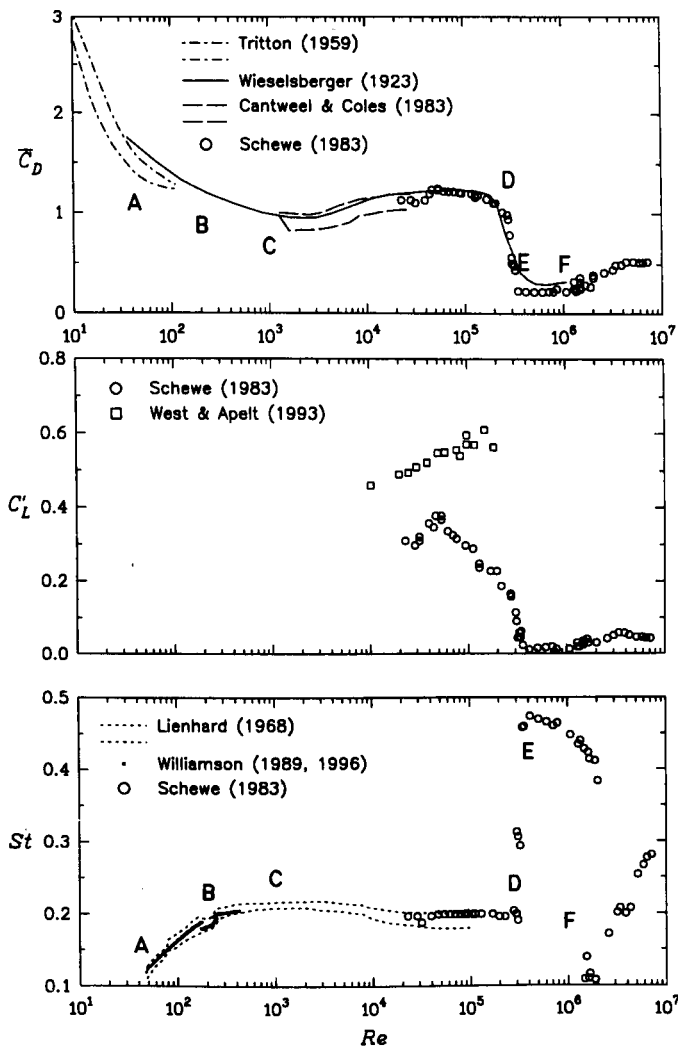
Figure 1.2: Vortex shedding parameters vs. Re for a smooth circular cylinder in a uniform low-turbulence stream: the mean drag coefficient (top), r.m.s. lift coefficient (middle) and Strouhal number (bottom).

forces can be measured either over the whole span of a cylinder (Schewe, 1983) or only

on the mid–span section (e.g. West and Apelt, 1993). Different results will be obtained if there is no perfect correlation between the fluctuating forces along the span, Figure 1.2 (middle).

The following flow regimes can be identified (with reference to the labels shown on Figure 1.2):

- *Laminar steady flow:* $Re < 40$ *(regime up to A)*. As Re increases, the drag coefficient decreases.

- *Unstable wake and laminar vortex shedding:* $Re \approx 40 - 190$ *(regime A-B)*. The drag coefficient continues to decrease, while the Strouhal number shows a strong increase.

- *Wake transitions:* $Re \approx 190 - 1000$ *(regime B-C)*. The wake becomes three-dimensional and undergoes a transition to a turbulent state.

- *Shear layer transition regime:* $Re \approx 1,000 - 3 \times 10^5$ *(regime C-D)*. A transition to turbulence in the shear layers is the main feature of this *subcritical* regime. At $Re \approx 10,000$ the transition occurs close to the separation point. However, it is preceded by laminar separation of the boundary layers. For $Re > 10^4$, the separation point has a quasi-constant value of 80° (Achenbach, 1968; Britter et al., 1979). The fairly constant values of ($\overline{C}_D = 1.0 - 1.2$, and $St \approx 0.20$) correspond with a turbulent motion in the vortex street and in the major portion of the shear layers.

- *Asymmetric reattachment (critical regime):* $Re \approx (3 - 4) \times 10^5$ *(regime D-E)*.

  The transition from laminar to turbulent flow happens just downstream from the laminar separation point ($\theta_s = 80° - 100°$). The *critical* flow regime appears when *one* of the shear layers reattaches itself to the cylinder wall, forming a *separation-reattachment bubble*. The revitalized turbulent boundary layer separates again, only much further downstream ($\theta_s = 120° - 140°$; Achenbach, 1968). This is followed by a significant decrease of the wake width and drag coefficient (the 'drag crisis'), and by an increase of St. In this transitional regime, with no regular vortex shedding, the flow is extremely sensitive to three-dimensional disturbances, the free-stream turbulence and surface roughness.

- *Symmetric reattachment (supercritical regime):* $Re \approx 4 \times 10^5 - 10^6$ *(regime E-F)*. The mean symmetric flow, with two separation-reattachment bubbles, and nearly constant minimal $\overline{C}_D \approx 0.22$ and maximal $St \approx 0.47$ characterize more or less regular vortex shedding in the *supercritical* flow regime.

- *Boundary layer transition (postcritical regime):* $Re > 10^6$ *(regime from F)*. At Re above $\approx 10^6$, the boundary layers become turbulent before separating at $\theta_s \approx (110 - 120)°$. For $Re > 5 \times 10^6$, the dominant frequency $St \approx 0.27 - 0.29$ indicates a strong vortex shedding process (see also Roshko, 1961 and Jones et al., 1969). The drag coefficient appears nearly constant ($\overline{C}_D \approx 0.5$) over this postcritical regime.

Square cylinder. In contrast to circular cylinder flows, bluff bodies with fixed separation points, like rectangular cylinders, have attracted much less attention. The available experimental results for a square cylinder are presented in Figure 1.3. Similarity of the
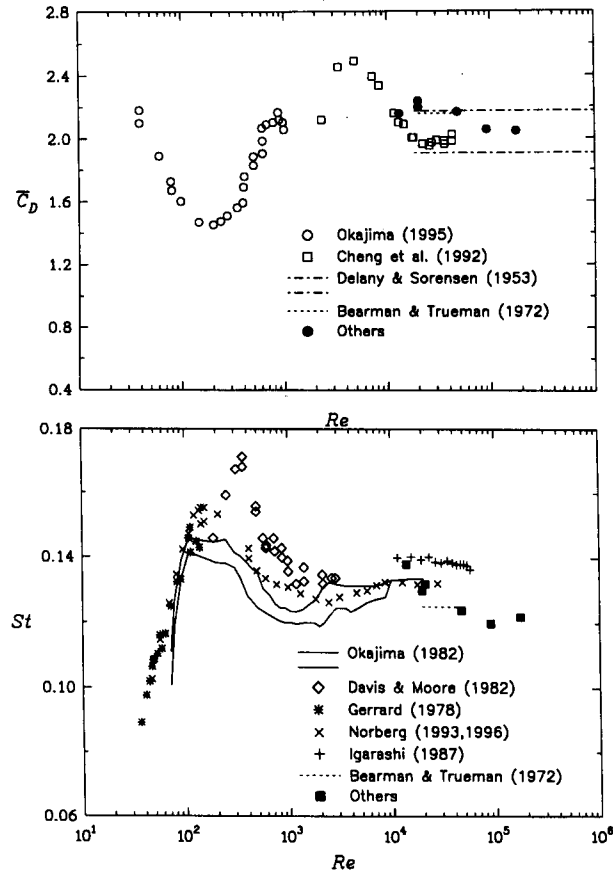
Figure 1.3: Vortex shedding parameters vs. Re for a smooth square cylinder in a uniform low-turbulence stream: the mean drag coefficient (top) and Strouhal number (bottom). Single Re-number results marked as 'others': Pocha (1971), Lee (1975), Bearman and Obasaju (1982), Obasaju (1983), Sarpkaya and Ihrig (1986), Durao et al. (1988) and Lyn (1992).

flow evolution here with that of a circular cylinder is obvious. At high Re, the flow does not exhibit the remarkable changes associated with a transition phenomenon of the critical regime seen for the case of a circular cylinder. According to Okajima (1982), the aerodynamic parameters are generally less sensitive to changes in the Re if the flow separates at fixed points. At low Re, - $Re < 150$, Franke (1991), the separation points are fixed at the rear corners of the square cylinder. At higher Re, the separation happens at the front corners, and as for the circular cylinder, a transition from laminar to turbulent vortex street can be expected. For example, the power spectra of the wake velocities measured by Okajima (1982) showed secondary frequencies at $Re = 250$. Beyond $Re = 10^4$, the mean drag coefficient and Strouhal number attain nearly constant values ($\overline{C}_D = 2 - 2.2$ and $St = 0.12 - 0.14$).

Finally, it should be mentioned that, apart from the Reynolds number, vortex shedding from circular and square cylinders is affected by the surface roughness, the free stream turbulence, the cylinder aspect ratio and wind tunnel blockage. The influence of the above parameters was reviewed by Basu (1985, 1986), Bell (1986), Coutanceau and Defaye (1991), and Williamson (1996).

1.3   Computational Background

The computational approach has followed the progress of computer technology in terms of the computing speed and memory. There are two issues to consider:

- the definition and closure of the governing transport equations, and

- the solution of these equations by an appropriate numerical method.

The first issue deals with turbulence, "the chief outstanding difficulty of our subject" (Lamb, 1932, p. 663; Bradshaw, 1994). Turbulent flows are three–dimensional and unsteady, irregular, rotational, diffusive and dissipative. They are also exactly described by the laws of conservation of mass, momentum, and energy. These are non-linear partial differential equations whose direct solution is, unfortunately, beyond the capabilities of existing computing resources, except, perhaps, for simple geometries and at low Reynolds numbers. This is due to the wide range of time and length scales that increases with the Reynolds number. *Direct Numerical Simulations* (DNS) must resolve all length and time scales. The smallest of these scales correspond to the Kolmogorov length and time scales ℓ_k and T_k:

$$\ell_k = \left(\frac{\nu^3}{\epsilon}\right)^{1/4} , \; T_k = \left(\frac{\nu}{\epsilon}\right)^{1/2} . \tag{1.8}$$

where ϵ represents the viscous dissipation rate per unit mass. It is a reasonable prognosis that the computer capacity and speed will always be limited. The alternative to DNS, and the efficient way to compute practical turbulent flows at present, is to construct statistical models following the suggestion of Reynolds (1895) that dynamical quantities (e.g. velocity and pressure) may be split into a mean part and a random, fluctuating part, $\widehat{U}_i = U_i + u_i$, $\widehat{P} = P + p$. Substitution of these quantities into the conservation equations and application of the ensemble averaging procedure leads to the ensemble–averaged or *Reynolds–Averaged Navier–Stokes equations* (RANS). These contain unknown products of one–point double velocity fluctuations – the Reynolds stresses $(- \langle u_i u_j \rangle)$ – that require determination by using a (statistical) turbulence model. Another route, which still requires extensive computational effort, but is potentially the next best alternative to DNS,

is *Large Eddy Simulation* (LES). The LES resolves the large–scale eddy motion specified by a filtering operation which, like the ensemble–averaging operation, introduces unknown sub–grid–scale stresses. These stresses represent the effects of the small-scale motion and are modelled by sub-grid scale models.

Whichever approach is used, the governing equations of the resolved flow need to be solved numerically. The governing equations can be formulated either in terms of a stream function ψ and vorticity ω (for two–dimensional flows $\omega = \Omega_3$) or in terms of primitive variables, i.e. the velocity components and the pressure. Solution methods that have been used for vortex shedding calculations include discrete vortex methods, finite difference, finite element, and finite volume methods. To our knowledge, Fromm and Harlow (1963) were the first to compute the vortex shedding flow. They analysed the uniform laminar flow past a normal flat plate. Since then, a great number of computational studies have been done, especially on laminar flows around a circular cylinder.

1.3.1   Previous studies on laminar vortex shedding flows

Bibliographical (since 1980) and other notes on the numerical computations of the flows around square and circular cylinders are included in Appendix A, Table A.1 and Table A.2. Studies performed prior to 1980 were restricted to coarse numerical grids and those have adversely affected their accuracy. The predictions are typically presented in the form of the basic physical parameters such as the Strouhal number, drag and lift coefficients, etc. The dependence on Reynolds numbers (for which the flow is laminar according to the experimental observations) has been investigated (for the circular cylinder) by Gresho et al. (1984), Borthwick (1986), Braza et al. (1986), Lecointe and and Piquet (1989), Karniadakis and Triantafyllou (1989), Franke et al. (1990), Sa and Chang (1991), and Li et al. (1991). Although the grid-size and time-step independent solutions have not been reported in all these studies, the numerical results for St and $\overline{C}_D$ are in reasonable agreement with the measurements. A similar conclusion can be made for the computations of the vortex shedding from a square cylinder; here Davis and Moore (1982), Younis (1988), Franke et al. (1990), Arnal et al. (1991), Suzuki et al. (1993), Hwang and Yao (1997), and Sohankar et al. (1997) should be mentioned. Comparisons of most previous numerical results for St and $\overline{C}_D$ with experiments are presented in Figures 4.26, 4.28, 4.29 and 4.30.

Since the pioneering study of Fromm and Harlow (1963), instantaneous streamlines and streaklines have been used by many authors. Eaton (1987) produced and analysed the sequence of the instantaneous streamlines around a circular cylinder ($Re = 110$) which showed what Perry et al. (1982) called "instantaneous alleyways"; areas through which fluid is drawn into the recirculation region. He also demonstrated agreement between

his and Gerrard's (1978) experimental streakline plots. Sa and Chang (1991), Wang and Dalton (1991a), and Kim and Benson (1992) also produced streakline patterns at $Re = 60 - 150$, similar to those depicted in literature (e.g. van Dyke, 1982). For a square cylinder, Davis and Moore's (1982) streaklines calculated at $Re = 250$ showed the centres of the shed vortices to lie on the wake's mid–plane. This is contrary to the streakline plots of Pereira and Durst (1988) and Kim and Benson (1992) which show these centres to lie on either side of the mid–plane.

1.3.2   Previous studies on turbulent vortex shedding flows

Previous computations of turbulent vortex shedding flows are summarized in Appendix A, Table A.3 and Table A.4. These computations have been performed by employing Reynolds stress models, Large-Eddy Simulations and by solving the Navier-Stokes equations without a turbulence model. Various turbulence models were used, e.g. algebraic (zero equation), two-equation eddy–viscosity models and differential Reynolds–stress transport models. In most cases, the usual wall functions approach was employed to provide the boundary conditions. In some cases, the near-wall region was resolved by a one-equation model or by using a low Reynolds number closure.

Studies employing a turbulence model

The Baldwin–Lomax algebraic model (Baldwin & Lomax, 1978) was used to compute vortex shedding flows by Stansby and Smith (1989) and Deng et al. (1993a,1993b). Stansby and Smith calculated the flow past a circular cylinder at $Re = 3.6 \times 10^6$ (the postcritical regime). By introducing in their method an exponential vortex decay, their results for the mean surface pressure coefficient, the Strouhal number and force coefficients followed the measured trends. Similar results for the postcritical regime were obtained by Deng et al. (1993b). Their results for lower values of Re, however, did not capture the well-known 'drag crisis': the Strouhal number was nearly constant ($St = 0.25$) while the drag coefficient was overpredicted in the critical regime and underpredicted in the subcritical regime. This failure of the Baldwin–Lomax model to simulate the separating (laminar) boundary layer on a smooth surface is to be expected. Nevertheless, the same model applied to the flow around a square cylinder ($Re = 22,000$), where separation is determined by the front corners, produced satisfactory results for both the global parameters (St, $\overline{C}_D$) and for the time–averaged and phase–averaged quantities.

The widely used $k - \epsilon$ model does not perform well in bluff–body flows where the normal stresses control the production of turbulence in the stagnation region. The overproduction of the turbulence energy in such regions is often seen as the main reason for the

very weak (or even non–existent) vortex shedding obtained when using the standard $k - \epsilon$ model (Franke and Rodi, 1991; Kato and Launder, 1993). Franke and Rodi (1991) used both wall functions and the one-equation Norris-Reynolds model (Norris and Reynolds, 1975) to bridge the near-wall region and obtained poor results in both cases. Dawes (1992), on the other hand, reported satisfactory results by using the low-Re number $k - \epsilon$ model of Lam and Bremhorst (1981). Dawes simulated the flow around a circular cylinder for $Re = 4,000$, using both fixed and adapted unstructured grids. By contrast, the Nagano–Tagawa's low-Re number model (Nagano and Tagawa, 1990) tested by Deng et al. (1993b) failed to produce acceptable results for both circular and square cylinders. Hadid et al. (1991) showed that vortex shedding from a square cylinder can be sustained using the non-linear $k - \epsilon$ model with standard wall functions. However, no quantitative comparisons were presented and thus no assessment of the real capabilities of that model can be made.

Another industry favourite, the RNG $k - \epsilon$ model, usually outperforms the standard $k - \epsilon$ model in flows where regions of flow separation or stagnation are present. The main difference between the standard and the RNG models arises from the way in which the production term in the dissipation rate equation is modelled. The RNG production term produces smaller levels of the turbulent kinetic energy ahead of the bluff body and this, apparently, allows the sustainable development of vortex shedding. This was verified by Orszag et al. (1993) for a circular cylinder and by Benodekar et al. (1994) for a square cylinder. Note that Orszag et al. reported the use of the low Re number variant of the RNG model without enough details about that variant. They simulated the flow at $Re = 14,500$ and obtained the St value of 0.185 which is very close to the experimental value of 0.19. Benodekar et al. used the high Re model with wall functions. The calculated results for the velocity profiles showed fairly good agreement with measurements. Unfortunately, the force coefficients were not reported in either of these two studies.

Kato and Launder (1993) modified the standard $k - \epsilon$ model by introducing the vorticity parameter into the calculation of the turbulent kinetic energy production. In this way the spurious production of the turbulent kinetic energy around the stagnation point was avoided. Although not consistent with the eddy viscosity modelling of the Reynolds stresses, this modification improved prediction of vortex shedding from a square cylinder at $Re = 22,000$. The Kato and Launder modification was later used by Bosch and Rodi (1996) in the simulation of vortex shedding from a square cylinder near a wall. Reasonable predictions were obtained over the whole range of gap widths between the cylinder and wall.

Physically better sounded (but also more costly) Reynolds stress transport models do not produce excessive rates of the turbulent kinetic energy in the stagnation regions since

they resolve properly the stress anisotropy. Franke (1991) performed calculations for the flow around the square and circular cylinders employing the model of Launder, Reece and Rodi (1975). In general, the model used with wall functions produced better results than one combined with the two-layer approach. In the case of a square cylinder, the results obtained for the time-averaged as well as phase-averaged quantities show reasonably good agreement with experiments of Lyn (1992). In comparison with the measured values, the periodic fluctuations were overpredicted while turbulent ones were underpredicted. However, the predictions of the flow around a circular cylinder at $Re = 140,000$ were not satisfactory. This can be expected since the thin laminar boundary layer, which prevails up to the separation point, was not properly resolved.

LES methods

Vortex shedding simulations with LES have typically utilized the simple Smagorinsky model (Smagorinsky, 1963) for the subgrid-scale Reynolds stresses. LES are, by nature, three–dimensional, but some studies were performed as two-dimensional calculations, e.g. Song and Yuan (1990), Murakami et al. (1992), and Sakamoto et al. (1993). Song and Yuan presented satisfactory results for vortex shedding past a circular cylinder at two high values of Reynolds numbers, corresponding to the subcritical and transcritical flow regimes. The predicted pressure distributions, drag and lift coefficients, St, and the time-averaged velocity distributions in the wake compared favourably with the available data. However, their approach cannot be regarded as consistent since they fixed the separation points empirically. Also, the boundary layers were not resolved, but approximated by a combination of slip, partial-slip and no-slip boundary conditions. Murakami et al. and Sakamoto et al. applied a "law of the wall" type boundary condition (Launder and Spalding, 1974) and compared results of two– and three–dimensional calculations for the flow around a two dimensional square cylinder at $Re = 10^5$. The measured distributions of the time-averaged and r.m.s. pressure coefficients on the cylinder walls were reproduced quite well in the three dimensional computations. It was concluded that 2D LES calculations are not acceptable, since the mechanism of vortex stretching, which is an important factor in the process of energy transfer, cannot be reproduced in such computations.

Murakami and Mochida (1995) performed 3D computations of vortex shedding from a square cylinder at $Re = 22,000$. Although the extent of the computational domain in the spanwise direction was only 2H (104x69x10 grid nodes), the results were similar to those of Franke (1991) obtained with a differential Reynolds–stress transport model . The LES of Frank and Mauch (1993) were done on the finer grid (128x64x64 cells) using no-slip conditions at the wall. They presented only St for the flow past a square cylinder at Re in the range 110–40,000. At $Re = 40,000$, the calculated St is slightly higher than its

measured value. Finally, the vortex shedding flow from a square cylinder at $Re = 22,000$ was selected as a test case for the Workshop on LES of Flows past Bluff Bodies held in Germany in 1995. The results, reported in Rodi et al. (1997), demonstrate the ability of LES to reproduce most of the physical features associated with vortex shedding. Nevertheless, there is also evidence from the same studies of significant differences between the various LES results.

Computations without turbulence modelling

Several authors have assumed flow homogeneity along the cylinder axis and computed the high Reynolds-number flow by solving the two-dimensional Navier-Stokes equations without the use of a turbulence model. This is clearly a 'hybrid' approach since it is neither DNS (in that it is two–dimensional) nor is it LES or unsteady RANS (hence the absence of a sub–grid scale or turbulence model). Examples of this approach can be seen in the works of Braza et al. (1990, 1992), Tamura and Kuwahara (1990), Tamura et al. (1990), Kondo (1993), and Kakuda and Tosaka (1993).

Tamura and co-workers also investigated the reliability of two–dimensional calculations by comparing the results of two- and three-dimensional cases obtained under the same numerical conditions. They observed important differences between the computed 2D and 3D flow patterns around circular and square cylinders. In the case of the 3D computations, the high-frequency fluctuations of the drag and lift coefficients which characterize the 2D calculations, were absent. The average drag coefficient and r.m.s. lift coefficient were smaller than that for the 2D flow, and in satisfactory agreement with the experimental results. For the flow past the circular cylinder, the 'drag crisis', where the $\overline{C}_D$ is suddenly reduced, has been also successfully simulated. Tamura et al. used a grid of $400 \times 100 \times 40$ nodes and a third–order accurate scheme, hence it is unlikely that their calculations have succeeded in resolving the small–scale turbulent motion or in capturing the laminar/turbulence transition of the boundary layers (Franke and Rodi (1991), Deng et al. (1993a), Ferziger (1993)). It can thus be argued that the surprisingly good predictions of the drag coefficient were simply an accidental consequence of using a coarse grid.

1.4   The Present Approach and Its Justification

In order to find a serious use in fluid–engineering applications, the numerical simulation of vortex shedding flows should be done by an **accurate** and **computationally cost–effective** CFD method. Accuracy of a CFD solution is affected by three groups of systematic errors (Demirdzic et al., 1997):

1. Modelling errors (modelling of turbulent flows, simplifications of solution domains and boundary conditions, etc.),

2. Discretisation errors (discretisation of space and time),

3. Convergence errors (the difference between iterative and exact solutions of the discretised equations).

The convergence errors can be easily reduced to a negligible level. To ensure small spatial discretisation errors, the commonly used second–order accurate methods require a large number of computational cells. The reason behind this is a fundamental problem with the discretisation of convection by second–order accurate central differencing (i.e. linear interpolation). Namely, the central differencing often produces unstable and unbounded solutions on a coarse numerical grid. Thus, alternative high–order accurate and bounded schemes need to be considered. Regarding the time discretisation, the fully implicit first–order accurate scheme is usually preferred because of its stability and efficiency.

The Reynolds stress modelling is an obvious choice to deal with practical turbulent flows. Simpler and efficient turbulence models such as the eddy viscosity models introduce, in general, larger modelling errors than more complex Reynolds stress transport models. As the review of turbulent vortex shedding simulations shows, the standard $k - \epsilon$ model is not adequate to capture the realistic vortex shedding process for flows around square and circular cylinders. Alternative, the RNG model, as well as the modification due to Kato and Launder (1993), seem to perform better in these type of flows. Therefore, there is the scope to test and refine the conventional two–equation $k - \epsilon$ models in order to determine their capabilities and limitations in the area of unsteady computations. In this area, however, the turbulence models calibrated against steady–flow data may need to be specifically modified to take explicit account of the interactions between the *organized* and the *random* fluid motions (Younis, 1988). The optimum form of such a modification is yet to be determined.

The main source of the modelling errors is associated with the near–wall treatment of turbulence. In practice, the wall–function approach (Launder and Spalding, 1974) is usually used. The alternatives are low Reynolds–number models (see Jones and Launder, 1972; Patel et al., 1985; Shih and Mansour, 1990; Rodi and Mansour, 1993) and one–equation models that have been used as a near–wall component of the two–layer turbulence models (see Rodi, 1991; Rodi et al., 1993). The low Reynolds–number models need to be integrated down to the wall and have not been sufficiently tested in complex flows. Their 'damping functions', for example, which work well for attached boundary layers, are not always suitable for separated flows, Rodi (1991), Ferziger and Peric

(1996). In the case of vortex shedding, Deng et al. (1993b) obtained unsatisfactory results with the tested low Reynolds–number model. The one–equation models need less computational points in order to resolve the viscous sublayer and seem better placed than the two–equation low Reynolds number models. However, Franke (1991) reported that these models did not perform better than wall functions in computations of vortex shedding from a square cylinder. It can be argued that the present wall functions cannot resolve the near–wall modelling problem properly since they are based on the logarithmic velocity profile which is not supported by measurements or DNS results in general flow situations. However, they offer a simple and computationally economical near–wall treatment.

1.5 Objectives

Having in mind the above considerations, the objectives of the present study are:

1. To develop the (two–dimensional) finite volume numerical method which is at least second order accurate in space and can handle complex geometries.

2. To address the numerical uncertainties that arise from both spatial and temporal discretisation errors and from other sources such as a simplification of the solution domains and boundary conditions.

3. To validate the numerical method by established experimental and numerical data for various laminar vortex shedding flow configurations (i.e. in the absence of errors caused by turbulence modelling). These configurations include

   - uniform flow around single square and circular cylinders,
   - uniform flow around two circular cylinders in tandem,
   - oscillatory flow past a single circular cylinder with or without steady current.

4. To analyse some physical features of the vortex shedding flows encountered in the above (laminar) flow configurations.

5. To examine modelling unsteady turbulent flows by two–equation $k - \epsilon$ models used in conjunction with the wall functions and propose adequate modification(s).

6. To validate appropriate variants of the $k - \epsilon$ model through comparisons with available experimental data for vortex shedding from square and circular cylinders.

1.6 Contents of Thesis

This thesis is written in six chapters. Chapter 2 presents the mathematical framework which includes the conservation equations of incompressible, unsteady flows, their ensemble–averaged counterparts and the closure of these averaged equations by the two–equation $k - \epsilon$ models. Several variants of the standard $k - \epsilon$ model are analysed and

a simple modification, aimed at sensitizing the standard $k - \epsilon$ model to the organized unsteadiness, is proposed. The wall functions used to bridge the near–wall region are outlined.

Chapter 3 describes the finite–volume numerical method that employs the nonorthogonal, body fitted grids, with the colocated variable arrangement. Term–by–term discretisation of a general transport equation over control volumes (arranged in a structured manner) is explained. The first–order accurate fully implicit time differencing is employed, while spatial differencing is formally second order accurate. For convection, the high–resolution bounded schemes such as MINMOD and SMART are formulated for non–uniform grids and implemented. A segregated solution algorithm, based on the SIMPLE method, is described, including the implementation of various boundary conditions.

The numerical results for the laminar vortex shedding flows are presented and discussed in Chapter 4. For single circular and square cylinders, emphases are placed on the numerical uncertainties, and benchmarking by available experimental and other numerical data. The limitations of two–dimensional simulations are also addressed. In the case of other flow configurations (uniform flow around two circular cylinders in tandem and a single circular cylinder submerged in oscillatory flows), the effects of additional factors (apart from the Reynolds number) are quantified and compared with existing experimental data.

Chapter 5 is concerned with the assessment of the $k - \epsilon$ turbulence models in turbulent vortex shedding flows from square and circular cylinders. After the preliminary assessment, the RNG and the modified, unsteady, $k - \epsilon$ model have yielded the most satisfactory results and they are selected for further computations. A number of refinement tests is performed to determine the sensitivity of numerical simulations to various numerical parameters associated with the temporal and spatial discretisation, and with the solution domain size. The results obtained by the selected models are compared with available experimental data and with other numerical simulations. Comprehensive comparisons are made for the case of a square cylinder at $Re = 20,000$, for which the measurements of ensemble–mean flow and turbulence quantities are available.

The summary of this thesis, its achievements and suggestions for future work are given in Chapter 6.

Chapter 2

MATHEMATICAL FORMULATION

2.1 Introduction

The basic laws of physics are expressed through the corresponding transport equations which accurately describe fluid flows, including the phenomenon of turbulence. There is no dispute about the validity of these equations but for the present their complete (numerical) solutions are restricted to simple, low Reynolds number situations. Engineers, who are only interested in obtaining the average quantities of a turbulent flow, usually use the Reynolds averaged approach. The main difficulty with this (statistical) approach comes from the appearance of the turbulent Reynolds stresses that must be modelled. The purpose of this chapter is to introduce the Reynolds stress modelling practice and present corresponding mathematical formulations.

First, Section 2.2 recalls the fundamental conservation equations in the Eulerian formulation. Then, the ensemble averaging procedure that leads to the Reynolds averaged equations is presented in Section 2.3. Features of the averaged equations and the closure problem are outlined in Section 2.4. Section 2.5 summarizes the exact transport equations for the Reynolds stresses. Then the two–equation $k - \epsilon$ models, which will be used in this work, are reviewed in Section 2.6. Section 2.7 outlines some deficiencies of the $k - \epsilon$ models and presents modifications which can improve predictions of the vortex shedding flows. The near–wall treatment by using wall functions is presented in Section 2.8. Concluding remarks about this chapter are given in Section 2.9.

2.2 The Conservation Equations

In fluid flows, the laws of continuum physics, namely the conservation of mass, momentum, energy and entropy are usually applied to a certain spatial region – control volume rather than to a given mass of fluid. For the infinitesimally small control volume the con-

servation equations can be transformed into either a differential coordinate–free form or a form specific to a chosen coordinate system. Here we use the Cartesian coordinate system (x, y, z), with the unit base vectors $\mathbf{i}$, $\mathbf{j}$ and $\mathbf{k}$ along the x, y and z coordinate axes, respectively. For compactness, tensor or index notation is employed, where, for instance, the position vector $\mathbf{r}$ can be written as:

$$\mathbf{r} = x_i \mathbf{i}_i \text{ representing } \mathbf{r} = x\mathbf{i} + y\mathbf{j} + z\mathbf{k} = \sum_{i=1}^{3} x_i \mathbf{i}_i \,. \tag{2.1}$$

The instantaneous velocity $\widehat{U}_i$ and pressure $\widehat{P}$ as well as other flow quantities vary both with position $\mathbf{r}$ and time t. However, for incompressible and isothermal flows of Newtonian fluids that are considered throughout this work, the density $\widehat{\rho} = \rho$, and dynamic viscosity $\widehat{\mu} = \mu$ are constant. The partial differential equations for conservation of mass, the continuity equation, and of momentum, the Navier–Stokes equations, can be written as follows (cf. Batchelor, 1967 or Schlichting, 1968):

$$\frac{\partial}{\partial x_j}(\rho \widehat{U}_j) = 0 \,, \tag{2.2}$$

$$\frac{\partial}{\partial t}(\rho \widehat{U}_i) + \frac{\partial}{\partial x_j}(\rho \widehat{U}_i \widehat{U}_j) = -\frac{\partial \widehat{P}}{\partial x_i} + \frac{\partial \widehat{\tau}_{ij}}{\partial x_j} + \rho \widehat{f}_{bi} \,. \tag{2.3}$$

In the above momentum equation, $\widehat{f}_{bi}$ denotes body forces per unit mass which are neglected in this work, while $\widehat{\tau}_{ij}$ is the viscous stress tensor. For Newtonian fluids, the viscous stresses are proportional to the rate of deformation (Stokes' law):

$$\widehat{\tau}_{ij} = 2\,\mu \widehat{S}_{ij} - \frac{2}{3}\,\mu \frac{\partial \widehat{U}_k}{\partial x_k}\,\delta_{ij} \,, \tag{2.4}$$

where $\widehat{S}_{ij}$ is the rate of instantaneous strain tensor defined as:

$$\widehat{S}_{ij} = \frac{1}{2}\left(\frac{\partial \widehat{U}_i}{\partial x_j} + \frac{\partial \widehat{U}_j}{\partial x_i}\right) \,, \tag{2.5}$$

and δ_{ij} is Kronecker symbol.

2.3 Averaging Concepts

Osborne Reynolds (1895) introduced the concept of decomposing the instantaneous values of velocity and pressure into average and fluctuating parts. Average values can be defined in different ways, Monin and Yaglom (1971). The time–averaging procedure is suitable for flows whose "mean" does not change with time (statistically stationary flows).

Accordingly, any flow variable $\widehat{\Phi}(\mathbf{r}, t)$, which is generally a *random* function of position $\mathbf{r}$ and time t, is given as the sum of the time–averaged quantity $\overline{\Phi}(\mathbf{r})$ and the fluctuating part $\varphi'(\mathbf{r}, t)$:

$$\widehat{\Phi}(\mathbf{r}, t) = \overline{\Phi}(\mathbf{r}) + \varphi'(\mathbf{r}, t)$$

$$\overline{\Phi}(\mathbf{r}) = \lim_{T \to \infty} \frac{1}{T} \int_{t_0-T/2}^{t_0+T/2} \widehat{\Phi}(\mathbf{r}, t) dt \,, \tag{2.6}$$

where T is the averaging interval which, in practice, should be at least two orders of magnitude larger than the characteristic turbulence time–scale (Bradshaw, 1996). The choice of the initial time t_0 is usually arbitrary. Since an experiment or a numerical simulation defines $\widehat{\Phi}$ as a discrete function of t, the average value in Equation (2.6), assuming the same sampling interval Δt, is redefined as:

$$\overline{\Phi}(\mathbf{r}) = \lim_{N \to \infty} \frac{1}{N} \sum_{n=0}^{N} \widehat{\Phi}(\mathbf{r}, t_n) \,, \quad t_n = t_0 + n\Delta t \,. \tag{2.7}$$

A general type of averaging is the *ensemble averaging* and it can be applied to any kind of flow. The ensemble average of random functions of space and time is defined as the arithmetic mean over many macroscopically identical realizations of $\widehat{\Phi}(\mathbf{r}, t)$, see for example Landahl and Mollo–Christensen (1986):

$$\left\langle \widehat{\Phi}(\mathbf{r}, t) \right\rangle = \lim_{M \to \infty} \frac{1}{M} \sum_{m=0}^{M} \widehat{\Phi}^{(m)}(\mathbf{r}, t) \,, \tag{2.8}$$

where the symbol $\langle\ \rangle$ denotes the ensemble average, and $\widehat{\Phi}^{(m)}(\mathbf{r}, t)$ is the m–th realization of $\widehat{\Phi}(\mathbf{r}, t)$. For fluid flows, the macroscopically identical realization means that statistically independent flows are exposed to the same set of initial and boundary conditions. Obviously, the ensemble averaged quantity may be time dependent. Using this broader definition of the averaging process, any flow variable can be decomposed into the ensemble mean Φ and random fluctuation φ around the ensemble–mean value Φ :

$$\widehat{\Phi}(\mathbf{r}, t) = \Phi(\mathbf{r}, t) + \varphi(\mathbf{r}, t) \,,$$

$$\Phi(\mathbf{r}, t) = \left\langle \widehat{\Phi}(\mathbf{r}, t) \right\rangle. \tag{2.9}$$

We assume the following averaging rules, Tennekes and Lumley (1972):

$$\langle \varphi(\mathbf{r}, t) \rangle = 0 \,,$$

$$\left\langle \varphi \widehat{\Phi} \right\rangle = \langle \varphi \rangle \, \Phi = 0 \,,$$

$$\left\langle \widehat{\Phi} \widehat{\Psi} \right\rangle = \langle (\Phi + \varphi)(\Psi + \psi) \rangle = \Phi\Psi + \langle \varphi\psi \rangle \,. \tag{2.10}$$

Therefore, Equation (2.9) splits the instantaneous motion, represented by the velocity field $\widehat{U}_i(\mathbf{r}, t)$, into an organized (ensemble averaged) part $U_i = \left\langle \widehat{U}_i \right\rangle$ and a stochastic, turbulent part u_i . The corresponding single–point second moments $\langle u_i u_j \rangle$ (see the last term in Equation (2.10)) are rarely zero. They are interpreted as apparent stresses within the fluid (known also as the kinematic Reynolds stresses) responsible for momentum transport by the turbulence. If one supposes that the coherent structures have their (generally random) phases of occurrence $\vartheta^{(m)}(t)$ at location $\mathbf{r}$, then the *phase average* of any quantity at a constant phase ϑ and a particular location $\mathbf{r}$ is (cf. Minh and Kourta, 1993):

$$\left\langle \widehat{\Phi}(\mathbf{r}, \vartheta) \right\rangle = \lim_{M \to \infty} \frac{1}{M} \sum_{m=0}^{M} \widehat{\Phi}^{(m)} \left[\mathbf{r}, \vartheta + \vartheta^{(m)}(t) \right] . \tag{2.11}$$

For unsteady periodic flows, characterized by the constant period T, the above relation implies the periodic phase average given as:

$$\left\langle \widehat{\Phi}(\mathbf{r}, \vartheta) \right\rangle = \left\langle \widehat{\Phi}(\mathbf{r}, t) \right\rangle = \lim_{M \to \infty} \frac{1}{M} \sum_{m=0}^{M} \widehat{\Phi}^{(m)} \left[\mathbf{r}, t + m\,T \right] , \tag{2.12}$$

where t is now the instance corresponding to the particular phase ϑ. The phase–averaged quantity (not averaged over the phase but at the particular phase) can be further decomposed into a global mean (long time–averaged) component and into a periodic mean component:

$$\left\langle \widehat{\Phi}(\mathbf{r}, t) \right\rangle = \Phi(\mathbf{r}, t) = \overline{\Phi}(\mathbf{r}) + \widetilde{\varphi}(\mathbf{r}, t) . \tag{2.13}$$

The global mean value $\overline{\Phi}$ is given by Equation (2.6), and assuming the periodic component with zero mean ($\overline{\widetilde{\varphi}} = 0$) and uncorrelated periodic and random motions ($\overline{\widetilde{\varphi}\varphi} = 0$), the following relations are obvious:

$$\widehat{\Phi}(\mathbf{r}, t) \;=\; \overline{\Phi}(\mathbf{r}) + \widetilde{\varphi}(\mathbf{r}, t) + \varphi(\mathbf{r}, t) ,$$

$$\varphi'(\mathbf{r}, t) \;=\; \widetilde{\varphi}(\mathbf{r}, t) + \varphi(\mathbf{r}, t) . \tag{2.14}$$

In the literature, the above relation is known as the triple decomposition. It shows a way to distinguish the periodic, coherent motion from the turbulent motion.

2.4   Mean–Flow Equations

The ensemble or phase averaging procedure, based on the decomposition $\widehat{U}_i = U_i + u_i$, $\widehat{P} = P + p$, and applied to the equations of motion, Equations (2.2) and (2.3), yields the following set of the Reynolds–averaged Navier–Stokes (RANS) equations:

$$\frac{\partial(\rho U_j)}{\partial x_j} = 0 \tag{2.15}$$

$$\frac{\partial(\rho U_j)}{\partial t} + \frac{\partial}{\partial x_j}(\rho U_i U_j) = -\frac{\partial P}{\partial x_i} + \frac{\partial}{\partial x_j}(\tau_{ij} + R_{ij}) \,, \tag{2.16}$$

where τ_{ij} denotes the mean viscous stress tensor:

$$\tau_{ij} = 2\,\mu S_{ij} \,, \tag{2.17}$$

proportional to the mean strain rate tensor S_{ij}:

$$S_{ij} = \frac{1}{2}\left(\frac{\partial U_i}{\partial x_j} + \frac{\partial U_j}{\partial x_i}\right) \,. \tag{2.18}$$

The last term is an unknown ensemble–averaged product of one–point random velocity fluctuations:

$$R_{ij} = -\rho\,\langle u_i u_j\rangle \,. \tag{2.19}$$

This term is known as the *Reynolds–stress tensor*. Physically, the Reynolds stresses represent the effect of the stochastic turbulent motion on the mean flow. Thus, the mean flow, seen as unsteady, usually large–scale, organized motion, and represented by the ensemble–averaged quantities, should be resolved numerically, irrespective of its size. On the other hand, fluid structures which have a random physical character are modelled through the Reynolds stresses.

In practice, the Reynolds stresses can be obtained either from the constitutive relation analogous to Equation (2.17) for τ_{ij} or by solving modelled transport equations for the Reynolds stresses. The first approach is known as first–order, eddy–viscosity modelling (EVM), while the second approach describes second–order or differential Reynolds–stress models (DSM). Besides the mean–velocity gradients and the Reynolds stresses, the turbulent kinetic energy k and its viscous dissipation rate ϵ are used to determine all the unknown higher–order correlations.

2.5   Turbulence Transport Equations

The Reynolds–stress transport equation

Derivation of the turbulence transport equations can be found in Hinze (1975) or Speziale (1991). Subtracting Equation (2.16) from (2.3) one obtains the fluctuating momentum equation written in a shorthand form $\mathcal{L}(u_i) = 0$. The Reynolds–stress equations result from the ensemble average of the products:

$$\langle u_i \mathcal{L}(u_j) + u_j \mathcal{L}(u_i)\rangle = 0 \,, \tag{2.20}$$

and they are given as:

$$
\frac{\partial}{\partial t} \left(\rho \left\langle u_i u_j \right\rangle \right) + \frac{\partial}{\partial x_k} \left(\rho U_k \left\langle u_i u_j \right\rangle \right) = \rho \overbrace{\left(-\left\langle u_j u_k \right\rangle \frac{\partial U_i}{\partial x_k} - \left\langle u_i u_k \right\rangle \frac{\partial U_j}{\partial x_k} \right)}^{\mathcal{P}_{ij}}
$$

$$
\overbrace{-\rho\, 2\nu \left\langle \frac{\partial u_i}{\partial x_k} \frac{\partial u_j}{\partial x_k} \right\rangle}^{\varepsilon_{ij}} + \overbrace{\left\langle p \left(\frac{\partial u_i}{\partial x_j} + \frac{\partial u_j}{\partial x_i} \right) \right\rangle}^{\Pi_{ij}} + \overbrace{\frac{\partial}{\partial x_k} \left(\mu \frac{\partial \left\langle u_i u_j \right\rangle}{\partial x_k} \right)}^{\mathcal{D}_{ij}^M}
$$

$$
\overbrace{-\frac{\partial}{\partial x_k} \left[\rho \left\langle u_i u_j u_k \right\rangle + \left\langle p u_i \right\rangle \delta_{jk} + \left\langle p u_j \right\rangle \delta_{ik} \right]}^{\mathcal{D}_{ij}^T} \tag{2.21}
$$

The left–hand side of the above equation represents the local rate of change and convective transport of $\rho \left\langle u_i u_j \right\rangle$. The terms on the right–hand side are:

- $\mathcal{D}_{ij}^M$ – the diffusion by molecular transport,

- $\mathcal{P}_{ij}$ – the production rate by mean velocity gradients,

- Π_{ij} – the pressure–strain correlation term (the redistribution tensor),

- ε_{ij} – the dissipation rate tensor, and

- $\mathcal{D}_{ij}^T$ – the turbulent diffusion by velocity and pressure fluctuations.

In order to close the Reynolds–stress transport equation (2.21), the pressure–strain, dissipation and turbulent diffusion require modelling.

The turbulent kinetic energy equation

Contraction of Equation (2.21) (i.e setting $i = j$) and division by 2 yields a transport equation for the turbulent kinetic energy per unit mass – a scalar defined as half the sum of the normal Reynolds stresses:

$$
k = \frac{1}{2} \left\langle u_i^2 \right\rangle = \frac{1}{2} \left(\left\langle u^2 \right\rangle + \left\langle v^2 \right\rangle + \left\langle w^2 \right\rangle \right). \tag{2.22}
$$

Its transport equation is:

$$
\frac{\partial}{\partial t} \left(\rho k \right) + \frac{\partial}{\partial x_k} \left(\rho U_k k \right) = \overbrace{\frac{\partial}{\partial x_k} \left(\mu \frac{\partial k}{\partial x_k} \right)}^{\mathcal{D}_k^M} \overbrace{- \rho \left\langle u_i u_k \right\rangle \frac{\partial U_i}{\partial x_k}}^{-\rho \mathcal{P}_k} \overbrace{- \rho\, \nu \left\langle \frac{\partial u_i}{\partial x_k} \frac{\partial u_i}{\partial x_k} \right\rangle}^{\epsilon}
$$

$$
\overbrace{- \frac{\partial}{\partial x_k} \left[\frac{1}{2} \rho \left\langle u_i u_i u_k \right\rangle + \left\langle p u_k \right\rangle \right]}^{\mathcal{D}_k^T}. \tag{2.23}
$$

Phenomenologically, the local and spatial rates of change of k are balanced by the rates of viscous diffusion $\mathcal{D}_k^M$, production $\mathcal{P}_k$, dissipation ϵ, and turbulent diffusion $\mathcal{D}_k^T$. The turbulent kinetic energy, i.e. $\sqrt{k}$, has been used to represent the turbulence velocity scale.

The turbulent dissipation rate transport equation

Combined with k, the isotropic part of the dissipation rate tensor ϵ_{ij}

$$\epsilon = \frac{1}{2}\varepsilon_{kk} = \nu\left\langle \frac{\partial u_i}{\partial x_k}\frac{\partial u_i}{\partial x_k}\right\rangle , \tag{2.24}$$

has been a very popular turbulence quantity to describe the turbulence time and length scales. Its transport equation is given as the moment:

$$2\nu\left\langle \frac{\partial u_i}{\partial x_k}\frac{\partial}{\partial x_k}[\mathcal{L}(u_i)]\right\rangle = 0 . \tag{2.25}$$

Thus, ϵ is governed by the following scalar equation:

$$\frac{\partial \epsilon}{\partial t} + \frac{\partial}{\partial x_j}(U_j\epsilon) = \overbrace{-2\nu\left\langle \frac{\partial u_i}{\partial x_k}\frac{\partial u_j}{\partial x_k}\right\rangle \frac{\partial U_i}{\partial x_j}}^{\mathcal{P}_\epsilon^1} \overbrace{-2\nu\left\langle \frac{\partial u_k}{\partial x_j}\frac{\partial u_k}{\partial x_i}\right\rangle \frac{\partial U_i}{\partial x_j}}^{\mathcal{P}_\epsilon^2}$$

$$\overbrace{-2\nu\left\langle u_j\frac{\partial u_i}{\partial x_k}\right\rangle \frac{\partial^2 U_i}{\partial x_j\partial x_k}}^{\mathcal{P}_\epsilon^3} \overbrace{-2\nu\left\langle \frac{\partial u_i}{\partial x_k}\frac{\partial u_j}{\partial x_k}\frac{\partial u_i}{\partial x_j}\right\rangle}^{\mathcal{P}_\epsilon^4} - \overbrace{2\nu^2\left\langle \left(\frac{\partial^2 u_i}{\partial x_j\partial x_k}\right)^2\right\rangle}^{\Upsilon_\epsilon}$$

$$+ \overbrace{\frac{\partial}{\partial x_j}\left(\nu\frac{\partial \epsilon}{\partial x_j}\right)}^{\mathcal{D}_\epsilon^M} - \overbrace{\frac{\partial}{\partial x_j}\left[\nu\left\langle u_j\left(\frac{\partial u_i}{\partial x_k}\right)^2\right\rangle + \frac{2\nu}{\rho}\left\langle \frac{\partial u_j}{\partial x_k}\frac{\partial p}{\partial x_k}\right\rangle\right]}^{\mathcal{D}_\epsilon^T} . \tag{2.26}$$

Again, one can identify the terms on the right–hand side of the ϵ–equation as the viscous diffusion $\mathcal{D}_\epsilon^M$, the production $\mathcal{P}_\epsilon = \mathcal{P}_\epsilon^1 + \mathcal{P}_\epsilon^2 + \mathcal{P}_\epsilon^3 + \mathcal{P}_\epsilon^4$, the viscous destruction Υ_ϵ, and the turbulent diffusion $\mathcal{D}_\epsilon^T$. Tennekes and Lumley (1972) analysed the order of magnitude of terms in the transport equation of fluctuating vorticity correlation $\langle \omega_i\omega_i\rangle$. Note that ω_i is a random part of instantaneous vorticity $\widehat{\Omega}_i$:

$$\widehat{\Omega}_i = e_{ijk}\frac{\partial \widehat{U}_k}{\partial x_j} , \tag{2.27}$$

i.e. $\widehat{\Omega}_i = \Omega_i + \omega_i$. They have shown that at high turbulence Reynolds numbers $Re_t \gg 1$, where Re_t is defined as:

$$Re_t = \frac{k^2}{\nu\epsilon} , \tag{2.28}$$

the total rate of change of ϵ , its production by vortex stretching $\mathcal{P}_\epsilon^4$ and viscous destruction Υ_ϵ are of the order of $\mathcal{O}(Re_t^{-1/2})$, while all other terms are of the order of $\mathcal{O}(Re_t^{-1})$ or less. Since $\epsilon = \nu \langle \omega_i \omega_i \rangle$ for homogeneous flows, Tennekes and Lumley's analysis has been widely extrapolated to the ϵ–balance, which is therefore at high Re_t dominated by the difference $\mathcal{P}_\epsilon^4 - \Upsilon_\epsilon$. The DNS data for the core region of the low–Re channel flow, Mansour et al. (1988), confirm the analysis of Tennekes and Lumley. However, near the wall the production terms by deformation of mean flow $\mathcal{P}_\epsilon^1$ and $\mathcal{P}_\epsilon^2$ are of the same order as the $\mathcal{P}_\epsilon^4$ term. The relatively smaller gradient production term $\mathcal{P}_\epsilon^3$ is comparable to the turbulent diffusion $\mathcal{D}_\epsilon^T$.

2.6   Modelling the Reynolds–Stress Tensor

The ensemble–averaging introduces the unknown Reynolds stresses $R_{ij} = -\rho \langle u_i u_j \rangle$ in the momentum equations. Consequently the Reynolds–stress closure problem arises, that is, the Reynolds stresses have to be determined by the turbulence model. The current turbulence models can be basically classified into three groups (Hanjalic, 1994), namely:

- Eddy Viscosity Models (EVM),

- Reynolds stress transport equation models (Differential Stress Models – DSM), and

- Hybrid models, like Algebraic Stress Models (ASM), that are hierarchically between EVM and DSM models.

With the exception of ASM models, both EVM and DSM models have been used to compute vortex shedding flows around bluff bodies. In this work, the two–equation EVM models are employed and their description is given below.

2.6.1   The eddy–viscosity formulation

These models are based on Bousinessq's analogy between molecular and turbulent transport in which the Reynolds stresses are obtained from a "constitutive" equation similar to Equation (2.17):

$$-\rho \langle u_i u_j \rangle = -\frac{2}{3}\rho k \delta_{ij} + 2\mu_t S_{ij} \, , \qquad (2.29)$$

where μ_t is the turbulent or eddy viscosity. The first term on the right–hand side of Equation (2.29) was added after Boussinesq to ensure that the model contracts properly. It represents the mean turbulence pressure which is usually added to the unknown static pressure of the resolved motion P by replacing it by the sum $(P + \frac{2}{3}\rho k)$. By using

different arguments – analogy with the kinetic theory of gases, dimensional analysis and phenomenological models (see for example Speziale, 1991), the turbulent viscosity is taken to be:

$$\mu_t = \rho \frac{\ell_t}{T_t} \ell_t = \rho v_t \ell_t \,, \tag{2.30}$$

with ℓ_t, t_t, and v_t denoting characteristic turbulence length–, time– and velocity scales, respectively.

2.6.2   Two–equation $k - \epsilon$ models

Together with the mean flow equations, transport equations for two turbulence parameters, that define characteristic turbulence scales for the turbulent viscosity, Equation (2.30), are solved in these models. Since Kolmogorov's pioneering work 1941 (cf. Spalding, 1991), the turbulent energy k has been used without exception as the first variable in two–equation models.

In order to close the equation of k, one can assume that its spatial gradient drives the turbulent transport by triple product of velocity fluctuations. The same assumption is physically unsound for the transport by pressure fluctuations, Bradshaw (1994). Since it appears that the turbulent transport by the velocity fluctuations is dominant one, modelling of both terms by a gradient transport hypothesis:

$$\mathcal{D}_k^T = -\frac{\partial}{\partial x_j} \left[\frac{1}{2} \rho \langle u_k u_k u_j \rangle + \langle p u_j \rangle \right] = \frac{\partial}{\partial x_j} \left(\frac{\mu_t}{\sigma_k} \frac{\partial k}{\partial x_j} \right) \,, \tag{2.31}$$

can be considered as an intentional approximation. A non–dimensional constant $\sigma_k \approx 1$ is the effective Prandtl number for the diffusion of k.

Harlow and Nakayama (1967) introduced the turbulent dissipation rate $\epsilon \propto k^{3/2}/\ell_t$ as the second turbulence scaling variable. Other alternative variables have also been used – interesting comments have been given by Spalding (1991) and Wilcox (1993b). Based on the work of Davydov (1961), Hanjalic (1970) (see also Hanjalic and Launder, 1972) proposed the modelled ϵ–equation for high Re–number flows. The gradient transport hypothesis is used to represent the turbulent diffusion term $\mathcal{D}_\epsilon^T$:

$$\mathcal{D}_\epsilon^T = \frac{\partial}{\partial x_j} \left(\frac{v_t}{\sigma_\epsilon} \frac{\partial \epsilon}{\partial x_j} \right) \,. \tag{2.32}$$

At high Re–numbers the source term $S_\epsilon = \mathcal{P}_\epsilon - \Upsilon_\epsilon \approx \mathcal{P}_\epsilon^4 - \Upsilon_\epsilon$ is assumed to be proportional to the production and dissipation of k, scaled by turbulence time scale k/ϵ (see for example Hanjalic, 1994 or Rodi and Mansour, 1993)

$$S_\epsilon = \mathcal{P}_\epsilon - \Upsilon_\epsilon = (C_{\epsilon 1} \mathcal{P}_k - C_{\epsilon 2} \epsilon) \frac{\epsilon}{k} \,. \tag{2.33}$$

However, other researches, among them Yakhot et al. (1992), Yakhot and Smith (1992), Jovanovic et al. (1995), argue that the term $C_{\epsilon 1}\mathcal{P}_k\epsilon/k$ approximates the production term $\mathcal{P}_\epsilon^1$, while the term $C_{\epsilon 2}\epsilon^2/k$ represents the difference of two dominant terms $(\mathcal{P}_\epsilon^4 - \Upsilon_\epsilon)$. Hanjalic (1970) also established empirical coefficients for high Re–number flows that differ a little from values proposed by other authors (cf. Jones and Launder, 1972, and Launder and Spalding, 1974). Thus the basic $k - \epsilon$ model, often referred to as the *standard* $k - \epsilon$ model (SKE), is described by the following equations:

$$\mu_t = \rho C_\mu \frac{k^2}{\epsilon} , \tag{2.34}$$

$$\frac{\partial(\rho k)}{\partial t} + \frac{\partial}{\partial x_j}\left(\rho k U_j\right) = \rho\left(\mathcal{P}_k - \epsilon\right) + \frac{\partial}{\partial x_j}\left[\left(\mu + \frac{\mu_t}{\sigma_k}\right)\frac{\partial k}{\partial x_j}\right] , \tag{2.35}$$

$$\frac{\partial(\rho\epsilon)}{\partial t} + \frac{\partial}{\partial x_j}\left(\rho\epsilon U_j\right) = \rho\left(C_{\epsilon 1}\mathcal{P}_k - C_{\epsilon 2}\epsilon\right)\frac{\epsilon}{k} + \frac{\partial}{\partial x_j}\left[\left(\mu + \frac{\mu_t}{\sigma_\epsilon}\right)\frac{\partial\epsilon}{\partial x_j}\right] , \tag{2.36}$$

where $\mathcal{P}_k$ is the production of the turbulent kinetic energy. The production of k is given as:

$$\mathcal{P}_k = -\langle u_i u_j\rangle\frac{\partial U_i}{\partial x_j} = \nu_t S^2 , \tag{2.37}$$

with S representing the strain tensor invariant defined by

$$S = \sqrt{2\,S_{ij}\,S_{ij}} . \tag{2.38}$$

The Renormalization Group Theory (RNG) applied to turbulence modelling by Yakhot and Orszag (1986), and the modification to ϵ–equation by Yakhot et al. (1992) (not strictly based on the RNG theory) offers an alternative RNG $k - \epsilon$ model. Compared to the basic $k - \epsilon$ model, the ϵ–equation has now an additional production term $(-\mathcal{P}_\epsilon^R(S^*))$ which is supposed to model the term $\mathcal{P}_\epsilon^2$ (the production by the mean velocity gradient), thus:

$$\mathcal{P}_\epsilon^R(S^*) = \left(1 - \frac{S^*}{S_0^*}\right)\frac{S^*}{1 + \beta_0(S^*)^3} , \tag{2.39}$$

$$S^* = S\frac{k}{\epsilon} , \tag{2.40}$$

where $S_0^* = 4.38$ and $\beta_0 = 0.012$. The model coefficients associated with the standard and RNG $k - \epsilon$ models are given in Table 2.1, where now the coefficient $C_{\epsilon 1}^*$ replaces the coefficient $C_{\epsilon 1}$ in Equation (2.36).

$k - \epsilon$ model	C_μ	σ_k	σ_ϵ	$C_{\epsilon 1}$	$C_{\epsilon 1}^*$	$C_{\epsilon 2}$
Standard	0.09	1.0	1.3	1.45	1.45	1.90
RNG	0.0845	0.719	0.719	1.42	$1.42 - \mathcal{P}_\epsilon^R(S^*)$	1.68

Table 2.1: Model constants for the high Reynolds number $k - \epsilon$ models.

The above two–equation models represent the simplest and *complete* turbulence closures based on the linear relationship between the Reynolds stress tensor and local mean strain rate tensor, Equation (2.29), where the proportionality coefficient is a scalar quantity – the turbulent viscosity μ_t. This simple framework is computationally efficient but has some physical shortcomings. The relation (2.29) can be expressed through anisotropy stress tensor b_{ij}:

$$b_{ij} = \frac{1}{2} \left(\frac{\langle u_i u_j \rangle}{k} - \frac{2}{3}\delta_{ij} \right) = -C_\mu \frac{k}{\epsilon} S_{ij} \,. \tag{2.41}$$

In reality, the stress anisotropy is far from what is predicted by the above model. Well–known examples, where the linear relation (2.29) or (2.41) badly predicts the normal stresses, are homogeneous shear flows and the fully developed flow in non–circular ducts where the turbulence–driven secondary flow is not captured. The linear models work well for simple shear flows and even for some recirculating flows dominated by pressure gradients – see the recent review of Hanjalic (1994). However, for complex flows (three–dimensional), involving separation, streamline curvature, rotation, buoyancy and other effects, the $k - \epsilon$ model can give satisfactory results if adequate modifications are introduced. Those that can improve the predictions of turbulent vortex shedding flows are considered in the next section.

2.7 Turbulence Model Development

Ideally, the turbulence model should be able to describe correctly the flow phenomena which take place in characteristic flow areas such as the stagnation region, the boundary layers, the shear layers and the wake (Figure 1.1). Unfortunately, the $k - \epsilon$ model used in conjunction with the wall functions cannot simulate the transition to turbulence in the laminar boundary layers and/or predict accurately the points of flow separation and reattachment. Therefore, there is limited scope to improve the performance of the conventional $k - \epsilon$ model in stagnation flows. 'Conventional' is used here to describe models that are calibrated with reference to steady–flow data. When separation is unsteady, intuition suggests that the conventional models should be modified for unsteady flows to take into account the effects of the organized (periodic) flow structures (Younis, 1988). This

section considers modifications related to the conventional $k - \epsilon$ model and introduces a new, unsteady modification.

2.7.1   Modifications to the conventional $k - \epsilon$ model

By exploiting the potential flow solution, it can be shown that the flow approaching a stagnation point is governed by the normal strains $S_{xx} = -S_{yy} \propto 0.5 U_0 D^2 / x^3$ (the x–coordinate has the same direction as the approaching flow and starts from the cylinder centre). The shear strain is negligible ($S_{xy} << S_{xx}$) and so is the vorticity Ω. The production of the turbulent kinetic energy, Equation (2.37), will be incorrectly obtained due to the inability of the $k - \epsilon$ model to resolve the stress anisotropy there (note that the shear stress production in that region is negligible). It was reported that the linear RNG model performs better than the standard one in regions around the stagnation point (Orszag et al., 1993), i.e. in front of the bluff body. On the other hand, the standard $k - \epsilon$ model overpredicts the level of the turbulent kinetic energy, and, transported downstream, this excessive level of k can seriously affect the accuracy of model predictions. Illustrative examples, apart from those related to vortex shedding (Section 1.3.2), were presented by Taulbee and Tran (1988) (flow around a circular cylinder), Launder (1991) (flow over a rectangular obstacle at the wall) and Craft et al. (1993) (impinging jet flow).

As observed by Durbin (1996), the transport equations for k and ϵ are coupled and during an iterative solution the turbulent time scale

$$T_t = \frac{k}{\epsilon} \tag{2.42}$$

can be sufficiently large (especially in the case of the standard $k - \epsilon$ model) as to diminish the production of ϵ:

$$\mathcal{P}_\epsilon = C_{\epsilon 1}^* \frac{\mathcal{P}_k}{T_t} . \tag{2.43}$$

This consequently leads to high levels of turbulent energy. Imposing the realizability constraint on the eddy–viscosity relation for the Reynolds stresses, written in the principal axes of S_{ij}, Durbin (1996) derived an upper bound on the turbulent time scale. This approach and other strategies which sensibly amplify the production of ϵ will prevent excessive levels of the turbulent kinetic energy in the stagnation flow region. For example, in the RNG model the production term in the dissipation equation depends on the non–dimensional strain invariant $S^* = Sk/\epsilon$ which provides increased values of the ϵ–production (obviously for $S^* > S_0^* = 4.38$, Equation (2.39)).

The idea of Hanjalic and Launder (1980) was to promote the influence of irrotational deformations or equivalently to augment the effects of normal strains. Their original

proposal can be expressed as:

$$C^*_{\epsilon 1} = C'_{\epsilon 1} - C_{\epsilon 3}\frac{\Omega^2}{S^2} \, , \tag{2.44}$$

with $C'_{\epsilon 1} = 4.44$, $C_{\epsilon 3} = 3$. Note that Ω denotes the mean vorticity tensor invariant, which is defined as:

$$\Omega = \sqrt{2\,W_{ij}\,W_{ij}} \, , \tag{2.45}$$

where W_{ij} is the mean vorticity (rotation) tensor:

$$W_{ij} = \frac{1}{2}\left(\frac{\partial U_i}{\partial x_j} - \frac{\partial U_j}{\partial x_i}\right) \, . \tag{2.46}$$

If one applies the above proposal to the shear flow (as intended by Hanjalic and Launder), where $\Omega^2 \approx S^2 - S^2_{nn}$ (the strain invariant S^2 can be split into the normal (irrotational) part S^2_{nn} and shear (rotational) part S^2_{ns}), the basic idea of the preferential influence of normal strains (stresses) can be clearly demonstrated by assuming that $(C'_{\epsilon 1} - C_{\epsilon 3})$ is greater (or equal) than the original constant $C_{\epsilon 1} = 1.44$, thus:

$$C^*_{\epsilon 1} = (C'_{\epsilon 1} - C_{\epsilon 3}) + C_{\epsilon 3}\frac{S^2_{nn}}{S^2} \, . \tag{2.47}$$

Albeit not tensor–invariant, the above preferential dissipation modification (PDM) can be implemented in the streamline direction (2D cases) as proposed by Leschziner and Rodi (1981). Various values for the constants $C'_{\epsilon 1}$ and $C_{\epsilon 3}$ have been reported in the literature; Leschziner and Rodi used $C'_{\epsilon 1} = 2.24$ and $C_{\epsilon 3} = 0.8$ for steady flow computations. Due to small rotational strains in the stagnation flow region, the effective coefficient $C^*_{\epsilon 1}$ is much higher (order of 2) than for the standard model. This reduces the levels of k in this region.

Another simple idea, emanating from Kato and Launder (1993), has been exploited recently in order to avoid the high levels of k in the stagnation region. Kato and Launder calculated the turbulent energy production $\mathcal{P}_k$ from the following expression:

$$\mathcal{P}_k = \nu_t S\Omega \, . \tag{2.48}$$

As mentioned earlier, Ω is virtually zero at the stagnation point and the Kato–Launder modification prevents the excessive growth of k. Applied to the vortex shedding flows around a square cylinder in a free stream (Kato and Launder, 1993) and near the wall (Bosch and Rodi, 1996) it yielded reasonable predictions. Jin and Braza (1994) considered a similar idea for unsteady separated flows around airfoils. They calculated $\mathcal{P}_k$ by using the vorticity invariant only:

$$\mathcal{P}_k = \nu_t\Omega^2 \, . \tag{2.49}$$

The ideas of Kato and Launder and Jin and Braza can be implemented in a consistent way by redefining the eddy–viscosity ν_t. In this work, a new formulation for the time scale, denoted as T_ω, which can replace the usual turbulent time scale T_t in an eddy viscosity equation $\nu_t = C_\mu k^2/\epsilon = C_\mu k T_t$, will be investigated. This formulation reads:

$$T_\omega = \frac{\Omega}{S}T_t + T_k = \frac{\Omega}{S}\frac{k}{\epsilon} + \sqrt{\frac{\nu}{\epsilon}}\,. \tag{2.50}$$

The time scale (here T_ω) is probably a more complex function of the turbulent and Kolmogorov time scales but the above simple relation achieves similar effects for stagnation flows as the modifications of Kato and Launder (1993) or Jin and Braza (1995).

2.7.2 Unsteady modification

In the past, turbulence models were developed with reference to statistically steady flows. Therefore, there is cause to question whether these models are applicable to the dynamics and turbulence of unsteady flows where both organized (periodic) and random turbulent fluctuations coexist; see also Younis (1988) and Minh and Kourta (1993). In his comments on turbulence, Lumley (1992) considered the most suitable choice for the time scale of a material region. He proposed a transport equation for an inverse time scale $\mathcal{S}$ and a dissipation rate model that depends on the history of this time scale. More precisely, only the production term of the dissipation equation differs from the standard modelling practice for ϵ. This term is written as:

$$\mathcal{P}_\epsilon \propto k\mathcal{S}\frac{\epsilon}{k}\,, \tag{2.51}$$

and for near equilibrium flows the inverse time scale $\mathcal{S}$ becomes the strain invariant S. The initial results for the plain free jet indicated better agreement with data than the standard $k - \epsilon$ model.

Obviously, Lumley's idea focuses on the definition of a time scale that is used to calculate the production term of the dissipation rate. Therefore, as suggested earlier by Younis (1988), there is the scope to sensitize the production of ϵ to the effects of unsteady periodicity while preserving the simplicity and robustness of the $k - \epsilon$ model. After various possible strategies, the following functional form for the model coefficient $C_{\epsilon 1}^*$ was developed:

$$C_{\epsilon 1}^* = C_{\epsilon 1}\left(1 + C_t\frac{k}{\epsilon}\frac{|\partial(q+k)/\partial t|}{q+k}\right)\,, \tag{2.52}$$

where q represents kinetic energy per unit mass of the ensemble–mean flow:

$$q = \frac{1}{2}U_i^2 = \frac{1}{2}(U^2 + V^2 + W^2)\,. \tag{2.53}$$

A new coefficient C_t is introduced; its value is taken as $C_t = 0.38$ assigned by computer optimization. Although the physical importance of the above unsteady modification will be sought through its *results*, possible justification for this proposal are given below.

We recognize the existence of various length and time scales in turbulent flows. In order to bring into play the time scale of the organized, periodic motion it is instructive to recall the definition of the Taylor micro–scale λ (Lesieur, 1987, p. 91):

$$\lambda = \sqrt{\frac{\langle u_i^2 \rangle}{\langle (e_{jkl} \partial u_l / \partial x_k)^2 \rangle}} \ . \tag{2.54}$$

By analogy with the above definition, the time scale of periodic motion can be introduced as:

$$T_p \propto \sqrt{\frac{\langle \tilde{q}^2 \rangle}{\langle (\partial \tilde{q}/\partial t)^2 \rangle}} = \frac{\tilde{q}}{|\partial \tilde{q}/\partial t|} \ , \tag{2.55}$$

where $\tilde{q}$ is the periodic component of the ensemble–mean kinetic energy. The latter can be written as:

$$q = \langle \hat{q} \rangle = \frac{1}{2} U_i^2 = \bar{q} + \tilde{q} \ . \tag{2.56}$$

The periodic component $\tilde{q}$ is unknown during an iterative solution. Since $\partial \tilde{q}/\partial t = \partial q/\partial t$, one can decide to use the ensemble–mean value q instead of $\tilde{q}$ in Equation (2.55). In order to avoid the theoretical singular solution when using q, the turbulent kinetic energy was added to the mean flow energy so that T_p reads in a final form as:

$$T_p \propto \frac{q + k}{|\partial (q + k)/\partial t|} \ . \tag{2.57}$$

It remains to look for a functional form which will take into account both the usual turbulent time scale $T_t = k/\epsilon$ and the time scale of periodic motion T_p. A simple linear combination of inverse values written below

$$\mathcal{P}_\epsilon = C_{\epsilon 1} \mathcal{P}_k \left(\frac{1}{T_t} + C_t \frac{1}{T_p} \right) \tag{2.58}$$

leads to Equation (2.52) for the modified coefficient $C_{\epsilon 1}^*$.

2.8 Near–Wall Treatment

The models presented so far are of the 'high Reynolds number' type in that they are not applicable in the near–wall region. The latter is characterized by high velocity gradients

and dominant molecular effects. In essence, the wall modifies the mean flow and the turbulence in its vicinity through *viscous* as well as *non–viscous* effects, the latter being due to the kinematic blocking of the velocity fluctuations normal to the wall (see, for example, Durbin, 1991). Also, the fluctuating pressure field is modified by the presence of the wall. In practice, the above effects have been modelled together by using either *low Reynolds number* turbulence models or *wall function* methods. The wall functions, which are used in the present work, are described below.

The universal velocity profile in the near–wall region, the "law of the wall", forms the basis of the 'wall–function' approach. It is given as:

$$U^+ = \frac{U}{U_\tau} = \frac{1}{\kappa} \ln\left(Ey^+\right) , \tag{2.59}$$

$$U_\tau = \sqrt{\frac{|\tau_w|}{\rho}} , \tag{2.60}$$

$$y^+ = \frac{\rho U_\tau y}{\mu} , \tag{2.61}$$

where U_τ is the friction velocity, y^+ is the non–dimensional distance of the near–wall point from the wall and τ_w denotes the wall shear stress. Further, $\kappa \approx 0.41$ is the von Karman constant, while E is another empirical constant whose value depends on the wall roughness; for smooth walls $E \approx 9$. The logarithmic velocity profile (log–law) exists for simple boundary layer flows in local equilibrium, that is when $\mathcal{P}_k = \epsilon$. It is valid for turbulent layer ($y^+ > 30$) and also within the buffer zone ($5 \leq y^+ \leq 30$) where the different constants κ and E apply. For convenience, the buffer zone can be excluded by extending the viscous and turbulent layers up to their point of intersection ($y^+ \approx 11.6$). In terms of Prandtl's mixing–length theory, the log–law can be obtained by assuming that the turbulence length scale ℓ_m in Equation (2.30) is proportional to y:

$$\ell_m = \kappa y . \tag{2.62}$$

When the turbulent layer is in local equilibrium, the following relations can be derived (say at point P within the turbulent layer):

$$U_\tau = C_\mu^{1/4} k_P^{1/2} \quad \text{or} \quad k_P = \frac{U_\tau^2}{\sqrt{C_\mu}} , \tag{2.63}$$

$$\epsilon_P = \frac{U_\tau^3}{\kappa y_P} = \frac{C_\mu^{3/4} k_P^{3/2}}{\kappa y_P} , \tag{2.64}$$

$$\mu_t = \rho \kappa U_\tau y_P = \rho \kappa C_\mu^{1/4} k_P^{1/2} y_P . \tag{2.65}$$

The iterative solution of Equation (2.59) yields τ_w, and Equations (2.63) and (2.64) can be then used to specify the boundary conditions for k and ϵ.

Most flows,however, do not generally follow the log–law and turbulence is far from the local equilibrium. By assuming that Prandtl–Kolmogorov relation for eddy viscosity near the wall, Equation (2.65) is valid, an integration of:

$$\tau_w = \mu_t \frac{\partial U}{\partial y} = \rho \kappa C_\mu^{1/4} k^{1/2} y \frac{\partial U}{\partial y} \, , \tag{2.66}$$

gives Launder and Spalding's (1974) log–low:

$$\frac{U}{U_\tau} = \frac{U_\tau}{\kappa U_*} \ln(E Y_P^*) \, , \tag{2.67}$$

$$U_* = C_\mu^{1/4} k^{1/2} \, , \tag{2.68}$$

$$Y_P^* = \frac{U_* y_P}{\nu} \, . \tag{2.69}$$

The ratio (U_*/U_τ) can be seen as a non–equilibrium index that changes the slope of the velocity profile in the turbulent layer (cf. Kim and Choudhury, 1995). For $U_*/U_\tau = 1$ the universal log–law, Equation(2.59), is recovered. Thus, we use the above equation to evaluate, explicitly, the wall shear stress:

$$\tau_w = \frac{\rho \kappa U_*}{\ln(E Y_P^*)} U_P \, . \tag{2.70}$$

The value of the turbulence kinetic energy at the node P is obtained from the solution of its equation with the production rate calculated from:

$$\rho \mathcal{P}_k = \tau_w \left(\frac{\partial U}{\partial y} \right)_{log-law} . \tag{2.71}$$

The value and the diffusion flux of k at the wall are taken to be zero. The transport equation of ϵ is not solved for the near–wall cells – its value is fixed according to Equation (2.64) which assumes that the turbulence is in local equilibrium. The same value is assigned to ϵ which appears in the k–equation.

Both the traditional, Equation (2.59), and Launder and Spalding's log–law, Equation (2.67), are based on the assumption of a constant shear stress through the near–wall layer. However, Launder and Spalding's approach can take into account some non–equilibrium departures expressed through the ratio (U_*/U_τ), i.e. when the production of k is not in balance with ϵ. Also, the direct relation between the wall shear stress and near–wall velocity, Equation (2.70), ensures that the correct wall shear–stress sign is obtained,

and avoids numerical difficulties associated with the use of the standard logarithmic profile (2.59) near separation points.

Many alternative variations on the wall function methods have been reported in the literature (e.g. Chieng and Launder, 1980; Amano, 1985; Launder, 1988; Ciofalo and Collins, 1989; Kim and Choudhury, 1995). They all consider the near–wall cell as one divided into the viscous and turbulent layer (two–layer wall function approach). This leads to more elaborate reconstructions of the average values of k and ϵ at the near–wall cells. Note that Kim and Choudhury extended this two–layer approach to include the pressure gradient effect. Each of these alternative methods was validated against a limited number of experiments, without producing significant improvements to justify its use in preference to the standard formulation.

2.9 Closure

This chapter presented the basic equations of incompressible, unsteady turbulent flows and considered the closure of the ensemble–averaged equations. The mathematical background of the two–equation $k - \epsilon$ models was emphasized, together with the physical arguments that were used to justify these models. Various modifications, related mainly to the generation term of the ϵ–equation, and their performances were discussed. It appeared that the RNG model could be a good choice to calculate flows that include stagnation and recirculation regions. This model, the preferential dissipation modification, originally due to Hanjalic and Launder (1980), and two new modifications proposed in this Chapter will be tested in Chapter 5. Finally, the important issue of near–wall modelling by the wall functions was discussed.

Chapter 3

NUMERICAL METHOD

3.1 Introduction

This chapter presents the main features of the numerical method employed in this work. As discussed in Chapter 2, description of the flow field requires the solution of a coupled system of nonlinear differential equations, together with specified initial and boundary conditions. These equations need to be *discretised* in order to obtain a system of algebraic equations at a set of discrete locations in space and time. A typical algebraic equation for a general variable ϕ at node P, surrounded by N (internal) neighbouring nodes denoted as N_j, $j = 1, N$, may be written as:

$$a_P \, \phi_P = \sum_{j=1}^{N} a_j \, \phi_{N_j} + S_P \, , \tag{3.1}$$

where a_P and a_j are coefficients, and S_P is the source term. Thus, the discretisation process converts the differential transport equations into a set of algebraic equations. Their solution describes the flow field by variables values at a finite number of discrete points in space and time. The discretisation method selected here is the finite volume method which uses the integral form of transport equations applied to a finite set of non-overlapping regions called control volumes (CV) or cells. The Cartesian coordinate system is used and the vector and tensor quantities are defined in terms of Cartesian components. In this way the strong conservation form of the transport equations can be preserved. The two–dimensional flow solving code used in this work can handle block–structured grids. It is derived from one developed by Peric (1985) for single–block structured grids and steady flows.

The chapter continues with Section 3.2 which considers a generic integral transport equation which is the starting point for the finite-volume method. Section 3.3 describes the discretisation procedure. It considers first the numerical grid and geometrical data which are required to calculate various surface and volume integrals. Then the time in-

tegration process is outlined, followed by details about the evaluation of the fluxes and the source terms. The central and upwind convective differencing schemes are also considered here. The resulting system of algebraic equations is then briefly presented. The high–resolution schemes are introduced in Section 3.4. The pressure–velocity coupling is achieved by the iterative SIMPLE algorithm which is presented in Section 3.5. Implementation of boundary conditions is explained in Section 3.6. Finally, the overall solution procedure is outlined in Section 3.7.

3.2   General Forms of Transport Equations

It is convenient to consider a single generic transport equation for a variable ϕ, where ϕ can stand for a scalar (k, ϵ), vector (U_i) or tensor $(\langle u_i u_j \rangle)$ field. The differential form of this equation can be written as:

$$\frac{\partial(\rho\phi)}{\partial t} + \frac{\partial}{\partial x_k}(\rho\phi U_k) - \frac{\partial}{\partial x_k}\left(\Gamma_\phi \frac{\partial\phi}{\partial x_k}\right) = s_\phi , \tag{3.2}$$

where Γ_ϕ is the diffusion or exchange coefficient for the quantity ϕ and s_ϕ denotes the specific source or sink of ϕ. Another, integral, form of the governing equations can be obtained by carrying out an integration over a given volume V, bounded by piecewise smooth surfaces $\mathcal{A}$ with the outward unit normal vector $\mathbf{n} = n_k \mathbf{i}_k$. Gauss's divergence theorem for the vector field (and its related theorems for scalar and tensor fields) is used (Borisenko and Tarapov, 1968):

$$\int_\mathsf{V} \nabla(\cdots)d\mathsf{V} = \oint_\mathcal{A} \mathbf{n}(\cdots)d\mathcal{A} , \tag{3.3}$$

where the ∇ operator is $\nabla = \mathbf{i}_k \frac{\partial}{\partial x_k}$ and $(\cdots)$ denotes some quantity or expression preceded when necessary by a dot $(\cdot)$ or a cross $(\times)$. Thus, the integral form of the general equation is:

$$\underbrace{\frac{d}{dt}\int_\mathsf{V} \rho\phi\, d\mathsf{V}}_{Rate\ of change:\ \mathcal{R}} + \underbrace{\oint_\mathcal{A} \rho\phi U_k n_k d\mathcal{A}}_{Convection:\ \mathcal{C}} - \underbrace{\oint_\mathcal{A} \Gamma_\phi \frac{\partial\phi}{\partial x_k}\, n_k\, d\mathcal{A}}_{Diffusion:\ \mathcal{D}} =$$

$$\underbrace{\int_\mathsf{V} s_\phi^\mathsf{V}\, d\mathsf{V} + \oint_\mathcal{A} s_\phi^\mathcal{A}\, n_k\, d\mathcal{A}}_{Sources:\ \mathcal{S}} . \tag{3.4}$$

The source terms in the integral relation (3.4) $\mathcal{S}$ are in balance with the terms on the left-hand side of the equation representing the rate of change $\mathcal{R}$ and the net fluxes by convection $\mathcal{C}$ and diffusion $\mathcal{D}$. They consist of the real (volumetric) source terms s_ϕ^V and those ($s_\phi^\mathcal{A}$) that are related to the cell–face area (the diffusion flux not represented by

$\Gamma_\phi(\partial\phi/\partial x_k)$ and the pressure forces). The diffusion coefficients and source terms are given in Table 3.1 for flow variables which describe the $k - \epsilon$ model. Depending on the

ϕ	Γ_ϕ	s_ϕ^V	s_ϕ^A
U_i	$\mu + \mu_t$	$\rho f_{bi} = 0$	$(\mu + \mu_t)\frac{\partial U_k}{\partial x_i} - (P + \frac{2}{3}\rho k)$
k	$\mu + \frac{\mu_t}{\sigma_k}$	$\rho(\mathcal{P}_k - \epsilon)$	0
ϵ	$\mu + \frac{\mu_t}{\sigma_\epsilon}$	$\rho(C_{\epsilon 1}\mathcal{P}_k - C_{\epsilon 2}\epsilon)\frac{\epsilon}{k}$	0

Table 3.1: Source terms and diffusion coefficients in the integral transport equation (3.4).

type of the field that the variable ϕ represents, the generic equations (3.2) and (3.4) are either scalars or vectors. Note that the continuity equation is not represented by a generic equation; combined with the momentum equation it provides an equation for the pressure or pressure correction.

3.3   Discretisation Procedure

3.3.1   Numerical grids and related issues

The numerical grid subdivides the solution domain into a finite number of control volumes. The boundary–conforming and non–orthogonal grids are an obvious choice for complex geometries since they offer greater flexibility in the distribution of the grid lines. Of the different types of grid arrangements (structured, block–structured and unstructured), the structured and the block–structured grids (both made of quadrilaterals) are used in this study. The latter are generated within a number of non–overlapping sub–domains (blocks) that represent the solution domain of interest.

A number of possibilities exist regarding the locations on a grid where the various dependent variables may be stored. The present flow solver utilizes a colocated arrangement for all the variables solved for and thus only one set of control volumes is required. Specifically, all the variables are stored at the geometric centre of the CV, denoted hereafter by P. A typical two-dimensional CV surrounding point P is shown in Figure 3.1. The centres of the neighbouring CVs to the west, east, south and north are labelled as W, E, S and N, while the lowercase letters denote CV faces. For reasons related to the solution strategy, values of the mass fluxes that enter or leave a particular CV are not stored at the centres but, rather, at the middle of the east and north faces of each cell. The governing equations are solved for all the interior computational nodes, i.e. over all physical CVs. Boundary nodes of the exterior CV faces (i.e. those that are adjacent to the exterior boundaries of the solution domain) are used for the implementation of the boundary conditions.
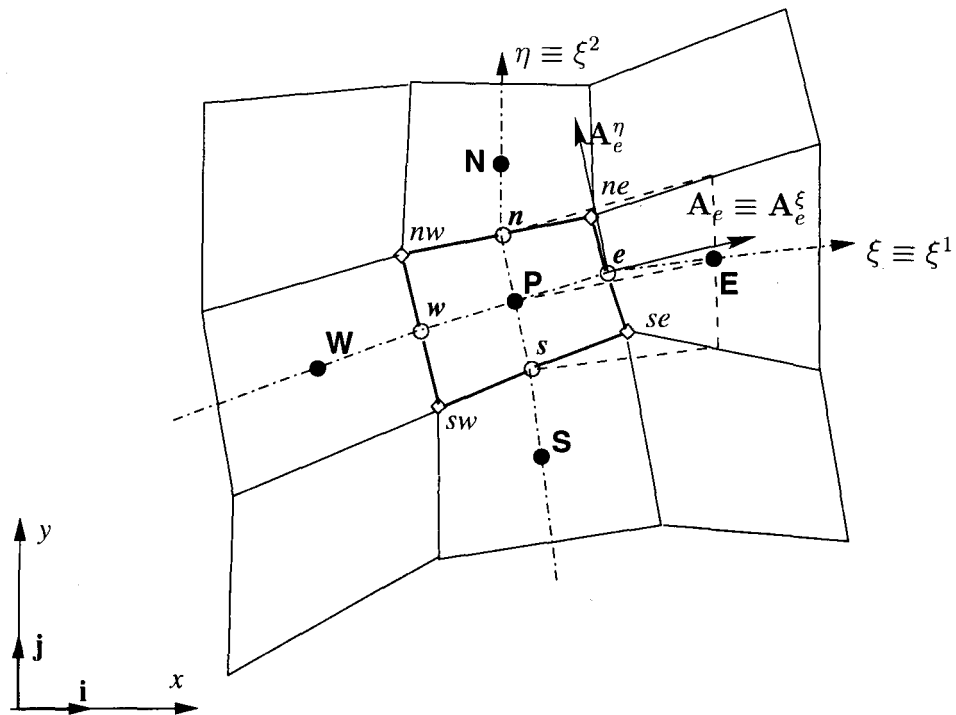
Figure 3.1: A typical control volume and the points–of–compass notation used for the cell–centred two–dimensional structured grid (•, locations of variables solved for; ∘, locations where fluxes are required).

The control volume is defined by its vertices (V_n, $n = 1, N_v$, $N_v = 4$), i.e. by the position vectors $r_n(x_i)$ which are defined with respect to a fixed Cartesian coordinate frame (x, y). These vertices can be also identified by points–of–compass notation (i.e. sw, se, ne and nw in Figure 3.1) and they are connected by straight line segments (edges) defining four CV faces.

The numerical grid and related connectivity data (mainly information needed to identify and connect each grid object - cell, face (edge) and vertex, adjacent to the given object) are physically defined by the position vectors of the CV vertices. For block–structured grids, two types of connectivity are used . Within each block, the connectivity is provided implicitly, by simple increment of one of the grid indices (I or J). These indices represent the counters along general curvilinear coordinates ($\xi \equiv \xi^1$, $\eta \equiv \xi^2$), Figure 3.1. Along block interfaces, the explicit connectivity data are defined for each block–face cell (node). They provide:

- indices of cells in the neighbouring block which are located in the first and the second row from the common face (first and second neighbours) and

- the neighbouring face orientation (that is the local coordinate direction associated with the west, east, south or north cell–face).

Geometrical quantities

The discretisation procedure requires definition of the coordinates of the cell centres, CV face centres, components of surface vectors and the cell volumes. These quantities are calculated from the coordinates of the CV vertices which are ordered in the counterclockwise direction for each cell. The normal or surface vectors $\mathbf{A}_j$ and areas $\mathcal{A}_j$ of the CV faces (j stands for e, w, s or n):

$$\mathbf{A}_j \quad = \quad (\mathbf{n}\,\mathcal{A})_j = A_{jx}\,\mathbf{i} + A_{jy}\,\mathbf{j}\,, \tag{3.5}$$

$$\mathcal{A}_j \quad = \quad \sqrt{(A_{jx})^2 + (A_{jy})^2}\,,\ j = w, e, s, n\,, \tag{3.6}$$

are defined by the surface vector components:

$$A_{jx} \quad = \quad y_{j2} - y_{j1}\,, $$

$$A_{jy} \quad = \quad x_{j1} - x_{j2}\,, \tag{3.7}$$

where $j1$ and $j2$ are the first and last CV face vertices. Note that the surface vector, for instance at the face 'e', represents the coordinate surface defined by the local coordinate $\xi^1 = \xi = const$. This vector can be denoted as

$$\mathbf{A}_e^\xi \equiv \mathbf{A}_e = (y_{ne} - y_{se})\,\mathbf{i} + (x_{se} - x_{ne})\,\mathbf{j}\,. \tag{3.8}$$

A similar surface vector, representing the area defined by $\xi^2 = \eta = const$, is defined as:

$$\mathbf{A}_e^\eta = (y_P - y_E)\,\mathbf{i} + (x_E - x_P)\,\mathbf{j}\,. \tag{3.9}$$

The cell volumes can be computed from the following expression:

$$\Delta\mathsf{V}_P = \frac{1}{2}\,|(\mathbf{r}_{ne} - \mathbf{r}_{sw}) \times (\mathbf{r}_{nw} - \mathbf{r}_{se})|\,. \tag{3.10}$$

Since a quadrilateral cell can be decomposed into two triangles, the coordinates of cell centres can be calculated as the average values of the centre coordinates of these triangles, weighted by their areas.

3.3.2 Time discretisation

For unsteady fluid flow problems, the rate of change term is finite and may be approximated as:

$$\mathcal{R} \quad = \quad \frac{d}{dt}\int_\mathsf{V}\rho\phi\,d\mathsf{V} \approx \frac{d\Psi}{dt}\,, \tag{3.11}$$

$$\Psi \quad = \quad \rho\phi\Delta\mathsf{V}\,, \tag{3.12}$$

where it is assumed that the value at the centre of CV represents an average over the volume ΔV. Next, replacing the fluxes and sources in Equation (3.4) by

$$\mathcal{F} = \mathcal{C} - \mathcal{D} - \mathcal{S} , \tag{3.13}$$

this equation becomes a first order ordinary differential equation with an initial condition:

$$\frac{d\Psi}{dt} + \mathcal{F} = 0 , \quad \Psi(t_0) = \Psi^0 . \tag{3.14}$$

Thus, by dividing time into an arbitrary number of time steps with size Δt, a wide range of time discretisation schemes can be employed, Ferziger and Peric (1996). Since the solution method advances in time step by step, the "marching" procedure can be constructed by integrating the above equation over each time interval Δt. In implicit procedures, all the fluxes and sources contained in $\mathcal{F}$ are evaluated at the current (new) time level t_n. A second order accurate and fully implicit scheme can be defined by using three time levels: the current t_n, and two previous, $t_{n-1} = t_n - \Delta t$ and $t_{n-2} = t_{n-1} - \Delta t$. Assuming a quadratic variation across the three levels, the time derivative in Equation (3.14) can be obtained as:

$$\left(\frac{d\Psi}{dt}\right)_n \approx \frac{3\Psi^n - 4\Psi^{n-1} + \Psi^{n-2}}{2\Delta t} . \tag{3.15}$$

Thus, the balance between the rate of change term and the combined fluxes and sources (represented by the quantity $\mathcal{F}$) is given as:

$$\frac{d}{dt} \int_V \rho\phi \, dV + \mathcal{F} \approx$$
$$\frac{\rho\Delta V}{\Delta t} \left[\left(\phi^n - \phi^{n-1}\right) + \gamma_t \frac{\phi^n - 2\phi^{n-1} + \phi^{n-2}}{2} \right] + (\mathcal{C}^n - \mathcal{D}^n - \mathcal{S}^n) = 0 . \tag{3.16}$$

In the above equation, a blending factor $0 \leq \gamma_t \leq 1$ is introduced. When this parameter is set equal to zero, the first–order accurate (Euler) formulation is obtained. A value of unity gives the second–order accurate formulation, while an intermediate value has the effect of 'blending' the two formulations. The Euler scheme is unconditionally stable but not so accurate for large time steps. The second–order scheme is also unconditionally stable (Ferziger and Peric, 1996) but suffers the obvious drawback of requiring the variables to be stored for all time levels involved. Nevertheless, and because of the memory constraints, only the implicit first–order accurate scheme is used in this work. In what follows, all terms are evaluated at their new time level values and the superscript 'n' will therefore be omitted for clarity.

3.3.3 Discretising the convection and diffusion fluxes

The sum of convective and diffusive fluxes through all the CV faces (see Equation (3.4)) can be written as:

$$
\mathcal{C} - \mathcal{D} = \sum_{j=1}^{4} \int_{A_j} \left[\left(\rho \phi U_k - \Gamma_\phi \frac{\partial \phi}{\partial x_k} \right) n_k \, d\mathcal{A} \right]_j
$$

$$
= \sum_{j=1}^{4} F_j , \tag{3.17}
$$

where F_j is an integrated flux over the cell face j ($j = 1, 4$ i.e. = e, w, s, n). The usual approximation used to evaluate the surface integral is to assume that the value of the integrand is that which prevails at the face centre. This is sometimes called the single–point quadrature (or the midpoint rule) and is formally second–order accurate. An example of how this may be done is presented in terms of east ('e') face of a typical CV. The integrated flux across this face is given as:

$$
F_e = F_e^c - F_e^d
$$

$$
\approx \dot{m}_e \phi_e - \left(\Gamma_\phi \frac{\partial \phi}{\partial x_k} A_k \right)_e , \tag{3.18}
$$

where the superscripts 'c' and 'd' refer, respectively, to convection and diffusion. In order to evaluate F_e, we first need to determine the values of the mass flux ($\dot{m}_e$), the dependent variable itself and its gradient across face 'e'. Consideration of how this is done follows next.

Mass fluxes - the continuity equation

We consider first determination of the mass fluxes across the cell faces. The mass flux through the cell face 'e' is evaluated as:

$$
\dot{m}_e = \int_{A_e} \rho U_k \, n_k \, d\mathcal{A}
$$

$$
\approx \rho_e \left(U A_x + V A_y \right)_e . \tag{3.19}
$$

The mass fluxes through the other faces are calculated from similar expressions. We adopt the convention of assigning the negative sign to the surface vectors and the corresponding fluxes on the west and south cell faces which means that the surface vectors at these faces are pointed inwards. It therefore follows that the sum of the mass fluxes defines the integral form of the continuity equation which is expressed as:

$$
\sum_j \dot{m}_j = \dot{m}_e - \dot{m}_w + \dot{m}_n - \dot{m}_s = 0 . \tag{3.20}
$$

In order to determine the cell face velocities (e.g. U_e) in Equation (3.19), use can be made of the values that pertain at the neighbouring nodes and an obvious choice here is linear interpolation. However, use of linear interpolation is known to cause the computed velocity field to become uncoupled from the computed pressure field. In order to ensure a strong pressure–velocity coupling and promote the numerical stability on colocated grids, a special interpolation technique is used to determine the interpolated cell face velocities. This technique, usually attributed to Rhie and Chow (1983), will be described later.

The convective fluxes

In an iterative procedure such as the present one, the convective fluxes at a particular iteration are evaluated from the mass fluxes obtained at the previous iteration. In this way the nonlinear convective fluxes are linearized, i.e. expressed as a product of the 'known' mass fluxes and 'unknown' values of the dependent variable ϕ_e, thus:

$$F_e^c = \dot{m}_e \, \phi_e \, . \tag{3.21}$$

On a non–uniform grid, linear interpolation (which amounts to the *central differencing scheme*, CDS) gives:

$$\phi_e = (1 - f_{e,P}) \, \phi_P + f_{e,P} \, \phi_E \, , \tag{3.22}$$

where $f_{e,P}$ is the interpolation factor defined in terms of the distances between the node P, the cell–face centre 'e' and the neighbouring node E (see Figure 3.1), thus:

$$f_{e,P} = \frac{\overline{Pe}}{\overline{Pe + eE}} \, . \tag{3.23}$$

The linear interpolation has the same accuracy as the midpoint approximation of the surface integrals, thus preserving second–order accurate spatial discretisation. However, use of central differencing can generate numerical oscillations yielding unbounded and non-monotonic solutions. A well–known remedy is to adopt the (first–order accurate) *upwind differencing scheme* (UDS) whereby the value at face 'e' is taken to be that which prevails at the 'upwind' nodes, thus:

$$\phi_e^{UDS} = \begin{cases} \phi_P & \text{if } \dot{m}_e \geq 0 \, ; \\ \phi_E & \text{if } \dot{m}_e < 0 \, . \end{cases} \tag{3.24}$$

The UDS is unconditionally bounded (monotonic) but produces excessive numerical diffusion, especially if the flow is not aligned with grid lines. In principle, grid refinement reduces the numerical diffusion but this is not always a realistic option.

A more refined approach is to blend the CDS scheme with some contributions from the UDS scheme. To facilitate the implementation of this approach, we define a 'flow–orientated' interpolation factor which, for face 'e', for example, is given by:

$$f_e = \begin{cases} f_{e,P} & \text{if } \dot{m}_e \geq 0 \\ 1 - f_{e,P} & \text{if } \dot{m}_e < 0 \end{cases} \tag{3.25}$$

Equation (3.22) can now be re–arranged as:

$$\phi_e^{CDS} = \phi_e^{UDS} + f_e \frac{\dot{m}_e}{|\dot{m}_e|}(\phi_E - \phi_P) . \tag{3.26}$$

The second part of the reformulated CDS approximation above is recognizably the difference between the CDS and UDS contributions. Therefore, a blend of these two schemes can simply be obtained by introducing a blending factor $0 \leq \gamma_\phi \leq 1$:

$$\phi_e = \phi_e^{UDS} + \gamma_\phi f_e \frac{\dot{m}_e}{|\dot{m}_e|}(\phi_E - \phi_P) . \tag{3.27}$$

With this blending factor, the convective fluxes are now obtained as:

$$F_e^c = \left(\max(\dot{m}_e, 0)\, \phi_P - \max(-\dot{m}_e, 0)\, \phi_E \right) + \underline{\gamma_\phi\, |\dot{m}_e|\, f_e\, (\phi_E - \phi_P)} \tag{3.28}$$

The first term in the above (the upwind contribution) is treated implicitly. The convective coefficient associated with node E (appears in the discretised equation (3.1)), is:

$$(a_E^c)_P = \max(-\dot{m}_e, 0) . \tag{3.29}$$

The second, underlined term, is usually treated explicitly, i.e. evaluated using values from the previous iteration. It is then introduced with the negative sign as an additional 'source term' $(S_{\phi,e}^c)_P$ in the discretised equation (3.1). This separate treatment of the two terms is sometimes referred to as the deferred correction approach (e.g. Khosla and Rubin, 1974). Since the same flux, but with opposite sign, prevails at the west face of the neighbouring node (i.e. $(F_w^c)_E = - (F_e^c)_P$), we can write:

$$(a_W^c)_E = \max(\dot{m}_e, 0) ,$$

$$\left(S_{\phi,w}^c\right)_E = - \left(S_{\phi,e}^c\right)_P . \tag{3.30}$$

When a particular value of the blending factor is used throughout the domain, the above flux–blending scheme is both simple and efficient. Also, for sufficiently high values of γ_ϕ (e.g. ≈ 0.9), the second–order accuracy is not too impaired. This approach has been advocated by Demirdzic and Peric (1990) (see also Demirdzic and Muzaferija, 1995; Ferziger and Peric, 1996) and is very attractive for unstructured grids. The blending of UDS with other higher–order bounded or unbounded schemes can be achieved in a similar manner. These schemes are subject of a separate section (Section 3.4).

The diffusive fluxes

Evaluation of the diffusive flux through the face 'e', which is approximated as (see Equation (3.18)):

$$F_e^d \approx (\Gamma_\phi \nabla \phi \cdot \mathbf{A})_e = \left(\Gamma_\phi \frac{\partial \phi}{\partial x_k} A_k \right)_e , \tag{3.31}$$

requires determination of the gradient of ϕ at the cell-face centre.

A coordinate–free representation of the gradient of a scalar field can be obtained by applying Gauss' theorem to the infinitesimal volume ΔV (Borisenko and Tarapov, 1968):

$$\nabla \phi = \lim_{\Delta V \to 0} \frac{1}{\Delta V} \oint_{\mathcal{A}} \phi \, \mathbf{n} \, d\mathcal{A} . \tag{3.32}$$

Applying this to the control volume around the cell face centre 'e' (Figure 3.1), the gradient is obtained by:

$$(\nabla \phi)_e \approx \frac{1}{\Delta V_e} \sum_{\jmath} \phi_{\jmath} \mathbf{A}_{\jmath}$$

$$\approx \frac{1}{\Delta V_e} \left[(\phi_E - \phi_P) \mathbf{A}_e^\xi + (\phi_n - \phi_s)_e \mathbf{A}_e^\eta \right] , \tag{3.33}$$

where the surface vectors $\mathbf{A}_e^\xi$ and $\mathbf{A}_e^\eta$ are calculated via Equations (3.8) and (3.9), respectively. The gradient given above has a non–conservative form since the surface vectors at 'e' (rather than at the adjacent nodes) are used. The quantity $(\phi_n - \phi_s)_e$ is evaluated by linear interpolation, thus:

$$(\phi_n - \phi_s)_e = (\phi_n - \phi_s)_P (1 - f_{e,P}) + (\phi_n - \phi_s)_E f_{e,P} . \tag{3.34}$$

The volume ΔV_e is evaluated from:

$$\Delta V_e = \mathbf{A}_e^\xi \cdot (\mathbf{r}_E - \mathbf{r}_P) . \tag{3.35}$$

The diffusive flux can be now expressed as:

$$F_e^d = \frac{\Gamma_{\phi,e}}{\Delta V_e} \left[(\phi_E - \phi_P) \left(\mathbf{A}_e^\xi \cdot \mathbf{A}_e^\xi \right) + \underline{(\phi_n - \phi_s)_e \left(\mathbf{A}_e^\eta \cdot \mathbf{A}_e^\xi \right)} \right] . \tag{3.36}$$

The term involving the neighbours P and E will be treated implicitly. The diffusive coefficient of the discretised equation for the node P is:

$$\left(a_E^d \right)_P = \frac{\Gamma_{\phi,e}}{\Delta V_e} \mathcal{A}_e^2 ,$$

$$\Gamma_{\phi,e} = \Gamma_{\phi,P}(1 - f_{e,P}) + \Gamma_{\phi,E} f_{e,P} . \tag{3.37}$$

The remaining underlined terms of the diffusive flux (the cross–derivative contribution) vanish for orthogonal grids. They are treated explicitly and included in the discretised equation as a source term:

$$\left(S_{\phi,e}^{d}\right)_P = \frac{\Gamma_{\phi,e}}{\Delta V_e} \left[(\phi_n - \phi_s)_e \left(\mathbf{A}_e^{\eta} \cdot \mathbf{A}_e^{\xi}\right)\right] . \tag{3.38}$$

3.3.4 Source terms

The volumetric sources (defined in Table 3.1 for each dependent variable) are approximated by the product of the specific source at the CV centre P and the CV volume (the second–order accurate approximation):

$$S_{\phi}^{\mathsf{V}} = \int_{\mathsf{V}} s_{\phi}^{\mathsf{V}} \, d\mathsf{V} \approx \left(s_{\phi}^{\mathsf{V}}\right)_P \Delta V_P . \tag{3.39}$$

The velocity gradients at the cell centres are needed to evaluate some of the source terms (e.g. those that contain the production of the turbulent kinetic energy, $\mathcal{P}_k$, Equation (2.37)). The approximation to these gradients (similar to Equation (3.33)), gives the following expression for the derivative of the velocity component $\phi = U_i$ with respect to x_j:

$$\left(\frac{\partial \phi}{\partial x_j}\right)_P \approx \frac{1}{\Delta V_P} \left[(\phi_e - \phi_w)\,\mathbf{A}_P^{\xi} \cdot \mathbf{i}_j + (\phi_n - \phi_s)\,\mathbf{A}_P^{\eta} \cdot \mathbf{i}_j\right] , \tag{3.40}$$

where the surface vectors $\mathbf{A}_P^{\xi^i}$, $\xi^i = \xi, \eta$ are computed as:

$$\mathbf{A}_P^{\xi} = (y_n - y_s)\,\mathbf{i} + (x_s - x_n)\,\mathbf{j} , \tag{3.41}$$

$$\mathbf{A}_P^{\eta} = (y_w - y_e)\,\mathbf{i} + (x_e - x_w)\,\mathbf{j} . \tag{3.42}$$

The velocities at the cell faces are calculated by linear interpolation (CDS approximation). When the volumetric source depends on the variable ϕ itself, it is often linearized as suggested by Patankar (1980):

$$S_{\phi}^{\mathsf{V}} = S_{\phi}' - S_{\phi}'' \, \phi_P \quad \text{with} \quad S_{\phi}' \quad \text{and} \quad S_{\phi}'' \geq 0 . \tag{3.43}$$

The negative part of the linearized source is treated implicitly, i.e. S_{ϕ}'' is added to the central coefficient of the coefficients matrix to enhance its diagonal dominance. This practice is also used for the source terms that are always negative since dependence on ϕ can be artificially introduced. The linearization of the source terms for turbulence model equations is given in Table 3.2. The source terms arising from the diffusive fluxes s_{ϕ}^A, Table 3.1, are calculated in a similar way as the generic diffusive fluxes, see Equation (3.36).

ϕ	S'_ϕ	S''_ϕ
k	$\rho \, \Delta V \, \mathcal{P}_k$	$\rho \, \Delta V \, \epsilon/k$
ϵ	$\rho \, \Delta V \, C_{\epsilon 1} \, \mathcal{P}_k \epsilon/k$	$\rho \, \Delta V \, C_{\epsilon 2} \, \epsilon/k$

Table 3.2: Linearization of the source terms in the $k - \epsilon$ model (all quantities are defined at the CV centre P).

The pressure contribution to the source term of the discretised momentum equations is obtained from:

$$S_{U_i}^P = -\oint_A P(\mathbf{n} \cdot \mathbf{i}_i) d\mathcal{A} = -\int_V \frac{\partial P}{\partial x_i} dV$$

$$\approx -\Delta V_P \left(\nabla P_P \cdot \mathbf{i}_i \right) . \tag{3.44}$$

Again, the non-conservative form of the gradient at the CV centre (see Equation (3.40)) is used, leading to the following pressure source terms in the momentum equations:

$$S_{U_i}^P \approx - \left[(P_e - P_w) \, \mathbf{A}_P^\xi \cdot \mathbf{i}_i + (P_n - P_s) \, \mathbf{A}_P^\eta \cdot \mathbf{i}_i \right] . \tag{3.45}$$

Note that the cell–face values of the pressure are calculated by linear interpolation.

3.3.5 Algebraic equations

After introducing the fluxes and sources of the variable ϕ into the balance equation (3.16), the outcome for each CV is the algebraic equation which has been presented earlier, Equation (3.1). The central coefficient $a_{\phi P}$, the coefficients $a_{\phi j}$ associated with values of ϕ at neighbouring nodes N_j and the source term $S_{\phi P}$ can now be assembled as:

$$a_{\phi P} = \sum_{j=1}^{N} a_{\phi j} + \left(\frac{\rho \Delta V}{\Delta t} \right)_P^n + S''_{\phi P} , \tag{3.46}$$

$$a_{\phi j} = a_{\phi j}^c + a_{\phi j}^d = \max(-\dot{m}_j, 0) + \frac{\Gamma_{\phi j} \mathcal{A}_j^2}{\Delta V_j} , \tag{3.47}$$

$$S_{\phi P} = S_{\phi P}^t + S'_{\phi P} + \sum_{j=1}^{N} \left(S_{\phi j}^c + S_{\phi j}^d + S_{\phi j}^{\mathcal{A}} \right) + S_{\phi P}^b . \tag{3.48}$$

For the first–order accurate time–discretisation scheme, the explicit part of the change of rate $S_{\phi P}^t$ is given by:

$$S_{\phi P}^t = \left(\frac{\rho \Delta V}{\Delta t} \phi^{n-1} \right)_P , \tag{3.49}$$

while $S_{\phi P}^b$ includes convective and diffusive fluxes at boundary CV faces.

For a computational domain with M control volumes, a system of M equations like Equation (3.1) need to be solved for each dependent variable. This system can be arranged in a matrix form as:

$$[\mathbf{A}]\phi = \mathbf{S} \,, \tag{3.50}$$

where $[\mathbf{A}]$ is the $M \times M$ coefficient matrix and ϕ and $\mathbf{S}$ are vectors of the unknown variable ϕ and source terms, respectively. The linearized system of algebraic equations is usually solved iteratively (*inner iterations*) by employing an iterative matrix $[\mathbf{P}] = [\mathbf{A}] + [\mathbf{N}]$ which is close to $[\mathbf{A}]$. $[\mathbf{N}]$ must be small if the method is to succeed. Denoting by l an iteration counter, the iterative solution can be defined as:

$$[\mathbf{P}]\delta = \mathbf{R} \,, \tag{3.51}$$

where δ and $\mathbf{R}$ are the correction and residual vectors, respectively. They are given as:

$$\delta = \phi^{(l)} - \phi^{(l-1)} \,, \tag{3.52}$$

$$\mathbf{R} = \mathbf{S} - [\mathbf{A}]\phi^{(l-1)} \,. \tag{3.53}$$

The new (inner) iteration starts by calculating the residual vector $\mathbf{R}$, Equation (3.53), after which the system (3.51) is solved for δ, and the solution is updated by adding the correction vector δ to the solution of the previous iteration.

The matrix $[\mathbf{A}]$ is always sparse and for the single block–structured grid the present discretisation method leads to the matrix which has non-zero elements on five diagonals (in 2D). In such situations, the Strongly Implicit Procedure (SIP) of Stone (1968), based on incomplete lower–upper decomposition, is a very effective method. In the case of block–structured grids, the conjugate gradient solvers are used: the symmetric conjugate gradient solver for the pressure correction equation and the bi–conjugate (Bi–CGSTAB) solver of Van Der Vorst (1992) for other equations. These solvers are derived from the classical conjugate gradient method of Hestens and Stiefel (1952) and they are usually used in combination with preconditioning techniques (cf. Meijerink and Van Der Vorst, 1988). Here, the incomplete Cholesky preconditioning is employed.

When solving the linearized system (3.50), under–relaxation is usually employed. This is done implicitly (Patankar, 1980) by re–defining the central coefficient and the source term in Equation (3.1) as shown below:

$$a_{\phi P}^* = \frac{a_{\phi P}}{\alpha_\phi} \,, \tag{3.54}$$

$$S_\phi^* = S_\phi + \frac{1 - \alpha_\phi}{\alpha_\phi} a_{\phi P} \phi_P^{(k-1)} \,, \tag{3.55}$$

where $(0 < \alpha_\phi \leq 1)$ is the under–relaxation factor and the superscript $(k-1)$ denotes the previous (outer) iteration. For brevity, the modified central coefficient and source term will be hereafter denoted as before, without the superscript $*$.

3.4 High–Resolution Convective Schemes

In Section 3.3.3, the concept of 'blending' of the first–order accurate UDS and second–order CDS scheme was introduced; its function is to eliminate non–monotonic solutions, and associated stability problems, from appearing with coarse–grid computations. This blending (Equation (3.27)) can also be used to avoid similar problems with other well-known schemes, such as the second–order accurate Linear Upwind Differencing Scheme (LUDS) of Warming and Beam (1976) and the third–order accurate Quadratic Upwind Interpolation for Convective Kinematics (QUICK) of Leonard (1979). Whilst computationally attractive, this technique lacks a strict mathematical foundation for assigning a value to the blending factor: one attempts to obtain, by trial and error, a converged solution with a value as close to unity as possible.

The blending technique introduces a certain amount of numerical diffusion which should ensure a convergent and bounded solution. This diffusion can be controlled by setting different criteria for the *computed boundedness* of the numerical solution (cf. Gaskell and Lau, 1988). These criteria and the development of higher–order composite schemes based on them are the subjects of this section. Before considering the boundedness criteria, a general form for all schemes of up to third–order accuracy is presented and properties of most popular schemes are outlined.

3.4.1 Formulation and properties of high–order schemes

On non–orthogonal grids, the high–order schemes are usually defined along the grid lines. Thus, by considering the transport of a scalar $\phi(x, y, t)$ along the local direction ξ, three computational nodes may be needed to approximate the CV face value ϕ_e: the upstream, central and downstream, denoted as U, C and D, respectively. The actual labelling of these nodes depends on the velocity direction, i.e. mass flow rate $\dot{m}_e$:

$$(U, C, D) = \begin{cases} (W, P, E) & \text{if} \quad \dot{m}_e \geq 0 \, ; \\ (EE, E, P) & \text{if} \quad \dot{m}_e < 0 \, . \end{cases}$$

This situation is illustrated in Figure 3.2. 'Upstream' and 'downstream' interpolation factors for node C can be defined with the aid of the interpolation factors introduced in
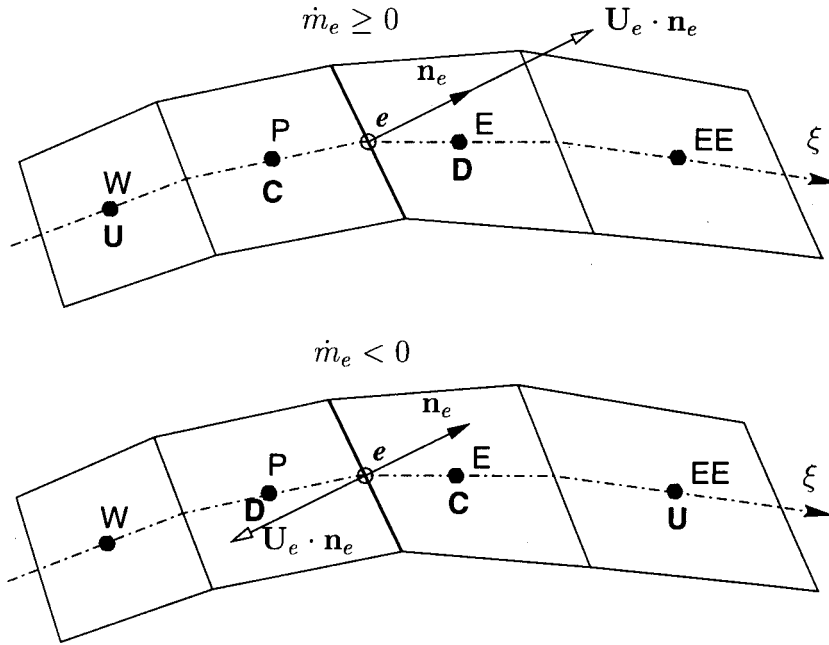
Figure 3.2: Definition of upstream, central and downstream cells.

Equation (3.23),thus:

$$f_D = \begin{cases} f_{e,P} & \text{if } \dot{m}_e \geq 0 \\ 1 - f_{e,P} & \text{if } \dot{m}_e < 0 \end{cases} \tag{3.56}$$

$$f_U = \begin{cases} 1 - f_{e,W} & \text{if } \dot{m}_e \geq 0 \\ f_{e,E} & \text{if } \dot{m}_e < 0 \end{cases} \tag{3.57}$$

Now, a Taylor–series expansion around 'e' is used to obtain three equations for ϕ at U, C and D. When these equations are solved for ϕ_e (cf. Gaskell and Lau, 1988 for the case of a uniform, orthogonal grid) a general upstream–weighted approximation for convection can be obtained:

$$\phi_e = \phi_C + G_D(\phi_D - \phi_C) + G_U(\phi_C - \phi_U) . \tag{3.58}$$

The above downstream and upstream geometric factors G_D and G_U are defined as:

$$G_D = g_D - \alpha_e \frac{f_D}{f_U} , \quad G_U = g_U + \alpha_e , \tag{3.59}$$

$$g_D = \frac{f_D^2(1 + f_U)}{f_D + f_U} , \quad g_U = \frac{f_U^2(1 - f_D)}{f_D + f_U} . \tag{3.60}$$

They contain the parameter α_e which defines a family of the second and third–order accurate schemes (see Table 3.3 below).

Instead of using the dimensional variable ϕ, it is more convenient to work with the normalized variable $\tilde{\phi}$ as proposed by Leonard (1988):

$$\tilde{\phi} = \frac{\phi - \phi_U}{\phi_D - \phi_U} \,, \tag{3.61}$$

so that $\tilde{\phi}_U = 0$ and $\tilde{\phi}_D = 1$. In this way, the general equation (3.58) can be simplified as:

$$\begin{aligned}\tilde{\phi}_e &= \tilde{\phi}_C + G_D(1 - \tilde{\phi}_C) + G_U\tilde{\phi}_C \\ &= \tilde{\phi}_C + \varphi_e(1 - \tilde{\phi}_C) \,,\end{aligned} \tag{3.62}$$

where φ_e is given by:

$$\varphi_e = \varphi(r_e) = G_D + G_U\, r_e \,. \tag{3.63}$$

The quantity $\varphi(r_e)$ can be interpreted as a flux limiter. It depends on the quantity r_e which is defined as:

$$r_e = \frac{\tilde{\phi}_C}{1 - \tilde{\phi}_C} = \frac{\phi_C - \phi_U}{\phi_D - \phi_C} \,. \tag{3.64}$$

The convective schemes in Table 3.3 are expressed in both the unnormalized and normalized forms. A graphical representation of these schemes takes the form of a 'Normalized Variable Diagram' (NVD). This diagram presents $\tilde{\phi}_e$ versus $\tilde{\phi}_C$ and is shown in Figure 3.3. All the schemes from Table 3.3 depend linearly on $\tilde{\phi}_C$. The higher–order schemes pass through point Q which has the coordinates $[f_D/(f_D + f_U)\,,\ (1 + f_U)f_D/(f_D + f_U)]$ which do not depend on α_e.

Desirable properties of a discretisation scheme are discussed, among others, by Peric (1985) and Gaskell and Lau (1988). These are: *accuracy, conservativeness, convective stability and boundedness* and they are summarized in Table 3.3. While most schemes are conservative (ensuring the relation $a_P = \sum_j a_j$), only upwind biased schemes (UDS, LUDS, QUICK) ensure convective stability, indicated by the negative sign of $\partial(\phi_w - \phi_e)/\partial\phi_C$, see Gaskell and Lau (1988). Note that the CDS scheme exhibits neutral convective stability. The numerical upwinding reflects the nature of convection, where the convective transport of the flow properties is always done from upstream to downstream, along the direction of flow. In general, the grid lines do not follow the flow direction and the positive effects of upwinding on the numerical stability are weakened. Unfortunately, only the first–order accurate upwind scheme is unconditionally bounded and there is an unavoidable conflict between the accuracy and boundedness. Note that the second–order CDS satisfies an interpolative boundedness criterion which simply requires that the value

Convective scheme	Expression for ϕ_e (non–uniform grid)	Normalized form: $\widetilde{\phi}_e = f(\widetilde{\phi}_C)$	Order of trunca– tion error term	Convective stability	Boundedness Interpolative	Boundedness Computed	α_e
UDS	ϕ_C	$\widetilde{\phi}_C$	$\propto \frac{1}{2}\Delta\xi(\partial\phi/\partial\xi)_e$	Stable	Yes	Yes	–
CDS	$\phi_C + f_D(\phi_D - \phi_C)$	$\widetilde{\phi}_C + f_D\left(1 - \widetilde{\phi}_C\right)$	$\propto -\frac{1}{8}\Delta\xi^2\left(\frac{\partial^2\phi}{\partial\xi^2}\right)_e$	Neutral	Yes	No	$-\frac{f_U^2(1-f_D)}{f_D+f_U}$
LUDS	$\phi_C + f_U(\phi_C - \phi_U)$	$\widetilde{\phi}_C + f_U\widetilde{\phi}_C$	$\propto \frac{3}{8}\Delta\xi^2\left(\frac{\partial^2\phi}{\partial\xi^2}\right)_e$	Stable	No	No	$\frac{f_D f_U(1+f_U)}{f_D+f_U}$
QUICK	$\phi_C + g_D(\phi_D - \phi_C)$ $+g_U(\phi_C - \phi_U)$	$\widetilde{\phi}_C + g_D(1 - \widetilde{\phi}_C)$ $+g_U\widetilde{\phi}_C$	$\propto -\frac{1}{16}\Delta\xi^3\left(\frac{\partial^3\phi}{\partial\xi^3}\right)_e$	Stable	No	No	0

$$\Delta\xi = \xi_E - \xi_P = \overline{Pe} + \overline{eE}$$

Table 3.3: Definition and properties of various convective schemes.
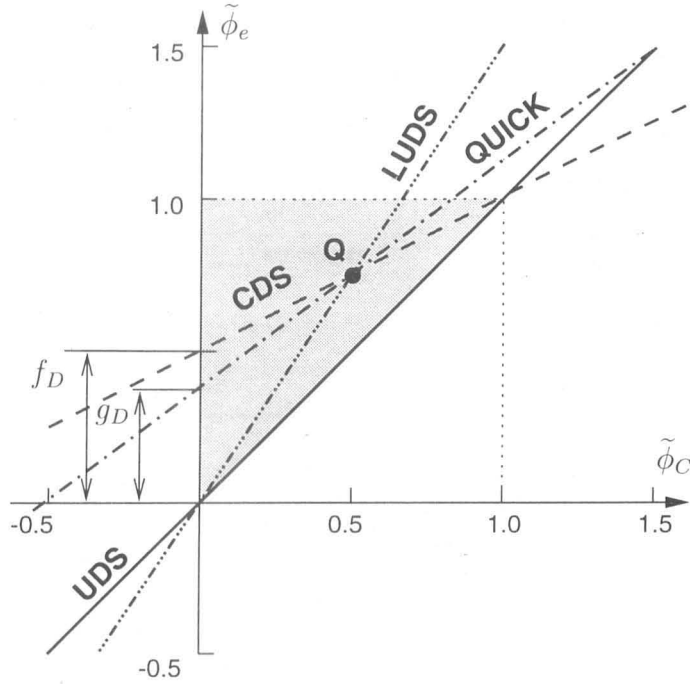
Figure 3.3: NVD diagram for several convective schemes.

of ϕ_e lies within the values at the neighbouring nodes ϕ_D and ϕ_C. However, this criterion, expressed also as (Gaskell and Lau, 1988):

$$\tilde{\phi}_e \in \begin{cases} [\tilde{\phi}_C, 1] & \text{if} \quad \tilde{\phi}_C \in (-\infty, 1] \\ [1, \tilde{\phi}_C] & \text{if} \quad \tilde{\phi}_C \in [1, \infty) \end{cases} \tag{3.65}$$

does not secure the computed boundedness. In what follows, different boundedness criteria will be considered and the construction of higher–order accurate and bounded schemes based on them will be demonstrated.

3.4.2 Boundedness criteria

Two boundedness criteria, one based on the total variation diminishing concept (TVD) (Harten, 1983; Sweby, 1984) and another based on the convection boundedness criterion (CBC) of Gaskell and Lau (1988), offer great flexibility in the construction and implementation of the higher–order bounded schemes.

In terms of normalized variables, the TVD constraints read as:

$$\tilde{\phi}_e \leq 1 \text{ and } \tilde{\phi}_e \leq 2\tilde{\phi}_C \text{ and } \tilde{\phi}_e \geq \tilde{\phi}_C \,, \text{ if } 0 < \tilde{\phi}_C < 1 \,,$$

$$\tilde{\phi}_e = \tilde{\phi}_C \text{ if } \tilde{\phi}_C \leq 0 \text{ or } \tilde{\phi}_C \geq 1 \,. \tag{3.66}$$

Leonard (1988) has shown that the TVD schemes, popular in unsteady compressible flows, can be used with the control volume methods designed for steady flows. The
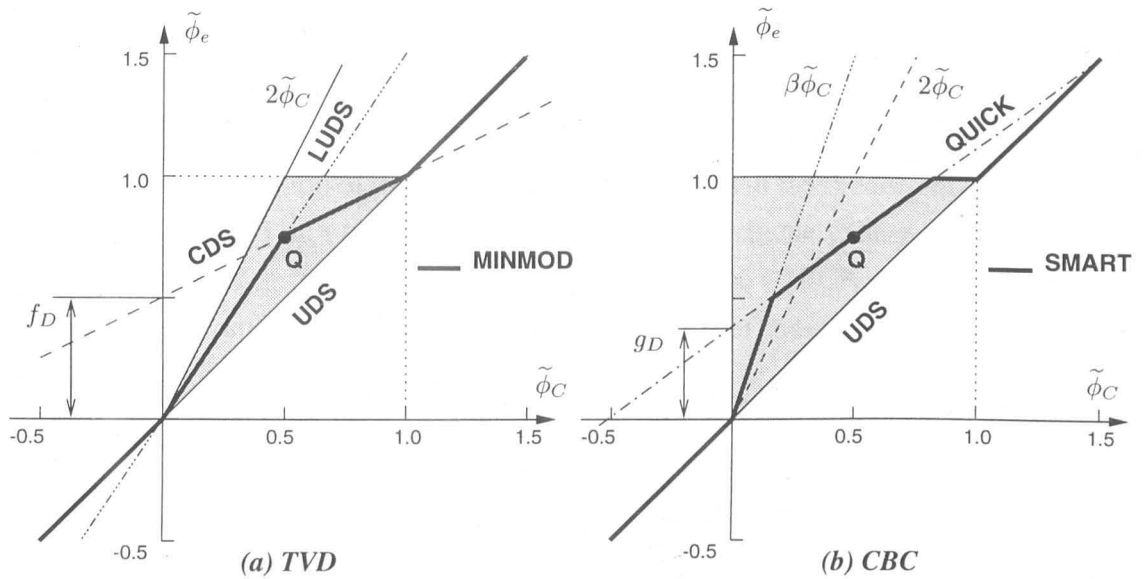
Figure 3.4: Graphical representation of TVD (left) and CBC (right) criteria and NVD characteristics of some bounded schemes.

physical understanding of the boundedness problem guided Gaskell and Lau to propose the following boundedness constraints:

$$\tilde{\phi}_e \;\leq\; 1 \text{ and } \tilde{\phi}_e \geq \tilde{\phi}_C \,, \text{ if } 0 < \tilde{\phi}_C < 1 \,,$$

$$\tilde{\phi}_e \;=\; \tilde{\phi}_C \text{ if } \tilde{\phi}_C \leq 0 \text{ or } \tilde{\phi}_C \geq 1 \,. \tag{3.67}$$

From the graphical representation of the TVD and CBC conditions (depicted in Figure 3.4) it follows that the cell–face values $\tilde{\phi}_e$ should lie within the shaded areas in the monotonic range $0 < \tilde{\phi}_C < 1$, and on the line $\tilde{\phi}_e = \tilde{\phi}_C$ outside the monotonic range.

Note that the TVD–derived constraints are more stringent than the CBC constraints. Obviously, the simple schemes with *linear* characteristics in the NVD diagram (see Figure 3.3) may violate the boundedness criteria (with the exception of the first order UDS) and some form of a non-linear or piecewise linear scheme must be used. It is also evident that in the case of non-monotonic variable profiles, the use of the UDS scheme is the only possible choice in order to satisfy the above boundedness constraints. Gaskell and Lau demonstrated the validity of their CBC in multi-dimensional cases and both CBC and TVD one-dimensional schemes can be applied in each (local) direction in multi–dimensional problems. This will produce less accurate results when the local direction along the grid lines departs significantly from the flow direction.

3.4.3 A choice of bounded schemes

A number of upwind TVD schemes have been used in compressible flow solvers for capturing shocks and flow discontinuities. These schemes may be written in a form given

by Equation (3.62) where the flux limiter $\varphi_e(r_e) \geq 0$ limits the flux of the variable ϕ to a level that ensures the bounded solution. Among different limiters (see Sweby, 1984), Roe's MINMOD limiter (also called as the SOUCOUP scheme by Zhu and Rodi, 1991) is a piecewise combination of the LUDS and CDS schemes in the monotonic range ($\tilde{\phi}_C \in (0,1)$). Gaskell and Lau (1988) proposed the SMART scheme (Sharp and Monotonic Algorithm for Realistic Transport) which coincides with the QUICK scheme over a large part of the monotonic range. Mathematical formulations of these two bounded schemes are given below in terms of the normalized variable $\tilde{\phi}_C$:

$$\text{MINMOD: } \tilde{\phi}_e = \begin{cases} (1 + f_U)\tilde{\phi}_C & \text{if} \quad 0 < \tilde{\phi}_C < \frac{f_D}{f_D + f_U} \\ f_D + (1 - f_D)\tilde{\phi}_C & \text{if} \quad \frac{f_D}{f_D + f_U} < \tilde{\phi}_C < 1 \\ \tilde{\phi}_C \, . & \text{if} \quad \tilde{\phi}_C \leq 0, \; \tilde{\phi}_C \geq 1 \end{cases} \tag{3.68}$$

$$\text{SMART: } \quad \tilde{\phi}_e = \begin{cases} \beta\tilde{\phi}_C & \text{if} \quad 0 < \tilde{\phi}_C < \frac{g_D}{\beta - g_C} \\ g_D + g_C\tilde{\phi}_C & \text{if} \quad \frac{g_D}{\beta - g_C} < \tilde{\phi}_C < \frac{1 - g_D}{g_C} \\ 1 & \text{if} \quad \frac{1 - g_D}{g_C} < \tilde{\phi}_C < 1 \\ \tilde{\phi}_C & \text{if} \quad \tilde{\phi}_C \leq 0, \; \tilde{\phi}_C \geq 1 \end{cases} \tag{3.69}$$

In the SMART scheme, the coefficients g_C and β are:

$$g_C = 1 - g_D + g_U \, , \quad \beta = g_C \left(1 + \frac{g_D}{g_U}\right) \; ; \quad \text{for TVD SMART } \beta = 2 \, . \tag{3.70}$$

The corresponding flux limiters $\varphi_e(r_e)$, where r_e is defined by Equation (3.64), are defined as:

$$\text{MINMOD: } \varphi_e = \max\left[0, \min\left(f_U r_e, f_D\right)\right] \, , \tag{3.71}$$

$$\text{SMART: } \quad \varphi_e = \max\left\{0, \min\left[(\beta - 1) r_e \, , \, g_D + g_U \, r_e \, , \, 1\right]\right\} \, . \tag{3.72}$$

The NVD characteristics of these simple but bounded schemes are presented in Figure 3.4. The SMART scheme violates the TVD constraints. Lien and Leschziner (1994) suggested a modified version of SMART (TVD SMART) which was later applied by Zijlema (1996) and C-H Lin and Lin (1997).

As a consequence of the flexible TVD and CBC constraints, various schemes have been proposed and tested. Examples were the scheme of Lin and Chieng (1991), the HLPA scheme of Zhu (1992) (which is the same as the CLAM TVD scheme of Van Leer, 1974), the STOIC scheme of Darwish (1993), UMIST (another monotonic version of QUICK, but with symmetric limiter) of Lien and Leschziner (1994) and Zijlema's (1996) ISNAS scheme. In terms of accuracy, none of the new schemes performed better than

the SMART scheme. The MINMOD scheme is more diffusive than the SMART scheme but the MINMOD scheme, with its good convergence properties, is well–suited for the use on the refined numerical grids. Therefore, the SMART and MINMOD schemes were implemented in the present flow solver.

By recasting the bounded schemes in terms of the flux limiter φ_e (see Equation (3.62)) and then using unnormalized variables, the cell–face value is approximated as:

$$\begin{aligned}
\phi_e &= \phi_C + \varphi_e(r_e)(\phi_D - \phi_C) \\
&= \phi_e^{UDS} + \varphi_e(r_e)\frac{\dot{m}_e}{|\dot{m}_e|}(\phi_E - \phi_P) \, .
\end{aligned} \tag{3.73}$$

The above relation has the same form as Equation (3.26) for the pure CDS or blended CDS and UDS schemes. The corresponding flux is then:

$$F_e^c = (\max(\dot{m}_e, 0)\,\phi_P - \max(-\dot{m}_e, 0)\,\phi_E) + \underline{\gamma_\phi\,|\dot{m}_e|\,\varphi_e(r_e)\,(\phi_E - \phi_P)} \, , \tag{3.74}$$

where γ_ϕ is now used to make a choice between the UDS and high– resolution bounded scheme. Comparing the above expression with Equation (3.28), it is clear that the TVD formalism enables an easy implementation of the bounded high–resolution schemes if one uses the deferred correction approach. The source term pertaining to the deferred correction is computed from the following equation:

$$\left(S_{\phi,e}^c\right)_P = \gamma_\phi\,|\dot{m}_e|\,\varphi_e(r_e)\,(\phi_P - \phi_E) \, . \tag{3.75}$$

3.5   Pressure–Velocity Coupling

The principal difficulty in solving the momentum equations for incompressible flows lies in the determination of the pressure. The 'correct' pressure field is one which allows the velocity components, when obtained from the solution of the momentum equations, to satisfy, simultaneously, the continuity equation. This can be achieved by using the iterative SIMPLE (Semi–Implicit Method for Pressure–Linked Equations) algorithm of Patankar and Spalding (1972) wherein the continuity equation is manipulated to obtain an equation for the pressure correction. The SIMPLE method has been developed with reference to the staggered–grid arrangement whereby the velocities and the pressure are stored at different locations. Application of this method to colocated grids leads to non–physical oscillations. These are due to the use of linear interpolation to obtain the pressure and velocities at the cell faces – something which leads to the de–coupling of the two fields. In order to overcome this problem, the method of Rhie and Chow (1983) is used. This method will be considered first.

The discretised momentum equations can be re–written in a vector form as:

$$\mathbf{U}_P = \mathbf{h}_P - \frac{\Delta V_P}{a_P^u} (\nabla P)_P \;, \tag{3.76}$$

where the quantity $\mathbf{h}_P$ is defined as:

$$\mathbf{h}_P = \frac{\sum_j a_j \mathbf{U}_{N_j} + \mathbf{S}_u}{a_P^u} \;, \tag{3.77}$$

Note that the source term $\mathbf{S}_u$ does not include the pressure terms.

A similar equation for the CV around the cell–face centre 'e' reads:

$$\mathbf{U}_e = \mathbf{h}_e - \left(\frac{\Delta V}{a_P^u}\right)_e (\nabla P)_e \;. \tag{3.78}$$

If the variation of the velocity field and the pressure gradient between nodes P and E is linear (as would be the case on very fine grids), then vector $\mathbf{h}_e$, denoted for this case as $\mathbf{h}_e^{(0)}$, would be given as:

$$\mathbf{h}_e^{(0)} = \overline{(\mathbf{U})}_e + \left(\frac{\Delta V}{a_P^u}\right)_e \overline{(\nabla P)}_e \;, \tag{3.79}$$

where the over-bars denote linear interpolation between neighbouring cells. By replacing the value of $\mathbf{h}_e$ in Equation (3.78) by $\mathbf{h}_e^{(0)}$, an expression for the cell–face velocity is obtained:

$$\mathbf{U}_e = \overline{(\mathbf{U})}_e - \left(\frac{\Delta V}{a_P^u}\right)_e \left[(\nabla P)_e - \overline{(\nabla P)}_e\right] \;. \tag{3.80}$$

As the pressure gradient calculated at the cell–face (∇P_e) involves the pressure values at neighbouring nodes P and E (see Equation (3.82) below), this ensures that the pressure and velocity fields would be coupled when the SIMPLE algorithm is used. The 'correction term', represented by the difference between the pressure gradient evaluated at the cell-face and the gradient interpolated from the adjacent nodes, vanishes if the final pressure gradient variation is linear. When the computed pressure gradient is not linear, the correction term is finite and acts to prevent the development of non–physical oscillatory profiles by smoothing pressure oscillations whose period is twice the cell width.

Note that the converged cell–face velocities may depend on the definition of the coefficient $(\Delta V/a_P^u)_e$. This coefficient is usually obtained as:

$$\left(\frac{\Delta V}{a_P^u}\right)_e = \Delta V_e \overline{\left(\frac{1}{a_P^u}\right)}_e \quad \text{or} \quad \left(\frac{\Delta V}{a_P^u}\right)_e = \overline{\left(\frac{\Delta V}{a_P^u}\right)}_e \;. \tag{3.81}$$

The first option above is used in the present work.

Since the coefficients a_P^u contain the under–relaxation factor, the converged solutions would also depend on this parameter. This is a clearly undesirable feature but one that can be simply avoided by excluding the the under–relaxation factors from a_P^u.

Finally, it should be mentioned that the basic idea of Equation (3.80) has been implemented in various ways, depending mainly on the type of numerical grid being used (see, for example, Rhie and Chow, 1983; Peric, 1985; Demirdzic and Muzaferija, 1995; Ferziger and Peric, 1996; Davidson, 1996; Mathur and Murthy, 1997; Rahman et al., 1997). When fine grids are used, the contribution of the 'correction term' remains smaller than the discretisation error (Ferziger and Peric, 1996). Here, the equation for the cell–face velocity (3.80) is written in terms of the Cartesian velocity components U_i as suggested by Peric (1985):

$$U_{i,e} = \overline{(U_i)}_e - \overline{\left(\frac{1}{a_P^{u_i}}\right)}_e \mathbf{A}_e^\xi \cdot \mathbf{i}_i \left(P_E - P_P\right) + \overline{\left[\frac{1}{a_P^{u_i}} \mathbf{A}^\xi \cdot \mathbf{i}_i \left(P_e - P_w\right)\right]}_e . \tag{3.82}$$

In the SIMPLE algorithm, the discretised momentum equations are solved for $\mathbf{U}_P^*$ by using the existing pressure P^*. The mass fluxes, computed using the cell–face velocity components from Equation (3.82), do not generally satisfy the continuity equation (3.20). A 'mass source' would thus result, defined by:

$$S_m^* = \dot{m}_e^* - \dot{m}_w^* + \dot{m}_n^* - \dot{m}_s^* \tag{3.83}$$

The basis of the SIMPLE algorithm is to drive this mass source to a negligibly small value. This is achieved by introducing the corrections:

$$\mathbf{U}_P = \mathbf{U}_P^* + \mathbf{U}_P' \quad \text{and} \quad P_P = P_P^* + P_P' . \tag{3.84}$$

The discretised momentum equation for $\mathbf{U}_P^*$ (see Equation (3.76)) provides the link between the velocity and pressure corrections at the node P:

$$\mathbf{U}_P' = -\frac{\Delta \mathsf{V}_P}{a_P^u} \left(\nabla P'\right)_P . \tag{3.85}$$

In a similar way, the cell–face velocity corrections are obtained as:

$$\mathbf{U}_e' = -\Delta \mathsf{V}_e \overline{\left(\frac{1}{a_P^u}\right)}_e \left(\nabla P'\right)_e . \tag{3.86}$$

After simplification the above relation becomes:

$$U_{i,e}' \approx -\overline{\left(\frac{1}{a_P^u}\right)}_e \left(P_E' - P_P'\right) \mathbf{A}_e^\xi \cdot \mathbf{i}_i . \tag{3.87}$$

The simplified expression is used in the present work. It takes into account only the pressure difference across the cell–face. This simplification is justifiable by the fact that all the pressure (and velocity) corrections become negligible when a converged solution is obtained.

The cell-face velocity corrections give the mass flux corrections as:

$$\dot{m}_e' = -\rho_e \left[\overline{\left(\frac{1}{a_P^u}\right)_e} A_{ex}^2 + \overline{\left(\frac{1}{a_P^v}\right)_e} A_{ey}^2 \right] (P_E' - P_P') \ . \tag{3.88}$$

The new mass fluxes:

$$\dot{m}_J = \dot{m}_J^* + \dot{m}_J' \tag{3.89}$$

must satisfy the continuity equation (3.20) which now takes the form:

$$\dot{m}_e' - \dot{m}_w' + \dot{m}_n' - \dot{m}_s' + S_m = 0 \ . \tag{3.90}$$

From the above equation, the *pressure correction* equation is obtained:

$$a_P P_P' = \sum_{J=1}^{4} a_J P_{N_J}' - S_m^* \ . \tag{3.91}$$

where, for example, the coefficient related to the east neighbour is given as:

$$(a_E)_P = \rho_e \left[\overline{\left(\frac{1}{a_P^u}\right)_e} A_{ex}^2 + \overline{\left(\frac{1}{a_P^v}\right)_e} A_{ey}^2 \right] \ . \tag{3.92}$$

After the solution of the algebraic equations for P', the nodal velocities, pressure and mass fluxes are corrected according to Equations (3.84) and (3.89). The pressure is corrected only by a fraction of P', i.e. $P = P^* + \alpha_P P'$, where α_P is the under–relaxation factor for the pressure.

3.6 Boundary and Initial Conditions

The convective and diffusive fluxes through the boundaries of the solution domain must be evaluated in order to close the generic balance equation (3.16). These fluxes can be discretised in the same manner as for the inner cell faces, Equations (3.28) and (3.36), respectively. For the convective fluxes, the UDS scheme is usually employed, thus Equation (3.28) is rewritten as:

$$F_b^c = \max\left(\dot{m}_b, 0\right)\phi_P - \max\left(-\dot{m}_b, 0\right)\phi_b \ , \tag{3.93}$$

where the subscript 'b' signifies the boundary cell–face with the outward surface vector $\mathbf{A}_b$. The diffusive flux at the (east) boundary face becomes:

$$F_b^d = \frac{\Gamma_{\phi,b}}{\mathbf{A}_b^\xi \cdot (\mathbf{r}_b - \mathbf{r}_P)} \left[(\phi_b - \phi_P) \left(\mathbf{A}_b^\xi \cdot \mathbf{A}_b^\xi \right) + (\phi_n - \phi_s)_b \left(\mathbf{A}_b^\eta \cdot \mathbf{A}_b^\xi \right) \right] . \qquad (3.94)$$

The above expressions accommodate both *Dirichlet conditions* (specified boundary values) and *Neumann conditions* (prescribed boundary fluxes). In the latter case, Equation (3.94) for the boundary diffusive flux is used to compute the boundary value ϕ_b.

The boundaries of a solution domain are either natural (walls and free surfaces) or artificial in the sense that they are truncated parts of the physical domain through which fluid may enter or leave. The latter comprise the inlet, outlet and symmetry planes. Treatment of each of these types will be discussed below.

Inlet boundaries

The values of the velocity components and of the turbulence quantities are usually prescribed at the inlet. The turbulent kinetic energy may be known from measurements or, more often, is estimated from knowledge of the relative free–stream turbulence intensity T_u. The Kolmogorov relation ($\epsilon \approx k^{3/2}/L_\epsilon$) can be used to estimate the dissipation rate at the inlet by specifying the length scale L_ϵ as a fraction of the characteristic (inlet) dimension. Equivalently, a ratio of the turbulent and molecular viscosity at the inlet may be prescribed.

Outlet boundaries

A condition of zero gradient, in general along the grid line connecting the interior node P and boundary node 'b', is commonly used to specify the boundary conditions at the outlet. Since this condition is strictly valid only for the fully developed flow (no diffusive fluxes), the outlet boundaries should be placed sufficiently far downstream from the regions where the flow exhibits significant changes. The first order backward approximation for the gradient can be used, leading to $\phi_b = \phi_P$. Note that the diffusive fluxes, calculated from Equation (3.94), are zero only if the grid lines are normal to the outlet boundary. Before solving the pressure–correction equation, the extrapolated velocity components $U_{i,b} = U_{i,P}$ are corrected in such a way that the total mass flux at exit exactly equals its value at the inlet.

The condition of zero gradient is often called a free open boundary condition (OBC) and has been employed for both steady and unsteady flows. For the latter, several non–reflective OBC (based on the Sommerfeld radiation condition) have been proposed (Sani

and Gresho, 1994; Nakamura et al., 1993). Nakamura et al. (1993) and Ferziger and Peric (1996) suggest the following simple unsteady condition:

$$\frac{\partial \phi}{\partial t} + U_{out}\frac{\partial \phi}{\partial n} = 0 \,, \tag{3.95}$$

where U_{out} can be taken to be either the free stream velocity or the averaged outlet velocity.

Wall boundaries

The walls are assumed to be smooth and impermeable. The *no–slip* wall boundary condition applies, meaning that the velocity of fluid in contact with the wall is equal to the wall velocity. The diffusive fluxes across the wall are evaluated differently for each of the dependent variables. This is explained next.

For the momentum equations, the diffusive fluxes at the walls are the components of the resultant shear force exerted by the wall. To demonstrate this, a local Cartesian system defined by the unit vectors $\mathbf{t}$ and $\mathbf{n}$, Figure 3.5, will be used.
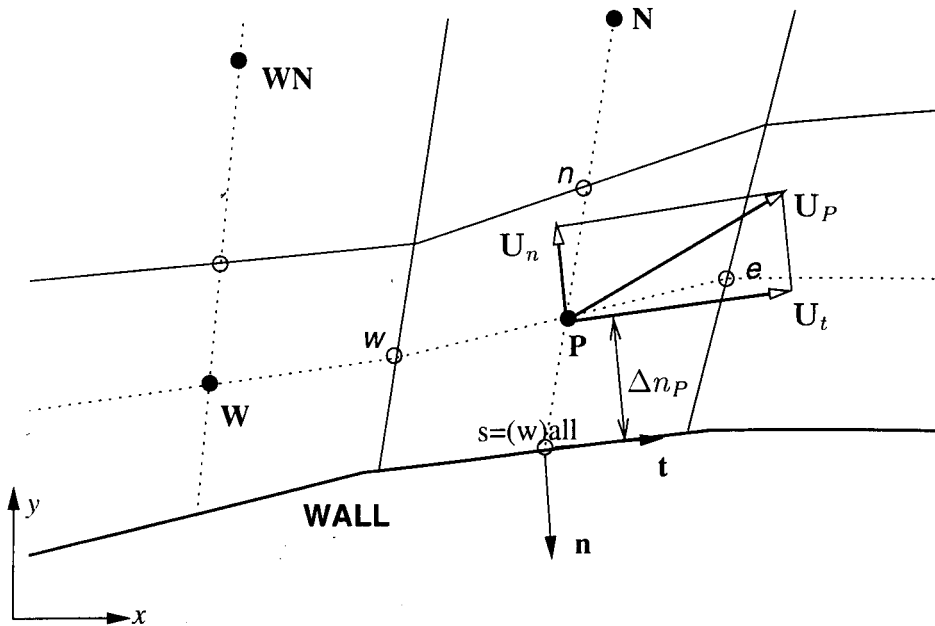
Figure 3.5: Application of the wall boundary conditions.

The unit vector $\mathbf{t}$ can be defined by the velocity $\mathbf{U}_t$ which is parallel to the wall boundary, thus:

$$\mathbf{t} = \frac{\mathbf{U}_t}{U_t} \,, \quad U_t = |\mathbf{U}_t| \,. \tag{3.96}$$

The velocity vector $\mathbf{U}_t$ is evaluated at the near–wall node P from the following relation:

$$\mathbf{U}_t = \mathbf{U} - U_n\mathbf{n} \,, \quad U_n = \mathbf{U} \cdot \mathbf{n} \,, \tag{3.97}$$

where U_n denotes the velocity component normal to the wall. With the help of the continuity equation, it can be shown that only the wall shear stress τ_{tn} is finite at the wall. The resulting shear force can be then approximated as:

$$\mathbf{F}_w = \int_{\mathcal{A}_w} \tau_{tn} \, \mathbf{t} \, dA \approx (\tau_{tn} \, \mathcal{A} \, \mathbf{t})_w \ . \tag{3.98}$$

By neglecting possible changes in the velocity vector direction between the wall and the node P, the wall shear stress is evaluated as:

$$\tau_{tn} = \mu_w \left(\frac{\partial U_t}{\partial n} \right)_w \approx \mu_w \frac{(U_t)_w - (U_t)_P}{\Delta n_P} \ , \tag{3.99}$$

where Δn_P is the normal distance from the wall. This distance is given by

$$\Delta n_P = (\mathbf{r}_w - \mathbf{r}_P) \cdot \mathbf{n} \ . \tag{3.100}$$

Equation (3.99) for the wall shear stress, with $\mu_w = \mu$, is valid for laminar flows and for the thin viscous sublayer in turbulent flows. When the 'wall functions' approach is used for turbulent flows (see Section 2.8), a different expression is used to evaluate the wall shear stress, see Equation (2.70). Note that all the relations presented in Section 2.8 are applicable to a general wall topology if the velocity U_P and the coordinate y (y_P) are replaced by the velocity parallel to the wall $(U_t)_P$ and by the coordinate n (Δn_P), respectively. For example, the non-dimensional wall unit (Equation (2.69)) is given as:

$$Y_P^* = \frac{U_* \Delta n_P}{\nu} \ . \tag{3.101}$$

By defining the effective near–wall viscosity μ_w as:

$$\mu_w = \begin{cases} \mu & , \ Y_P^* < 11.6 \\ \rho \kappa U_* \Delta n_P / \ln(EY_P^*) & , \ Y_P^* \geq 11.6 \end{cases} \tag{3.102}$$

the wall shear stress can be computed from Equation (3.99) for both laminar and turbulent flows.

Considering now a non-moving wall, and by introducing $\mathbf{t}$ (Equation (3.96)) and τ_{tn} (Equation (3.99)) into Equation (3.98), the wall shear force can be written in terms of the Cartesian components as:

$$(F_i)_w = - \frac{\mu_w \mathcal{A}_w}{\Delta n_P} (U_i)_P + \underline{\frac{\mu_w \mathcal{A}_w}{\Delta n_P} (U_n)_P} \ \mathbf{n} \cdot \mathbf{i}_i \ . \tag{3.103}$$

It is customary to treat the first term on the right hand side of the above equation implicitly as this will allow the coefficient a_P^u to remain the same for all velocity components. The underlined term is treated explicitly.

The wall boundary conditions for k and ϵ are presented in Section 2.8, in conjunction with the wall function approach.

Symmetry planes

There are many steady flows whose solution is symmetrical around 'natural' symmetry planes or axes. For such flows, the velocity component normal to the plane is zero, yielding zero convective fluxes. In addition, the normal derivatives of the velocity components parallel to the plane are zero. This is also true for the scalar variables k and ϵ. By setting the diffusive flux to zero, Equation (3.94) can be used to determine the boundary values. Since the normal stress at the symmetry plane, approximated as:

$$\left(\tau_{nn}\right)_{sym} \approx -2\left(\mu + \mu_t\right)\frac{(U_n)_P}{(\mathbf{r}_{sym} - \mathbf{r}_P)\cdot\mathbf{n}}\ , \qquad (3.104)$$

is finite, the corresponding force is given by

$$\mathbf{F}_{sym} \approx \left(\tau_{nn}\mathbf{n}\mathcal{A}\right)_{sym}\ . \qquad (3.105)$$

The components of this force, that replace the diffusive fluxes at the symmetry planes in the momentum equations, can be cast in a form which ensures the same central coefficients a_P^u for all velocity components. This form is:

$$\left(F_i\right)_{sym} \approx \frac{2\left[(\mu + \mu_t)\mathcal{A}\right]_{sym}}{(\mathbf{r}_{sym} - \mathbf{r}_P)\cdot\mathbf{n}}\left(\mathbf{U}_{sym} - \mathbf{U}_P\right)\cdot\mathbf{i}_i\ . \qquad (3.106)$$

The above velocity vector at the symmetry plane $\mathbf{U}_{sym}$ is updated before solving the momentum equations in order to satisfy a condition of the zero shear stress, thus:

$$\mathbf{U}_{sym} = \mathbf{U}_P - \left(\mathbf{U}_P\cdot\mathbf{n}\right)\mathbf{n}\ . \qquad (3.107)$$

The symmetry boundary conditions are very often applied at boundaries which are not natural symmetry planes. Examples are the boundaries parallel to uniform free streams.

Boundary conditions for the pressure

The pressure must be specified at all the domain boundaries in order to calculate the pressure forces at the boundary cell-faces. Generally, linear extrapolation of the pressure values from the interior nodes can be used for all types of boundaries (e.g. inlets, outlets, walls, symmetry planes). At all these boundaries, the velocities are known before solving the pressure correction equation, and the mass flux corrections $\dot{m}'_j$ there are therefore zero. This implies that the normal gradients of the pressure correction (P') are also zero. This condition is enforced directly when calculating the mass imbalance S_m^* (Equation (3.83)). To evaluate the gradients of P' at the near–boundary cells, the boundary values of P' are linearly extrapolated from inside the solution domain. Note that the pressure must be fixed at one CV in order to obtain the unique solution (Patankar, 1980; Ferziger and Peric, 1996).

Initial conditions

Equation (3.14) for the rate of change shows that each dependent variable must be prescribed at the initial time (t_0) over the whole solution domain. In many cases, arbitrary initial values can be used (as in this study), usually taken to be those prescribed at the inlet. An initial perturbation in the initial velocity field is often used to trigger the vortex shedding process (Section 4.3.1).

3.7   Overall Solution Procedure

The solution method is an iterative one and involves the following main steps:

1. Provide the numerical grid and calculate geometrical quantities.

2. Initialize the field values of the dependent variables (at the initial time t_0).

3. Begin the time stepping loop. Save the current variable values as the old ones.

4. Assemble and solve Equation (3.50) for the velocity components using the available values for the mass fluxes and the pressure.

5. Calculate the cell–face velocities using Equation (3.82). Determine the mass imbalance, Equation (3.83).

6. Assemble and solve the pressure–correction equation (3.91). Use the outcome to update the velocity components, the pressure and the mass fluxes.

7. In the case of turbulent flow, assemble and solve Equation (3.50) for k and ϵ. Update the eddy viscosity.

8. Repeat the procedure from the *Step* 4 until a converged solution (for the current time level) is obtained. This is defined as when the sum of absolute values of the residuals for each variable (normalized by the appropriate inlet flux) has fallen below a pre–specified level (typically below 10^{-4}).

9. Return to *Step* 3 and repeat up to the prescribed number of time steps.

For each dependent variable, the system of linearized algebraic equations (3.50) is solved only to a certain level of convergence. Iterations performed within the linear equation solver are called *inner iterations*. The sequence that consists of *Steps* 4 to 8 is termed as the *outer iteration*.

Note that for the case of block–structured grids, the solution of each variable is carried out on the globally unstructured grids, i.e. block by block without imposing boundary conditions at block interfaces. In this way, the implicitness of the method is preserved. The implementation of this strategy requires neighbourhood connections for the cells adjacent to the internal block faces (see Section 3.3.1).

3.8   Closure

In this chapter, a description has been provided of the finite–volume method used in this work to solve the two-dimensional Reynolds–averaged Navier–Stokes equations for incompressible flows.

It was shown how the differential equations were discretised by their formal integration, term–by–term, over control volumes arranged in a structured or block–structured form. A colocated storage arrangement for all dependent variables is employed. The midpoint rule integration of the surface and volume integrals was employed wherein a linear distribution was assumed for the variable values at locations between the cell centres. Therefore, the spatial discretisation is formally second–order accurate. Occurrence of non–physical oscillations requires the evaluation of the convective fluxes by the blending of the first–order accurate upwind and the second– order central–differencing scheme. Apart from this, the formulation and implementation of the high–resolution bounded MINMOD and SMART schemes is presented. The first–order Euler temporal discretisation is adopted in this work. The most frequent types of boundary conditions (and their numerical treatments) are also described. The outcome of the discretisation procedure is a set of linearized algebraic equations that are solved here using either the SIP procedure of Stone (1968) or conjugate gradient solvers. The overall solution algorithm is sequential and iterative and utilizes the SIMPLE method to couple the computation of the pressure and velocity fields. The pressure–velocity decoupling problems on the colocated grids are avoided by adopting the practice suggested by Rhie and Chow (1983) and Peric (1985).

The numerical solution method has been implemented in a computer code which is used to compute the laminar and turbulent vortex shedding flows. The results of these computations will be analysed in the following two chapters.

Chapter 4

LAMINAR FLOW PREDICTIONS

4.1 Introduction

In this chapter, the present finite volume method is validated against experimental and numerical data for vortex shedding from square and circular cylinders in laminar flow conditions. Attention is focused on issues affecting the accuracy and validity of the numerical solutions. Some physical features of vortex shedding, encountered in the considered flow configurations, are discussed.

The chapter is organized as follows. In Section 4.2, the numerical aspects of the prediction of flows around single square and circular cylinders are presented. These include the size of the computational domains and grids, the boundary and initial conditions and other numerical details. In the next section, the results for the flow around a circular cylinder at the $Re = 105$ are used to emphasize common features of the periodic vortex shedding flows, Section 4.3. In Section 4.4, attention is focused on the sources of numerical uncertainties and an effort is made to quantify these uncertainties. After that, the results for the single cylinders are presented and discussed in Section 4.5. Suitable experimental and numerical results are used to check the present predictions. The remaining Sections 4.6 and 4.7 are organized in a similar way as the previous section and include simulations for:

- uniform flow past two circular cylinders in tandem,

- oscillatory flow past a single circular cylinder with or without steady current.

The main results to emerge from this phase of the work are summarized in a concluding section.

4.2   Numerical Considerations

4.2.1   Solution domains and grids

Numerical grids employed for the predictions of laminar vortex shedding flows were gen-
erated within a single block. A schematic representation of the uniform flow around a
square cylinder is shown in Figure 4.1. The size of the solution domain is described by
three characteristic dimensions: X_i, X_o and Y_s. These specify, respectively, the locations
of the inlet, outlet and symmetry boundaries. These dimensions are usually given in terms
of the cylinder's height H (or diameter D for a circular cylinder). The extent of the com-
putational domains and the geometric parameters of all grids used for the case of a square
cylinder are presented in Table 4.1.
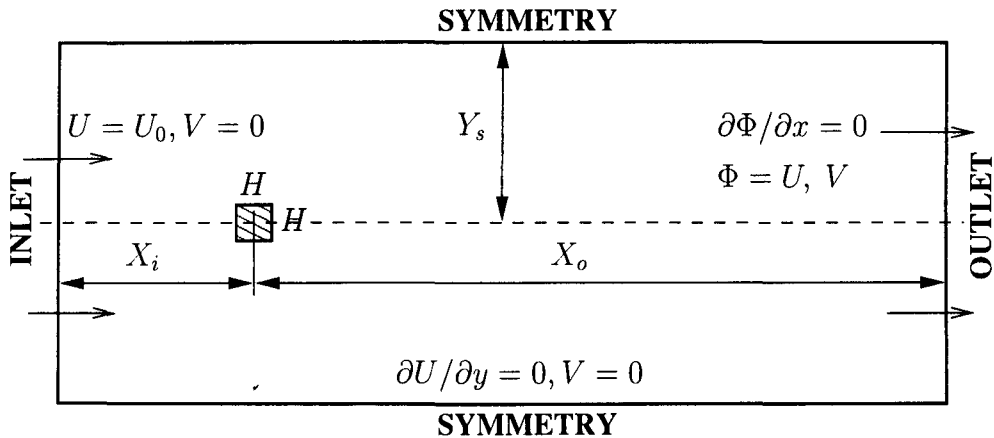
Figure 4.1: Typical solution domain and boundary conditions.

Grid [Domain-NI×NJ]	X_i/H	X_o/H	Y_s/H	$f_{ex} = f_{ey}$	$\Delta n_c/H$
$D1 - 136 \times 118$	12	30	12	1.125	5×10^{-3}
$D1 - 160 \times 142$	12	30	12	1.125	2.5×10^{-3}
$D2 - 123 \times 106$	6	30	6	1.125	5×10^{-3}
$D2 - 169 \times 150$	6	30	6	1.10	2.5×10^{-3}
$D2 - 167 \times 140$	6	30	6	1.08	5×10^{-3}
$D3 - 134 \times 112$	9	31	9	1.125	5×10^{-3}
$D4 - 139 \times 122$	15	31	15	1.125	5×10^{-3}

Table 4.1: Domain size and grid parameters for a square cylinder.

66
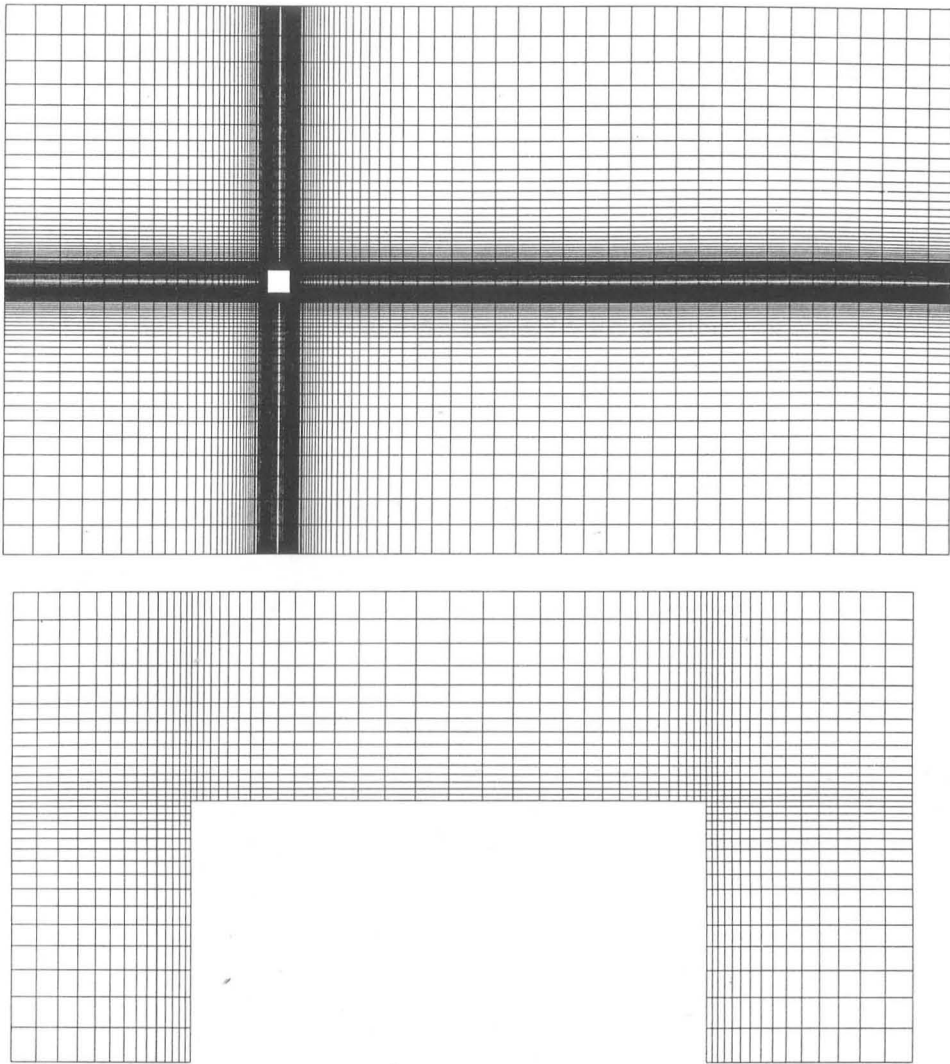
Figure 4.2: Representative numerical grid of $D1 - 136 \times 118$ for a square cylinder.

Two parameters have been chosen to describe the grid resolution:

1. The smallest (non-dimensional) distance $\Delta n_c/H$ between the cylinder wall and the centre of the first adjacent cell,

2. the grid expansion factor, f_e. Note that the same factors were used in the x and y directions.

Thus, all grids are non–uniform, expanding in each direction away from the cylinder corners. This is illustrated in Figure 4.2. The walls of the square cylinder in that figure are subdivided into 32 cells. The circular cylinder flows were also computed with several grids, on two domains, Table 4.2. The expansion factors in the x and y directions are not identical. The grid $D1 - 143 \times 98$ with 156 cells over the cylinder surface is displayed in Figure 4.3.

Grid [Domain-NI×NJ]	X_i/D	X_o/D	Y_s/D	f_{ex}	f_{ey}	$\Delta n_c/H$
$D1 - 143 \times 98$	12	30	12	1.18	1.10	5×10^{-3}
$D1 - 170 \times 98$	12	30	12	1.15	1.10	5×10^{-3}
$D2 - 134 \times 88$	5.5	24.5	6	1.18	1.10	5×10^{-3}

Table 4.2: Domain size and parameters for a circular cylinder grid.
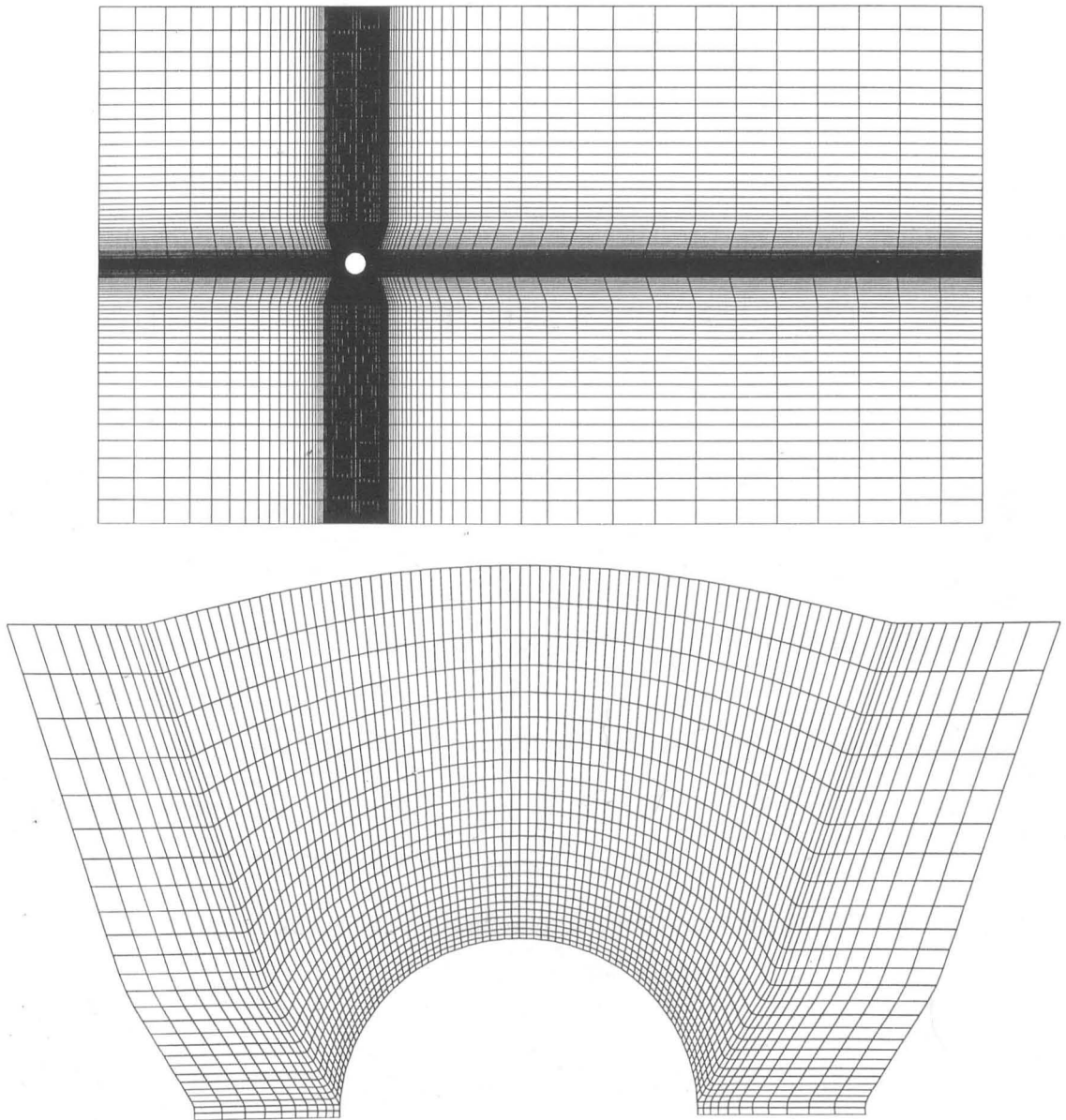
Figure 4.3: Representative numerical grid $D1 - 143 \times 98$ for a circular cylinder.

4.2.2 Boundary and initial conditions

The boundary conditions for the velocity components are also shown in Figure 4.1. At the inlet plane, a uniform profile was specified for the axial velocity ($U = U_0$) and the normal component was set equal to zero. Symmetry boundary conditions were applied at the two free-stream boundaries: $V = 0$, $\partial U/\partial y = 0$. For the present, the issue of *open* or outflow boundary conditions (OBC) still raises many questions, see Sani and Gresho (1994). Free or zero gradient OBC:

$$\frac{\partial U}{\partial x} = \frac{\partial V}{\partial x} = 0 \,, \tag{4.1}$$

and the Sommerfeld radiation conditions (based on the free stream velocity components $U_\infty \approx U_0$, $V_\infty = 0$):

$$\frac{\partial U}{\partial t} + U_\infty \frac{\partial U}{\partial x} = 0 \,; \quad \frac{\partial V}{\partial t} + U_\infty \frac{\partial V}{\partial x} = 0 \,, \tag{4.2}$$

have been the most popular and in many cases successful OBC's for the finite difference and control volume methods. Nakamura et al. (1993) showed clearly that the free outflow condition deforms the velocity and pressure fields near the outflow boundary. The Sommerfeld condition, Equation 4.2, had the least influence on the flow. However, the influence of all types of OBC conditions tested by Nakamura et al. (free OBC and three variants of the Sommerfeld radiation conditions including the above one) was confined to a zone of approximately $(6 - 8)H$ upstream from the outflow boundary. The integral vortex shedding parameters (e.g. the lift and drag coefficients and the Strouhal number) and the flow variables in the near-wake of a cylinder are not affected significantly by the type of OBC for long distances X_o/D. Consequently, the free OBC's imposed at outflow boundaries located at $X_o/H \approx 30$ have been used in this study. On the cylinder surface, zero velocity was specified.

To start vortex shedding calculations, one of the following two initial conditions was employed:

- A uniform (symmetric) velocity field or

- an asymmetric velocity field in order to trigger vortex shedding earlier and reduce the 'start-up' time needed to obtain a cyclical solution.

4.2.3 Computational details

The time–step size

At each new time–step, the governing equations are solved iteratively till the sum of absolute normalized residuals for *all* variables fall below 1×10^{-4}. The time–step size

depends on the grid spacing, which should be small enough to resolve accurately the variable gradients, particularly near the walls. This dependence can be established considering some physical restrictions imposed on the time–step size (cf. Mukhopadhyay et al., 1992 and Anderson, 1995, p.457). First, the time-step size should be smaller than the local convective time scale T_{con} and viscous time scale T_{vis}:

$$\Delta t \;=\; \min(T_{con}, T_{vis}) \, , \tag{4.3}$$

$$T_{con} \;=\; \left(\frac{|U|}{\Delta x} + \frac{|V|}{\Delta y} \right)^{-1} , \tag{4.4}$$

$$T_{vis} \;=\; \left(\frac{2\nu}{\Delta x^2} + \frac{2\nu}{\Delta y^2} \right)^{-1} . \tag{4.5}$$

By defining a non–dimensional time–step (Δt^*) as:

$$\Delta t^* = \frac{\Delta t \, U_0}{H} \tag{4.6}$$

and by approximating Δx and Δy in the above by the smallest grid spacing Δh, and U and V by the reference velocity U_0, one can arrive at variants of the Courant-Friedrichs-Lewy (CFL) condition:

$$\Delta t^* < \frac{1}{2} \frac{\Delta h}{H} \, , \tag{4.7}$$

and the Fourier–number condition:

$$\Delta t^* < \frac{1}{4} \left(\frac{\Delta h}{H} \right)^2 Re \, . \tag{4.8}$$

By reducing the time-step size below the values imposed by the above (approximate) CFL or the Fourier-number conditions, the need for using under-relaxation factors was avoided. For the calculations reported below, Δt^* varied from 1×10^{-3} to 5×10^{-3}. The number of time steps required to advance the calculations over a complete vortex shedding period was generally of the order of 1,000. Note that the number of the time steps per vortex shedding cycle is given as $1/(\Delta t^* St)$. Typically 3–5 outer iterations per time-step were required once a periodic or quasi-periodic solution was established.

Presentation of results

In order to analyze the vortex shedding results, values of the force coefficients (C_D, C_{Dv}, C_L, C_{Lv}), pressure coefficient C_p at the stagnation point, and the velocity components at two locations on the centreline of the cylinder wake, were stored periodically. In the case

of a circular cylinder, the separation angle θ_s, measured from the stagnation point along the upper wall, was also monitored. The time histories of these quantities were used to determine the appropriate time-averaged and root-mean-square values and the characteristic frequencies. A simple method was devised to calculate the vortex shedding frequency of the purely periodic fluctuations. Use was also made of a Fast Fourier Transform algorithm, adopted from Press et al. (1988), to calculate the power spectrum (PS).

Streakline plots were constructed to allow for the tracking of the motion of different fluid structures. This is analogous to the use in experiments of dye continuously injected from a fixed point. Construction of these streaklines is straightforward. Initially (i.e. at time t=0), a number of massless particles is introduced upstream of the cylinder. Then, with knowledge of the local velocity field, the new positions of these same particles are obtained from integration of the velocity equation, thus:

$$\Delta \mathbf{r} = U_p \, \Delta t \, \mathbf{i} + V_p \, \Delta t \, \mathbf{j}. \tag{4.9}$$

The particle velocities U_p and V_p in the above are calculated as averages over the time-step Δt and over the distance $|\Delta \mathbf{r}|$. The locus of positions of particles injected from the same initial location constitutes a streakline.

The time histories of the monitored quantities as well as other results obtained for square and circular cylinders, reflect some common features of the periodic vortex shedding phenomenon. These features are described in the following section.

4.3 Periodic Vortex Shedding: Common Features

4.3.1 Initiation

The present numerical method does not require the introduction of a disturbance to trigger vortex shedding. However, tests were conducted in which the initial flow field was perturbed in one of two ways. The top half of the flow domain was assigned a certain value of streamwise velocity $((U_{up} = U_0))$. The velocity in the bottom half $((U_{lo}))$ was assigned a value that is either 5% greater or less than this value. The results of these tests are shown in Figure 4.4 where the resulting time histories of the drag and lift coefficients for a circular cylinder at $Re = 100$ are plotted. Both methods of perturbation produce the same time histories of the drag coefficients, while the lift–coefficient curves are shifted by a half of the vortex shedding period. These results can be expected since the initial asymmetric velocities U_{lo} are 'symmetric' around the free-stream velocity U_0.
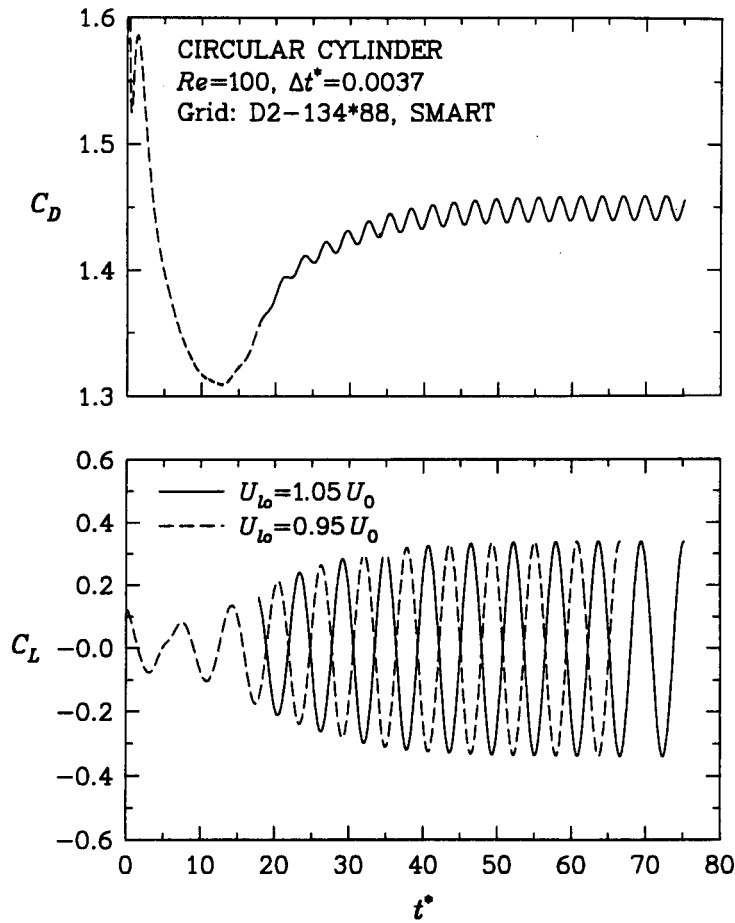
Figure 4.4: Circular cylinder at $Re = 100$. Time histories of the drag coefficient (top) and lift coefficient (bottom) as obtained with two initial asymmetric perturbations.

4.3.2 Development

By using suitable initial perturbations it is possible to reduce the 'start up' time needed to arrive at a periodic solution. This is clearly seen from Figure 4.4 where perturbation was used, and Figure 4.5 where no initial perturbation was applied. For the latter case, calculations were started with a uniform symmetric velocity field ($U = U_0$, $V = 0$) everywhere. The computational grid consisted of $D1 - 170 \times 98$ nodes (similar to that shown in Figure 4.3). The spatial and temporal resolutions (SMART convective scheme and $\Delta t = 0.5$ s or $\Delta t^* = 0.00082$) were selected in accordance with the numerical uncertainty experiments conducted in Section 4.4.

The time histories of the drag and lift coefficients and separation angle (Figure 4.5) show different transient phases of the vortex shedding development. During the first, relatively short period, characterized by no lift force and by decrease of the drag coefficient, a quasi-steady flow with two symmetric vortices is established at $t^* \approx 10$. This is illustrated by the streamlines in Figure 4.6(a). After that, asymmetry was introduced by numerical roundoff effects and two slightly asymmetric vortices evolved behind the cylinder, Fig-

72
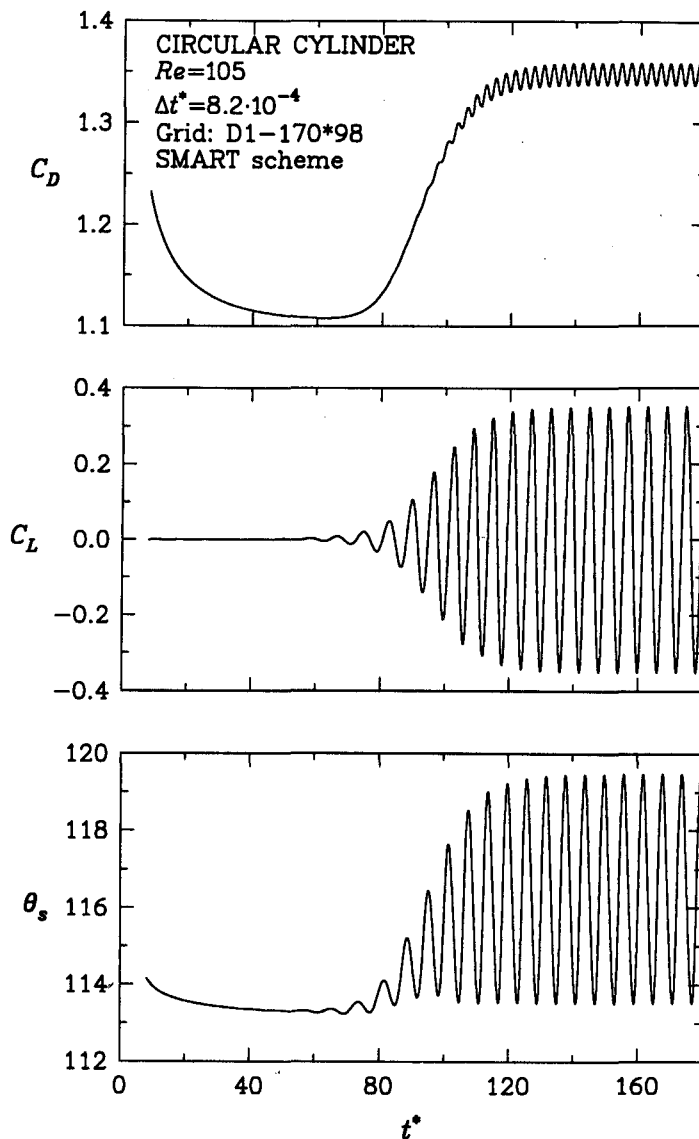
Figure 4.5: Time histories for the flow past a circular cylinder at $Re = 105$: drag coefficient (top), lift coefficient (middle), and angle of separation (bottom).

ure 4.6(b). There is strong evidence to consider the appearance of the asymmetric field as a continuous process (for example, the lift coefficient has insignificant but oscillatory non-zero values). However, the swift changes are visible after the drag coefficient attains its minimum value ($t^* \approx 62$) and after that point vortex shedding begins to develop.

The streamlines appropriate to the first phase of the vortex shedding development (approximately two vortex shedding cycles after the end of symmetry) are shown in Figure 4.7. During this transition period, large quasi-standing vortices elongate and then detach. At the end, the progressively reduced standing vortices disappear and the alternate shedding of vortices from the cylinder starts, Figure 4.7(d) (one pair of vortices over the vortex shedding cycle). This marks the second phase in the vortex shedding development. Its principal characteristics are the gradual reduction of the recirculation region and the increase of the drag coefficient and of the amplitudes of other flow parameters such as the

(a) $t^* = 8.25$, $C_L = 0$

(b) $t^* = 61.96$, $\min(C_D)$
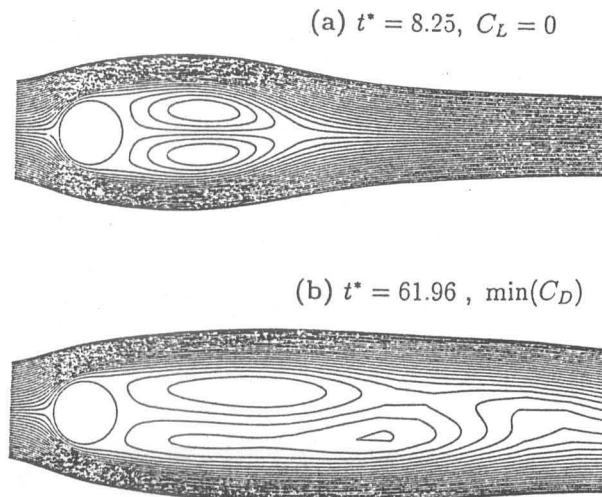
Figure 4.6: Streamline patterns for the flow past a circular cylinder at $Re = 105$: (a) symmetrical wake at $t^* = 8.25$; (b) asymmetrical vortices at the instant $t^* = 61.96$ when the drag coefficient has a minimum value (see also Fig. 4.5).

lift coefficient and separation angle. Another important change, related to reduction of the recirculation zone, is the disappearance of existing shed vortex before a new one is shed, Figure 4.8.

4.3.3 The Karman vortex street

A sequence of streamline patterns for a fully periodic flow is given in Figure 4.9. This sequence covers one complete vortex shedding cycle of period T. The first plot (at $t/T = 0$) corresponds to the instant where the lift coefficient is at maximum. Eaton's sequence of streamlines (Eaton, 1987), computed at $Re = 110$, is very similar to the present one. However, the start of the vortex shedding cycle was not referred to any easily identifiable event (e.g. the point of maximum lift coefficient as is done here).

Figure 4.10 is constructed in order to understand the process of vortex formation. It is based on the sequence of streamlines shown in Fig. 4.9. This process has been interpreted in terms of separatrices, which are the streamlines that contain either a viscous or an inviscid saddle point (cf. Perry et al., 1982). A loop formed by a separatrix bounds the area with closed streamlines (a vortex) whose centre is the inviscid critical point. The streamline plots in Figure 4.9 and vortex formation model in Figure 4.10 confirm the main features of the model proposed by Perry et al. (1982). When a vortex has been shed from the cylinder, for example the upper vortex **A** in Figure 4.10(b), an "alleyway" would be opened. This has the effect of drawing fluid from below the cylinder (around the growing

74

(a) $t^* = 66.69$, $\max(C_L)$

(b) $t^* = 70.83$, $\min(C_L)$

(c) $t^* = 74.93$, $\max(C_L)$

(d) $t^* = 79.01$, $\min(C_L)$
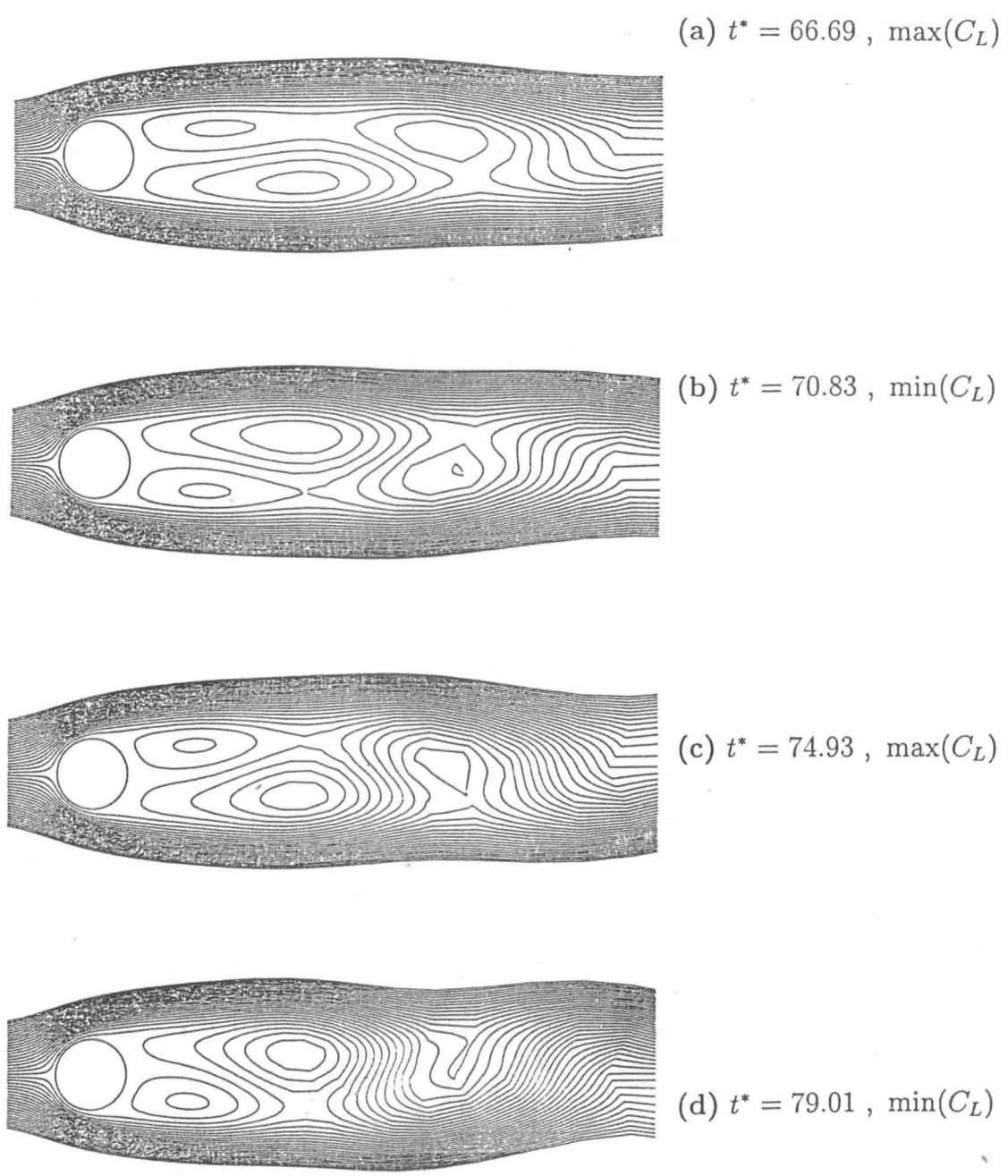
Figure 4.7: Development of vortex shedding past a circular cylinder at $Re = 105$. Streamline patterns showing the time evolution of the flow regimes after the onset of vortex shedding.

(a) $t^* = 82.92$

(b) $t^* = 89.97$

(c) $t^* = 96.54$

(d) $t^* = 114.9$
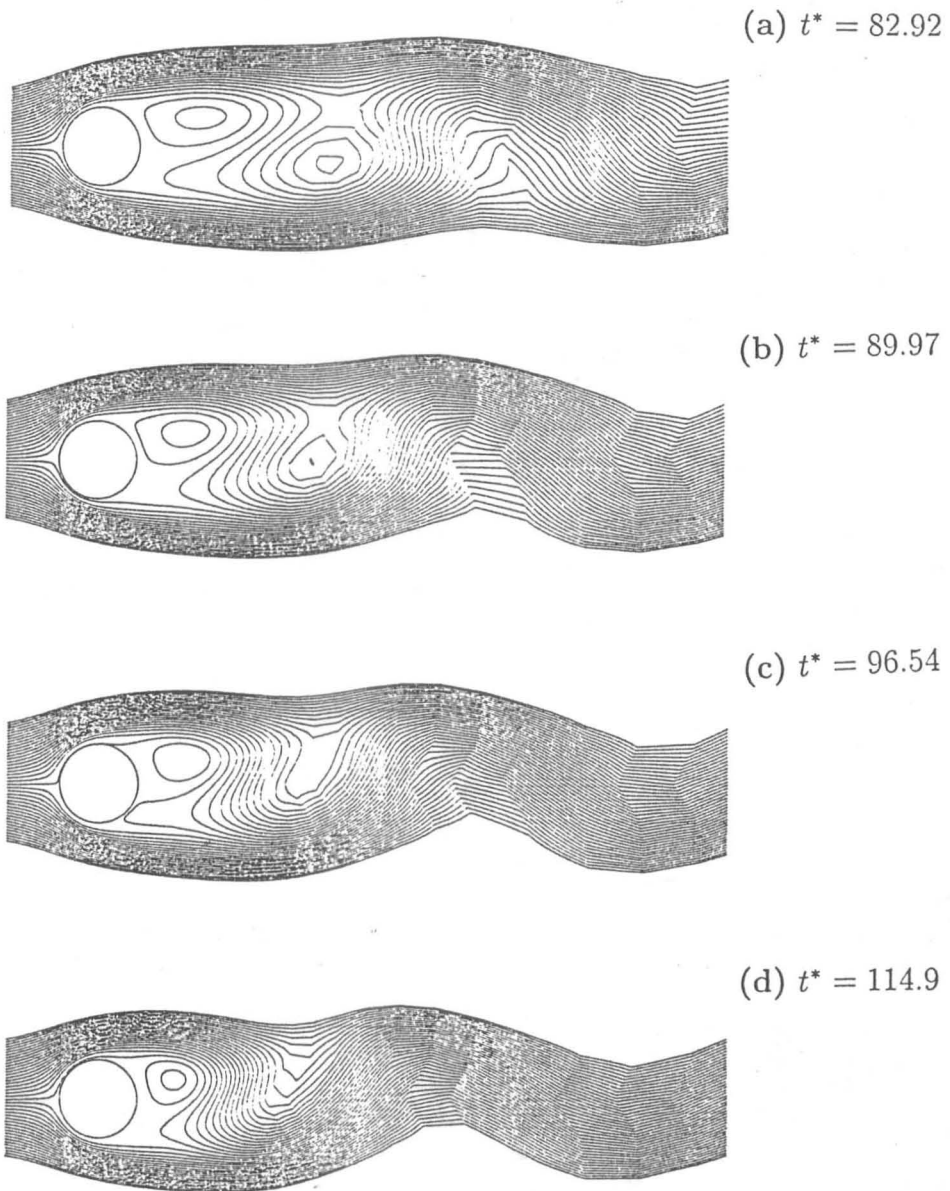
Figure 4.8: Development of vortex shedding past a circular cylinder at $Re = 105$. Streamline patterns obtained at moments when the lift coefficient has maximum values illustrate reduction of the recirculation region and disappearance of two coexisting shed vortices.
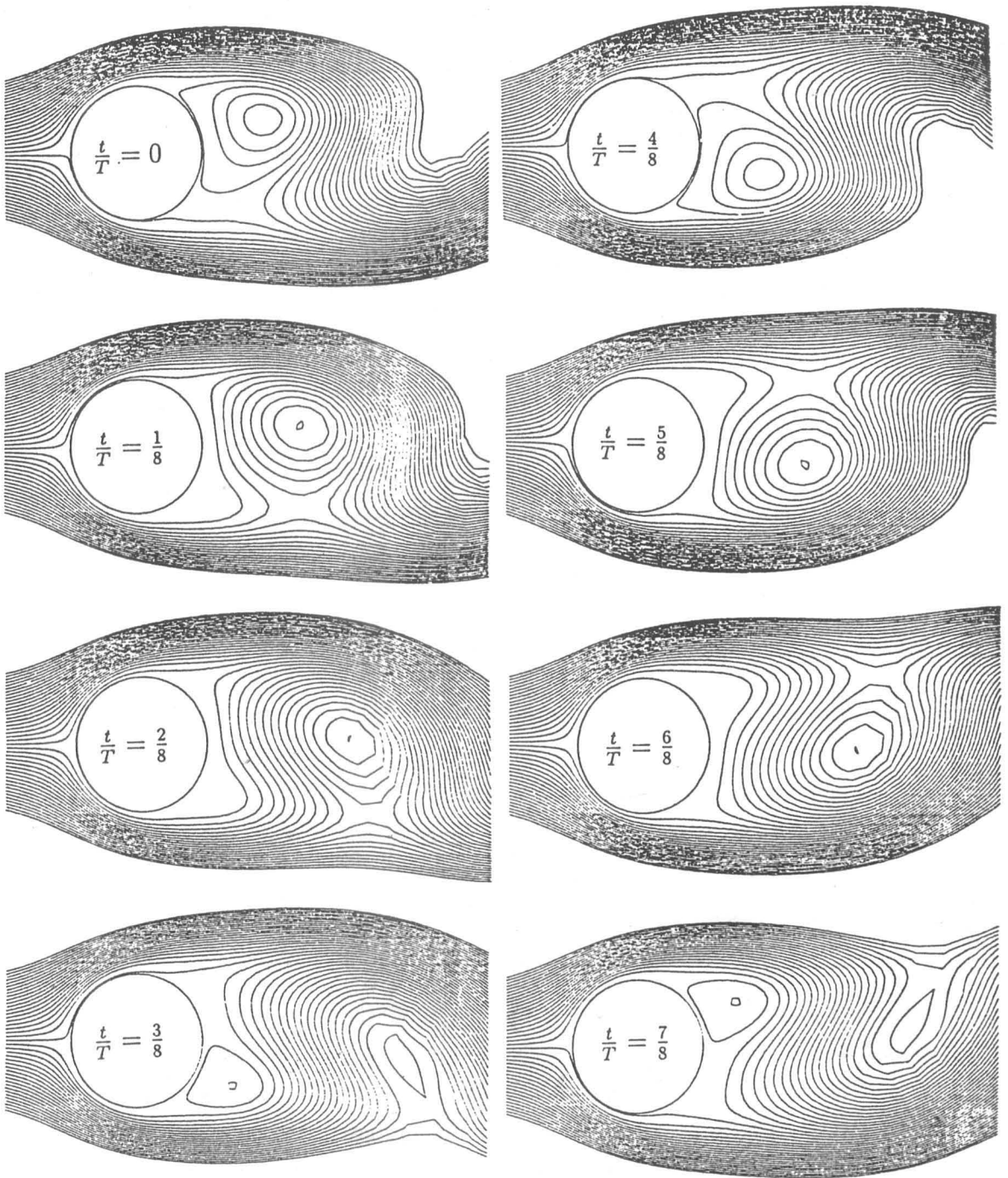
Figure 4.9: Periodic vortex shedding from a circular cylinder at $Re = 105$. Streamlines in the near wake representing a complete shedding cycle (successive plots at intervals of $T/8$).
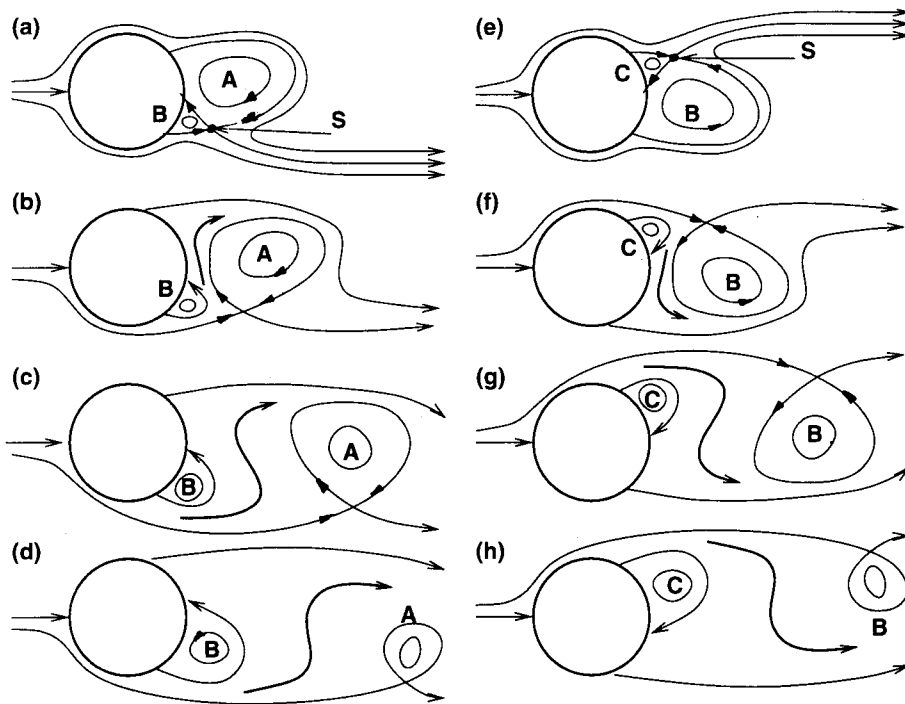
Figure 4.10: Model of periodic vortex shedding using topology of instantaneous stream-lines (separatrices).

vortex **B**) into the upper recirculation region (instantaneous alleyways are indicated by bold lines in Figure 4.10). As vortex **A** is convected away, vortex **B** increases in strength and size, as shown in Figure 4.10(c,d) and Figure 4.9 for $t/T = 3/8$. Before the instant $t/T = 4/8$, a new vortex **C** is born and at this instant the vortex **B** is about to be shed from the cylinder. Note that at $t/T = 4/8$, the lift coefficient attains the minimum value, see Figure 4.13 below. After shedding, vortex **B** is convected away, and the shedding process is repeated. Now, however, the instantaneous alleyway is opened above the cylinder and carries fluid to the bottom of recirculation region, Figure 4.10(f-h).

Perry et al. (1982) did not explain the precise mechanism of the transition processes during which one alleyway, for instance from below the cylinder, closes, and a new one, from above the cylinder, opens, and vice versa. This was tackled by Eaton (1987) who produced streamline plots at intervals of $T/124$, covering the shedding process around the present phase $t/T = 4/8$. Based on these plots, Eaton concluded that an existing alleyway closes and new one opens at the instant when the vortex is shed from the cylinder. The present streamlines at $t/T = 0$ (at maximum C_L) and $t/T = 4/8$ (minimum C_L) indicate that the vortices **A** and **B** have reached their maximum sizes. This means that the instant of transition, analysed by Eaton, can be associated with the maximum or minimum values of the lift coefficient. According to Eaton, at the instant of transition, separatrices are similar to ones for a closed recirculation region containing two counter-rotating vortices; they are drawn in Figure 4.10(a,e), where new saddle points are marked as **S**. Eaton also showed
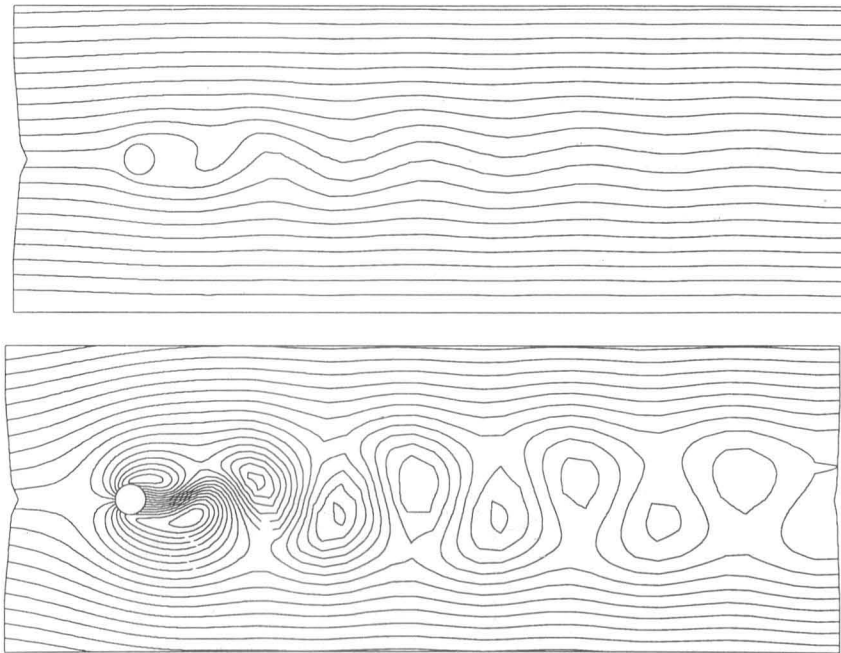
Figure 4.11: Karman vortex street for a circular cylinder at $Re = 105$. Streamlines using fixed frame of reference (top) and with frame of reference in translation at velocity $0.85\,U_0$ (bottom).

that a new vortex (**C**), always with opposite circulation than existing one, is formed before the existing vortex (**B**) is shed (approximately before $T/40$ units).

The general vortex shedding model of Perry et al. (1982) is not reproduced completely here, nor by Eaton (1987). Compared to the model given in Figure 4.10, Perry et al.'s model shows one more vortex being convected away before a new vortex is shed from the cylinder. This situation appears during the vortex shedding development, Figure 4.7(d) and Figure 4.8(a-c), where the recirculation region is longer than in the case of the developed vortex–shedding process.

Streamline patterns in Figure 4.9 suggest that the shed vortices (**A** and **B** in Figure 4.10(d,h)) 'disappear' after leaving the recirculation region. This, however, is due to the difficulties involved in defining a vortex by streamlines (Lugt, 1983, Ch. 2), which are not invariant if the reference frame changes. By adopting a moving frame of reference, the shed vortices become visible again (Figure 4.11(b)) in the form of the Karman vortex street, which comprises two parallel and symmetrical rows of staggered vortices of opposite sign. The use of streaklines is often the clearest way to visualize the shed vortices. The computed streaklines are shown in Figure 4.12(a). Immediately noticeable is the close resemblance between the computed streaklines and the flow visualizations of Tanida (as reported in van Dyke, 1982), Figure 4.12(b). The streaklines look like spirals, directed from the outer edge of the vortex towards its interior. The streaklines in Figure 4.12(a) reveal that the fluid entrained into the recirculation region from one side of the
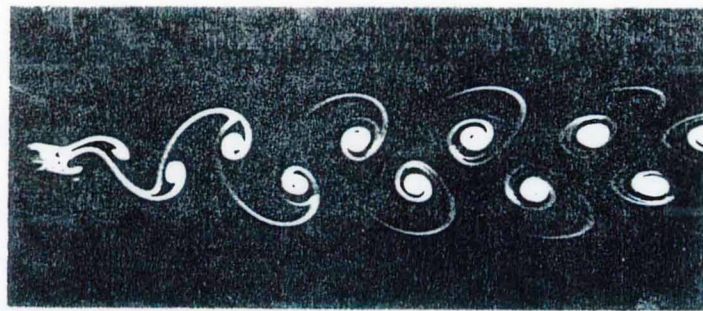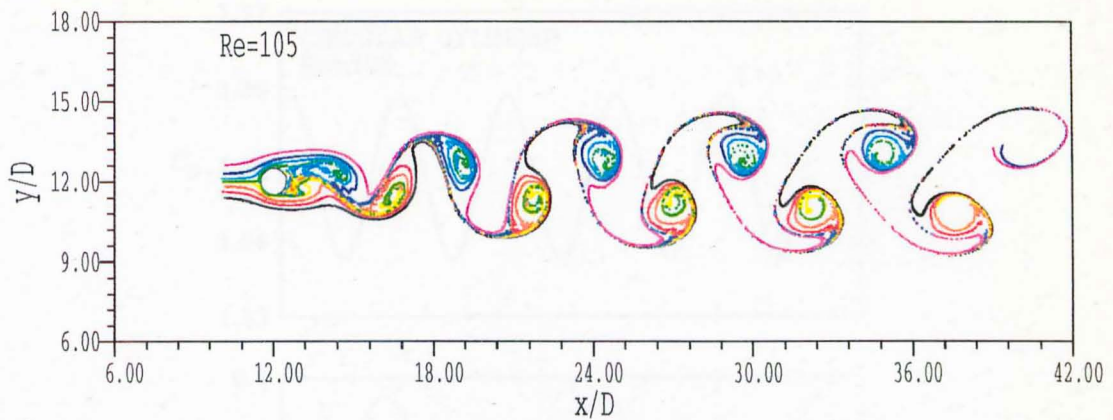
Figure 4.12: Streaklines for a circular cylinder at $Re = 105$: (a) computed at $t^* = 204.9$ (where the lift coefficient is at maximum); (b) photograph from experiments by S. Taneda, van Dyke (1982).

cylinder remains on that side and does not find its way into vortices generated from the opposite side.

When a fully periodic vortex shedding flow is established, all the flow parameters fluctuate periodically around a mean value. Further, the mean lift coefficient becomes zero. This is illustrated in Figure 4.13. It is interesting to examine the relative phase between the parameters plotted in Figure 4.13. It is clear that the lift coefficient and separation angle have the same period of oscillation, but are not in the phase. The relative phase between them is about a quarter of the vortex shedding period. Further, the period of oscillation of the drag coefficient is exactly one half that of the lift coefficient. When the upper separation angle attains a maximum, the drag coefficient is at minimum. There is no such correspondence between the drag and lift coefficients; the shift in their phase is about 1/8th of the vortex shedding period.

Plots of the power spectra (Figure 4.14) show the sinusoidal nature of the flow since only one dominant peak (which defines the dimensionless frequency, i.e. the Strouhal number) exists in all the plots. The fundamental vortex shedding frequency corresponds to the frequency of the lift fluctuations, and it is apparent from the above figures that
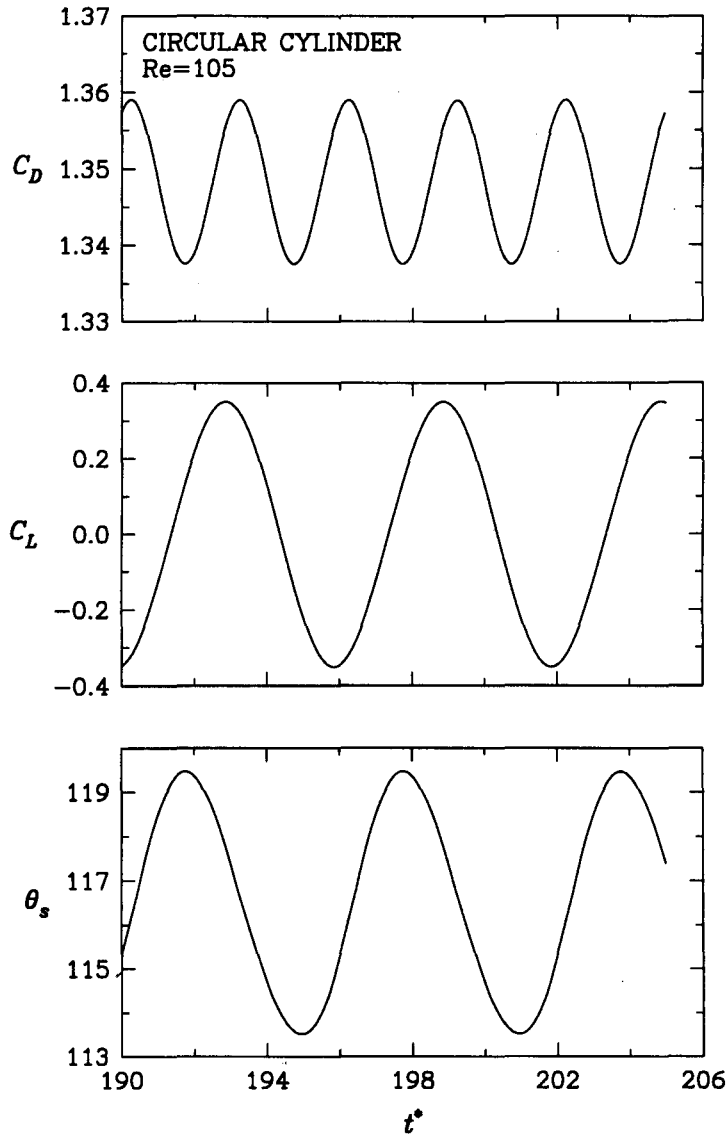
Figure 4.13: Developed vortex shedding from a circular cylinder at $Re = 105$: the drag coefficient (top), lift coefficient (middle), and angle of separation (bottom).

the drag coefficient oscillates at twice the fundamental frequency. This result is due to the fact that the pressure fluctuations at the rear of the cylinder go through a full cycle each time the vortex is shed either from the upper or lower part of the cylinder. Note that the pressure drag and the lift coefficients, C_{Dp} and C_{Lp}, and therefore their viscous counterparts, oscillate with the same frequencies as the total coefficients C_D and C_L.

Figure 4.14 shows that the separation angle oscillates with the fundamental vortex shedding frequency. This is also the case for the stagnation pressure and for the V-velocity component at the monitoring point in the wake. The U-velocity component, however, has the same frequency as the drag forces. All these frequencies are very close to each other, and all yield a Strouhal number value of 0.1668. It is noted that all the Strouhal numbers values reported in the present study have been obtained as the non-dimensional frequencies for the total lift coefficient. In literature, the contribution of the viscous forces

81

to the total forces is often neglected. For low Reynolds-number flows, this is not always justifiable as the viscous contribution can be quite substantial (in this flow, for example, $\overline{C}_D = 1.3483$ and $\overline{C}_{Dv} = 0.3349$ so the viscous contribution is 24.84% of the total drag).
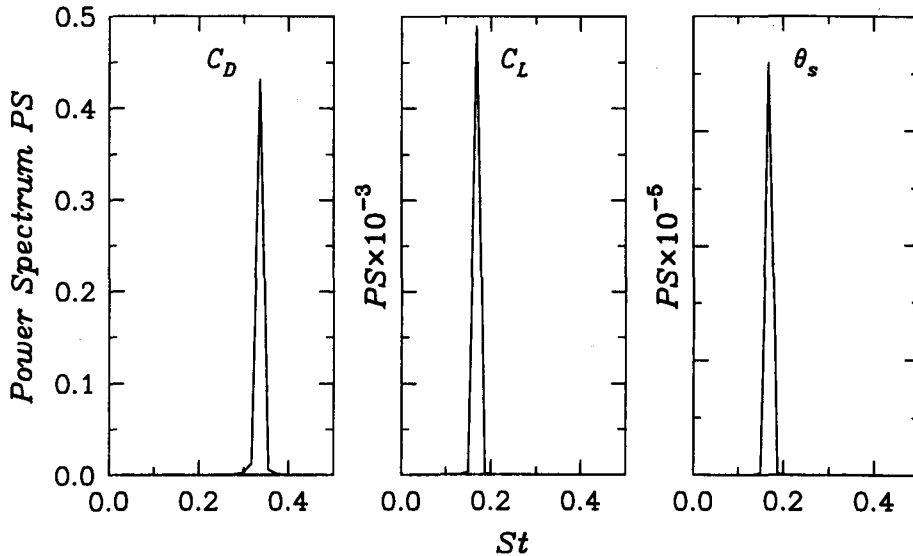

Figure 4.14: Power spectra for the flow past a circular cylinder at $Re = 105$: drag coefficient (left), lift coefficient (middle), and angle of separation (right).

It should finally be noted that a similar picture emerges from the analysis of the flow around a square cylinder. This was done in the course of the present study as well as by Franke (1991) and Kim and Benson (1992). In all cases, plots of the velocity vectors and streamlines over a vortex shedding cycle for both circular and square cylinders showed the growth and shedding of the two "classical", alternating vortices at $Re \approx 100 - 200$. At the end of each half of the cycle, the attached vortex, generated either from the top or from the bottom of the cylinder, reaches almost cylinder size before it is shed into the wake. The main differences between the square and circular flows are attributed to the fact that the separation points in the former are essentially fixed and occur near either the rear or front corners depending on whether Re is less or greater than 150.

4.4 Numerical Uncertainties

Although the vortex shedding problem has been investigated by many authors, the numerical errors (uncertainties) have been only rarely addressed. Rosenfeld (1994) studied the flow over a circular cylinder at $Re = 200$, and obtained a grid-converged solution over the whole domain using the grid with 513×513 nodes. He found that the effects of grid resolution are more paramount in determining the phase, rather than the magnitude of the oscillations. The magnitude of parameters such as the force coefficients can be computed

with coarser grids, while very fine grids are required to resolve the characteristics of the far-wake region. Closely related to the grid resolution effects are temporal resolution effects and the use of high–order accurate convective schemes. Besides these factors, the vortex shedding results can be affected by the size of the computational domain (Behr et al., 1991; Karniadakis and Triantafyllou, 1992; Zhang et al., 1995) and by implemented boundary conditions at the outlet plane (Sani and Gresho, 1994; Abarbanel et al., 1991; and Nakamura et al., 1993).

While the sources of the numerical errors have been identified, it is not always clear how estimates of such errors can be obtained. In this section, the Richardson error estimator (cf. Roache, 1994), described in Appendix B (Equations (B.5) and (B.9)), is used to quantify and report on the grid and time refinement tests. Detailed assessment of the numerical uncertainties is presented below for vortex shedding from single square and circular cylinders.

4.4.1 Time discretisation

The effect of the time-step size was investigated for the flow past a square cylinder at $Re = 200$. The SMART convective scheme was used. Having in mind the grid refinement test of Rosenfeld [1] (1994) and the effect of the domain size reported by Karniadakis and Triantafyllou (1992), a grid ($D1$) of 136 × 118 nodes was employed. The Strouhal number and force coefficients were computed for four values of the time step and the results are presented in Table 4.3 and Figure 4.15.   It is clear that the use of smaller

Test	$\Delta t(s)$	$\Delta t^* \times 10^3$	St	$\overline{C}_D$	$C'_D \times 10^2$	C'_L
1	0.325	1.01	0.1541	1.4606	2.739	0.4079
2	0.65	2.02	0.1543	1.4575	2.695	0.4034
3	1.30	4.04	0.1543	1.4535	2.619	0.3972
4	1.95	6.06	0.1541	1.4506	2.549	0.3919
E_{1t} (%)			0.13	-0.21	-1.61	-1.10
E_{3t} (%)			0.17	-0.65	-5.84	-3.49

Table 4.3: Temporal refinement tests for the flow past a square cylinder at $Re = 200$ (grid $D1 - 136 \times 118$; SMART scheme).

time-step sizes slightly increases the force coefficients, while the changes in the Strouhal numbers are practically negligible. In addition to the integral parameters, the above Table

---

[1] Rosenfeld considered the flow around a circular cylinder at $Re = 200$. For a mesh of 129 × 129 nodes, he reported a maximal error of 16 and 33 % for the pressure and U-velocity, respectively, at a distance of 12 D in the wake. In the vicinity of the cylinder, the errors were negligible.
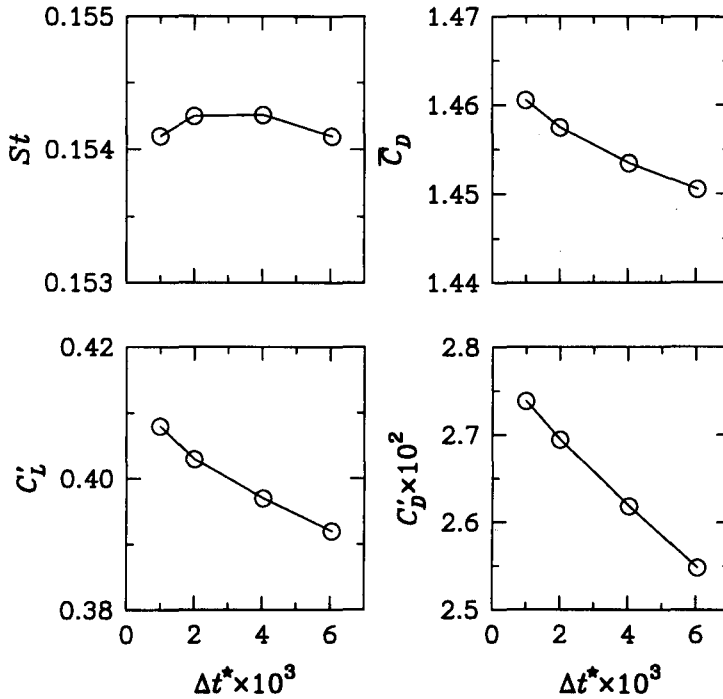
Figure 4.15: Flow past a square cylinder at $Re = 200$. Effect of the time step size on the vortex shedding parameters (grid D1-136x118, SMART scheme).

Test	$\Delta t(s)$	$\Delta t^* \times 10^3$	St	$\overline{C}_D$	$\pm\tilde{C}_D$	$\pm\tilde{C}_L$
1	1.2	1.867	0.1744	1.451	0.010	0.3416
2	2.4	3.733	0.1741	1.449	0.010	0.3387
E_{1t} (%)			-0.17	-0.14	–	-0.85
E_{2t} (%)			-0.34	-0.28	–	-1.70

Table 4.4: Temporal refinement tests for the flow past a circular cylinder at $Re = 100$ (grid $D2 - 134 \times 88$; SMART scheme).

contains the estimated errors E_{1t} for the smallest time-step size $\Delta t = 0.325$ s, and the estimated errors E_{3t} for the $\Delta t = 1.3$ s. For this Reynolds number, the approximate Fourier-number condition, Equation (4.8), gives a time-step size close to the value for which E_{3t} is reported.

The time resolution tests for a circular cylinder at $Re = 100$ are presented in Table 4.4. In this table, the estimated temporal errors E_{2t} correspond to the time-step sizes that are slightly larger than the values obtained from Equation (4.8).

4.4.2 Spatial discretisation

The spatial discretisation error is analysed by grid refinement tests and by use of higher order convective schemes.

Effects of convective schemes

A variety of convective differencing schemes have been implemented in the present code, while the central differencing scheme is used for the diffusion terms. Therefore, the overall accuracy of the spatial discretisation can be the second order. All the implemented schemes were used to compute the flow past a square cylinder at $Re = 250$. The grid $D1 - 136 \times 118$ was employed and the time-step size was $\Delta t^* = 3.89 \times 10^{-3}$.

Figure 4.16 depicts the time evolution of the drag and lift coefficients for the different convective schemes. The computed streaklines are shown in Figure 4.17. Both the time histories and the streakline plots show that the Upwind scheme (UDS) and Central Differencing Scheme (CDS) are inadequate for the present purposes. The unbounded Linear-Upwind scheme (LUDS) is formally second-order accurate and produces a von Karman vortex street with regions of concentrated vorticity preserved well downstream of the shedding points. The centres of vorticity are displaced further from the centreline than has been obtained with other schemes. Accordingly, the mean drag coefficient, amplitudes and r.m.s. values of the drag and lift coefficients attain their highest values, which is also evident from Table 4.5. The bounded MINMOD scheme, as a combination of the

Scheme	St	$\overline{C}_D$	C'_D	$\overline{C}_L$	C'_L	$\pm\widetilde{C}_L$
SMART	0.1381	1.520	5.12×10^{-2}	-1.52×10^{-4}	0.686	0.975
QUICK	0.1387	1.520	4.88×10^{-2}	-1.63×10^{-4}	0.674	0.960
MINMOD	0.1442	1.507	4.39×10^{-2}	-1.22×10^{-4}	0.549	0.779
LUDS	0.1364	1.625	7.04×10^{-2}	-4.69×10^{-4}	0.884	1.260
CDS	0.1664	1.444	1.44×10^{-2}	-9.59×10^{-4}	0.321	0.529
UDS	0.1269	1.383	1.35×10^{-2}	-2.31×10^{-4}	0.280	0.397

Table 4.5: Flow past a square cylinder at $Re = 250$. Strouhal number and force coefficients computed with different convective schemes.

CDS and LUDS schemes, gives satisfactory results that lie in between those of the two schemes. The undesirable properties of CDS and LUDS are eliminated, when necessary, by switching to the UDS scheme. The third-order accurate QUICK scheme is also unbounded with the result that calculated values may over- or undershoot their appropriate levels – sometimes with quite unphysical results. Here, it seems to predict the centres of the shed vortices to lie too close to the centreline, a result which is not supported by experiments, see Figure 4.12(b). The SMART scheme can be seen as the bounded QUICK scheme, thus formulated so as to be of third-order accuracy and dropping to first-order if necessary to preserve boundedness. Its predicted streaklines reveal patterns similar to those visualized in physical experiments. Comparing the time evolution of the drag and
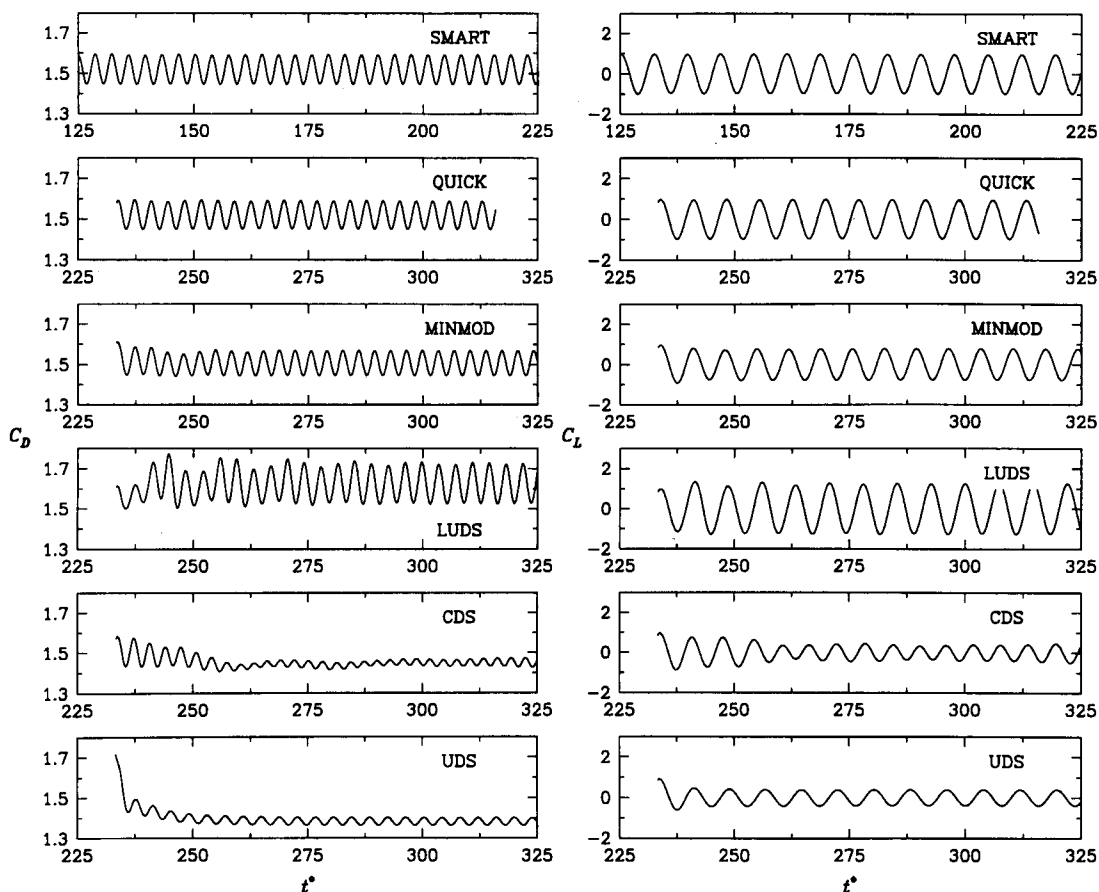
Figure 4.16: Flow past a square cylinder at $Re = 250$. Time history of the drag (left) and lift (right) coefficient as obtained with various convective schemes (grid D1-136x118, $\Delta t^\star = 3.89 \times 10^{-3}$).

lift coefficients and integral parameters, it is clear that the SMART and QUICK schemes produce very similar results. That the same results obtained with other schemes differ more is not surprising, since they are less accurate than SMART and QUICK.

To summarize, vortex shedding flows can be computed by the simple and bounded upwind convective scheme but it will require a large number of the grid nodes but then the CDS scheme can also be used. This number is significantly reduced by using the higher order schemes. Physical considerations have emphasized the necessity to use bounded convective schemes. Among the two bounded schemes tested here, the SMART scheme needs less grid nodes than MINMOD to achieve grid-independent solutions.

Grid refinement

Grid refinement tests have been carried out with reference to the Strouhal number and the force coefficients. The SMART scheme was used throughout. As already mentioned, the grid density was varied by changing the grid expansion factor and non-dimensional distance of the near-wall cells from the wall. The last parameter determines the resolution
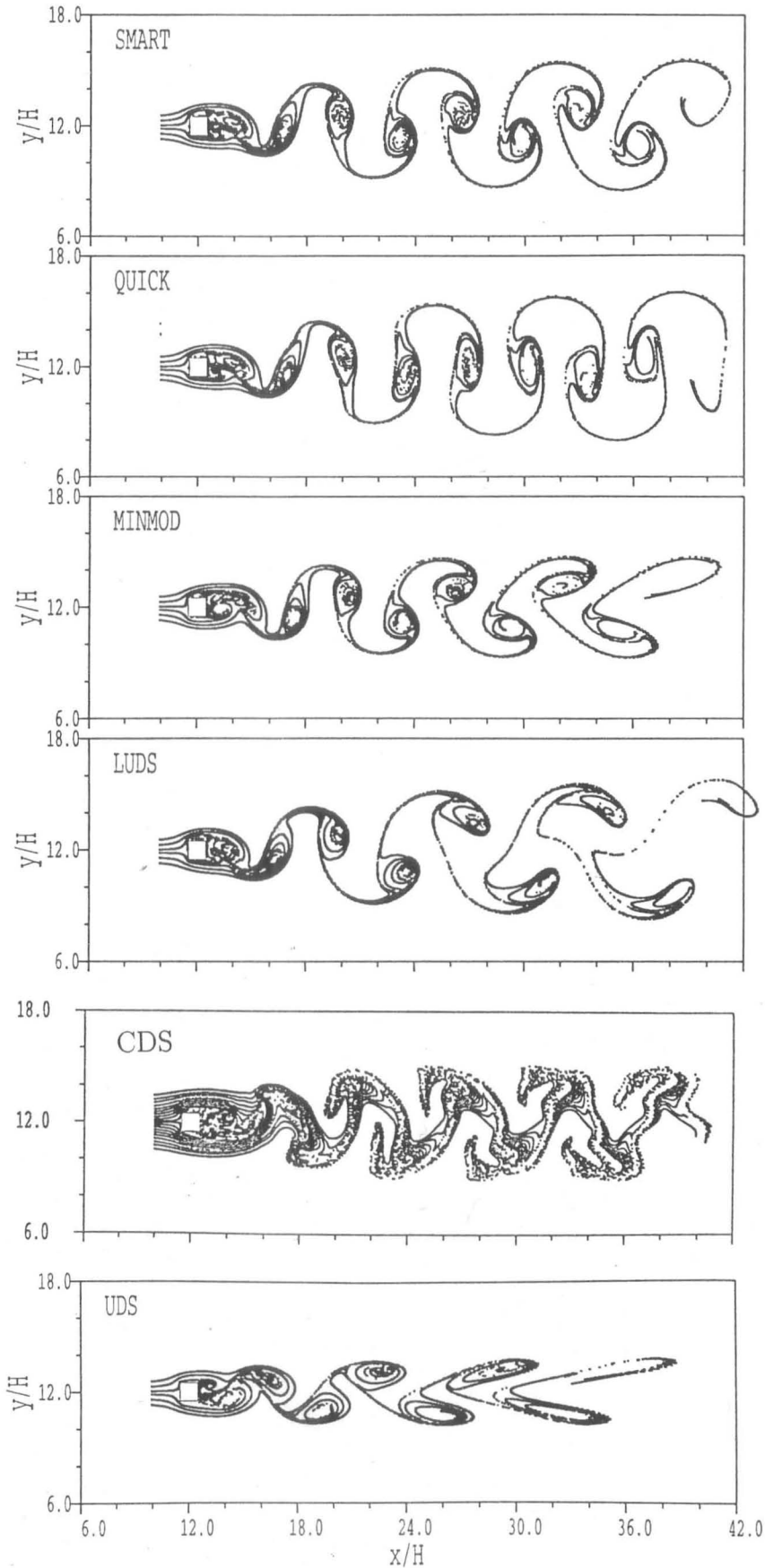
Figure 4.17: Flow past a square cylinder at $Re = 250$. Streaklines computed with different convective schemes.

Domain-Grid	f_e	St	$\overline{C}_D$	C'_D	C'_L
$D3 - 134 \times 112$	1.125	0.1473	1.498	4.53×10^{-3}	0.181
$D3 - 169 \times 150$	1.080	0.1488	1.508	4.96×10^{-3}	0.187
E_1[fine grid] (%)		-1.47	-0.96	-12.58	-4.66
E_2[coarse grid] (%)		-2.48	-1.62	-21.26	-7.88
$D2 - 123 \times 106$	1.125	0.1539	1.589	4.57×10^{-3}	0.173
$D2 - 167 \times 140$	1.080	0.1554	1.597	4.96×10^{-3}	0.179
E_1[fine grid] (%)		-1.21	-0.63	-9.91	-4.22
E_2[coarse grid] (%)		-2.17	-1.13	-17.77	-7.57

Table 4.6: Flow past a square cylinder at $Re = 100$. Influence of the grid expansion factor on the integral parameters ($\Delta n_c/H = 0.005$, $\Delta t^* = 0.78 \times 10^{-3}$).

Domain-Grid	$\Delta n_c/H$	St	$\overline{C}_D$	C'_D	C'_L
$D1 - 136 \times 118$	0.005	0.1381	1.520	5.12×10^{-2}	0.686
$D1 - 160 \times 142$	0.0025	0.1375	1.527	5.46×10^{-2}	0.707
E_1[fine grid] (%)		0.96	-1.11	-14.91	-6.97
E_2[coarse grid] (%)		1.36	-1.57	-21.11	-9.87

Table 4.7: Flow past a square cylinder at $Re = 250$. Influence of the near-wall distance on the integral parameters ($f_e = 1.125$, $\Delta t^* = 0.38 \times 10^{-3}$).

of a boundary layer generated on the cylinder surface.

The influence of the grid expansion factors can be deduced from Table 4.6, where the results are given for $Re = 100$. This effect is also shown in Figure 4.18 which includes the additional results for the grid $D2 - 169 \times 150$ with $\Delta n_c/H = 0.0025$ and $f_e = 1.10$. Note that a very small time-step size was used in order to minimize the time resolution errors. It is obvious that for this Re all the global parameters increase on the finer grids, obtained here by using smaller grid expansion factors. A similar trend characterizes the effect of the near-wall distance $\Delta n_c/H$ on the force coefficients at $Re = 250$, while the Strouhal number slightly decreases on the finer grid, Table 4.7 and Figure 4.19. Thus, one can expect very close results when they are obtained on relatively fine grids, refined to

Domain-Grid	f_e	$\Delta n_c/H$	St	$\overline{C}_D$	$C'_D \times 10^3$	C'_L
$D2 - 167 \times 140$	1.08	0.005	0.1554	1.597	4.96	0.179
$D2 - 169 \times 150$	1.10	0.0025	0.1548	1.598	4.92	0.178
Difference χ (%)	-	-	0.39	-0.06	0.81	0.56

Table 4.8: Comparison of two types of the grid refinement for the flow past a square cylinder at $Re = 100$.
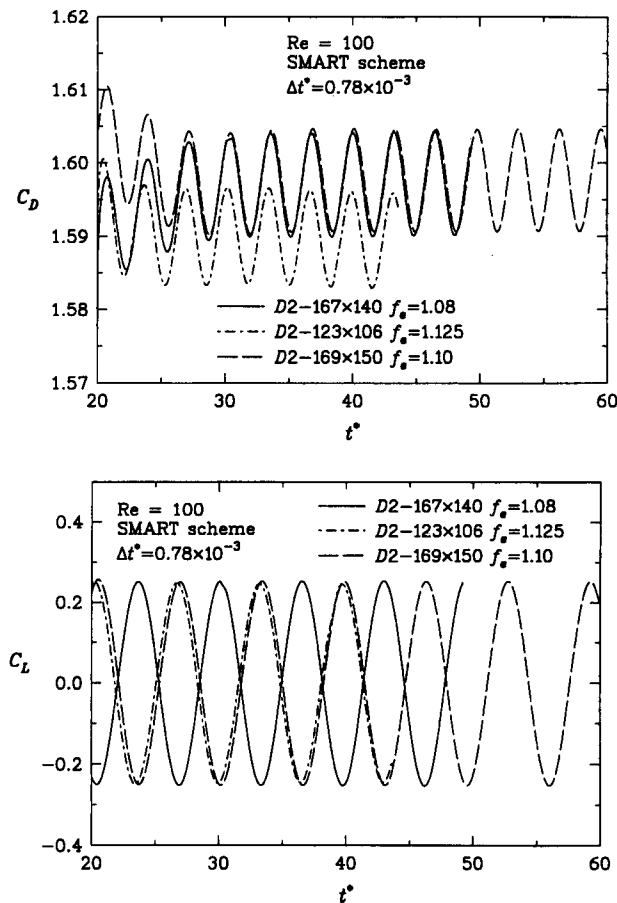
Figure 4.18: Flow past a square cylinder at $Re = 100$. Effect of the grid expansion on the drag coefficient (above) and lift coefficient (below).

the similar size by reducing either the grid expansion factor or the near-wall distance. The results for two fine grids at $Re = 100$, shown in Table 4.8, confirm the above conclusion. Both Tables 4.6 and 4.7 include the estimated errors for the fine and coarse grids. For these errors, Equations (B.5) and (B.9) were used with the order $\varpi = 2$ and the grid refinement ratio r was computed from Equation (B.8).

4.4.3   Size of the computational domain

In Figure 4.1, three parameters X_i, X_o, and Y_s are used to describe the size of the computational domain. Behr et al. (1991) analysed the influence of the location of the outflow boundary X_o for the flow past a circular cylinder at $Re = 100$. For both types of outlet boundary conditions used in that study, the force coefficients and Strouhal number did not show significant variations for the $X_o/D > 14.5$. The same conclusion was drawn by Nakamura et al. (1993) who computed the flow past a square cylinder at $Re = 100$ (uniform grids– $\Delta n_c/H = 0.05$, $\Delta t^* = 0.01$) with four types of outlet boundary conditions and for two locations $X_o/H = 28$ and $X_o/H = 68$. They found that the differences between the results for the force coefficients and Strouhal numbers were less than 1%.
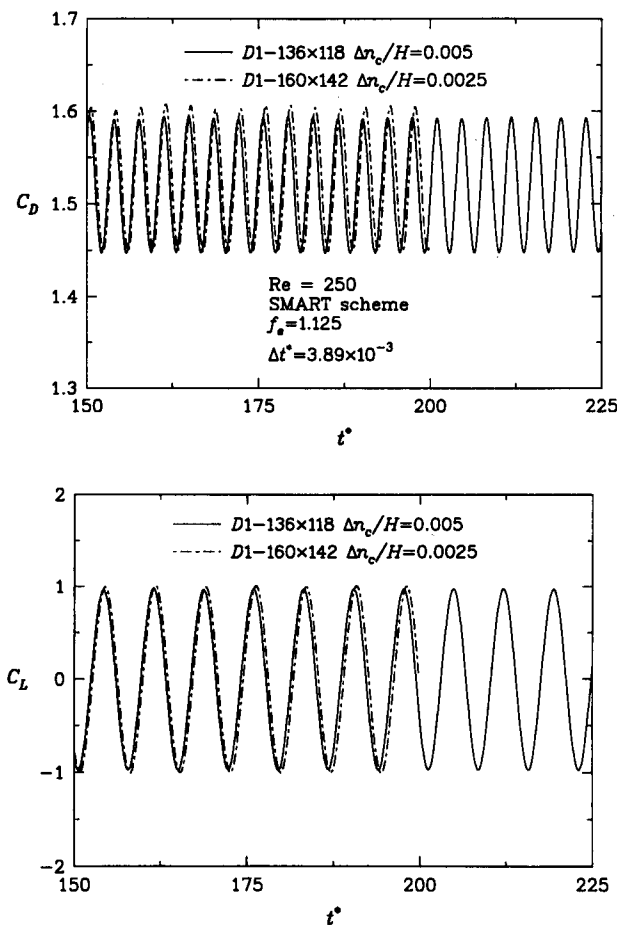
Figure 4.19: Flow past a square cylinder at $Re = 250$. Effect of the near-wall distance on the drag coefficient (above) and the lift coefficient (below).

As the tests of Karniadakis and Triantafyllou (1992) have indicated, the placement of symmetry boundaries is more critical. Table 4.9 summarizes the effects of the dimensions Y_s/H and X_i/H (see also Table 4.1) on the vortex shedding parameters for the flow around a square cylinder at $Re = 100$. Four cases were computed with the *confinement* or *blockage factor*:

$$B_f = \frac{H}{2Y_s} \tag{4.10}$$

ranging from 8.33 to 3.33 %. It is obvious that the values of the vortex shedding parameters decrease for smaller values of the blockage factor B_f. The placement of the symmetry boundaries closer to the cylinder reduces the effective flow area around it and increases local velocities. Accordingly, the force coefficients are greater than those in a large (unbounded) domain.

The estimated uncertainties due to the domain sizes E_d[domain] are also given in Table 4.9. In order to calculate them, variations of the vortex shedding parameters with the blockage factor B_f are plotted in Figure 4.20. Essentially, the plotted results, with the exception of the C_L', exhibit linear dependence on the blockage factor for small values of

Domain-[Grid size]	B_f (%)	St	$\overline{C}_D$	$C_D' \times 10^3$	C_L'
$D2 - 123 \times 106$	8.333	0.1539	1.5899	4.577	0.1733
$D3 - 134 \times 112$	5.556	0.1473	1.4981	4.531	0.1813
$D1 - 136 \times 118$	4.167	0.1444	1.4614	4.214	0.1690
$D4 - 139 \times 122$	3.333	0.1430	1.4430	4.085	0.1689
Extrapolated values	0	0.1374	1.3694	3.569	0.1685
E_d[D2] (%)		12.00	16.10	28.24	2.85
E_d[D3] (%)		7.21	9.40	26.95	7.60
E_d[D1] (%)		5.09	6.72	18.07	0.30
E_d[D4] (%)		4.08	5.37	14.46	0.24

Table 4.9: Domain size effect on the vortex shedding parameters for the flow past a square cylinder at $Re = 100$ ($\Delta t^* = 0.778 \times 10^3$, $\Delta n_c/H = 0.005$, $f_e = 1.125$)

this factor. This is in agreement with theoretical and empirical correction formulae for the wall effects on unsteady forces of two-dimensional bluff bodies; see for example Ota et al. (1994). Thus, uncertainties presented in Table 4.9 are calculated from Equation (B.4), where the extrapolated value for the zero blockage ratio is treated as the exact solution Φ_0.

The reported domain size uncertainties should be regarded as approximate. Firstly, they were calculated neglecting the influence of the dimension X_i/H. Secondly, the resolution near the domain boundaries was inadequate. For reasons of expediency, most of the earlier vortex shedding studies were done using solution domains similar to $D2$ and, more rarely, $D3$. In such cases one can expect much higher uncertainties due to the domain size (say of around 10% for the St-number and mean-drag coefficient) than due to either temporal or spatial resolutions.

4.4.4 Summary

The intriguing fact that the domain size errors in many cases cancel the time and space discretisation errors further complicates quantification of the numerical uncertainties. The previously reported errors have been used to establish approximate error bands for the integral vortex shedding parameters computed here

- on the grids generated inside domains $D1$ (see Table 4.1 and 4.2),

- by using the SMART convective scheme,

- with $\Delta n_c/H \approx 0.005$, $f_e \approx 1.125$,
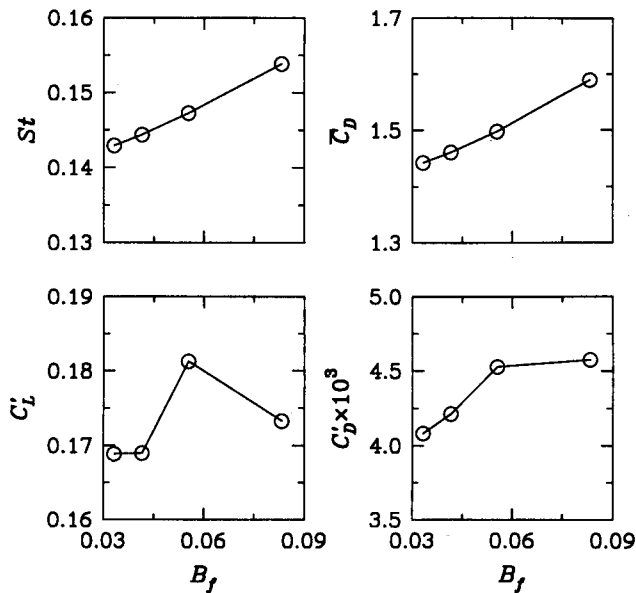
Figure 4.20: Flow past a square cylinder at $Re = 100$. Variations of the Strouhal number (top, left), the mean drag, (top, right), r.m.s. drag (below, left) and r.m.s. lift (below, right) coefficients with the blockage factor.

Estimated errors for	St	$\overline{C}_D$	C'_D	C'_L
Time discretisation, E_{1t} (%)	< 1.	< 1.	-6.	-3.5
Space discretisation, E_{1xy} (%)	±2.	-2.	-20.	-8.5
Domain size, E_{1d} (%)	5.	7.	18.	< 1.

Table 4.10: Estimated error bands for the laminar vortex shedding results ($\Delta n_c/H \approx$ 0.005, $f_e \approx 1.125$, domain $D1$, SMART).

- with time-step sizes chosen according to the Fourier number condition, Equation (4.8), or to the CFL condition, Equation (4.7),

- and for the Reynolds numbers up to $Re = 250$.

These error bands, are given in Table 4.10. The signs of errors have been entered as they were obtained for the computed Re–values and cylinder geometries; for other conditions the signs may change.

4.5 Single Cylinders in Uniform Flows

The principal parameter that determines the flow regimes in the case of smooth square and circular cylinders is the Reynolds number. Different vortex shedding regimes for these geometries have been discussed in Introduction, Section 1.2. It appears that the wake becomes three-dimensional at $Re \approx 200$ and the transition to turbulent state can be expected for Reynolds number values in the range $200 - 1000$. The present predictions

were obtained for Reynolds number values up to 1000 for the case of a square cylinder and up to 2000 for the circular cylinder. The grids used were $D1 - 136 \times 118$ for the square, and $D1 - 143 \times 98$ for the circular cylinder. It is expected that the uncertainties associated with these predictions will be of the same order as shown in Table 4.10.

4.5.1   Square cylinder: results and discussion

Simulations were carried out for Reynolds numbers in the range $70 - 1000$. The calculated integral parameters are presented in Table 4.11. It is seen from this Table that the average

Re	$\Delta t^* \cdot 10^3$	St	$\overline{C}_D$	C'_D	$\overline{C}_{Dp}$	$\overline{C}_L$	C'_L	$\pm \tilde{C}_L$
70	0.82	0.129	1.533	0.0015	1.423	$2.6 \cdot 10^{-5}$	0.109	0.156
100	2.49	0.144	1.460	0.0042	1.412	$-1.9 \cdot 10^{-5}$	0.169	0.238
150	3.73	0.156	1.426	0.0124	1.436	$1.6 \cdot 10^{-4}$	0.257	0.364
200	4.04	0.154	1.454	0.0262	1.492	$1.1 \cdot 10^{-4}$	0.397	0.564
250	3.89	0.138	1.520	0.0512	1.569	$-1.5 \cdot 10^{-4}$	0.686	0.975
300	3.49	0.134	1.629	0.1410	1.679	$2.3 \cdot 10^{-4}$	0.945	≈ 1.7
500	3.11	0.139	1.750	0.4110	1.781	$-3.7 \cdot 10^{-3}$	0.982	≈ 2.30
1000	3.11	0.129	2.337	0.6780	2.349	$-7.7 \cdot 10^{-2}$	1.535	≈ 3.07

Table 4.11: Square cylinder. Predicted integral parameters as obtained with grid D1-136x118 and the SMART scheme.

drag coefficient $\overline{C}_D$ decreases with Reynolds number (in the range $70 - 150$) but thereafter starts to increase. At $Re = 150$, the pressure drag coefficient $\overline{C}_{Dp}$ is larger than the total drag coefficient indicating that the viscous forces change sign (becomes negative) at this Reynolds number. This implies that the separation points move from the rear to the front corners of the cylinder.

The velocity vectors for $Re = 100$, plotted in Figure 4.21(top), show that the flow separates at the rear corners. At $Re = 150$, Figure 4.21 (bottom) shows that separation occurs from the front corner of the upper surface, and from the rear corner of the bottom surface. Since the flow is periodic, this means that the separation points alternate between the front and rear corners.

The effect of Reynolds number on the time histories of the drag and lift coefficients can be seen from Figure 4.22. The amplitudes of the force coefficients increase monotonically with Reynolds number. Periodic vortex shedding is strongly in evidence for Reynolds numbers up to 250. For $Re = 300$, repeatable patterns are evident (i.e. quasi-periodic vortex shedding). The lift coefficient exhibits an asymmetrical pattern, although
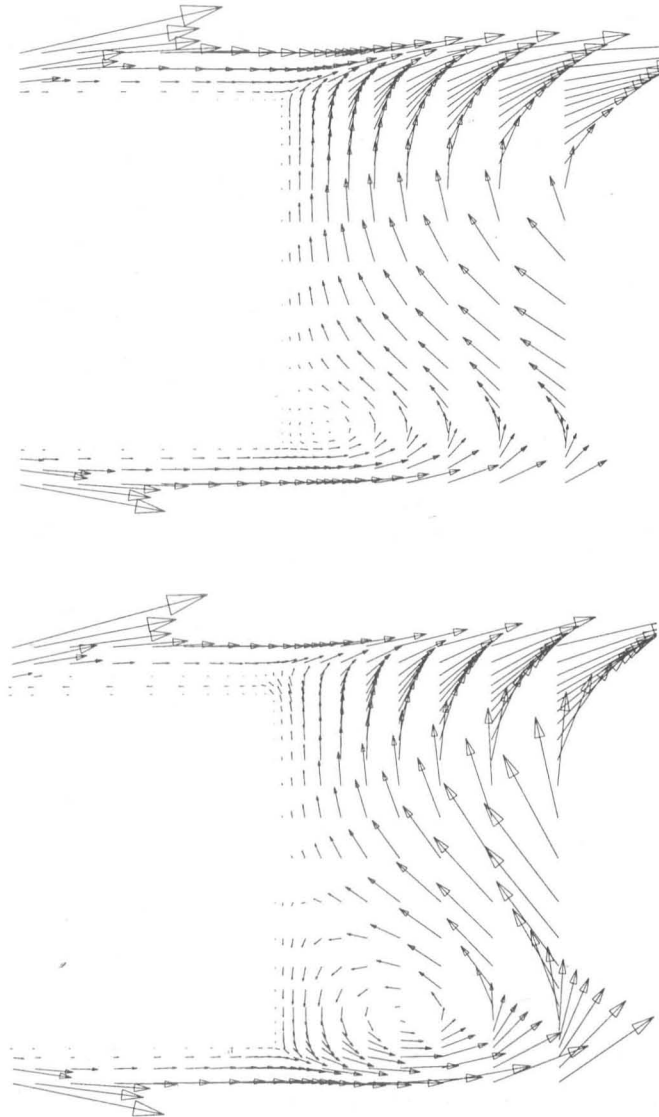
Figure 4.21: Velocity vectors around a square cylinder as calculated at two Reynolds numbers: (top) $Re = 100$, (bottom) $Re = 150$ (grid D1-136x118, SMART scheme).

its long–time mean value is still close to zero, Table 4.11. There is still some evidence of repeatable patterns for $Re = 500$, while for the higher Re–value of 1000 the behaviour appears to be somewhat chaotic.

As can be seen from Table 4.11, the long–time mean of the lift coefficient is not negligible for $Re = 500$ and 1000. Obviously, when the value of Re exceeds a certain limit, which is close to the one when the three-dimensionality appears, the flow does not exhibit symmetry in a sense that the flow patterns above and below the centre line repeat, with a 180° phase difference. This feature has been reported by other researchers. Asymmetrical vortex shedding from a square cylinder was noticed at $Re \geq 500$ by Arnal et al. (1991), Lin (1991) ($Re = 1000$). It can also be seen in Franke's study (1991) (at $Re = 300$) from examination of the time history of the lift coefficient. Those authors (and others, e.g. Davis and Moore (1982), Ramaswamy and Jue (1992) and Okajima et

al. (1992)) reported cycle-to-cycle variations in their results, with multiple frequencies becoming apparent at the Reynolds numbers after the onset of three-dimensionality. Additional frequencies occurred at different Reynolds numbers and this can be explained by different grid resolutions, especially near the walls. The tests carried out in this work confirm that with increased near-wall grid resolution, the additional frequencies appear at lower Reynolds numbers. This also occurs when computations are performed in the narrower solution domains. Thus, for example, the onset of asymmetric shedding was shifted from $Re = 300$ to $Re = 250$ when the domain $(D2)$ i.e. the grid $D2 - 123 \times 106$ was used.

A question arises here as to whether there exists a direct connection between the additional frequencies and the occurrence of asymmetrical vortex shedding. At present, there is no satisfactory answer to this question. However, it is worth looking for the origins of cycle-to-cycle variations in the force coefficients that produce additional vortex shedding frequencies. A change from a periodic to quasi-periodic and eventually irregular behaviour of the force coefficients must be associated with changes of the flow structures around the cylinder. As can be seen in Figure 4.23, the flow reattachment at the cylinder sides is a new and important feature which certainly affects the time evolution of the flow quantities for Reynolds number values greater than 300. Although the plots in Figure 4.23 were not obtained at the same phase of the shedding cycle, one can easily notice an increase of the reattachment zone with the Reynolds number (the reattachment happens at lower side of a square for all plotted cases). For $Re = 300$, a very small reattachment zone originates close to the rear corner (this was detected by an enlarged plot not shown here). For higher Reynolds numbers, the reattachment point moves towards the centre of the bottom side, and the detached vortex is clearly visible for $Re = 1000$.

Lin (1991) reported an asymmetrical vortex shedding pattern for a square cylinder at $Re = 1000$ (a quite coarse grid 70×47 was used) and a non-zero value of the mean lift coefficient. Another asymmetrical pattern, a mirror-image counterpart to the first one, was obtained by inverting the initial perturbation method. Similar mirror-image time records of the lift coefficients are depicted in Figure 4.24(top). Two initial perturbations, explained in Section 4.3.1, were used. The patterns of the lift coefficient, computed without any artificial perturbation, show a close resemblance to the patterns obtained with the second perturbation ($U_{lo} = 1.05\,U_0$), Figure 4.24(bottom). As in the case of truly periodic flow (see Figure 4.4), the same time records were obtained for the drag coefficient, Figure 4.25(top). A comparison with the case without initial disturbance, Figure 4.25(bottom), suggests that for this Reynolds number the drag coefficient is practically not affected by the initial perturbations. Further remarks on this phenomenon will be presented in Section 4.5.3.
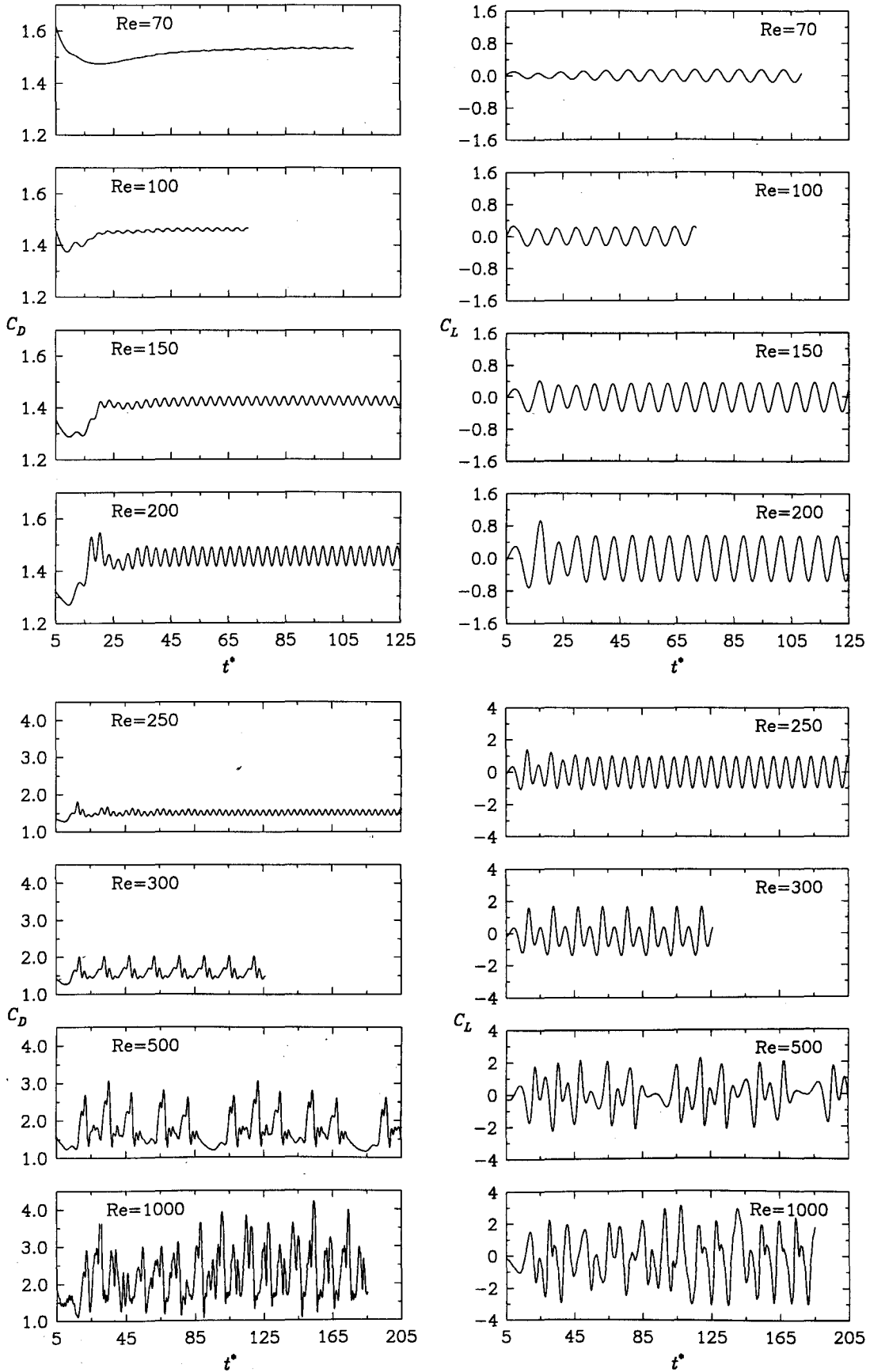
Figure 4.22: Time histories of the drag coefficient (left) and the lift coefficient (right) for the flow around a square cylinder as calculated at different Reynolds numbers (grid D1-136x118, SMART scheme).
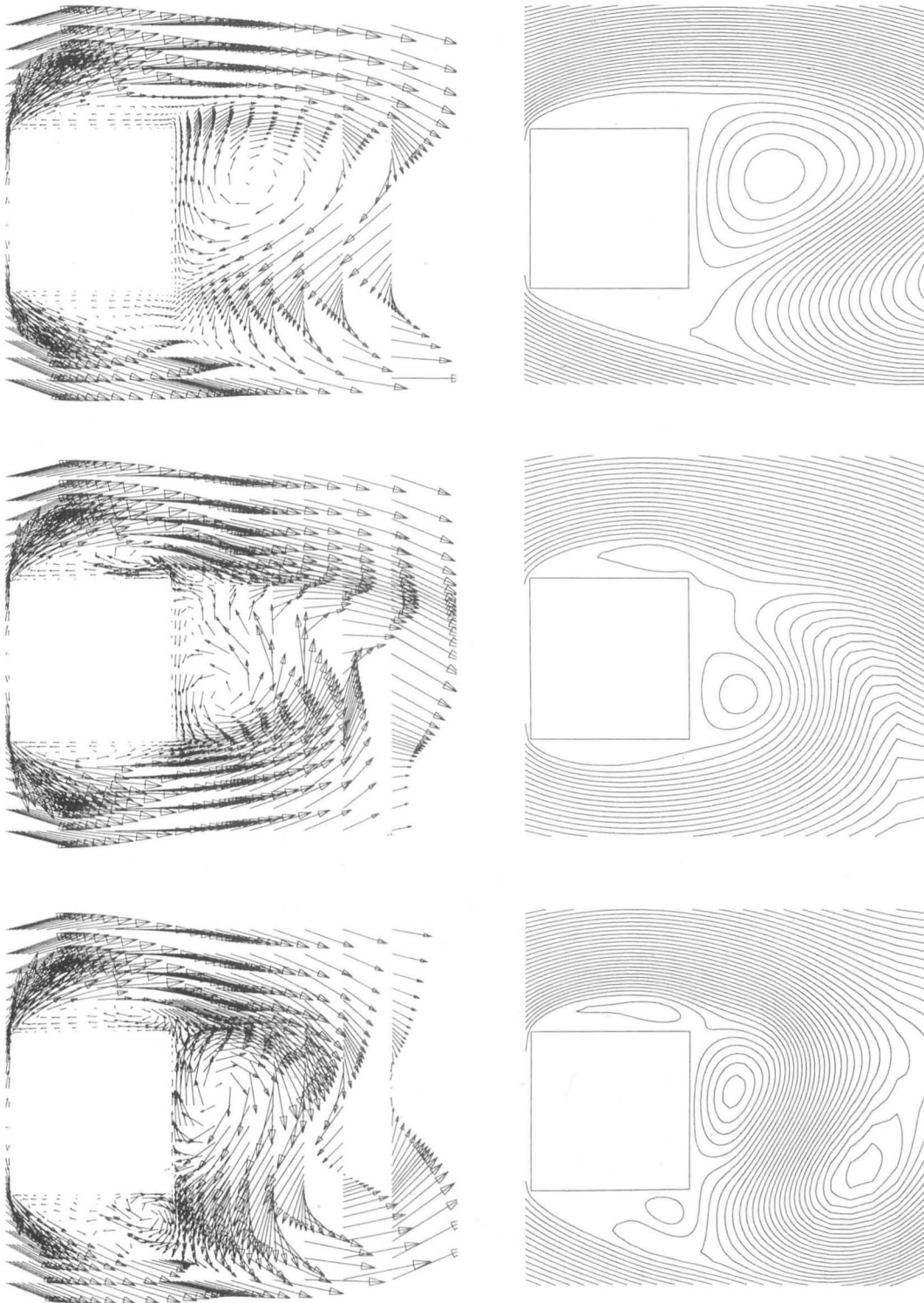
Figure 4.23: Velocity vectors and streamlines around a square cylinder showing the flow reattachment at the cylinder sides: (top) $Re = 300$, (middle) $Re = 500$, and (bottom) $Re = 1000$ (grid D1-136x118, SMART scheme).
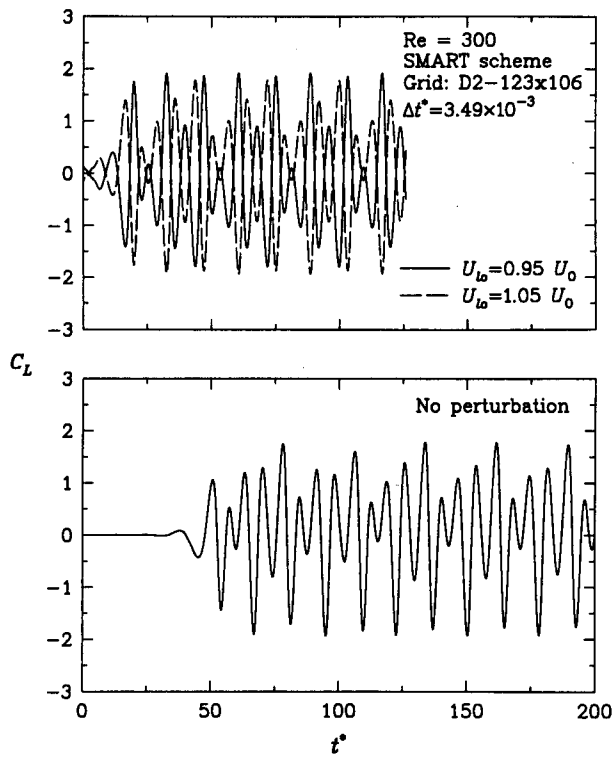
Figure 4.24: Flow around a square cylinder at $Re = 300$. Time traces of the lift coefficient as calculated with two initial perturbations (top) and without it (below).
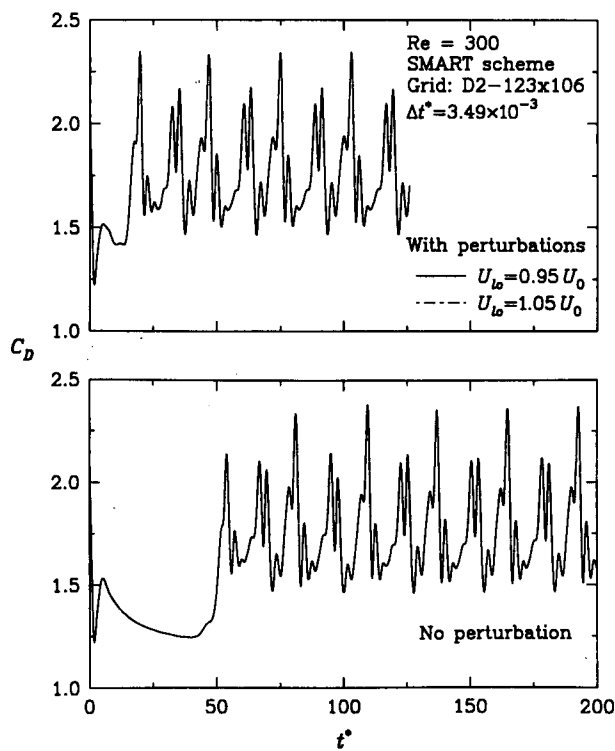
Figure 4.25: Flow around a square cylinder at $Re = 300$. Time traces of the drag coefficient as calculated with two initial perturbations (top) and without it (below).

The present predictions for the mean drag coefficient and the Strouhal number are compared with the results of others in Figure 4.26.
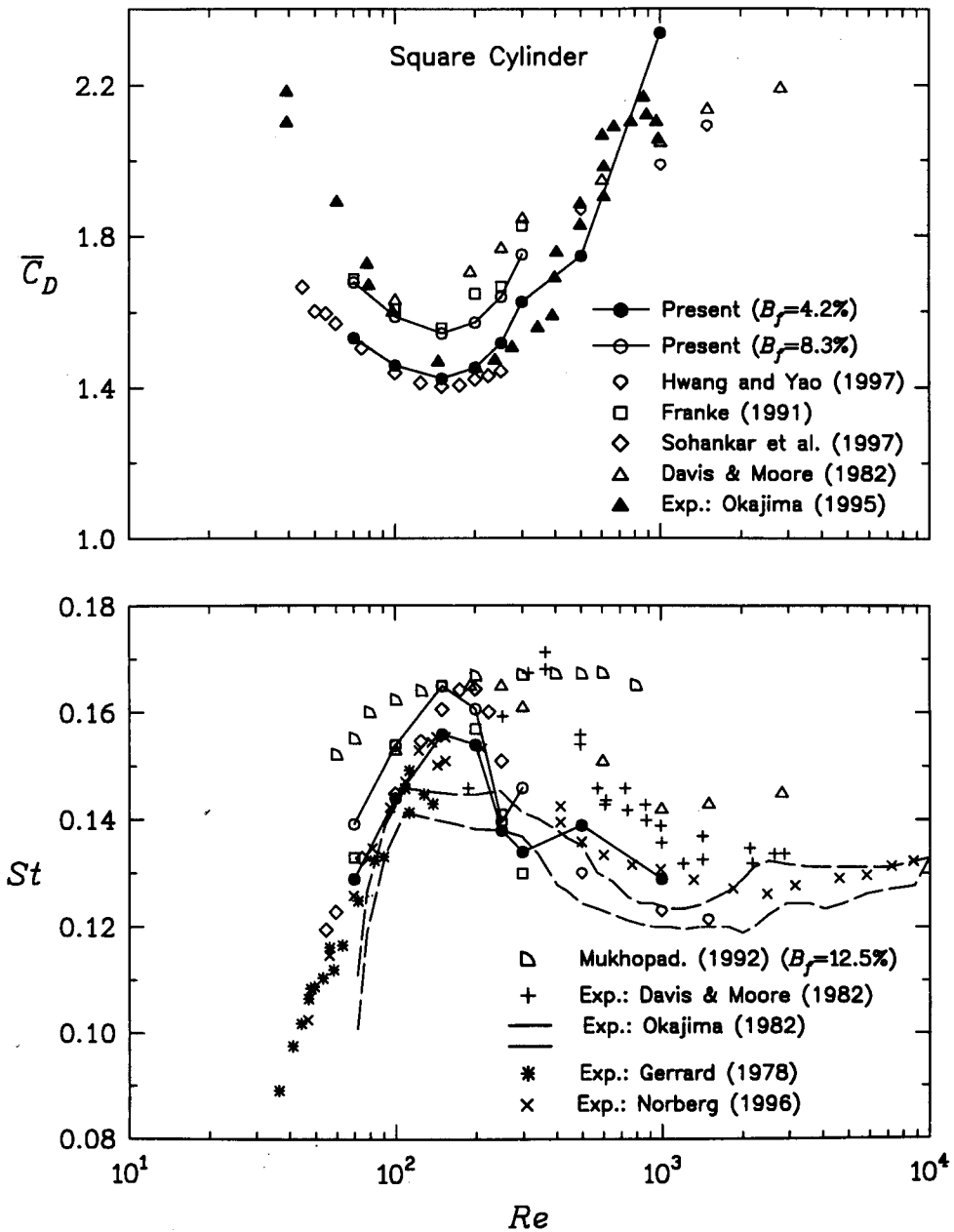
Figure 4.26: Square cylinder. Predicted and measured mean drag coefficients and Strouhal numbers (grids D1-136x118 and D2-123x106; SMART scheme).

Two sets of the present results, obtained with different solution domains (represented by the blockage factor B_f) are included. The effect of the placement of the symmetry boundaries is clearly illustrated by these sets. Both the drag coefficient and the Strouhal number are increased when the width of the solution domain is reduced. This conclusion is supported by the Strouhal–number results of Mukhopadhyay et al. (1992) calculated for $B_f = 12.5\%$. Franke (1991) performed calculations on a solution domain similar to

the present one (grid $D2 - 123 \times 106$) and his results agree well with the present results ($B_f = 8.3\%$) for most Reynolds numbers.

There is good agreement between the present results for the mean drag coefficient ($B_f = 4.2\%$) and those of Sohankar et al. (1997). When both results are compared with the measured data of Okajima (1995), satisfactory agreement exists only for Re-numbers from 150 to 500. Considering other results, note that Hwang and Yao (1997) used the grids of similar fineness as here, while Davis and Moore (1982) employed coarser grids.

Four sets of experimental results exist for the Strouhal number. Gerrard's (1978) data have been rarely acknowledged by CFD researchers, while the results of Okajima (1982) and Davis and Moore (1982) have become a standard reference. However, the large discrepancies between the measurements of Okajima and Davis and Moore, ranging from 14% to 21% for $Re > 250$, pose many questions. After analysing all possible sources of experimental uncertainties, Li and Humphrey (1995) suspected "*that at least one of the two experiments was affected by unknown systematic error(s)*". The present results as well as the results of Franke (1991) and Sohankar et al. (1997) display a clear maximum at $Re \approx 150 - 200$. Excluding the results for $Re = 250$ and 300, the present predictions for a large domain ($B_f = 4.2\%$) agree well with the recent measurements of Norberg (1996).

4.5.2   Circular cylinders results and discussion

The predicted vortex shedding parameters in the range 50–2000 are summarized in Table 4.12. In contrast to the square cylinder, the total drag coefficient here is always greater than the pressure drag. The latter quantity increases monotonically with Reynolds number. The total drag coefficient displays a minimum value around $Re = 150$ (as was the case for the square cylinder) but the Strouhal–number maximum is shifted now from $Re = 150$ to $Re \approx 1000 - 2000$. This is in agreement with the measurements (see Figure 4.28 below). The amplitudes of all the force coefficients increase with Reynolds number whilst the angle of separation θ_s decreases. Turning now to the time evolution of the drag and lift coefficients, plotted in Figure 4.27, it is noted that symmetric, periodic patterns prevail, even for Reynolds number of 1000. Asymmetric vortex shedding is evident for $Re = 2000$. Note that this flow shares certain features with the flow around a square cylinder at $Re = 300$, e.g. repeatable patterns in the time records and an asymmetrical behaviour for the lift coefficient. In addition, the use of two initial asymmetric perturbations produced qualitatively the same results as those presented in Figures 4.25 and 4.24 for a square cylinder at $Re = 300$.

The relatively recent data of Williamson (1989, 1996) for Strouhal number (given in
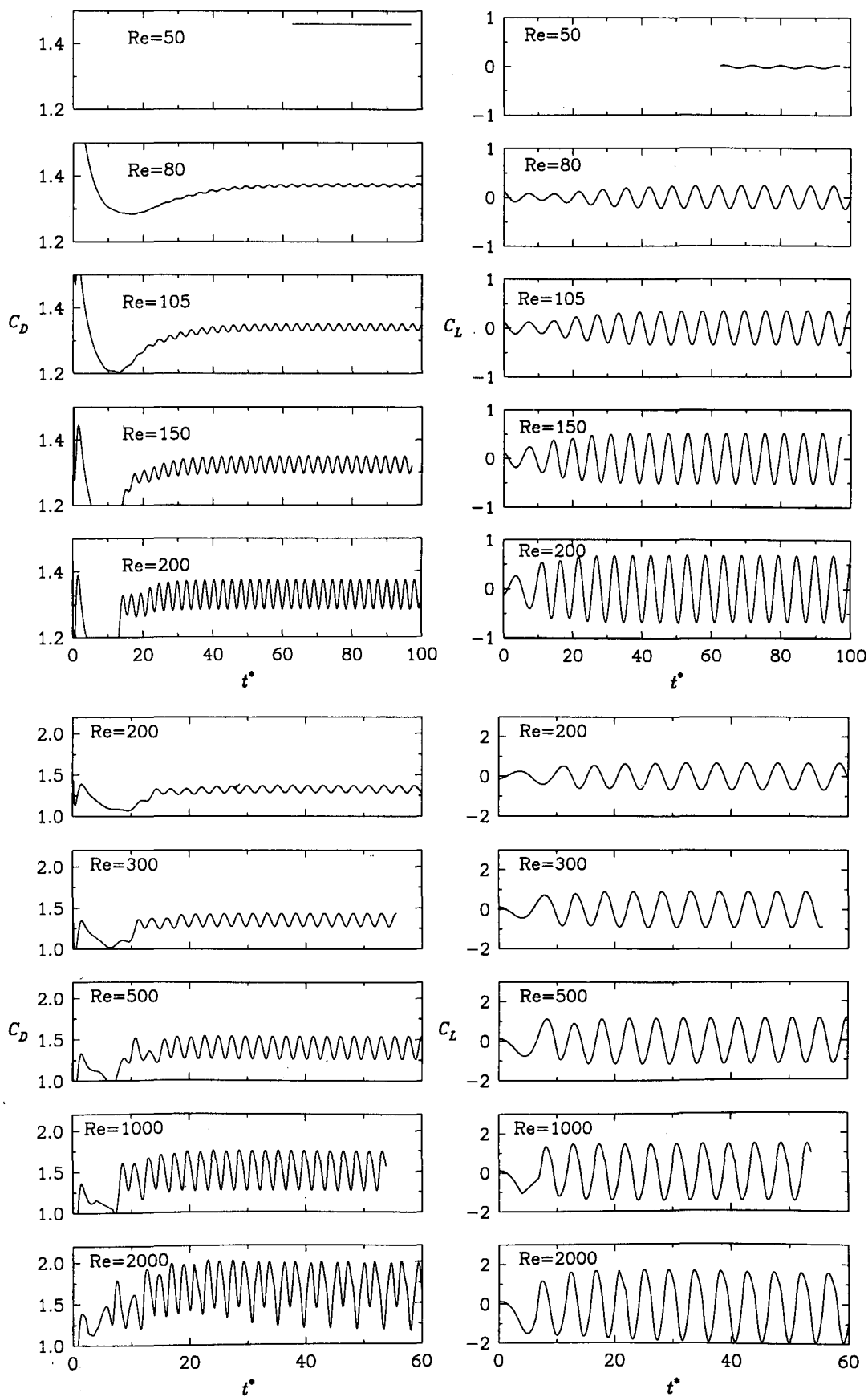
Figure 4.27: Time history of the drag coefficient (left) and the lift coefficient (right) for vortex shedding from a circular cylinder as a function of Reynolds numbers (grid D1-143x98, SMART scheme).

Re	$\Delta t^* \cdot 10^3$	St	$\overline{C}_D$	C_D'	$\overline{C}_{Dp}$	$\overline{C}_L$	C_L'	$\pm \widetilde{C}_L$	$\overline{\theta}_s,^\circ$
50	0.78	0.124	1.465	0.0031	0.993	$-2.4 \cdot 10^{-4}$	0.020	0.028	123.4
80	0.78	0.153	1.373	0.0029	0.995	$2.1 \cdot 10^{-5}$	0.168	0.238	118.8
105	0.78	0.165	1.341	0.0075	1.007	$-1.2 \cdot 10^{-6}$	0.247	0.349	116.4
150	1.52	0.181	1.325	0.0182	1.041	$4.6 \cdot 10^{-5}$	0.369	0.523	113.6
200	2.49	0.191	1.329	0.0312	1.079	$-2.0 \cdot 10^{-4}$	0.482	0.683	111.6
300	2.33	0.203	1.359	0.0568	1.149	$-7.4 \cdot 10^{-4}$	0.645	0.914	109.2
500	2.49	0.214	1.409	0.0982	1.244	$8.5 \cdot 10^{-5}$	0.819	1.158	108.7
1000	2.49	0.223	1.527	0.1690	1.407	$-1.6 \cdot 10^{-3}$	1.047	1.459	107.5
2000	2.49	0.223	1.688	0.2300	1.601	$-3.8 \cdot 10^{-2}$	1.277	≈ 1.78	107.4

Table 4.12: Flow around a circular cylinder. Predicted integral parameters as obtained with the grid D1-143x98 (see Table 4.2) and the SMART scheme.

a tabulated form) provide an excellent benchmark case for the numerical simulations of vortex shedding from circular cylinders. The measurements are in the Reynolds number range $50 - 450$. This range spans both the unstable wake and periodic laminar vortex shedding regime ($Re = 40 - 190$) and the wake transition regime ($Re = 190 - 1000$). Table 4.13 shows that the present results for periodic vortex shedding stand in good comparison with the measurements of Williamson. This table also includes the drag coefficient values obtained from the high-resolution numerical simulations of Henderson (1995). Henderson reported that his results were fitted well by the following function:

$$\overline{C}_D = \overbrace{1.4114 - 0.2668 Re^{0.1648} \exp(-0.003375 Re)}^{\overline{C}_{Dp}} + \overbrace{2.5818/Re^{0.4369}}^{\overline{C}_{Dv}} . \qquad (4.11)$$

The relative errors presented in Table 4.13 are smaller than the estimated error bands given earlier in Table 4.10. This does not necessarily mean the estimated errors are too conservative since cancellation of errors is always possible.

The computed Strouhal numbers and the drag coefficients versus Reynolds number are shown in Figures 4.28 and 4.29. Also plotted there are the 'benchmark' solutions of Rosenfeld (1994) (obtained for $Re = 200$ on a large domain equivalent to the present $D1$) and Engelman and Jamnia (1990) ($Re = 100$, domain $D2$). The present predictions agree well with those results. The influence of the distance between the cylinder and the symmetry boundaries (i.e. the blockage effect B_f) is again quantified by comparing the results for domains $D1$ ($B_f = 4.2\%$) and $D2$ ($B_f = 8.3\%$). Domain sizes typically used in most of earlier studies (e.g. Gresho et al., 1984; Karniadakis, 1989; Zhang et al., 1995) – domains like $D2$ with a distance $Y_s \approx \pm 6D$ – produce artificially high values for the drag coefficient and the Strouhal number. The simulations of Zhang (1995) are very close to the present ones for the narrower domain $D2$. The Strouhal-number

	Strouhal number		Differ.	Drag coefficient		Differ.
Re	Williamson (1989) [a]	Present	%	Henderson (1995) [b]	Present	%
50	0.1231	0.1237	0.49	1.449	1.465	+1.10
80	0.1528	0.1515	-0.85	1.373	1.373	+0.02
105	0.1667	0.1652	-0.90	1.346	1.341	-0.39
150	0.1834	0.1806	-1.53	1.333	1.325	-0.63

[a]Experiment
[b]Simulations

Table 4.13: Flow past a circular cylinder. Comparison of the computed Strouhal number and the drag coefficient (D1-143x98, SMART scheme) with data of Williamson (1989) and simulations of Henderson (1995), respectively.

results of Karniadakis (1989) and Gresho et al. (1984) fall a little above those of Zhang and the present results, along the upper experimental bounds. Other numerical results, where the blockage factor is unknown but might be insignificant (Li et al., 1991; Sa and Chang, 1991; Braza et al., 1986; Borthwick, 1986), are in general within the experimental uncertainty range. Focusing again on the present predictions for a large domain $D1$, they are in a good agreement with the predictions of Henderson (1995) and Franke et al. (1990).

All recent two-dimensional simulations at Reynolds numbers above the one for which the experimental flow becomes three-dimensional ($Re \approx 200$) have inaccurately predicted the vortex shedding parameters, especially the force coefficients. Thus, for example, while measured drag coefficient (e.g. Wieselsberger, 1923) continuously decreases up to $Re = 2000$ (as shown in Figure 4.29), the computed values start to increase at $Re \approx 180$ where a transition from a two-dimensional to a three-dimensional wake begins. Three-dimensional effects on the vortex shedding flow are the subject of the next section.

4.5.3 Three-dimensionality and limitations of 2–D simulations

The onset of three–dimensional motions, for nominally two–dimensional cylinder geometries, has been the most challenging and problematic aspect of vortex shedding flows. We assume that the three-dimensional flow is caused by natural flow instabilities (*intrinsic* three-dimensionality) and not by geometry or boundary conditions (*extrinsic* effects). The critical Reynolds number Re_c^{3D}, where a secondary flow instability of the two-dimensional wake develops, varies with the cylinder geometry but usually occurs at around 200.

Williamson (1988, 1996) associated the onset of three-dimensionality at $Re = 180 - $
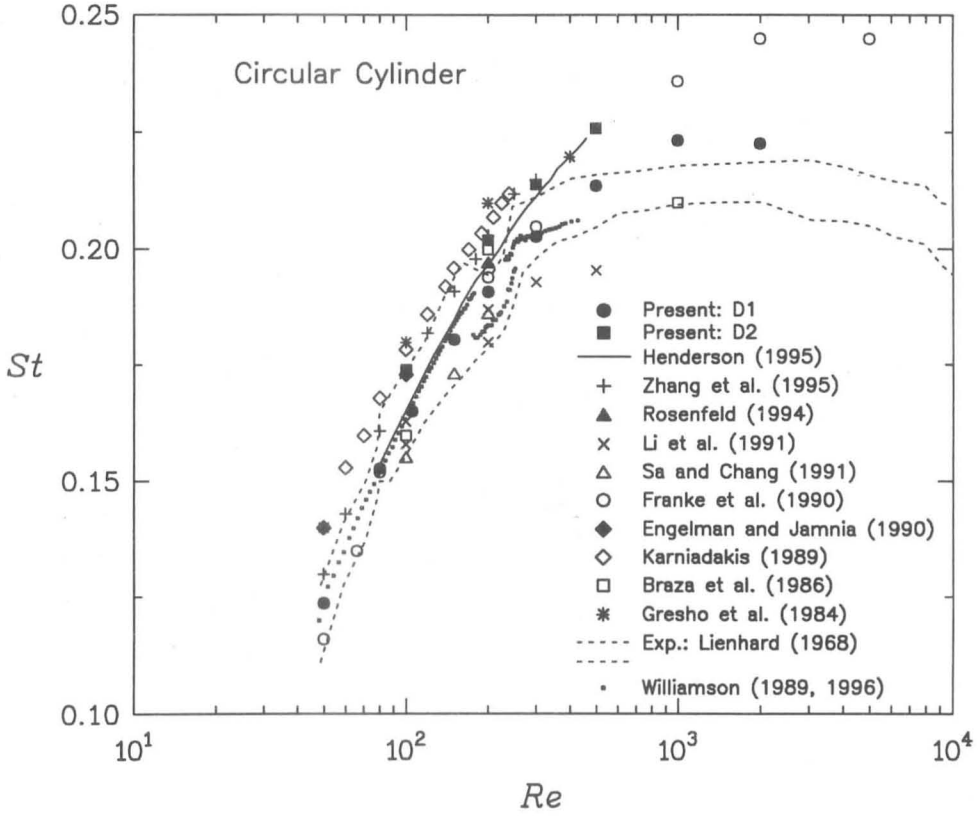
Figure 4.28: Flow past a circular cylinder. Comparison of the computed Strouhal numbers (the grids D1-143x98 and D2-134x88; SMART scheme) with others.
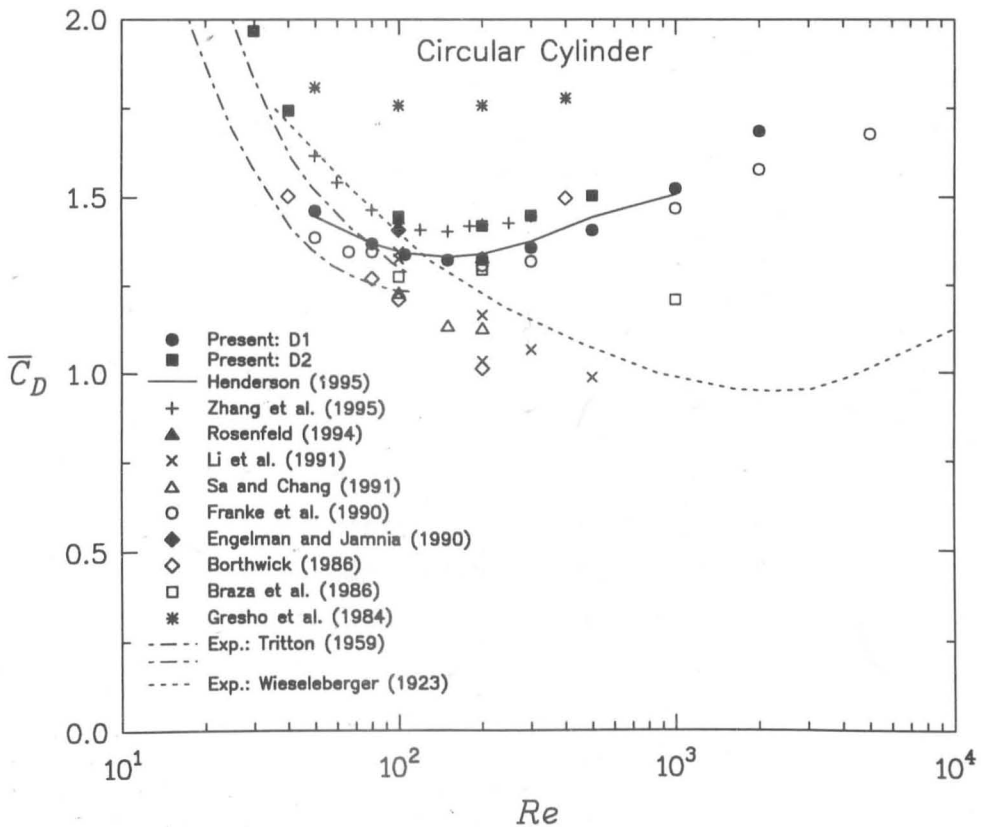
Figure 4.29: Flow past a circular cylinder. Comparison of the computed mean drag coefficients (the grids D1-143x98 and D2-134x88; SMART scheme) with others.

194 with the generation of large spanwise patterns – vortex loops and pairs of stream-wise vortices whose spanwise wavelength is between 3 and 4 diameters. In a transition, the above shedding mode (Williamson's mode A) is accompanied by large structures known as *vortex dislocations*. Zhang et al. (1995) interpreted the vortex dislocations as a *vortex adhesion* mode. They visualized vortices which appeared to be glued to the body (giving an impression of no shedding) through a number of vortex-adhesion points along the cylinder span. At $Re = 230 - 250$ there is another change to the finer-scale streamwise vortices with a spanwise wavelength of about one diameter and without vortex dislocations (a mode B). According to Williamson (1996), the natural wake transition involves first mode A with vortex dislocations (his flow state A^*) and then the mode B. This transition is manifested by discontinuities in the $St - Re$ relationship as shown in Figure 4.30(top) by Williamson's results. Note that the first transition is hysteretic while the second is not. Apart from this natural wake transition path $2D \rightarrow A^* \rightarrow B$, Williamson (1996) and also Zhang et al. (1995) recognize other transient or unstable flow states which can occur in experimental and numerical studies.

The results of several three-dimensional simulations of the flow around two– dimensional bluff bodies appeared recently. The three-dimensional predictions of the Strouhal number and the mean drag coefficient in the case of a circular cylinder are displayed as the bold symbols in Figure 4.30. Henderson (see Williamson, 1996) reproduced the Strouhal numbers close to the measured values that describe the first natural transition (the lower experimental curve after the first discontinuity in Figure 4.30(top)). This transition is labelled as a "hard" transition (**HT**) by Zhang et al. (1995). In order to simulate the hard transition they had to introduce strong localized spanwise perturbations in the initial conditions. Also, a large enough spanwise domain had to be used ($24D$). With nearly two-dimensional initial conditions, they reproduced modes A and B or a "soft" transition (**ST**). In this case the vortex shedding parameters depend continuously on Reynolds number which is the characteristic of two-dimensional computations. The two-dimensional results, including the present ones, are shown by open symbols in Figure 4.30.

As mentioned earlier, in comparison with the experimental results, the mean drag coefficient is overpredicted by the two–dimensional simulations for $Re > Re_c^{3D}$. In contrast, the three-dimensional predictions match fairly well with experimental results and follow their trend. Mittal and Balachandar (1995) studied in details the differences between the results of two– and three–dimensional simulations for flows past elliptic and circular cylinders. They found higher levels of the Reynolds stresses and shorter wakes in the two-dimensional cases. The latter are the main cause for the overprediction of the drag coefficient and the amplitudes of the lift coefficient. Bluffer bodies produced larger differences between the two– and three–dimensional results for the drag coefficients. Najjar and Vanka (1995) investigated the effects of intrinsic three-dimensionality on the flow
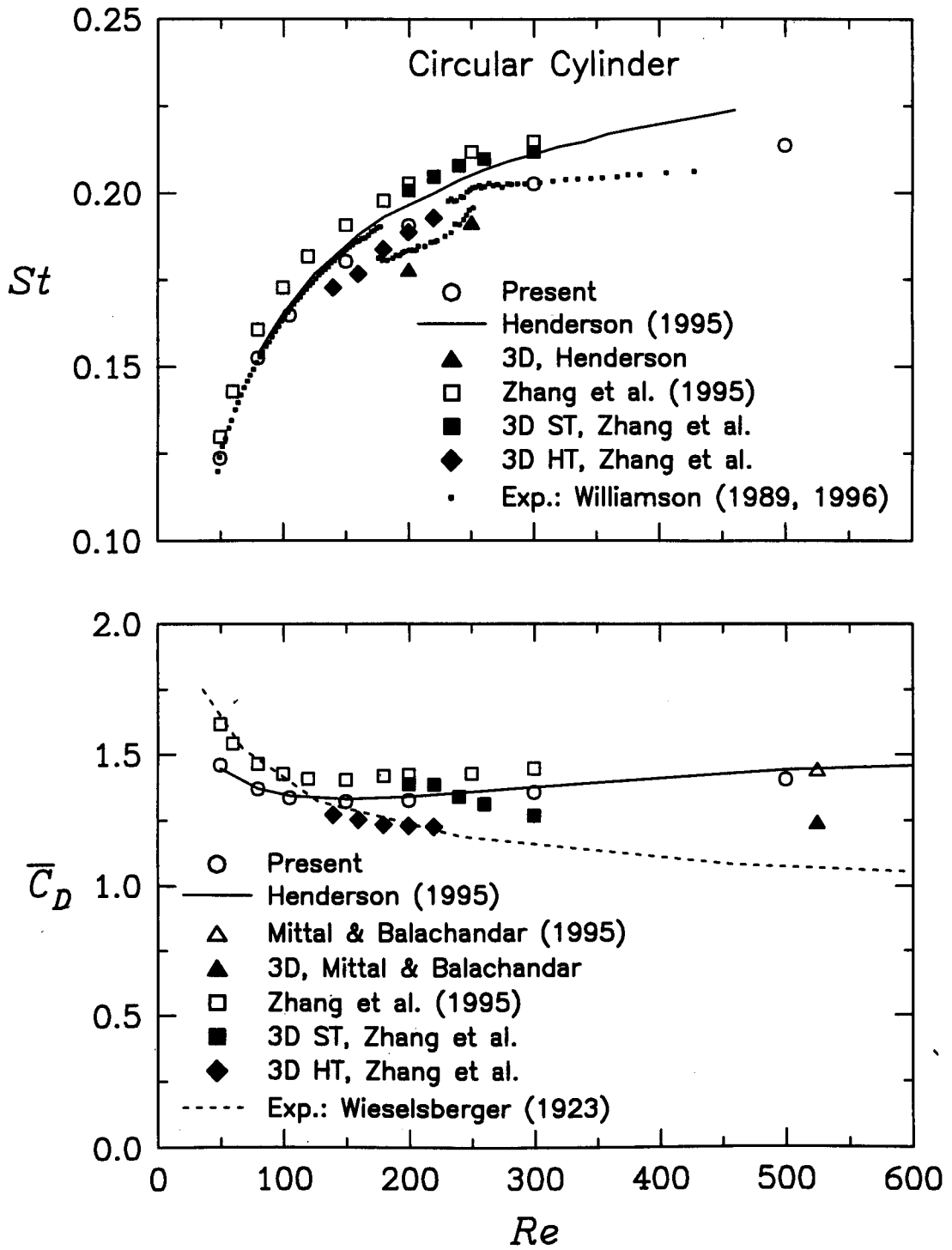
Figure 4.30: Flow past a circular cylinder. Comparisons between 2-D and 3-D simulations and experiments (present predictions with the grid $D1 - 143 \times 98$ and SMART scheme).

past a normal flat plate at $Re = 1000$. Their two– and three–dimensional computations produced markedly different results for the drag coefficient and the flow structures. Close agreement was reported between the three-dimensional results for the drag coefficient and experimental values. Finally, the DNS study of Karniadakis and Triantafyllou (1992) for the flow around a circular cylinder at Re up to 500 needs to be mentioned. They showed that a secondary instability of the 2-D vortex street induces three-dimensionality in the wake. Further, additional bifurcations have led to a chaotic flow state at Re around 500. They concluded that 3D flow oscillates at the fundamental vortex shedding frequency around a spanwise modulated time-average flow.

A question arises as to the interpretation of some of the interesting phenomena realized in two–dimensional simulations. The previous Section 4.5.1 described the asymmetric vortex shedding process for the flow past a square cylinder at $Re \geq 300$. The same process was encountered in the case of a circular cylinder (Section 4.5.2) at Re above 1000. Arnal et al. (1991) and Lin (1991) also captured the occurrence of asymmetrical vortex shedding for a square cylinder: the time-averaged lift coefficient had a non–zero value. Further, Karniadakis and Brown (1995) computed the flow past a half-cylinder with its flat surface facing downstream. The instantaneous vorticity field for the two-dimensional case, at $Re = 250$, showed an asymmetric vortex street. The attainment of two asymmetric vortex shedding patterns by inverting the initial perturbations motivated Lin (1991) to relate this process to the bifurcation theory and chaos. Similarly, a simple explanation could be that additional vortex shedding frequencies, closely related to the asymmetric shedding, indicate the wake transition processes towards three-dimensionality and turbulence. However, the problem is that one can elucidate the phenomenon that might be the aftermath of two-dimensional numerical approach. In the worst case, unsteady solutions obtained by some numerical methods can be contaminated by numerical diffusion, see Breuer et al. (1993). Although the present results and those of Karniadakis and Brown (1995) (fine-resolution simulations using two different spectral element codes) were obtained with an acceptable level of numerical diffusion, further high-resolution computations with different numerical algorithms will help to assess the influence of numerical diffusion on vortex shedding solutions.

4.6   Two Cylinders in Tandem

The flow around two circular cylinders in a tandem arrangement is considered in this section. This case provides a good approximation to the flows around chimney stacks, offshore structures and in-line heat exchanger tubes.

4.6.1   Background

Zdravkovich (1977) and Ohya et al. (1989) reviewed the experimental work concerned with the flow around two cylinders of equal diameters in the various arrangements, including the tandem one. A spacing ratio L/D, where L is defined as the distance between the cylinders' centres, is a new parameter, which, together with Reynolds number, influences the vortex shedding from this arrangement. At smaller distances, a critical spacing ratio exists, whereby the separated shear layers from the upstream cylinder attach on the downstream one. This ratio may range from 1.9 to 3.8, depending on the Reynolds number and the free–stream turbulence. For a spacing ratio below the critical, the vortex shedding from the upstream cylinder is suppressed. Many investigators found abrupt changes in the Strouhal number and the force coefficients in the proximity of the critical spacing ratio, Ohya et al. (1989).

Numerical studies on the laminar flow past two circular cylinders in tandem are reviewed in Table 4.14. They show the existence of the critical cylinder spacing ratio and two distinct flow regimes. The numerical values of Strouhal number obtained by Stansby and Slaouty (1991), and the mean pressure distribution around the downstream cylinder calculated by Li et al. (1991, 1992) were compared with Ishigai et al.'s (1972) measurements for $Re = 3900$. In spite of the large Reynolds number differences, a qualitatively similar behaviour of the numerical results and the experimental data was evident.

Authors & year	Numerical method	Re	L/D	Remarks
Stansby & Slaouti, 1991	Vortex-in-cell; ω, ψ	200	1.2; 1.5; 2; 3; 4; 5	St in general agreement with experiments obtained at higher Re-numbers.
Li et al., 1991; Li et al., 1992; Sun et al., 1993	Finite element; primitive variables	80; 100	2.2–8	The critical spacings are well-defined: 3.7 at $Re = 80$ and 3.0 at $Re = 100$.

Table 4.14: Previous predictions of the flow around two circular cylinders in tandem.

4.6.2 Discussion of results

The flow around two circular cylinders in tandem, placed in a uniform stream, was calculated for Reynolds numbers of 200 and 500, and for various spacing ratios L/D. The effects of these parameters were quantified for the force coefficients induced on each cylinder and the corresponding Strouhal numbers. The numerical grids were generated inside domains defined by the following distances: (i) from the inlet boundary and the centre of the upstream cylinder $X_i = 5.5D$, (ii) from the centre of the downstream cylinder and the outlet boundary $X_o \approx 15D$, and (iii) from the centre–line and the symmetry plane $Y_s = 6D$. The non-dimensional distance from the wall to the near-wall cells $\Delta n_c/D = 0.01$ and the expansion factors $f_{ex} = 1.15$ and $f_{ey} = 1.09$ resulted in the grids with typically 114 and 70 cells in the x and y directions, respectively. Thus, the grids were coarser than those used for the single cylinders. A representative computational grid is displayed in Figure 4.31. All results were obtained by using the linear upwind scheme (LUDS) and are summarized in Table 4.15.

An overall impression of the predicted flow field around the two cylinders in tandem is given by streaklines in Figure 4.31. The figure also shows the predicted time history of the lift and drag coefficients on the two cylinders. For this particular case, the parameter L/D was set to 4 and Reynolds number was 200. It is immediately obvious that the downstream cylinder experiences a 'shielding' effect evidenced by the marked reduction in the mean value of its drag coefficient. This beneficial effect does not extend to the peak-to-peak variations in the in-line and transverse components of force, both of which are seen to increase significantly.

The effects of Reynolds number and the spacing between the two cylinders can be seen from Figure 4.32. Note the dramatic changes in the values of Strouhal number and the lift and drag coefficients at L/D of about 2.4 (for Reynolds number of 200) and 1.9 (Re = 500). This is the *critical spacing ratio* which signals a sudden change between two very different flow patterns, namely between the vortex suppression regime (at least in the near-wake region) and the vortex formation regime, Sun et al. (1993). At L/D of 5, both the mean drag coefficient on the upstream cylinder and the value of the lift coefficient amplitude revert to levels appropriate to an isolated cylinder at the same Reynolds number. However, the effects of the wake interaction on the downstream cylinder are still quite profound at this separation. On the other hand, the mean drag on the downstream cylinder may become negative for values of L/D smaller than the critical spacing. This is due to the strength of the interaction with the low pressure region generated behind the upstream cylinder. The present results (together with those of Sun et al. (1993) and Li et al. (1992), Figure 4.33) confirm the experimental finding (e.g. Ohya et al., 1989) that the critical spacing reduces with increasing Reynolds number.

(a) $Re = 200$

Spacing	Upstream Cylinder			Downstream Cylinder		
L/D	St	$\overline{C}_D$	$\pm\tilde{C}_L$	St	$\overline{C}_D$	$\pm\tilde{C}_L$
1.2	0.1660	1.184	0.051	0.1660	-0.197	0.105
1.8	0.1435	1.165	0.047	0.1435	-0.205	0.180
2.0	0.1425	1.163	0.046	0.1424	-0.202	0.222
2.2	0.1417	1.162	0.045	0.1415	-0.184	0.275
2.5	0.1447	1.335	0.787	0.1447	0.665	1.322
3.0	0.1640	1.337	0.782	0.1640	0.884	1.579
4.0	0.1854	1.381	0.769	0.1854	1.032	2.012
5.0	0.1862	1.396	0.758	0.1861	1.120	2.082
6.0	0.1852	1.386	0.708	0.1852	1.169	2.029

Single cylinder: $\overline{C}_D = 1.400$; $St = 0.193$.

(b) $Re = 500$

Spacing	Upstream Cylinder			Downstream Cylinder		
L/D	St	$\overline{C}_D$	$\pm\tilde{C}_L$	St	$\overline{C}_D$	$\pm\tilde{C}_L$
1.2	0.1674	1.106	0.196	0.1674	-0.263	0.380
1.8	0.1524	1.074	0.143	0.1524	-0.274	0.401
2.0	0.1561	1.379	1.208	0.1561	0.852	1.596
2.2	0.1673	1.398	1.149	0.1673	0.954	1.738
2.5	0.1782	1.377	1.213	0.1783	1.004	1.885
3.0	0.2008	1.407	1.246	0.2004	1.165	2.103
4.0	0.2157	1.401	1.140	0.2155	0.831	2.360
5.0	0.2099	1.442	1.185	0.2099	0.548	2.100
6.0	0.2096	1.430	1.170	0.2097	0.569	1.940

Single cylinder: $\overline{C}_D = 1.467$; $St = 0.220$.

Table 4.15: Predicted vortex shedding parameters for the flow around two circular cylinders in line as a function of L/D: (a) $Re = 200$, (b) $Re = 500$.
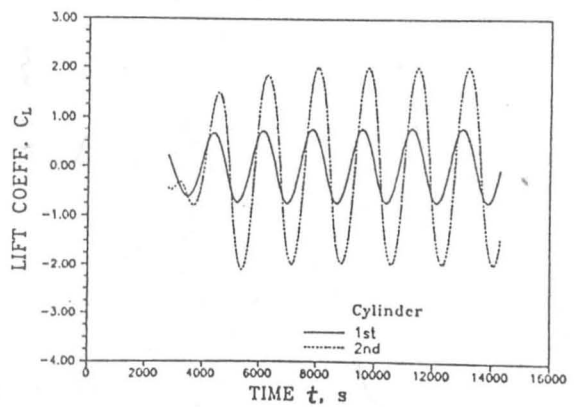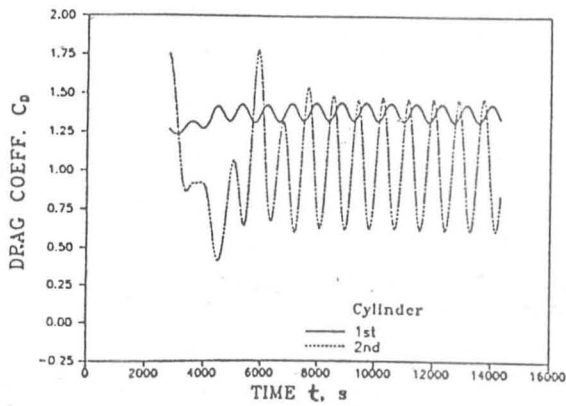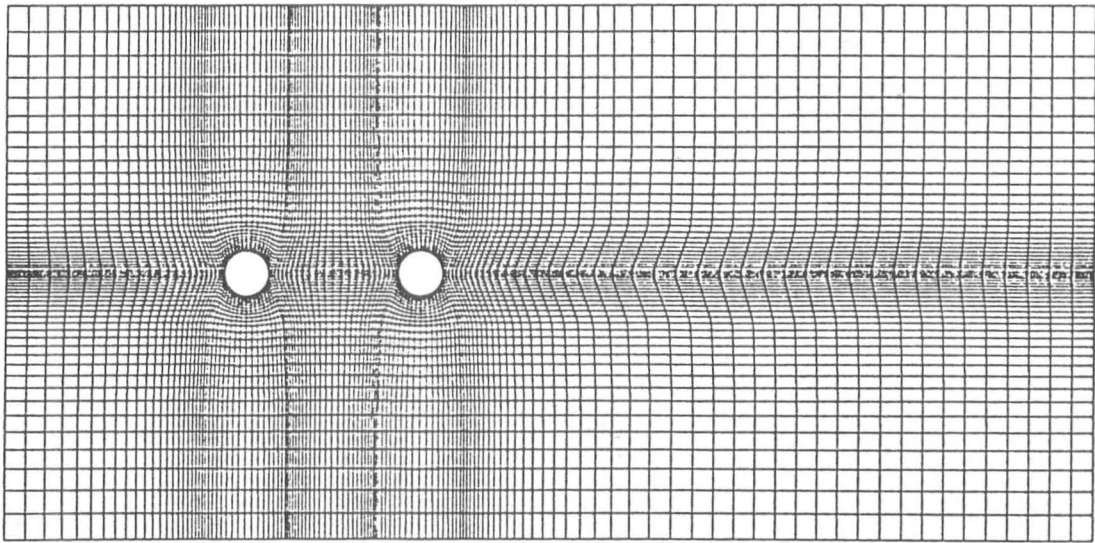
Figure 4.31: Two circular cylinders in line with the spacing ratio $L/D = 4$: the grid (top), streaklines for $Re = 200$ (middle) and time histories of the drag and lift coefficients also at $Re = 200$ (bottom).
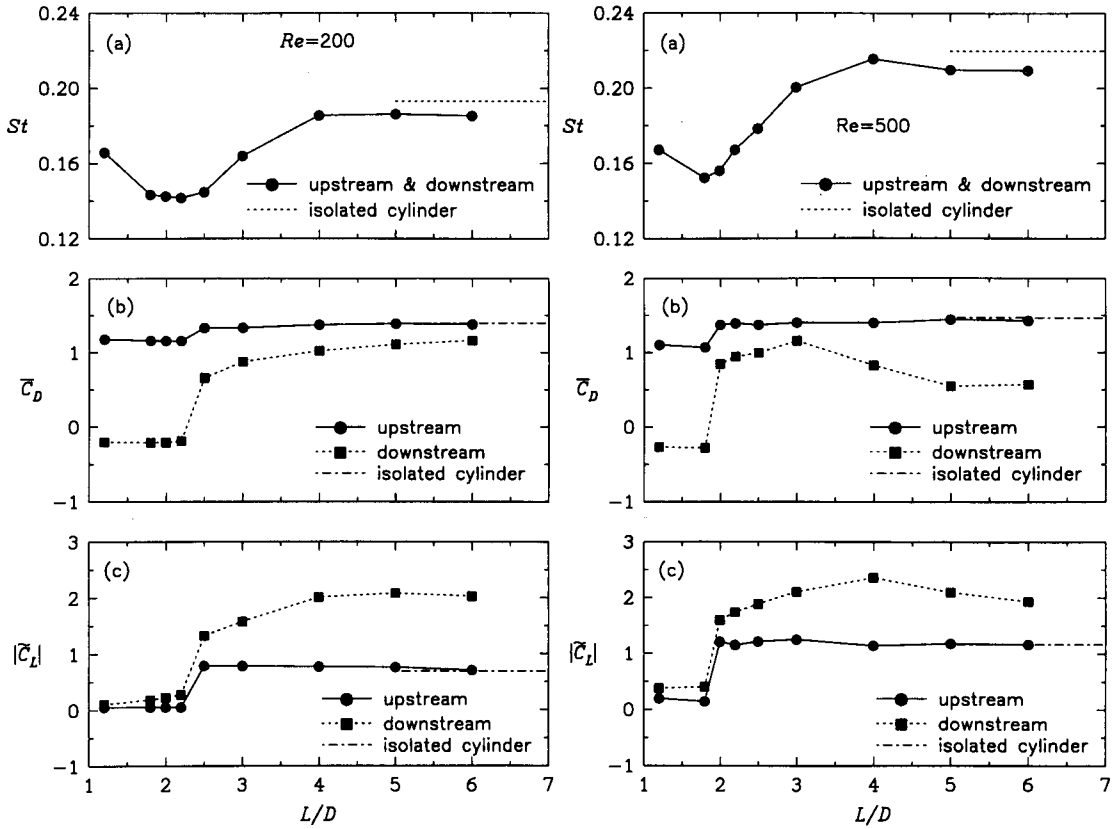
Figure 4.32: Variation of the Strouhal number (a), mean drag (b) and lift coefficient amplitude (c) with cylinders spacing.
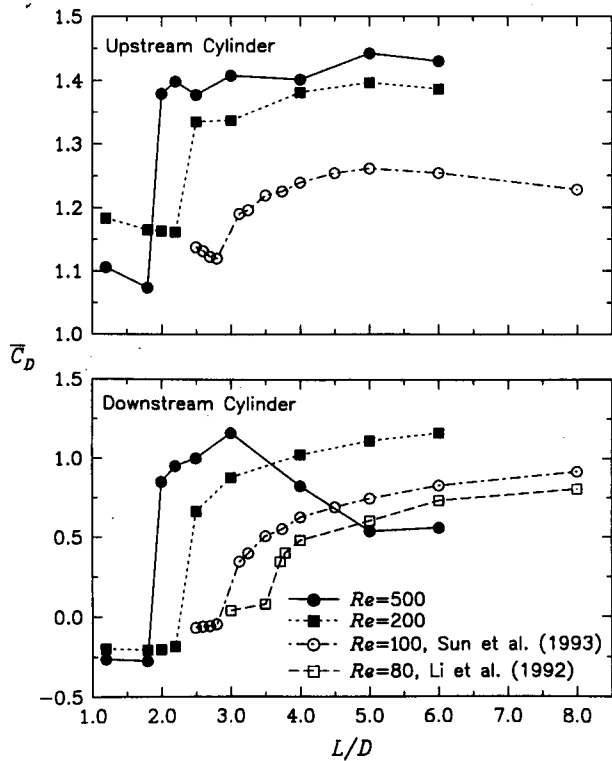
Figure 4.33: Reynolds number effect on the mean drag coefficient of the upstream (top) and downstream (bottom) cylinder versus cylinder spacings.

4.7   Oscillatory Flows

Two-dimensional, oscillating flows, with both a zero and a non-zero value of the time-mean inlet velocity, are the subject of this section. Attention is confined to a single circular cylinder. An oscillatory flow past a circular cylinder is a representation of the wave action on the offshore platform leg, away from the free surface.

In a general case of uniform current (U_0) with superimposed sinusoidal oscillations, the time–dependent inlet (incident) velocity is given as:

$$U_{in}(t) = U_0 + U_m \sin \frac{2\pi t}{T_{os}} \tag{4.12}$$

where U_m is the maximum velocity and T_{os} is the period of oscillations. The inverse value of the Strouhal number which is based on the free stream oscillating frequency $f_{os} = 1/T_{os}$ is known as the *Keulegan-Carpenter* number Kc. From the definition of Reynolds number Re_m:

$$Re_m = \frac{\rho U_m D}{\mu}, \tag{4.13}$$

and the Stokes parameter β:

$$\beta = \frac{D^2}{\nu T_{os}}, \tag{4.14}$$

Kc can be expressed as a combination of the Reynolds number Re_m and parameter β:

$$Kc = \left(\frac{f_{os}D}{U_m}\right)^{-1} = \frac{U_m T_{os}}{D} = \frac{Re_m}{\beta}. \tag{4.15}$$

Another parameter is needed to scale the current velocity U_0. The usual choice is to define a 'relative velocity' U_r as:

$$U_r = \frac{U_0}{U_m}. \tag{4.16}$$

The instantaneous forces on a circular cylinder can be normalized in the usual way, Equation (1.4). The maximum oscillating velocity U_m is employed instead of U_0 so that the total drag (in-line) force is given as:

$$F_D = \frac{1}{2}\rho D U_m^2 C_D. \tag{4.17}$$

However, the in-line force is traditionally expressed by Morison's equation (cf. Sarpkaya and Isaacson, 1981), which may be written as:

$$F_D = \frac{1}{2}\rho D C_{dm} U_{in} |U_{in}| + \rho \frac{D^2 \pi}{4} C_m \frac{dU_{in}}{dt}. \tag{4.18}$$

The above equation takes into account two contributions to the in-line force: first from a drag part (proportional to the squared velocity), and second from the inertial part (proportional to the fluid acceleration). Corresponding coefficients are Morison's drag coefficient C_{dm} and inertia coefficient C_m. By introducing a new variable:

$$\vartheta = \frac{2\pi}{T_{os}}t , \qquad\qquad (4.19)$$

and with the incident flows used here (Equation (4.12)), Morison's equation in dimensionless form reads:

$$C_D = C_{dm}(U_r + \sin\vartheta)\,|U_r + \sin\vartheta| + C_m\frac{\pi^2}{Kc}\cos\vartheta . \qquad\qquad (4.20)$$

The drag and inertia coefficients are then derived as the Fourier averaged coefficients:

$$C_{dm} = \frac{1}{I_r}\int_0^{2\pi} C_D \sin\vartheta\, d\vartheta , \qquad\qquad (4.21)$$

$$I_r = \begin{cases} 2\pi U_r & \text{if} \quad U_r \geq 1 \\ 4\left[U_r \arcsin(U_r) + \frac{1}{3}\sqrt{1 - U_r^2}(2 + U_r^2)\right] & \text{if} \quad 0 \leq U_r < 1 \end{cases} \qquad (4.22)$$

$$C_m = \frac{Kc}{\pi^3}\int_0^{2\pi} C_D \cos\vartheta\, d\vartheta \qquad\qquad (4.23)$$

In the case of a pure oscillatory flow ($U_r = 0$) the quantity I_r, which depends on the relative velocity U_r, reduces to 8/3 so that the drag coefficient takes a form:

$$C_{dm} = \frac{3}{8}\int_0^{2\pi} C_D \sin\vartheta\, d\vartheta . \qquad\qquad (4.24)$$

Note that one can derive the Morison root-mean-square drag coefficient by exploiting Equation (4.20). For a purely oscillatory flow, this coefficient, denoted as C_F', is given as:

$$C_F' = \left\{\frac{1}{2\pi}\int_0^{2\pi}\left[C_D(\vartheta) - \overline{C}_D\,\big|_0^{2\pi}\right]^2 d\vartheta\right\}^{1/2} = \left(\frac{\pi^4 C_m^2}{2Kc^2} + \frac{3}{8}C_D^2\right)^{1/2} . \qquad (4.25)$$

4.7.1 Background

Several experimental studies (Williamson, 1985; Bearman et al., 1985; Sarpkaya, 1986; Obasaju et al., 1988; Tatsuno and Bearman, 1990) highlighted the physical features of pure oscillatory flows. Since the flow changes its direction during each period of oscillations, the wake properties are carried with the vortices as they move backwards and forwards around the cylinder. At a given location, different flow regimes (laminar, laminar - turbulent, and turbulent) may evolve over the oscillation period. For smooth cylinders,

the flow structure and force coefficients are functions of Re_m and β. Most authors used Kc–number instead of Re_m ($Kc = Re_m/\beta$). At very small values of Kc ($Kc << 1$), the laminar boundary layer is attached to the cylinder and the flow is stable and symmetrical. As Kc increases, for a given β, the flow becomes unstable and then separates. The instability which precedes the flow separation has a three-dimensional character and was first observed by Honji (1981). According to Sarpkaya, above the critical Kc-number, and for $\beta \leq 2600$, the boundary layers undergo laminar separation followed by transition to turbulence. For $\beta > 2600$, the transition occurs before the separation of the boundary layers. At higher Kc-numbers, $Kc \geq 3-4$, a number of vortex shedding patterns has been identified across the ranges of the Kc and β: Williamson (1985), Obasaju et al. (1988), and Tatsuno and Bearman (1990). Tatsuno and Bearman reported three-dimensional instabilities along the cylinder span for most of their flow patterns.

Earlier experimental studies of the combined mean current and oscillatory flow were reviewed by Sarpkaya and Isaacson (1981). Later, the forces on a circular cylinder have been measured by Sarpkaya and Storm (1985) and Bearman and Obasaju (1989). Sarpkaya and Storm (1985) reported that the vortex–shedding patterns were affected even by a very small current ($U_r = 0.05$). For example, the precarious transverse vortex street pattern, found in the pure oscillatory flow, quickly evolved into another - the diagonal type pattern. An increase in the relative current velocity U_r was followed by a decrease of the drag coefficient for small current velocities.

Previous numerical studies, summarized in Table 4.16, were performed for the two-dimensional laminar flows. In some computations the Reynolds number was beyond the upper bounds, where the 3-D effects and turbulence become important. The computed force coefficients of the pure oscillatory flow - usually Fourier averaged drag and inertia coefficients or the r.m.s. drag and lift coefficients, have shown satisfactory agreement with the measured values in the studies referred to in Table 4.16.

4.7.2   Numerical considerations

All the present calculations of oscillatory flows are carried out for a circular cylinder placed symmetrically in a rectangular domain. The upstream and downstream boundaries are located at distances of $X_i = X_o = 20D$ from the centre of the cylinder. The width of the computational domain, defined by the positions of the symmetry boundaries, is $2Y_s = 12D$ (the domain dimensions are defined in Figure 4.1). A relatively coarse numerical grid is used, with 98×64 cells in the x and y directions, respectively. The cylinder itself is covered with 56 cells.

Authors & year	Numerical method	Kc-number	Parameter β	$U_r = U_0/U_m$	Re_m
Baba and Miyata, 1987	Finite difference; primitive variables	5; 7	200; 100	0	1000; 700
Murashige et al., 1989	Finite difference; primitive variables	5; 7; 10	2000; 1429; 1000	0	10000
Stansby and Smith, 1989	Random vortex; ω, ψ	0.2-6	483; 1035	0	97-2898; 207-2070
Graham et al., 1989	Cloud-in-cell; ω, ψ	0.5-6	196; 483	0	98-2898
Skomedal et al., 1989	Vortex-in-cell; ω, ψ	0.5-22.5	534	0	267-12015
Wang and Dalton, 1991b	Finite difference; ω, ψ	1-12	8.3-300	0	100-3000
Justesen, 1991	Finite difference; ω, ψ	0.2-26; 0.2-3	196 483; 1035	0	39.2-5096; 96.6-3105
Sarpkaya and Dalton, 1992	Finite difference; ω, ψ	4	200	0.2-1.1	160-880
Yeung et al., 1992	Random vortex; ω, ψ	0.25-6	483	0	121-2898
Graham et al., 1993	Cloud-in-cell/Finite volume; ω, ψ	0.2-26	200	0.25-1	10-5200

Table 4.16: A survey on the numerical studies for oscillating and combined uniform current and oscillating flows around a circular cylinder.

The correct choice for velocity boundary conditions at the inlet and exit planes is not obvious. The values of velocity at both inlet and exit may be prescribed as a function of time (see Equation (4.12)). Alternatively, the values at only one plane may be prescribed while the gradient across the other plane is set to zero. Both approaches were tried and produced similar results for the drag and inertia coefficient. It was concluded that the prescribed velocities at both the inlet and exit are the simpler of the two alternatives, and produced good convergence rates, and were therefore selected for further numerical runs. In regard to the initial conditions, the computations were started with a zero oscillatory contribution as it follows from Equation (4.12) for $\vartheta = 2\pi t/T_{os} = 0$. When the accelerated inlet velocity reaches the maximum value ($t/T_{os} = 1/4$) an asymmetric velocity field is introduced in a form $U_{lo} = 0.95U_{in}$ (see Section 4.3.1).

The time-mean and root-mean-square force coefficients ($\overline{C}_D$, C'_D, C'_L) are calculated by averaging the instantaneous values over at least last five oscillating periods. In the case of Morison's coefficients, Equations (4.21) and (4.23) are integrated numerically for each period and the values then averaged.

Simulations with finer grids and wider domains for the number of planned runs were

not affordable. In order to gain an insight into the possible numerical uncertainties, additional calculations were performed on a finer grid with 126×116 cells (88 cells over the cylinder surface) generated inside a square domain of width of $2Y_s = 40D$. The force coefficients calculated for the grids 98×64 and 126×116 at $Kc = 8$ are compared with the experimental data of Bearman et al. (1985), Table 4.17. This table also includes a

$$\beta = 196, \ U_r = 0$$

Force	$Kc = 2$			$Kc = 8$				
Coeff.	Data	Grid 1	Error,%	Data	Grid 1	Error,%	Grid 2	Error,%
C_{dm}	1.73	1.48	-14.5	2.00	1.789	-10.55	1.748	-12.60
C_m	2.17	2.12	-2.30	1.50	1.488	-0.80	1.752	+16.80
C_F'	7.65	7.45	-2.61	1.79	1.698	-5.14	1.866	+4.25

Data: Bearman et al. (1985); Grid 1: 98×64; Grid 2: 126×116

Table 4.17: Oscillatory flow past a circular cylinder. Estimated numerical uncertainties for the Morison force coefficients ($\beta = 196$, $\Delta t^* = 3.66 \times 10^{-3}$, QUICK scheme).

comparison of the results for $Kc = 2$ calculated on the grid 98×64. The relative errors are calculated by using the experimental results as reference values. Assuming the experimental data as reliable, the level of estimated errors of 10 % indicates that the use of the coarser grid (98×64) constitutes a reasonable compromise between accuracy and computational effort.

4.7.3 Results and discussion

Oscillatory flows without current

A pure oscillatory flow around a circular cylinder was computed with $\beta = 196$ and Kc in the range 0.5–22, Table 4.18. This value of β was selected in order to attain smaller Reynolds numbers, especially for high Kc. For those computations, the QUICK scheme was used. Beside Morison's force coefficients, Table 4.18 contains the root-mean-square values of the conventional drag and lift coefficients. The values of C_F' and C_D' are very close to each other, an indication of how well the force time histories reconstructed from Morison's equation (4.20) reproduce the statistical properties of the computed time histories. The time-mean values of the drag and lift coefficients (not shown) are in most cases negligible (being of the order of 10^{-2}). As for the period of drag oscillations, its value is statistically equal to the period of the free–stream oscillations.

Inspection of the time evolution of the force coefficients over the range of Kc numbers investigated here reveals the presence of a number of distinct flow regimes. At low Kc

$$\beta = 196$$

Kc	Re_m	$\Delta t^* \times 10^3$	C_{dm}	C_m	C_F'	C_D'	C_L'
0.5	98	5.0	2.802	2.090	29.22	29.270	0
2	392	0.49	1.477	2.119	7.450	7.450	0
3	588	5.0	1.298	2.061	4.860	4.879	0.015
4	784	3.66	1.484	1.976	3.565	3.582	0.669
8	1568	3.66	1.789	1.488	1.698	1.756	1.384
10.9	2134	3.32	2.168	1.112	1.483	1.551	1.068
16	3136	2.93	1.476	1.323	1.072	1.125	0.995
22	4312	2.0	1.107	1.337	0.799	0.852	0.677

Table 4.18: Circular cylinder in laminar oscillatory flows. Predicted force coefficients in terms of the Kc-number ($T_{os} = 327.988s$, grid 98×64, QUICK scheme).

values ($Kc < 3$ for this value of β), the flow is symmetric and the lift coefficient is negligible.
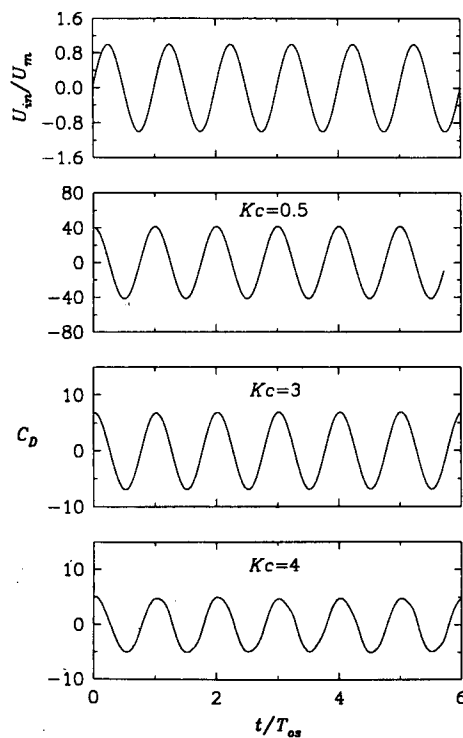
Figure 4.34: Circular cylinder in pure oscillatory flows. Computed drag coefficients versus time at $Kc = 0.5$, 3, and 4 and $\beta = 196$ (the top curve shows the inlet velocity variation).

The drag coefficient time histories, depicted in Figure 4.34, exhibit a sinusoidal behaviour, with the maximum and minimum amplitudes nearly in phase with the zero incident ve-
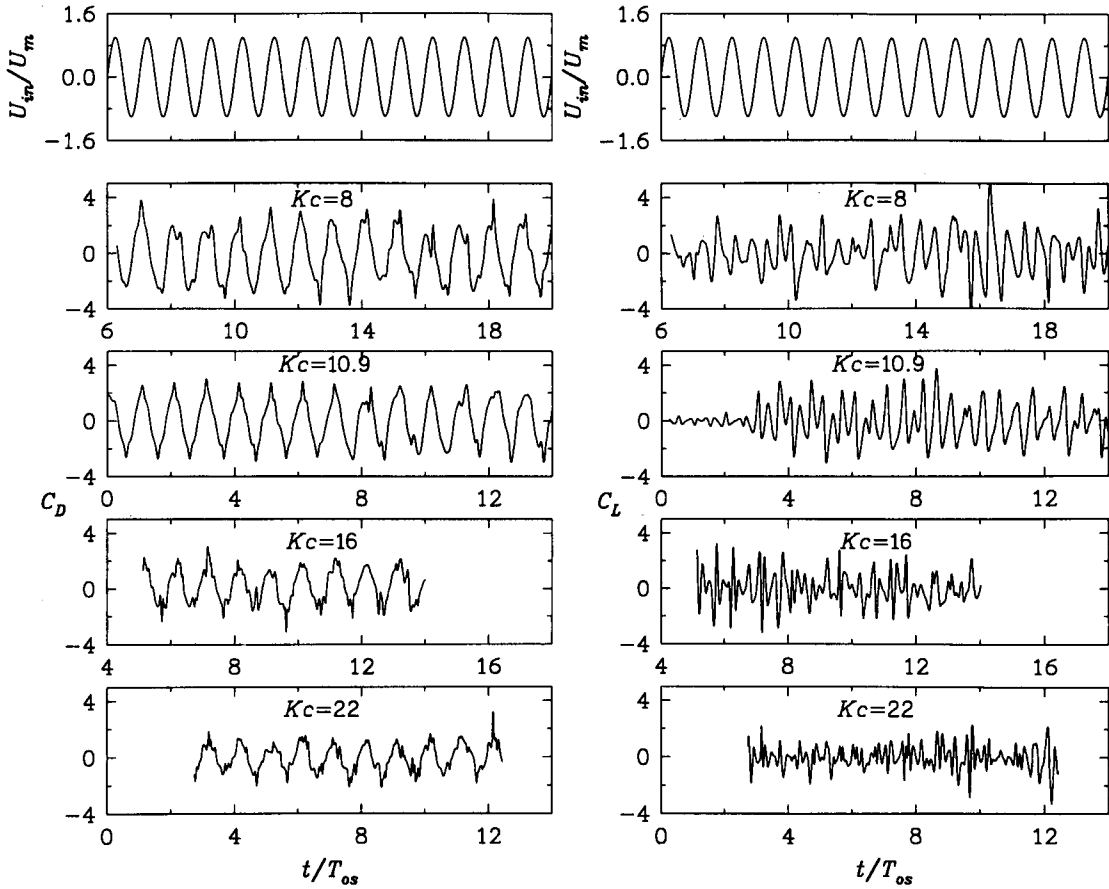
Figure 4.35: Circular cylinder in pure oscillatory flows. Computed drag (left) and lift (right) coefficients versus time at various higher Kc–numbers for $\beta = 196$ (top curves show the inlet velocity variation).

locities. These amplitudes progressively decrease with increasing Kc. For higher Kc values ($Kc \geq 4$), lift is no longer zero – an indication of the onset of vortex shedding. The time traces of the force coefficients are no longer sinusoidal, as Figure 4.35 displays. Increased randomness at higher Kc–numbers (16 and 22) are in evidence. It is possible that, in the real flow, the wake becomes turbulent in these conditions but this is not likely to be captured in the present, laminar and two-dimensional, simulations.

Finally, Figure 4.36 compares the predicted and measured variation of Morison's drag and inertia coefficients as well as the root-mean-square lift coefficients with Kc ($\beta = 196$). The figure also includes the numerical predictions of Justesen (1991) obtained by using a finite–difference method with a grid of 128×80 nodes. The computed drag and inertia coefficients show satisfactory agreement with the measurements of Bearman et al. (1985) and Obasaju et al. (1988). Overall, the present predictions are closer to the experiments than those of Justesen, particularly with respect to the maximum and minimum values of the force coefficients observed at $Kc = 10.9$. As Kc increases above this value, the predictions for C_{dm} (present) and C_m (Justesen's) depart from the experimental data. The data for C'_L show significant scatter and it is therefore difficult to assess the ac-
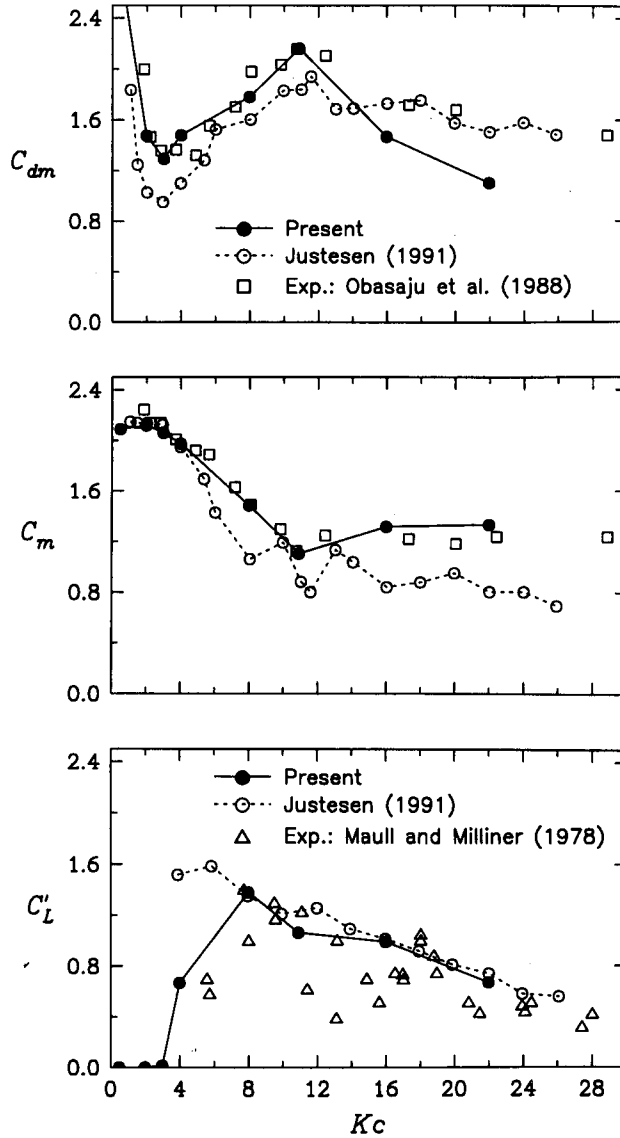
Figure 4.36: Circular cylinder in pure oscillatory flows. Comparisons of Morison's drag (top) and inertia (middle) coefficients and the root-mean-square lift coefficient (bottom).

curacy of the numerical predictions. The present results agree fairly well with Justesen's predictions for $Kc \geq 8$.

Oscillatory flows with currents

The case of combined current plus oscillations around a circular cylinder was computed at $Kc = 4$ and $\beta = 200$. In order to investigate the influence of small current velocities, their ratio to the maximum oscillating velocity U_r was between 0 and 1. All the results were obtained with the SMART scheme, on a grid of 98 × 64 and with $\Delta t^* = 0.0025$. The predicted values of various force coefficients (presented here in terms of the relative velocity U_r) are given in Table 4.19.

$$Kc = 4, \ \beta = 200$$

U_r	C_{dm}	C_m	$\overline{C}_D$	C'_D	C'_L
0	1.484	1.976	0.043	3.582	0.669
0.2	1.443	1.905	0.057	3.456	0.671
0.4	1.647	1.796	0.367	3.307	0.483
0.6	2.236	1.683	0.803	3.260	0.067
0.8	2.538	1.616	1.132	3.235	0.097
1.0	2.906	1.537	1.560	3.250	0.668

Table 4.19: Circular cylinder in current plus oscillations. Predicted variation of force coefficients with velocity ratio.
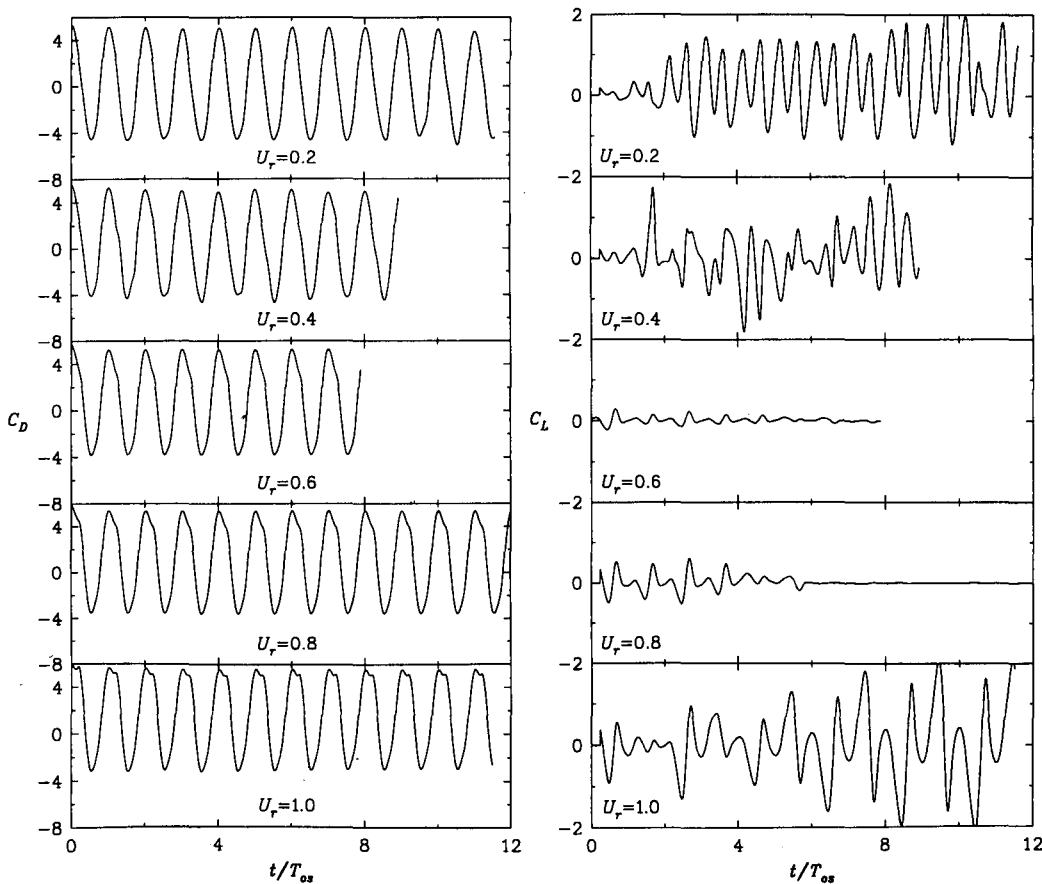
Figure 4.37: Circular cylinder in current plus oscillations. Time histories of the drag (left) and lift (right) coefficients as a function of velocity ratio.

Figure 4.37 shows the time histories of the drag and lift coefficients as a function of the velocity ratio. For the drag coefficient, the computed time records are periodic for all values of U_r and with the (positive and negative) peaks of C_D very well preserved. At $U_r \leq 0.2$, the drag coefficient is periodic and symmetric with a zero long–time average (see also Figure 4.38). At $U_r > 0.2$, the drag coefficient oscillates around the
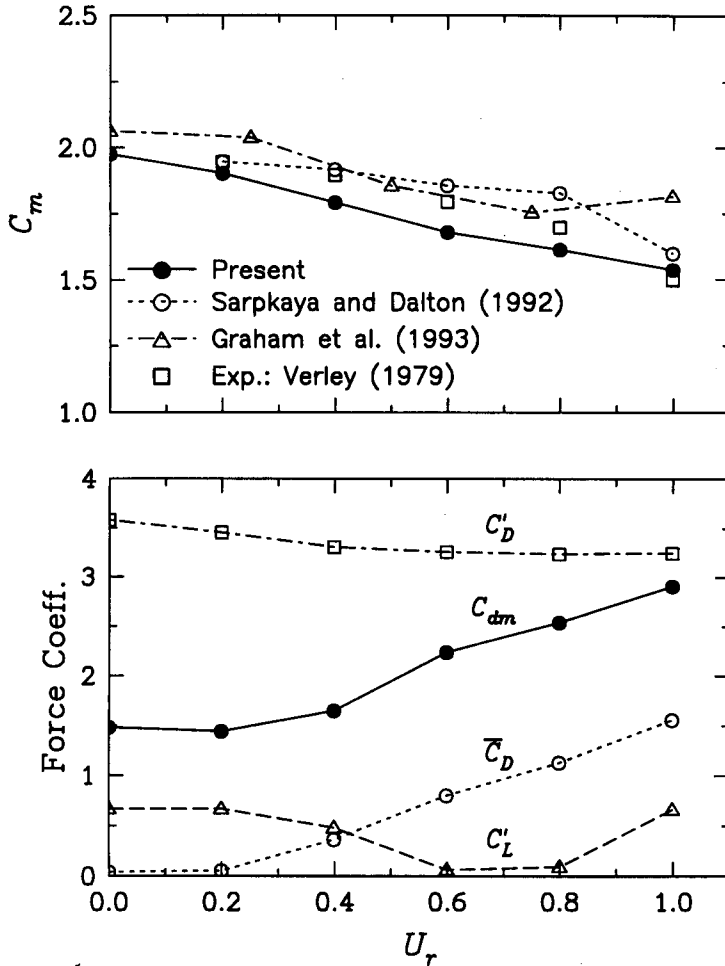
Figure 4.38: Circular cylinder in current plus oscillations. Morison's inertia coefficient (top) and other force coefficients (bottom) as obtained with $Kc = 4$ and $\beta = 200$ (present results: grid 98×64, $\Delta t^* = 2.5 \cdot 10^{-3}$, SMART scheme).

time-mean values $\overline{C}_D$ which continuously increase with U_r (Figure 4.38). Morison's drag coefficient C_{dm} also shows a monotonic increase, while the inertia coefficient C_m and C_D' decrease with U_r. In sharp contrast to the periodic behaviour of the drag coefficient, the time histories of the lift coefficient, Figure 4.37(right) are largely non-repetitive. The results for $U_r = 0.6$ and 0.8 are quite spectacular as they suggest the possibility of zero (or negligible) lift coefficient going hand in hand with quite large periodicity in the drag coefficient. The existing experimental results lack sufficient detail to support or contradict this finding. Note that Sarpkaya and Dalton (1992) visualized, numerically, and at the same Kc and β used here, a symmetric three-row vortex street only in the range of $U_r = 0.6 - 0.7$. Finally, Figure 4.38(top) compares the computed and measured inertia coefficients C_m. The results from all three numerical studies (Sarpkaya and Dalton, 1992; Graham et al., 1993, and the present) resemble the trend shown by the experimental data of Verley (1979). Verley's measurements were for the higher β value of 600 and hence it is difficult to make definite conclusions about the present predictions.

4.8 Closure

Several important issues regarding the numerical prediction of laminar, two-dimensional vortex shedding flows have been addressed in this chapter:

- numerical uncertainties,

- physical aspects,

- validation against experimental data, and

- limitations of two-dimensional laminar computations.

The numerical uncertainties arise from well-known discretisation errors (both spatial and temporal) as well as from the presence of blockage effects akin to those present in wind-tunnel tests. These uncertainties were quantified for the case of vortex shedding from single cylinders by using an error estimator based on the Richardson extrapolation. The principal difficulty is associated with the fact that errors arising from the choice of domain size very often cancel errors arising from the other sources. Detailed comparisons of results from various schemes have demonstrated the advantages of higher–order and bounded schemes such as SMART and MINMOD.

Accurate simulations of the *periodic* vortex shedding from a circular cylinder ($Re =$ 105) were used to analyse some physical aspects of the vortex shedding process. In the real flows, a number of different sources of small disturbances can introduce asymmetric flow field and lead to periodic vortex shedding. As these disturbances are stochastic, this suggests that the *magnitudes* of vortex shedding quantities do not depend on the nature of the disturbances. In consequence, a variety of artificial disturbances used in numerical studies should influence the vortex shedding until the periodic state is reached. This conclusion is supported by the present computations which were conducted both without initial perturbation as well as with two initial asymmetric perturbations.

For a single cylinder, laminar vortex shedding is only affected by the Reynolds number. At $Re < Re_c^{3D}$, periodic vortex shedding is always established and characterized by the two-dimensional von Karman street (visualized by streaklines in Figure 4.12). The sequence of streamlines covering one vortex shedding cycle was analysed in order to verify the vortex formation model of Perry et al. (1982). The outcome was a model shown in Figure 4.10 which confirms the main features of Perry's model. Similarities between vortex shedding from the square and circular cylinders are identified, as well as certain differences. These differences were associated with the location of the flow separation points, which in the case of a square cylinder jump between the rear and front corners at $Re = 150$. The flow reattachment at the cylinder sides was observed at $Re \geq 300$

for a square cylinder as well as additional vortex shedding frequencies and asymmetric vortex shedding with non-zero lift. Qualitatively, the same features were also obtained for the flow past a circular cylinder at $Re = 2000$. Predicted integral vortex shedding parameters such as the Strouhal number and the mean drag coefficient stand comparison with experimental data and numerical results obtained with alternative CFD methods

Numerical predictions are reported for the magnitude and frequency of the forces induced on two circular cylinders in tandem. The effects of the cylinders' spacing and mean-flow Reynolds number are quantified. The latter were shown to be particularly important in determining the position of the critical spacing ratio.

The simulations carried out for an oscillatory flow around a circular cylinder reproduced many of the salient features observed in experimental studies. In the case of pure oscillatory flows, the flow is predicted to be symmetrical at small Kc or Re_m numbers (here for $Re_m < 600$ and $\beta = 196$), with no lift and no vortex shedding. Above the certain critical number ($Re_m = 600 - 800$), the vortex shedding process is in strong evidence. A fairly good agreement among the predicted and measured Morison's drag and inertia coefficients is found in the range $0.5 \leq Kc \leq 12$. Numerical experiments with combinations of small steady current and oscillatory flow confirmed the significant influence of the current velocity ratio on the force coefficients. An interesting flow feature was observed for the ratio $U_r = 0.6 - 0.8$ at $Kc = 4$ and $\beta = 200$; namely flow conditions giving rise to negligible lift forces on the cylinder. The predicted inertia coefficients agree reasonably well with those obtained from other numerical and experimental studies.

The effects of three-dimensionality were discussed in detail in Section 4.5.3. The onset of three-dimensional motion at low Reynolds numbers (for steady flow around a single cylinder at $Re_c^{3D} \approx 200$) reduces the applicability of two-dimensional (laminar) simulations to a Reynolds number range that is not relevant to most engineering situations. Thus, the use of two-dimensional laminar vortex shedding results alone (obtained at high Reynolds numbers) in order to understand some real physical processes can be regarded as inappropriate. The next chapter focuses on the validity of two-dimensional methods that include turbulence models.

Chapter 5

TURBULENT FLOW PREDICTIONS

5.1 Introduction

In this chapter, the two-dimensional, turbulent vortex shedding flows around single square and circular cylinders are investigated. Since the numerical results are verified by comparisons with experimental data, homogeneity of the experimental mean-flow along the cylinder axis is the crucial assumption. Thus, the mean-flow periodicity caused by large scale vortex shedding remains two-dimensional, while the small scale three-dimensional turbulent fluctuations are accounted for by the turbulence models. The $k - \epsilon$ models in conjunction with the wall functions are employed.

The chapter is organized as follows. Section 5.2 presents experimental evidence which is relevant to the definition of boundary conditions and validation of turbulence models. Section 5.3 deals with numerical details of the vortex shedding simulations, such as the domains and grids used. Then, the preliminary assessment of several variants of the $k - \epsilon$ model, reviewed in Section 2.7, is done in Section 5.4. The RNG and unsteady variants of the standard model are selected for further predictions. Numerical uncertainties associated with the prediction of turbulent vortex shedding flows are considered in Section 5.5. The vortex shedding results for the flow past a square cylinder are presented and discussed in Section 5.6. Section 5.7 presents the results for a circular cylinder.

5.2 Experimental Evidence

Evolution of flow regimes with the Reynolds number for smooth circular and square cylinders in low–turbulence free streams was discussed in Section 1.2. The force coefficients and Strouhal numbers, presented there in Figures 1.2 and 1.3, as well as other quantities obtained by long–time averaging, are very good benchmark tests for turbulence models. However, the conventional long–time averaging hides the nature of the flow fluc-

tuations. For example, the global 'Reynolds stresses' obtained by this procedure (see Equation (2.14)) contain the contributions from the periodic and random motions:

$$\overline{u_i' u_j'} = \overline{\widetilde{u}_i \widetilde{u}_j} + \overline{\langle u_i u_j \rangle} \,. \tag{5.1}$$

Similarly, the global fluctuating kinetic energy k_f consists of the periodic component $\widetilde{q}$ and the turbulent kinetic energy k, thus:

$$\begin{aligned} k_f &= \frac{1}{2} \left\langle \left(\widehat{U}_i - \overline{U}_i \right)^2 \right\rangle \\ &= \widetilde{q} + k \,, \end{aligned} \tag{5.2}$$

Therefore, experimental turbulence statistics are meaningful if the experimental method correctly separates and quantifies the periodic (quasi-periodic) and random turbulent fluctuations.

Because of experimental difficulties, there have been only few such experimental studies. The turbulent near wake of a circular cylinder was analysed by Cantwell and Coles (1983) at $Re = 1.4 \times 10^5$, and by Owen and Johnson (1980) at $Re = 1.67 \times 10^5$. Matsumura and Antonia (1993) investigated the turbulent intermediate wake of the circular cylinder ($5 < x/D < 50$, x - the streamwise distance measured from the cylinder centre) at $Re = 5830$, including both momentum and heat transfer. In the case of a square cylinder, Lyn and others (Lyn, 1992; Lyn and Rodi, 1994; Lyn et al., 1995) presented the near wake results of the phase-averaged velocity components and turbulence quantities for various phases during a vortex shedding cycle at $Re = 21400$. Although these results are reliable, the remark of Rodi et al. (1997) about some modulation of the wake periodicity in the experiments questions the reported periodicity in the original papers. Less detailed measurements at $Re = 14000$ were carried out by Durao et al. (1988). They also claimed that the periodic and turbulent fluctuations have been separated using band-reject filtering of the velocity time series. However, Lyn and Rodi (1994) and Lyn et al. (1995) suspected the correctness of this method.

All the studies indicate the importance of both periodic (organized) and random (turbulent) fluctuations. In regions of the highest velocity fluctuations, the turbulence kinetic energy can contribute up to 40 % of the global or total fluctuating kinetic energy; Lyn (1992). Note that for two-dimensional flows, the turbulent kinetic energy k can be estimated by assuming $\langle w^2 \rangle = 2k/3$ which gives:

$$k = \frac{3}{4} \left(\langle u^2 \rangle + \langle v^2 \rangle \right) \,. \tag{5.3}$$

By analogy, the total fluctuating kinetic energy, Equation (5.2), is calculated as:

$$k_f = \frac{3}{4} \left(\widetilde{u}^2 + \widetilde{v}^2 \right) + k \,. \tag{5.4}$$

Experimental study	$Re \times 10^{-3}$	$B_f,\%$	$T_u,\%$	L_x/H	St	$\overline{C}_D$	C'_D	C'_L
Pocha (1971)	91	-	-	-	0.120	2.06	0.18	1.40
Bearman & Trueman (1972)	20-70	6.0	0.30	-	0.123*	2.19*	-	-
Lee (1975)	176	3.6	0.5 4.4	0.7-1.1	0.122	2.05* 1.98*	0.23 0.18	1.22 1.00
Bearman & Obasaju (1982)	20	5.5	0.04	-	0.130	-	-	1.20
Obasaju (1983)	47.4	5.5	0.04	-	0.124*	2.17*	-	-
Gartshore (1984)	-	8.3	0.5 4.0	0.2-0.5	-	-	-	1.1 1.01
Igarashi (1987)	20	7.5	0.5	-	0.139	2.24	-	-
Durao et al. (1988)	14	13.0	6.0	-	0.138	-	-	-
Cheng et al. (1992)	27.4	1.7-4.2	4.0 3.75	1.1 2.05	-	1.73 1.85	0.07 0.05	0.225 0.10
Lyn (1992)	21.4	7.0	2.0	-	0.132	-	-	-
Norberg (1993)	13	1.6	0.06	-	0.132	2.16	-	-

Note: Data denoted by an upper index * are corrected for the blockage.

Table 5.1: Experimental conditions and measured integral vortex shedding parameters for the flow over a square cylinder.

In the case of the measured data, the turbulent kinetic energy can be deduced from Equation (5.3) as done by Lyn (1992). In this (numerical) study, the same equation (5.4) for k_f is used but k is the solution of its transport equation.

The case of a square cylinder will be analysed in more details in the following sections. For this case, the turbulent vortex shedding results practically do not depend on the Reynolds number, Figure 1.3. However, these results depend on the free stream turbulence and experimental conditions (the cylinder aspect ratio, end conditions, and the wind tunnel blockage). The effects of these factors, including experimental uncertainties, are well illustrated by dispersion of the results for a square cylinder, Table 5.1. This table includes data from several experimental studies in which the relative turbulence intensity T_u was less than 5 %. Note that two quantities, namely the relative turbulence intensity:

$$T_u = \frac{u'}{U_0} \ , u' = \sqrt{\overline{u^2}} \tag{5.5}$$

(here u represents velocity fluctuations around the steady i.e. long–time averaged streamwise component U), and the integral length scale ratio of turbulence L_x/D (L_x/H) are usually used to quantify the free stream turbulence. The third parameter, the turbulence spectrum, can also be important (e.g. West and Apelt, 1993). A limited number of the

results in the above table (Lee, 1975; Gartshore, 1984; Cheng et al., 1992) indicates the effects of the free stream turbulence. Regarding the blockage effect, Bearman and Trueman (1972) and Obasaju (1983) corrected the time-mean drag coefficient and Strouhal number for this effect. Lee (1975) also reported the corrected values only for the mean drag coefficient. According to Lee (1975) and Obasaju (1983), the corresponding corrections reduced the measured values typically for 7 and 5 %, respectively.

5.3   Numerical Considerations

5.3.1   Solution domain and grids

The unsteady flow around a square cylinder was computed at $Re = 20,000$. The numerical grid used for most of the present computations is presented in Figure 5.1. The figure also shows the extent of the solution domain in terms of the cylinder's height, H. A total of 139×122 cells was used, with the grid lines concentrated near the cylinder walls (24 cells per side, $\Delta n_c/H = 0.014$) and expanding away from it with an expansion ratio of 7.5 % in each direction. The blockage effect produced by using the above solution domain was $B_f = 4.17$ %. The selection of this value has been guided by the values obtained in the experiments of Lee (1975) and Bearman and Obasaju (1982), although the higher values would be more suitable regarding the data of Lyn (1992), Table 5.1. Other grids

$$V = 0,\ \partial\phi/\partial y = 0$$
$$\phi = U, k, \epsilon$$

$U = U_0$
$V = 0$

$k = k_0$
$(\nu_t/\nu)_0$

2Ys=24H

$\partial\phi/\partial x = 0$

$\partial V/\partial y = 0$

$X_i = 12H$ $X_o = 30H$
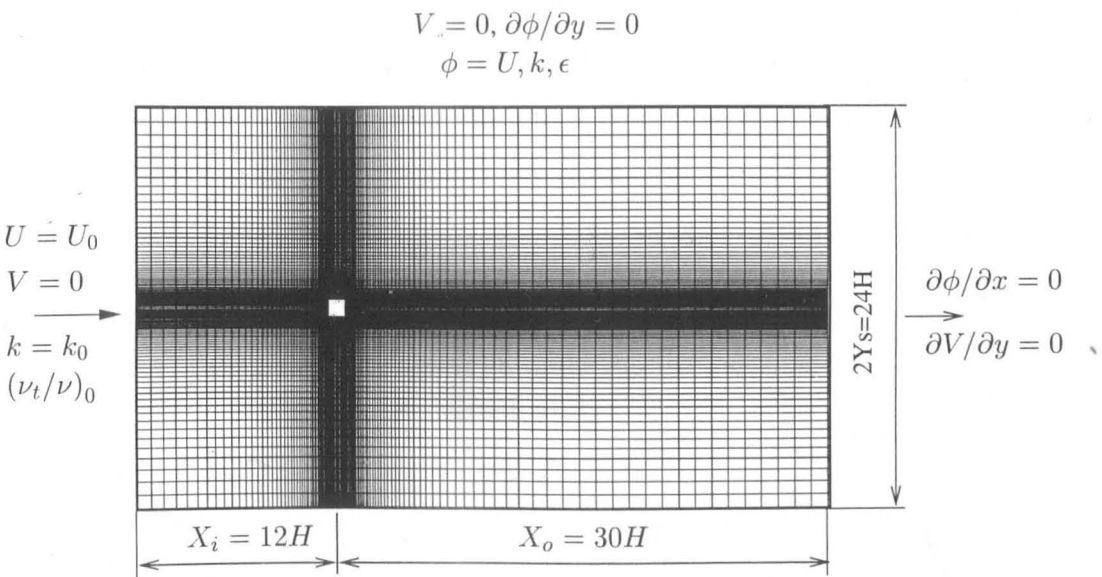
Figure 5.1: Numerical grid $D1 - 139 \times 122(a)$ and boundary conditions for the flow around a square cylinder.

were also tested, including the grid $D2 - 114 \times 92$ with the blockage of 8.33 % and 24 nodes per cylinder side. Parameters of all the grids are given in Table 5.2.

Grid [Domain-NI×NJ]	X_i/H	X_o/H	Y_s/H	f_{ex}	f_{ey}	$\Delta n_c/H$	$B_f, \%$
$D1 - 139 \times 122(a)$	12	30	12	1.075	1.075	0.014	4.17
$D1 - 139 \times 122(b)$	12	30	12	1.0635	1.062	0.02	4.17
$D1 - 106 \times 108$	12	30	12	1.10	1.10	0.02	4.17
$D2 - 114 \times 92$	5.5	29.5	6	1.076	1.076	0.02	8.33

Table 5.2: Parameters of numerical grids used for computations of the turbulent flow past a square cylinder.

Vortex shedding from a circular cylinder was computed for various Reynolds numbers by using the domain $D1$. The employed grids are described in Section 5.7.

5.3.2 Boundary and initial conditions

The boundary conditions used here are also shown in Figure 5.1. In specifying the inlet boundary conditions for the flow past a square cylinder, reference is made to the measurements of Lee (1975) and Gartshore (1984) (see also Table 5.1). These measurements show that the global parameters are practically insensitive to the levels of turbulence intensity T_u in the approach stream provided that $0 < T_u \le 0.02$. The higher limit was chosen for this study - a level similar to that obtained in Lyn's (1992) experiments. The turbulent kinetic energy is deduced from the isotropic relation:

$$k_0 = \frac{3}{2} (T_u U_0)^2 \ .$$

(5.6)

The inlet values for the dissipation rate ϵ were determined by inverting the eddy-viscosity relation (2.34) and using Kolmogorov expression for ϵ:

$$\epsilon = C_\mu \frac{k^{\frac{3}{2}}}{L_\epsilon} \ .$$

(5.7)

According to Bearman and Morel (1983), the dissipation scale L_ϵ/C_μ is about twice the integral scale L_x and the above equation gives :

$$\left(\frac{\nu_t}{\nu}\right)_0 \approx 0.22 \, T_u \, Re \left(\frac{L_x}{H}\right)_0 \ .$$

(5.8)

For $L_x/H \approx 1$ the inlet value of $(\nu_t/\nu)_0$ is 88, which is close to the selected value for present computations of $(\nu_t/\nu)_0 = 100$.

In the case of a circular cylinder, the low values for T_u (from 0.5 to 1 %) and for $(\nu_t/\nu)_0$ (from 1 to 10) were used, in accordance with the turbulence level encountered in majority of the experimental studies.

The symmetry boundary conditions were applied at the lateral boundaries, while the zero gradient conditions were used at the outlet plane. The usual wall function boundary conditions were applied at the walls. Actual implementation of all these boundary conditions is explained in Section 3.6.

Regarding the initial conditions, the computations were usually started from a symmetric velocity field. In some cases the asymmetric velocity field was used in order to obtain periodic vortex shedding earlier, see Section 4.3.1.

5.3.3 Computational details

As for laminar calculations, at each new time step the iterative solution of the discretised equations was stopped when the sum of normalized absolute residuals for each variable became smaller than 10^{-4}. For the first–order accurate fully–implicit temporal differencing, small time steps must be used. For instance, the non-dimensional time-step size Δt^* of 0.0078 was found necessary for the flow around a square cylinder at $Re = 20000$, requiring 909 time steps to cover a complete vortex shedding cycle. No under-relaxation was used and 3-5 outer iterations were required to satisfy the prescribed convergence criterion within each time step. Several convective schemes were evaluated earlier, in Section 4.4.2. Most of turbulent flow results reported in this chapter were obtained with the SMART scheme.

5.4 Assessment of Turbulence Models

Several variants of the $k - \epsilon$ model were discussed and selected for further testing in Chapter 2. These are:

- Standard $k - \epsilon$ model (SKE),

- RNG $k - \epsilon$ model (RNG),

- Modified, unsteady $k - \epsilon$ model (UKE), Equation (2.52),

- Modified $k - \epsilon$ model, with the preferential dissipation modification (PDM), Equation (2.47),

- Modified $k - \epsilon$ model, with a new definition of the time scale T_ω, Equation (2.50).

Behaviour of the above models is first examined in the stagnation flow region. After that, the models are validated for the vortex shedding flow from a square cylinder.

5.4.1   Conventional $k - \epsilon$ models

The flow approaching a circular cylinder at $Re = 27,400$ is considered. For this flow experimental data of Britter et al. (1979) exist. Predictions with several $k - \epsilon$ models and with the SSG Reynolds stress transport equation model of Speziale, Sarkar and Gatski (1991) are depicted in Figure 5.2. The turbulence intensities of the axial $(u' = \sqrt{\langle u^2 \rangle})$ and normal $(v' = \sqrt{\langle v^2 \rangle})$ velocity components, normalized by the inlet values, are given as a function of the relative distance from the cylinder frontal point. Plotted experimental values were obtained for $L_x/D = 1.43$ and $T_u = 0.057$. Only half of the solution domain was considered since the steady solution was appropriate for the comparison of different models. The computations were carried out by using wall functions on the numerical grid with 134 cells $(\Delta n_c/D = 0.0055)$ and with the SMART convective scheme. Notably,
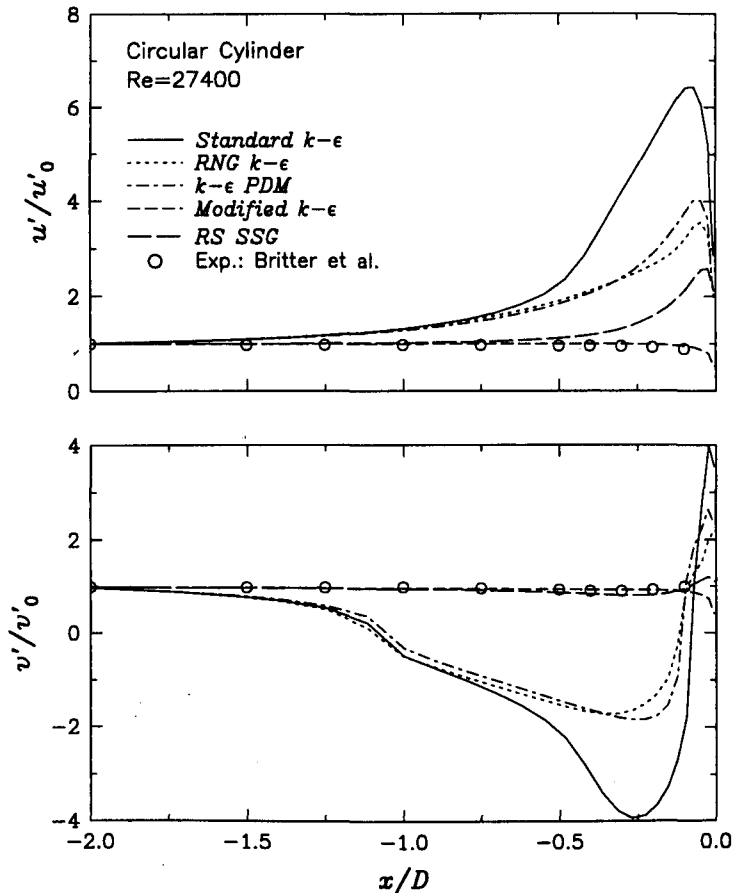
Figure 5.2: Effects of turbulence models on the turbulence intensities as calculated along the stagnation line for the steady flow approaching a circular cylinder.

only the present $k - \epsilon$ model with a new time scale T_ω shows good agreement with measurements for both intensities u' and v'. The results for the u' component obtained by other $k - \epsilon$ models depart much more from the experiments than those calculated by the Reynolds stress equation model. Inability of eddy viscosity models to cope with stress

anisotropies is clearly demonstrated by the results for the v' intensity, where non-physical (negative) values were obtained. As expected, the Reynolds stress equation model performs well in this case. In summary, the standard $k - \epsilon$ model produced the worst results, while the RNG model gave slightly better results than the PDM modification. Note that the PDM model constants were $C'_{\epsilon 1} = 2.30$ and $C_{\epsilon 3} = 0.85$. These values were found after vortex shedding experiments with the PDM modification.

The behaviour of turbulence models in the stagnation region certainly influences the flow development downstream. This is obvious after testing the above $k - \epsilon$ models for the vortex shedding flow past a square cylinder. Time histories of the drag and lift coefficients, depicted in Figure 5.3 for the standard and RNG model, show that the high levels of k (and hence the eddy viscosity) transported from the stagnation region tend to suppress vortex shedding in the case of the standard model. Obviously, in this case the RNG
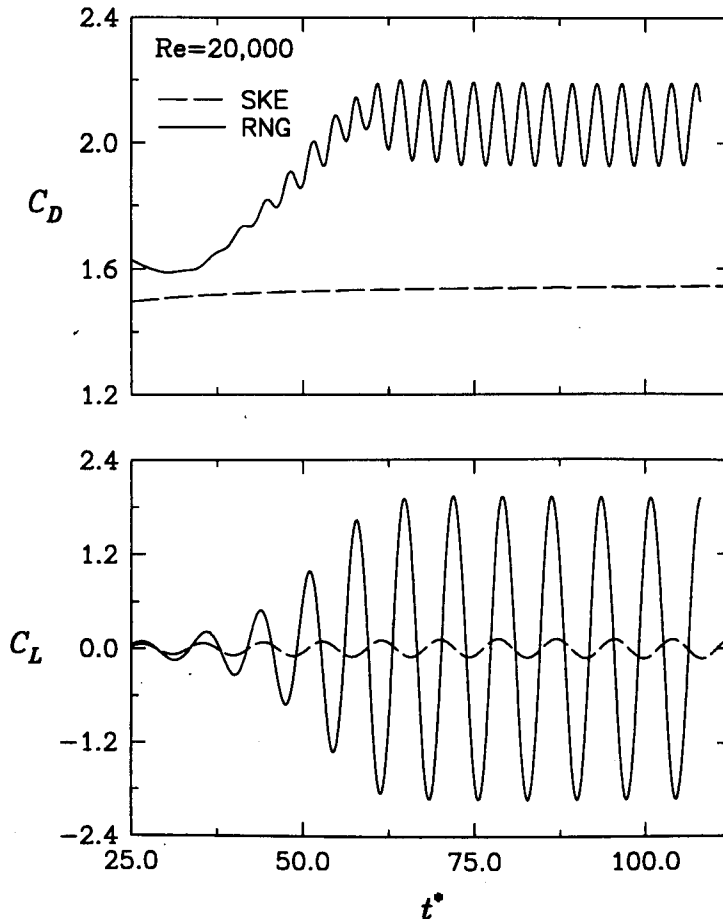
Figure 5.3: Turbulent flow past a square cylinder at $Re = 20,000$. Time evolution of the drag (top) and lift (bottom) coefficients as predicted by the standard and RNG $k - \epsilon$ models (grid $D1 - 139 \times 122(a)$, SMART scheme).

model produces the mean-drag coefficient and force oscillations close to the experimental observations. However, the next Figure 5.4 reveals the high sensitivity of this model to

the near-wall grid resolution. Two grids were selected ($D1 - 139 \times 122(a)$ and $D1 - 139 \times 122(b)$). These grids have the same number of cells but the near-wall distances are larger in the second grid. While the amplitudes of the drag and lift oscillations are not too affected by the near-wall distances, the mean-drag coefficient is significantly lower for $\Delta n_c = 0.02$ in comparison to $\Delta n_c = 0.014$.
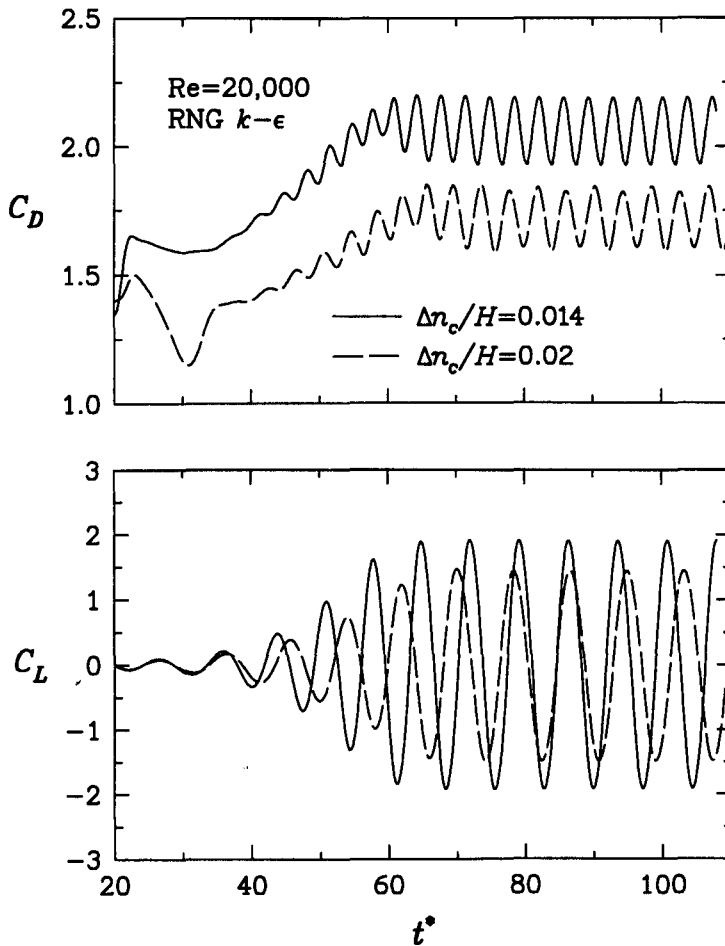
Figure 5.4: Turbulent flow past a square cylinder at $Re = 20,000$. Time evolution of the drag (top) and lift (bottom) coefficients as predicted by RNG $k - \epsilon$ model with two near-wall cell distances (grids $D1 - 139 \times 122(a,b)$, SMART scheme).

The $k - \epsilon$ model with the PDM modification was also extensively tested. The main finding is sensitivity of the model to the constants $C'_{\epsilon 1}$ and $C_{\epsilon 3}$. The tests with vortex shedding from a square cylinder suggested the following values: $C'_{\epsilon 1} = 2.30$ and $C_{\epsilon 3} = 0.85$. With these constants, the PDM model is capable of delivering the results of the same quality as the RNG model or unsteady $k - \epsilon$ model developed in this work. However, since the PDM modification does not satisfy the tensor invariance and there is no obvious way to implement it in the streamline direction in the 3D flow situations, the RNG model seems a better choice for many practical flow calculations. Preliminary vortex shedding results obtained by using the modified time scale T_ω in the eddy viscosity formula were

satisfactory and very encouraging. Because of its implications on the wide range of steady complex flows this proposal needs to be verified first for such types of flows.

5.4.2 Unsteady modification

The consequences of the unsteady modification on both the average and peak-to-peak levels of the lift and drag coefficients are clear from Figure 5.5. However, we should
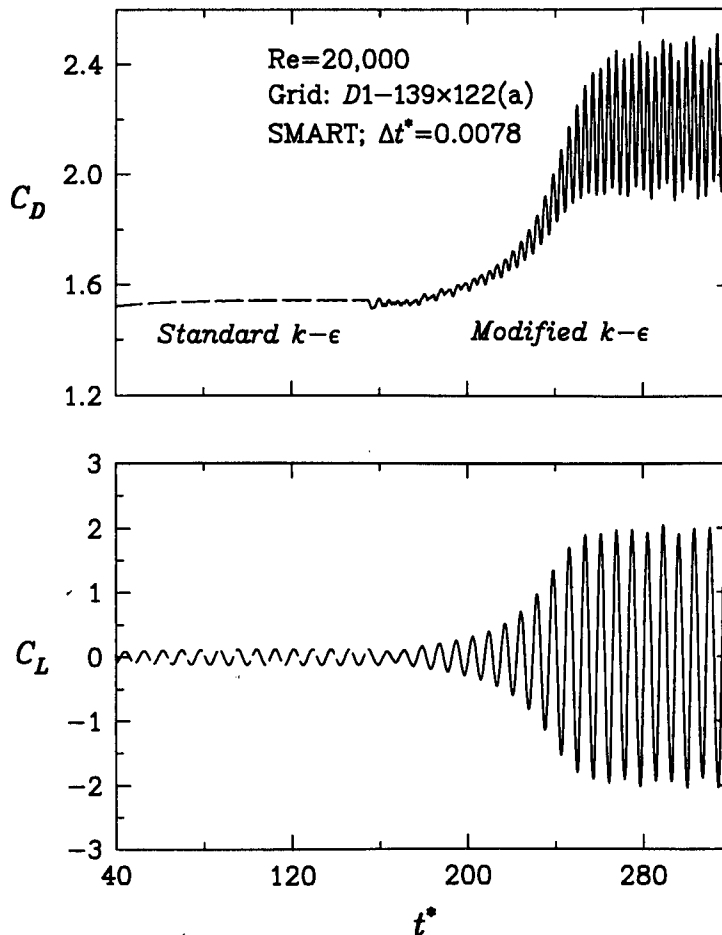
Figure 5.5: Turbulent flow past a square cylinder at $Re = 20,000$. Time evolution of the drag (top) and lift (bottom) coefficients as predicted by the $k - \epsilon$ model before and after the unsteady modification.

not expect too much from the present unsteady modification. By its nature, it does not influence steady flows. In a stagnation flow region, the turbulent kinetic energy is still overestimated, especially when compared with the RNG model, Figure 5.6. This suggests the ability of the proposed modification to remove (at least partly) the negative effects of the stagnation point anomaly when turbulence properties are transported towards the upper and lower cylinder wall sides. A more subtle relation than usually anticipated might exist between the (high) levels of k and ϵ leading to more correct levels of the
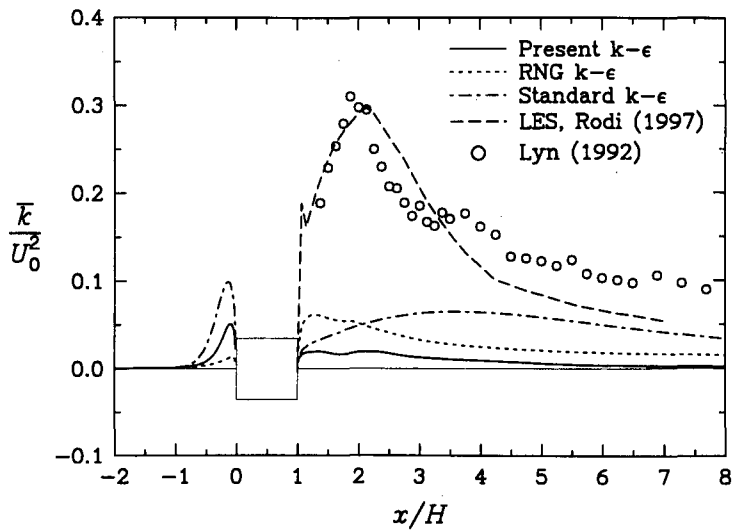
Figure 5.6: Effects of the $k - \epsilon$ turbulence models on the time-averaged centreline distribution of the turbulent kinetic energy for the flow past a square cylinder at $Re = 20000$.
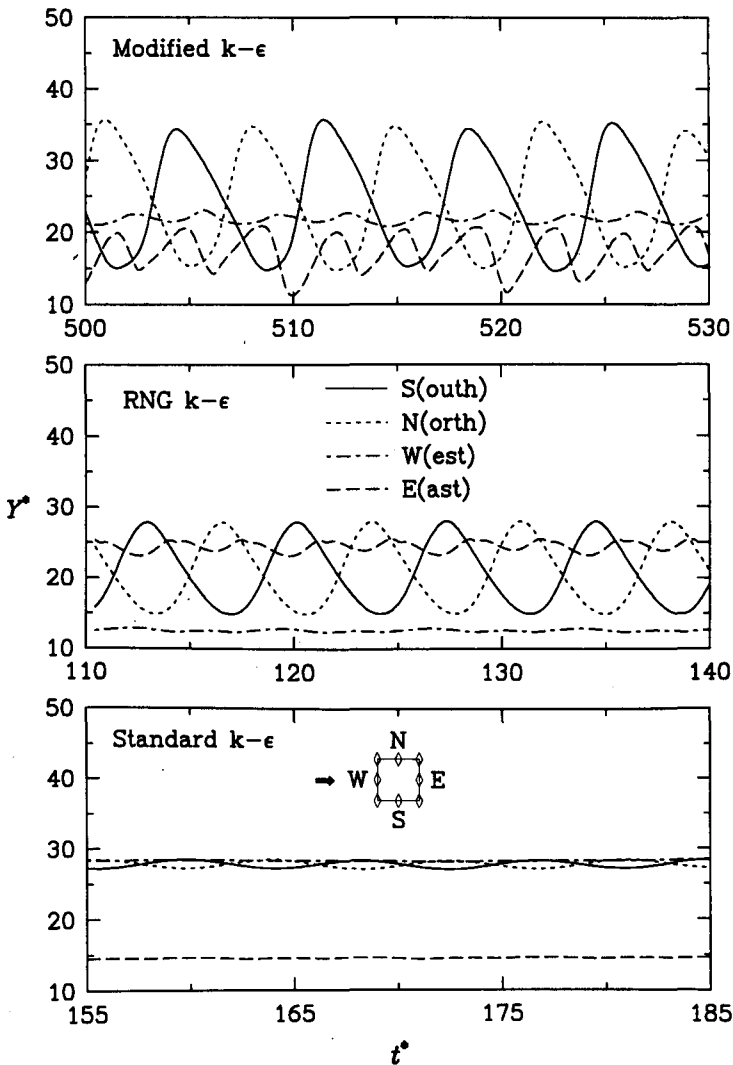
Figure 5.7: Wall units Y^* versus time as predicted by the $k - \epsilon$ models ($Re = 20000$).

eddy viscosity ν_t. Paradoxically, the shear layers formed after flow separation from the forward corners can benefit from the convected higher levels of k since the tested models generate too low levels of k in these zones. This is illustrated by the time-averaged Reynolds stress $\langle u^2 \rangle$ profile shown later in Figure 5.18(top) where the present and RNG model results are compared with experimental data. The time histories of dimensionless wall units $Y^* = C_\mu^{0.25} k^{0.5} \Delta n_c / \nu$, displayed in Figure 5.7, also reflect effects of the stagnation point anomaly on models' performances. The wall units Y^* were monitored at the cylinder side centres. Periodic behaviour is in evidence and nearly constant values in the case of the standard model indicate its failure to simulate correctly vortex shedding. The higher mean and peak-to-peak values were calculated by unsteady modification in comparison with the RNG model. In contrast to the RNG model, the present model predicts incorrectly the higher mean values at the west side than at the east side.

Based on the above tests, the unsteady and RNG model are selected for further computations of vortex shedding flows in this chapter. The next section, which considers the effects of numerical parameters on the calculated results, will show that the unsteady model performs significantly better in terms of larger near-wall distances Δn_c than the RNG model.

5.5   Numerical Uncertainties

In comparison with laminar flows, it is even more important to solve the governing equations accurately in both time and space since differences between two numerical solutions with the same turbulence model can be as large as the differences between two turbulence models. Analysis of numerical uncertainties presented in this section follows the practice employed for laminar flows, Section 4.4. In most of computed cases the present $k - \epsilon$ model with the modified ϵ-production term is used to predict vortex shedding from a square cylinder. Apart from integral vortex shedding parameters, the mean and root-mean-square pressure coefficient distributions around the cylinder walls as well as the time-averaged velocity and global fluctuating kinetic energy along the centreline are compared. The point in the wake where the mean centreline axial velocity changes the sign defines the time-averaged length of a recirculation region $\overline{L}_r$. This length, measured from the rear cylinder wall, will be used as an additional bulk parameter.

5.5.1   Temporal resolution

Temporal resolution effects have been investigated by computing two cases with smaller time-step sizes than the reference one ($\Delta t^* = 0.0078$), Table 5.3. The moderate increase
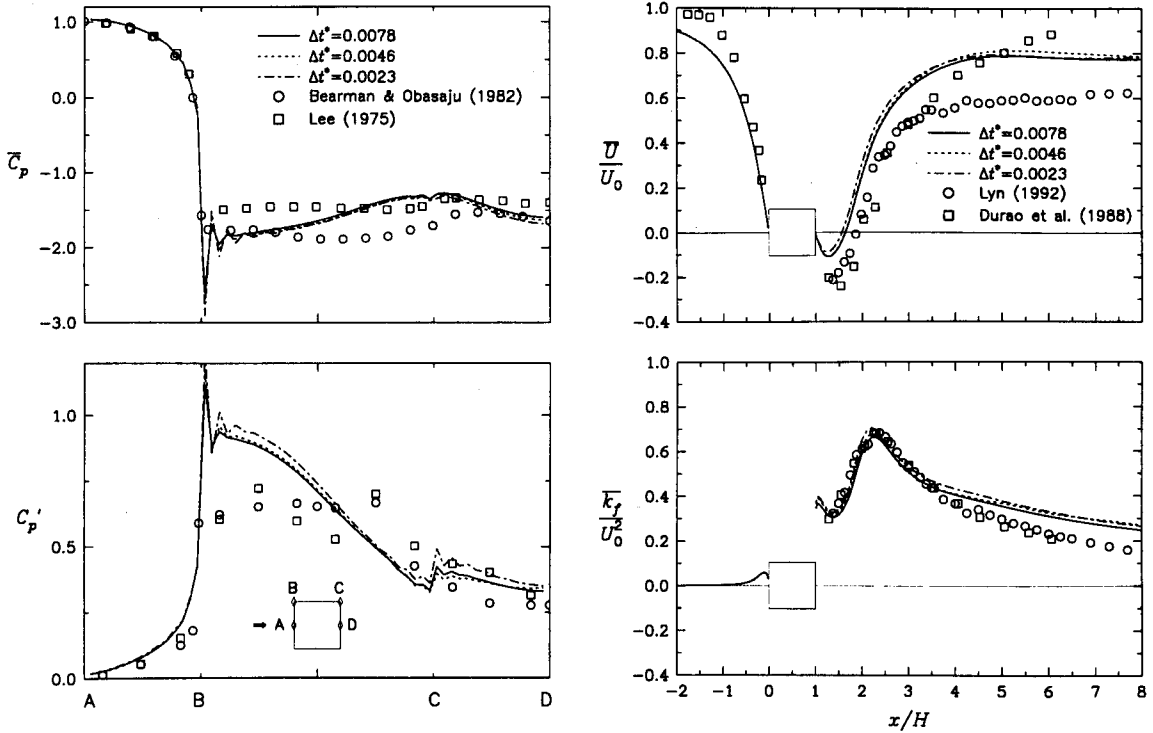
Figure 5.8: Effects of the time-step size on the distribution of time-averaged flow variables: (left) the pressure coefficients, (right) the streamwise velocity and fluctuating kinetic energy.

of the St-number and the drag coefficients is evident for the reduced time-step sizes, while the r.m.s. lift coefficient first increases and then decreases. The table also includes the errors calculated for the smallest time-step size from Equation (B.5) and for the largest (reference) from Equation (B.9). These errors are denoted as E_{1t} and E_{3t}, respectively. In both cases the first order accuracy is assumed, with $\varpi = 1$ in the above equations. Not all

$\Delta t(s)$	$\Delta t^* \times 10^3$	St	$\overline{C}_D$	C_D'	C_L'	$\overline{C}_L \times 10^3$	$\overline{L}_r/H$
0.025	7.77	0.1414	2.199	0.186	1.386	-8.0	0.654
0.015	4.66	0.1435	2.226	0.201	1.398	-7.9	0.644
0.0075	2.33	0.1440	2.253	0.207	1.376	-16.4	0.577
E_{3t} (%)		-2.41	-3.20	-13.53	0.97	-	17.8
E_{1t} (%)		-0.35	-1.12	-2.89	1.60	-	11.6

Table 5.3: Temporal refinement tests for the turbulent flow past a square cylinder at $Re = 20000$ (grid $D1 - 139 \times 122(a)$; SMART scheme).

quantities ($\overline{C}_D$, C_L', $\overline{L}_r$) show an expected convergence trend (the progressively reduced differences between successive refinement tests). The tests with even smaller time-step sizes or the second order accurate time schemes should be useful. However, the averaging

procedure itself (for instance, the length of an averaging period and cycle-to-cycle variations of considered quantities) will always contaminate the final, time-averaged values. More detailed are comparisons for the distributions of various time-averaged flow quantities depicted in Figure 5.8. In terms of the result convergences, similar conclusions can be drawn as for the comparisons of integral vortex shedding parameters. An interesting trend should be noticed: the smaller pressure coefficient values along the cylinder side and rear walls correspond to the shorter recirculation region and higher (maximum) values of the fluctuating energy in the wake. Note that lower pressure coefficients at the rear wall are responsible for the higher mean drag coefficients. The above trend characterizes also the spatial refinement tests which are considered next.

5.5.2   Spatial resolution

Regarding the spatial discretisation, it is always beneficial to employ the high order convective schemes and refined numerical grids, particularly in regions where the intensive turbulence generation or/and laminar to turbulent transition take place.

Effects of convective schemes

Deductions from laminar flow predictions suggest the use of the SMART bounded convective scheme. Here, we again examine effects of two bounded schemes- SMART and MINMOD, and the most accurate but unbounded QUICK scheme. The reference grid $D1 - 139 \times 122(a)$ with $\Delta t^* = 0.0078$ is used. The time traces of the drag and lift coefficients displayed in Figure 5.9 show larger cycle-to-cycle oscillations for more accurate schemes but more or less repeatable patterns are preserved for all three schemes. The predicted bulk parameters are given in Table 5.4 together with their relative differences with reference to the results obtained by the SMART scheme. The SMART and MINMOD

Scheme	St	$\overline{C}_D$	C_D'	C_L'	$\overline{C}_L \times 10^4$	$\overline{L}_r/H$
SMART (S)	0.1414	2.199	0.186	1.386	-80	0.654
MINMOD (M)	0.1425	2.118	0.163	1.270	-2.4	0.850
QUICK (Q)	0.1396	2.023	0.152	1.176	-5.5	0.657
(M-S)/S, %	0.78	-3.68	-12.37	-8.37	-	29.9
(Q-S)/S, %	-1.27	-8.00	-18.27	-15.15	-	0.5

Table 5.4: Turbulent flow around a square cylinder at $Re = 20000$. Effects of three convective schemes on the integral parameters.

schemes behave in the same way as for laminar cases (see Table 4.5): the more diffusive
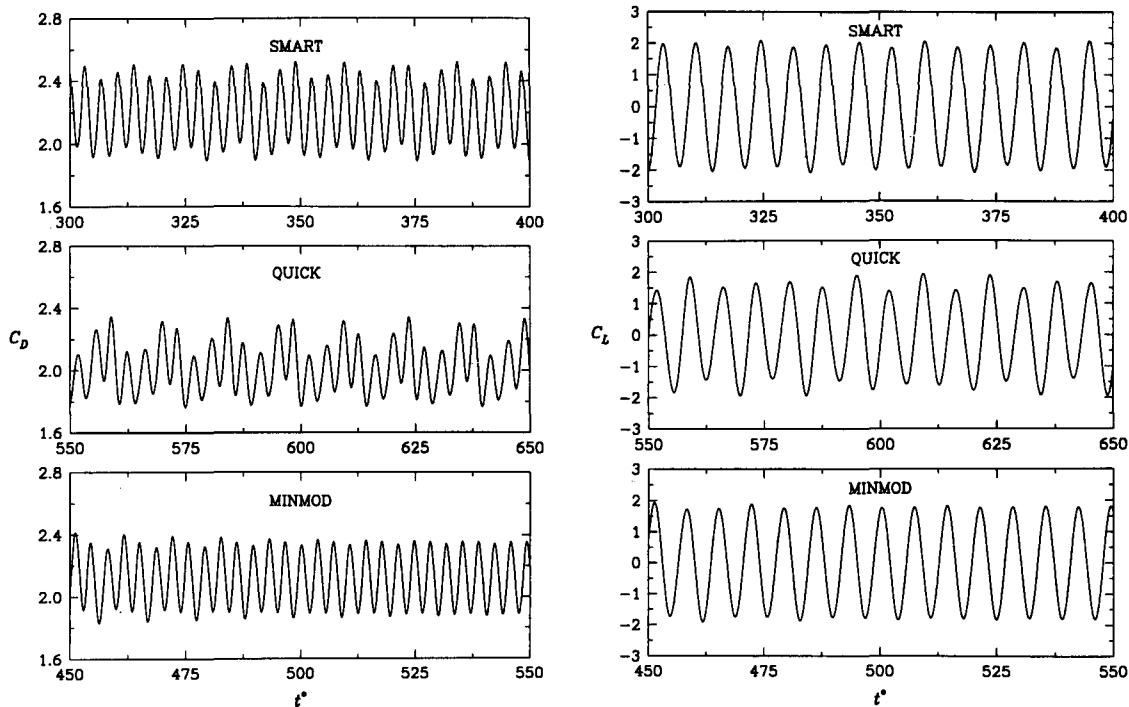
Figure 5.9: Turbulent flow around a square cylinder at $Re = 20000$. Time traces of the drag (left) and lift (right) coefficients as calculated by three convective schemes.
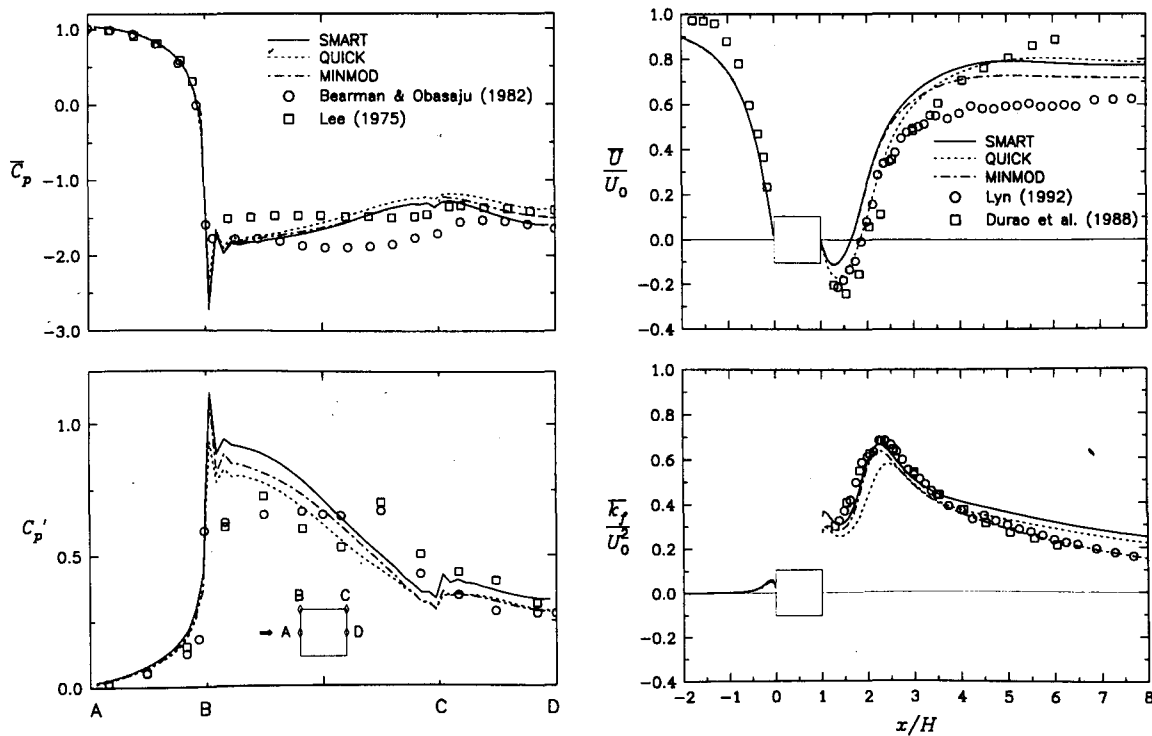

Figure 5.10: Effects of convective schemes on the distribution of time-averaged flow quantities: (left) the pressure coefficients, (right) the streamwise velocity and fluctuating kinetic energy.

139

MINMOD scheme gives smaller force coefficients and higher St-numbers. While the SMART and QUICK schemes produced very close results in the case of laminar flow, their results now show larger discrepancies than between the SMART and MINMOD schemes. Actually, the St-number and force coefficients have the smallest values when the QUICK scheme is employed. The larger differences between the SMART and QUICK schemes in this case certainly indicate existence of the flow regions where the grid resolution is not adequate and where the QUICK scheme may produce unphysical results. If compared with experimental data, Table 5.1, the force coefficients calculated by the QUICK scheme seem underestimated. This is also suggested by the mean pressure coefficient distribution shown in Figure 5.10. Note that results for the centreline velocity profiles, presented also in this figure, may suggest better predictions by QUICK scheme than by others. This is not the case since the underestimated values of the drag coefficient are linked with the longer recirculation zones. Also, the QUICK scheme in this case underestimates the levels of fluctuating kinetic energy.

Effects of grid resolution

Three grids, described in Table 5.2, are used to investigate the effect of grid resolution. When using wall functions, the smallest cell size in a direction normal to the wall is usually limited by the non-dimensional distance $Y^* \approx 11.6$. The grids $D1 - 139 \times 122(a)$ and $D1 - 139 \times 122(b)$ have similar expansion factors but different wall distances, while the coarsest grid $D1 - 106 \times 88$ has the larger expansion factors and the same wall distances as the grid $D1 - 139 \times 122(b)$. The time histories of the drag and lift coefficients, calculated by using these grids and the present $k - \epsilon$ model, are presented in Figure 5.11, while Table 5.5 shows the results for the bulk parameters. One can notice different behaviour of the unsteady and RNG models in regard to predictions of the length of the time-mean recirculation zone. With finer grids, this length increases for the RNG model but decreases in the case of the unsteady dissipation modification. A tendency of the numerical diffusion (with higher levels for the coarser grids) to diminish intensity of the vortex shedding process is in strong evidence. Its manifestations are reduced mean and r.m.s. values of the force coefficients as it is shown by comparison of the results for two coarser grids. While the present unsteady modification shows acceptable sensitivity to the wall distances, the RNG model simulates the vortex shedding process properly only for the wall distances that give wall units Y^* close to the lower limit of ≈ 11.6 (according to Figure 5.7 between 11 and 30). The mean value of the drag coefficient is particularly sensitive to the wall distances so we should avoid assessments of turbulence models based only on the Strouhal number values and/or some velocity distributions, which was the case in some of published vortex shedding studies. For instance, the Strouhal num-
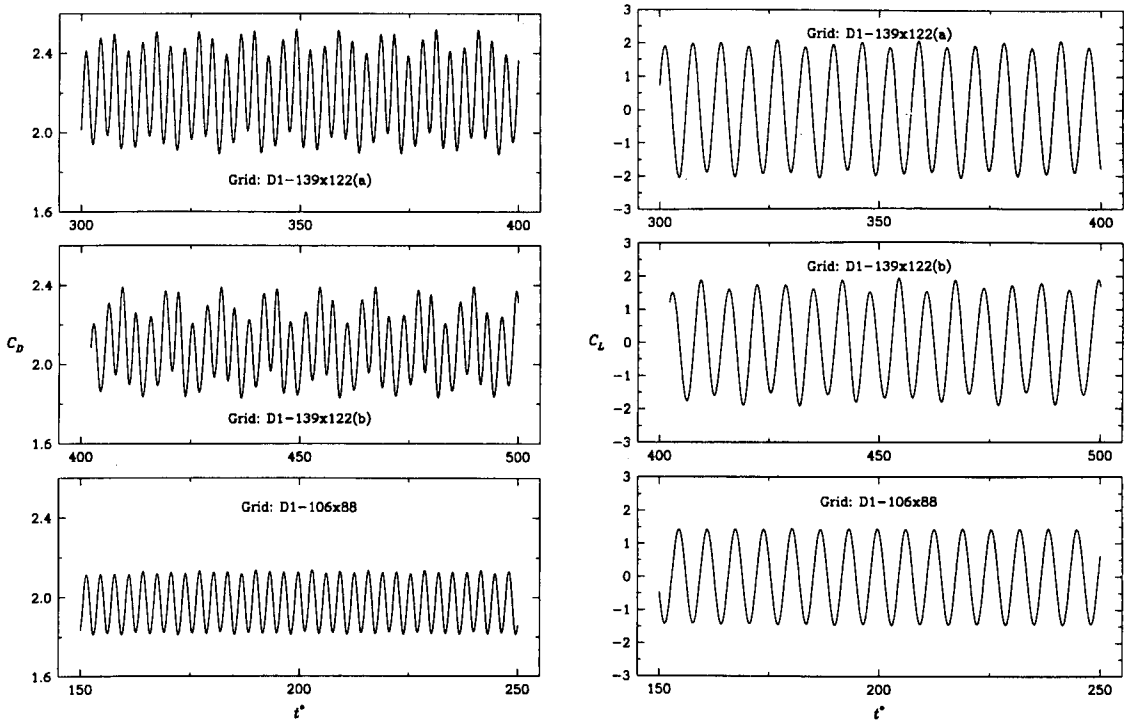
Figure 5.11: Turbulent flow around a square cylinder at $Re = 20000$. Time traces of the drag (left) and lift (right) coefficients as obtained on three different numerical grids (the present $k - \epsilon$ model with the SMART scheme and $\Delta t^* = 0.0078$).

(a) Present $k - \epsilon$ model

Grid	St	$\overline{C}_D$	C_D'	C_L'	$\overline{C}_L \times 10^4$	$\overline{L}_r/H$
$139 \times 122(a)$ (A)	0.1414	2.199	0.186	1.386	-80.0	0.654
$139 \times 122(b)$ (B)	0.1413	2.093	0.157	1.202	+6.9	0.801
106×88 (C)	0.1412	1.972	0.110	1.009	-7.9	0.912
(B-A)/A, %	-0.07	-4.8	-15.6	-13.3	-	22.5
(C-A)/A, %	-0.14	-10.3	-40.9	-27.2	-	39.4

(b) RNG $k - \epsilon$ model

Grid	St	$\overline{C}_D$	C_D'	C_L'	$\overline{C}_L \times 10^4$	$\overline{L}_r/H$
$139 \times 122(a)$ (A)	0.1387	2.064	0.092	1.369	-7.1	0.590
$139 \times 122(b)$ (B)	0.1207	1.722	0.082	1.048	-3.2	0.540
(B-A)/A, %	-12.98	-16.6	-10.9	-23.45	-	-8.5

Table 5.5: Turbulent flow around a square cylinder at $Re = 20000$. Grid refinement effects on the bulk parameters as obtained by present (a) and RNG (b) $k - \epsilon$ models ($\Delta t^* = 0.0078$, SMART scheme).
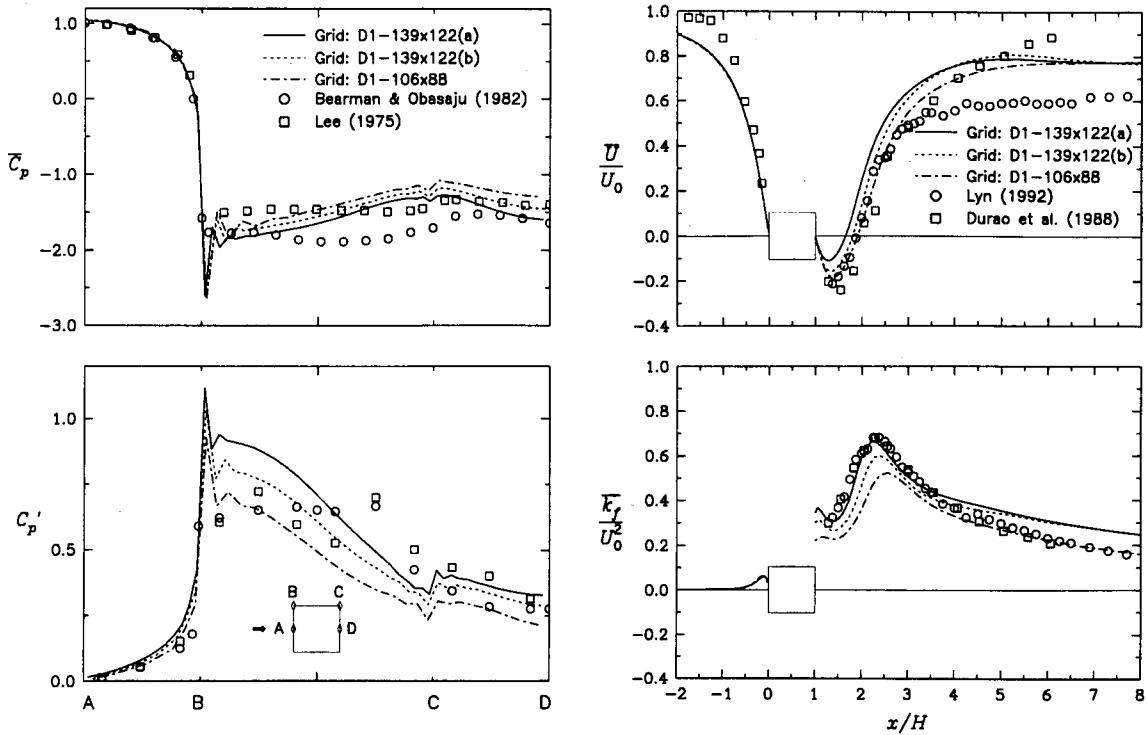
Figure 5.12: Grid resolution effects on the distribution of time-averaged flow quantities: (left) the pressure coefficients, (right) the streamwise velocity and fluctuating kinetic energy.

ber computed by the present modification is practically insensitive to the grid refinement, Table 5.5(a). The pressure coefficients distributions and the centreline velocity and fluctuating kinetic energy profiles, given in Figure 5.12, also emphasize importance of the proper grid resolution. That the results for the mean U-velocity component for the coarsest grid show very good agreement with measurements is not surprising in the light of the remark upon the results obtained by using the QUICK scheme.

5.5.3   Size of the solution domain

Considerations of laminar flows have shown a significant influence of the solution domain size, where the placement of lateral boundaries or the blockage effect is the most important factor. Here, the grids generated within two domains $D1$ and $D2$, Table 5.2, are used to investigate the blockage effect. In terms of the wall units Y^*, it is appropriate to assess the blockage effect by comparing the results calculated on the grids $D1 - 139 \times 122(a)$ and $D2 - 114 \times 92$. The bulk parameters predicted by using the present ϵ-production modification are given in Table 5.6. The relative differences between the calculated values are also included. With exception of the r.m.s. lift coefficient, other predicted parameters increase for the smaller domain $D2$. This trend is demonstrated by the distributions of

Domain-[Grid size]	B_f (%)	St	$\overline{C}_D$	$C_D' \times 10^3$	C_L'	$\overline{C}_L \times 10^4$	$\overline{L}_r/H$
$D1 - 139 \times 122(a)$	4.17	0.1414	2.199	0.186	1.386	80.	0.654
$D2 - 114 \times 92$	8.33	0.1442	2.239	0.186	1.247	-4.8	0.846
(D2-D1)/D1 (%)		1.9	1.8	0.0	-10.0	-	29.4

Table 5.6: Influence of domain size on the vortex shedding parameters for the turbulent flow past a square cylinder at $Re = 20000$ (the present $k - \epsilon$ model, SMART scheme, $\Delta t^* = 0.0078$, $\Delta n_c/H = 0.02$).
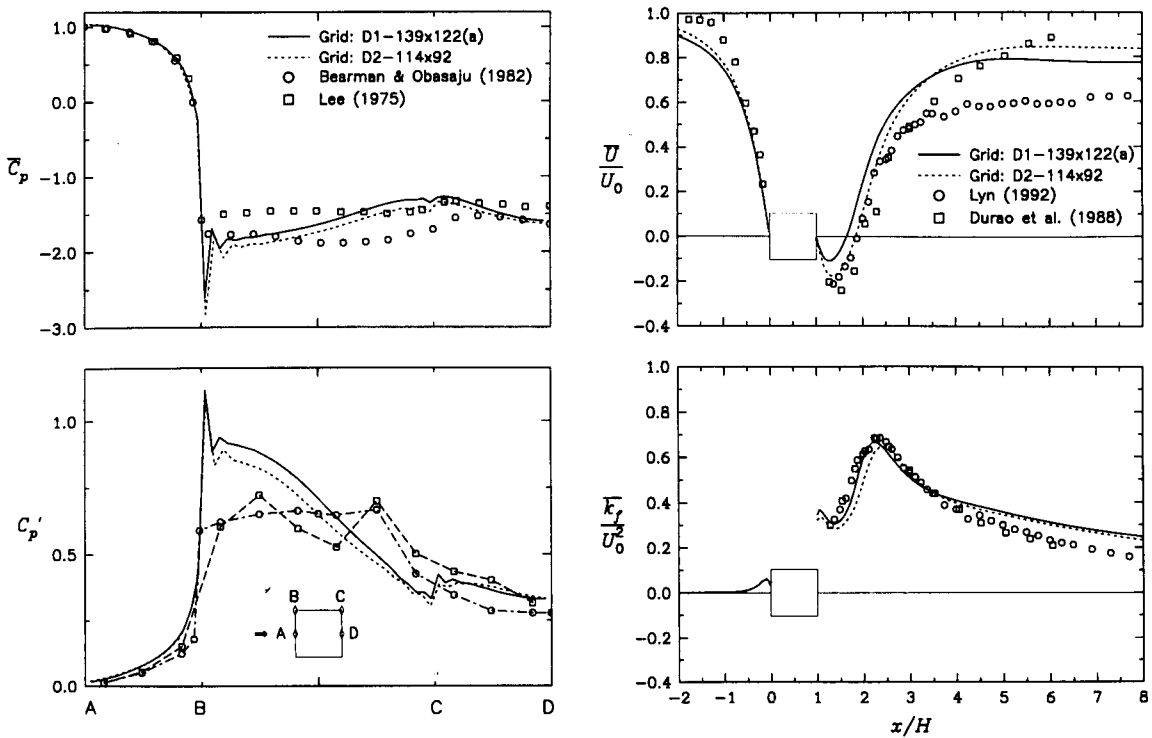

Figure 5.13: Domain size influence on the distributions of time-averaged flow quantities: (left) the pressure coefficients, (right) the streamwise velocity and fluctuating kinetic energy.

the mean and r.m.s. pressure coefficients in Figure 5.13(left). The mean pressure coefficient values are smaller everywhere for the smaller domain $D2$. Consequently, the reduced values at the rear wall result in the higher value of the mean drag coefficient. For the smaller domain, the pressure r.m.s. values are reduced along the side wall(s) giving smaller values for the C_L'. On the other hand, differences between C_p' along the rear wall cancel each other out so that apparently the blockage does not influence the r.m.s. drag coefficient. The results for $\overline{L}_r/H$, Table 5.6 and Figure 5.13(right), show a large difference and obviously the length of the recirculation zone predicted for the narrow domain $D2$ agrees well with the measured value of 0.88. By contrast to the trend encountered in the time and spatial refinement tests, now the mean drag coefficient increase corresponds to the longer recirculation zone. The time-averaged fluctuating kinetic energy is

not significantly influenced by the blockage effect.

5.5.4   Summary

In summary, the sensitivity of numerical solutions to the time and space discretisation was clearly demonstrated. The simple relative difference between two numerical solutions (χ in Equation(B.6)) is not the best estimate of the actual error. However, for a number of refinement tests reported here it is a suitable choice. In regard to reference computational parameters, Table 5.7 summarizes these estimated errors for the integral quantities and also reports on the total estimated errors. The total errors are calculated as the root-mean-square values of individual errors, a practice usually employed in experimental studies.

Estimated errors for	St	$\overline{C}_D$	C_D'	C_L'	$\overline{L}_r/H$
Time discretisation, χ_t (%)	-2.4	-3.2	-13.5	1.0	17.8
Space discretisation, χ_{xy} (%)	-0.1	-4.8	-15.6	-13.3	22.5
Domain size, χ_d (%)	2.0	1.8	0.0	-10.0	29.4
Total, χ_{rms} (%)	3.1	6.1	20.6	16.7	41.1

Table 5.7: Estimated numerical errors for the turbulent vortex shedding results predicted by the present $k - \epsilon$ model, the grid $D1 - 139 \times 122(a)$, $\Delta t^* = 0.0078$ and SMART scheme.

5.6   Square Cylinder: Results and Discussion

In this section, computational results from this work and from other numerical studies are compared against experimental data in order to assess performances of various turbulence models. Present results, based on the RNG and unsteady $k - \epsilon$ models, were computed by using the reference numerical parameters for which possible numerical errors have been summarized in Table 5.7. Three groups of data, namely integral vortex shedding parameters, time-averaged and phase-averaged flow quantities ensure a comprehensive comparison. Before presenting this comparison , it is useful to have an overall impression of the flow features around a cylinder. Figure 5.14 shows plots of the instantaneous streamlines, velocity vectors and contours of the turbulent kinetic energy, all taken at a phase when the lift coefficient has a maximum value. In present simulations this phase corresponds to a minimum value of the pressure coefficient C_p^M monitored at the centre of a square top side and it is equivalent to the phase 12 in Lyn (1992) experiments. The streamlines and velocity vectors indicate a vortex centre behind the cylinder at $(x, y) \approx (0.9H, -0.1H)$

```
                    TURBULENCE INTENSITY
              KEY  TO  CONTUOR  VALUES
                  A      0.000E  0
                  B      0.500E -2
                  C      0.200E -1
                  D      0.600E -1
                  E      0.100E  0
                  F      0.140E  0
                  G      0.180E  0
```
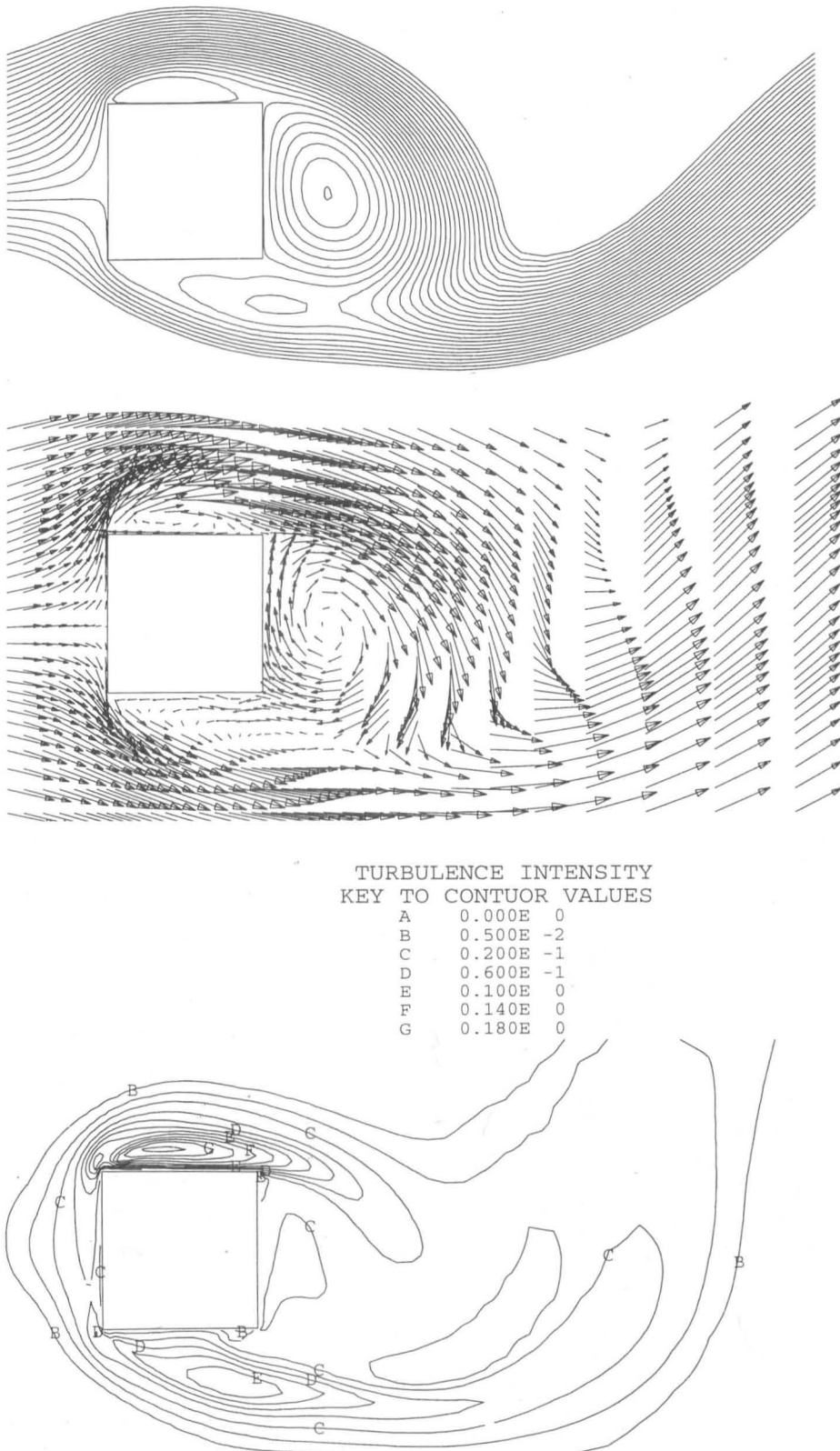
Figure 5.14: Instantaneous streamlines (top), velocity vectors (middle) and turbulent kinetic energy contours (bottom) as computed by the present $k - \epsilon$ model at the phase corresponding to the maximum C_L.

relative to the centre of a cylinder. Regarding the turbulence kinetic energy contour plots, the highest levels of k appear above the upper cylinder side, within the separated shear layer.

5.6.1   Integral parameters

In several previous numerical studies vortex shedding from a square cylinder ($Re = 20000$ or 22000) has been extensively investigated. For these studies, the employed turbulence models, wall boundary conditions and other numerical conditions are reviewed in Table 5.8. Next Table 5.9 compares the predicted and measured values of the five impor-

Authors	Model	Time scheme	Conv. scheme	Wall b.c.	Grid	$\Delta n_c/H$	$B_f, \%$
This work	SKE	EU(1st)	SMART	WF	139×122	0.014	4.17
	UKE-1	EU(1st)	SMART	WF	139×122	0.014	4.17
	RNG	EU(1st)	SMART	WF	139×122	0.014	4.17
	UKE-2	EU(1st)	SMART	WF	114×92	0.02	8.33
Deng et al. (1993a)	BL	EU(2nd)	CPI(2nd)	No slip	121×94	0.0015	1.67
Franke (1991)	DSM-1	EU(1st)	QUICK	WF	70×64	0.022	7.14
	DSM-2	EU(1st)	QUICK	2L	186×156	0.00125	7.14
Kato & Launder (1993)	KL	EU(1st)	QUICK	WF	104×70	-	7.14
Rodi et al. (1997)	LES	AB(2nd)	CDS	WF	$146 \times 146 \times 20$	-	7.14

Legend: UKE=Unsteady $k - \epsilon$, BL=Baldwin-Lomax, DSM=Differential Reynolds stress, KL=Modified $k - \epsilon$, EU=Implicit Euler, AB=Adams-Bashforth, WF=wall functions, 2L=two-layer, 1st=first order accurate, 2nd=second order accurate.

Table 5.8: Summary of computations on the turbulent vortex shedding from a square cylinder ($Re \approx 20000$): authors, turbulence models and numerical parameters.

tant bulk parameters: the Strouhal number, the mean drag coefficient, r.m.s. values of the drag and lift coefficients, and the time-mean length of the recirculation region. Compared with Table 5.1, the ranges of the measured values for St and $\overline{C}_D$ are updated to allow for the blockage effects in studies that were mentioned in Table 5.1. All predictions are broadly in agreement with each other and with the consensus of the experimental data. However, some discrepancies are obvious, most notably the overestimation of the St-number and the drag coefficient by DSM model with the two-layer near-wall approach, Franke (1991). Also, the Baldwin-Lomax model, Deng et al. (1993a), gives higher r.m.s.

Contribution	St	$\overline{C}_D$	C'_D	C'_L	$\overline{L}_r/H$
Experiments ($B_f > 1.6\%$)	0.13-0.139	2.16-2.28	0.18-0.23	1.1-1.4	0.88-1.0
Present, SKE	0.118	1.544	0.0008	0.088	2.39
Present, UKE-1	0.141	2.199	0.186	1.386	0.65
Present, RNG	0.139	2.064	0.092	1.369	0.59
Present, UKE-2	0.144	2.239	0.186	1.247	0.85
Deng et al. (1993a), BL	0.133	2.242	0.320	0.982	0.74
Franke (1991), DSM-1	0.136	2.150	-	-	0.48
Franke (1991), DSM-2	0.159	2.43	-	-	0.48
Kato & Launder (1993), KL	0.145	2.050	-	-	1.25
Rodi et al. (1997), LES	0.130	2.300	0.140	1.150	0.96

Table 5.9: Present and previous predictions and measurements of integral parameters for the turbulent flow around a square cylinder.

values for the drag and lower values for the lift force than in other studies. The present unsteady modification of the ϵ-production term produces results close to the experimental ones. For instance, for the basic computational case UKE-1, relative differences with reference to the average experimental values are *5.1, -1.0, -9.3, 10.9, and -25.7 %* for the Strouhal number, the mean drag coefficient, r.m.s. drag and lift coefficients, and the recirculation zone length, respectively. It looks that the RNG model slightly underestimates the mean and r.m.s. drag coefficients and the length of the recirculation zone. Previous comparisons found in literature did not point out the data that were corrected for the blockage effect. For example, the corrected value for $\overline{C}_D = 2.05$ from Lee's (1975) study suggested that, in general, the numerical simulations overpredicted the mean drag coefficient. Therefore, it is not surprising that LES simulations produced $\overline{C}_D$ slightly above the upper experimental values. Among all presented bulk parameters, the length of the recirculation zone behind a cylinder shows the largest variations. Computations from this study indicate its sensitivity to all numerical parameters and to the turbulence models employed. However, for the well resolved time and space computations the blockage ratio seems to have conclusive influence on the recirculation zone length. This is supported by two results: $\overline{L}_r = 0.88$ for $B_f = 7\%$, and 1.0 for $B_f = 14\%$, extracted from the measured data of Lyn (1992) and Durao et al. (1988), respectively. The present model with unsteady modification reproduces fairly well the length measured by Lyn when the solution domain implies a similar blockage ratio. For the computed case UKE-2 the relative difference is -3.9%; the LES simulations of Rodi et al. (1997) also predicts a value close to the measured one, with the difference of 9%.

5.6.2   Time–averaged distributions

Pressure coefficients distributions around the cylinder together with the centreline velocity and total fluctuating kinetic energy profiles have been already used in analysis of numerical errors. Figure 5.15 compare the predicted and measured mean and root-mean-square pressure coefficients on the cylinder's surface. The Reynolds stress model results of Franke (1991) with wall functions and LES simulations are also included. Measurements were performed at somewhat higher Reynolds numbers and with different blockages (see Table 5.1) but they are not corrected for the blockage effects. On the upstream face (AB in Figure 5.15), the mean pressure is predicted quite well by all models but significant differences exist on the other faces. These differences are within experimental
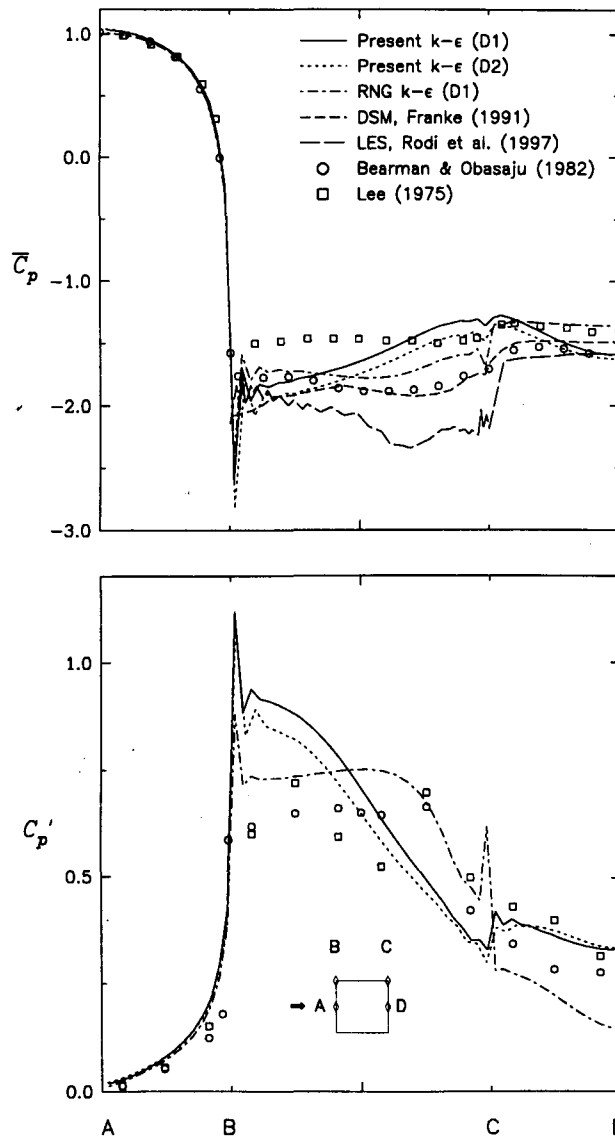
Figure 5.15: Predicted and measured time–averaged (top) and r.m.s. (bottom) pressure coefficients around a square cylinder ($Re = 20000$).

variations on the back (base) face (CD) and they cause the variations in predicted mean drag coefficients as discussed earlier. Although the present unsteady model predicts fairly well the mean drag coefficient, the mean pressure near the rear corner (C) exhibits a high maximum after which the pressure decreases faster than the data suggest. This is probably a consequence of the continuous pressure increase along the top face (BC). Clearly, the subtle experimental variation on the top face is captured fairly well by the RNG model and less successfully by the DSM model. The LES method follows the experimental trend but the mean pressure coefficient is too much underestimated along the top face. Only the present predictions of the r.m.s. pressure coefficient are compared with the measured data, Figure 5.15(bottom). Both the unsteady and RNG model predict the r.m.s. values on the upstream and back faces satisfactory. As for the mean pressure along the top face, the RNG model resembles the trend observed in Bearman and Obasaju's (1982) measurements.

Figure 5.16(top) is a plot of the time averaged streamwise velocity along the centre-line. The size of the recirculation zone downstream of the cylinder is captured quite well by the present unsteady model when the domain D2 is used, providing a similar blockage ratio as in the Lyn's (1992) experimental study. Also the LES method predicts the size of zone fairly well. The other two cases from this work (D1 and RNG) were computed with the smaller blockages and this explains somewhat shorter recirculation zones, although the RNG model under-predicts the size of zone in comparison to the present unsteady model. However, the DSM model obviously underestimates the size of the recirculation zone. Further downstream, the data of Lyn (1992) and Durao et al. (1988), both with Laser Doppler Anemometry, are significantly at variance and it is therefore difficult to assess whether either model, including LES, is successful in reproducing the correct recovery. For the specified inlet conditions, the velocity distribution in front of the cylinder seems to be influenced by the blockage effect. This is suggested by the present predictions obtained with domains D1 ($B_f = 8.33\%$) and D2 ($B_f = 4.17\%$) as well as by the measured data of Durao et al. (1988) ($B_f = 14\%$). Note that the DSM and LES results (not shown in this region by above figure) are very close to the present ones for the domain D2.

The total fluctuating kinetic energy, defined by Equation (5.4), is plotted in Figure 5.16(bottom). Upstream of the cylinder, the present unsteady $k - \epsilon$ model produces larger levels of this quantity which, as discussed in Section 5.4.2, do not cause the suppression of the vortex shedding process. Both computed cases with the unsteady model (D1 and D2), as well as the Reynolds stress model (DSM) reproduce the measured distribution fairly accurately. This is an interesting result since the DSM model under-predicts the size of the recirculation zone. The RNG model predictions are also close to the experiments, particularly in the far wake region. On the other hand, the LES method under-
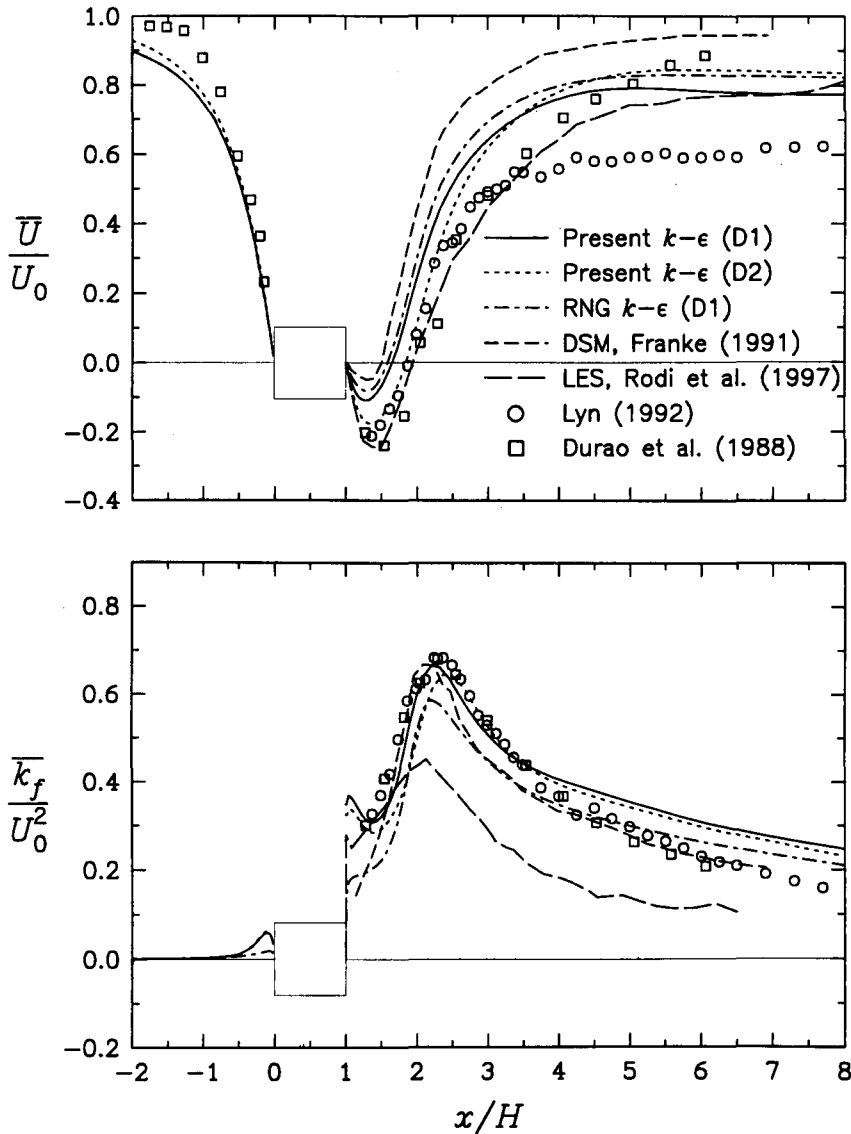
Figure 5.16: Predicted and measured time-averaged velocity (top) and total fluctuating kinetic energy (bottom) along the centreline ($Re = 20000$).

estimates considerably the total kinetic energy fluctuations. Note that both the unsteady model results and LES results exhibit similar peaks near the cylinder's back face.

The sum of apparent normal Reynolds stresses (see Equation. (5.1)) defines the fluctuating kinetic energy k_f and it is of interest to show their individual contributions to k_f, Figure 5.17. Only the predictions from this work with two $k - \epsilon$ models are displayed. Both the unsteady and RNG models underestimate the axial normal stresses which are in general much smaller than the transversal ones. The present unsteady model performs well in capturing the peak values of the measured stresses in the y direction. The results for two domains D1 and D2 indicate the blockage effect which can be used to explain variations of two experimental sets of data. The computed results for two domains show a shift between locations of peak values which is also present in the measured data for the
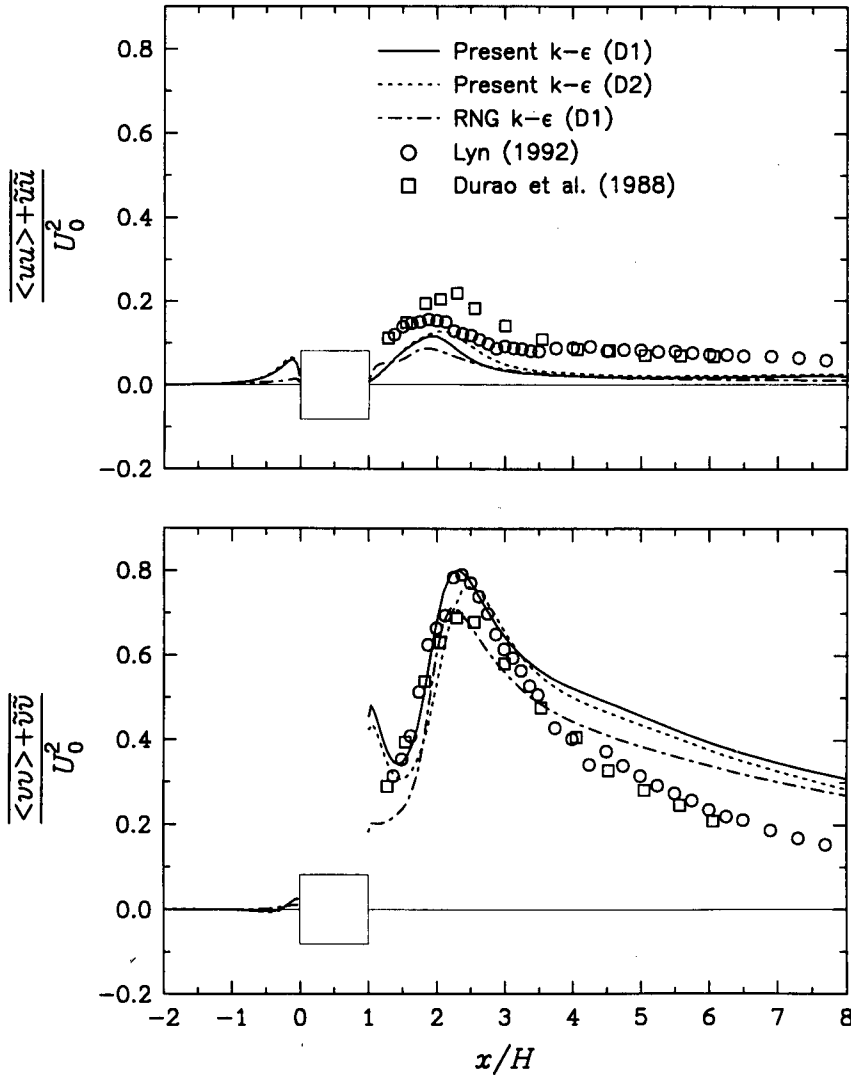
Figure 5.17: Centreline distributions of predicted and measured time-mean apparent normal Reynolds stresses in x (top) and y (bottom) directions ($Re = 20000$).

axial normal stresses.

Capabilities of the present unsteady model and RNG model can be further assessed by analysing their predictions in the shear layer region, above the top face of a square cylinder, Figure 5.18. In this figure, the results for the large domain D1 are compared with two sets of Lyn's (1992) data. The measurements were generally obtained with a two-component laser-Doppler system (two-component data denoted as 2CD in the figure), but in the near-wall region only one-component measurements (1CD) were possible. The evolution of the normal Reynolds stresses in the x direction, Figure 5.18(top), shows that the tested models fail to match the levels of the experimental normal stresses. The predicted levels are underestimated by an average factor of 3. Behaviour of the models along the first half of the face is obviously affected by levels of turbulent fluctuations transported from the stagnation region. As in the wake region, the measured levels of the total fluctuations are captured reasonably well by both models as the results for the apparent normal
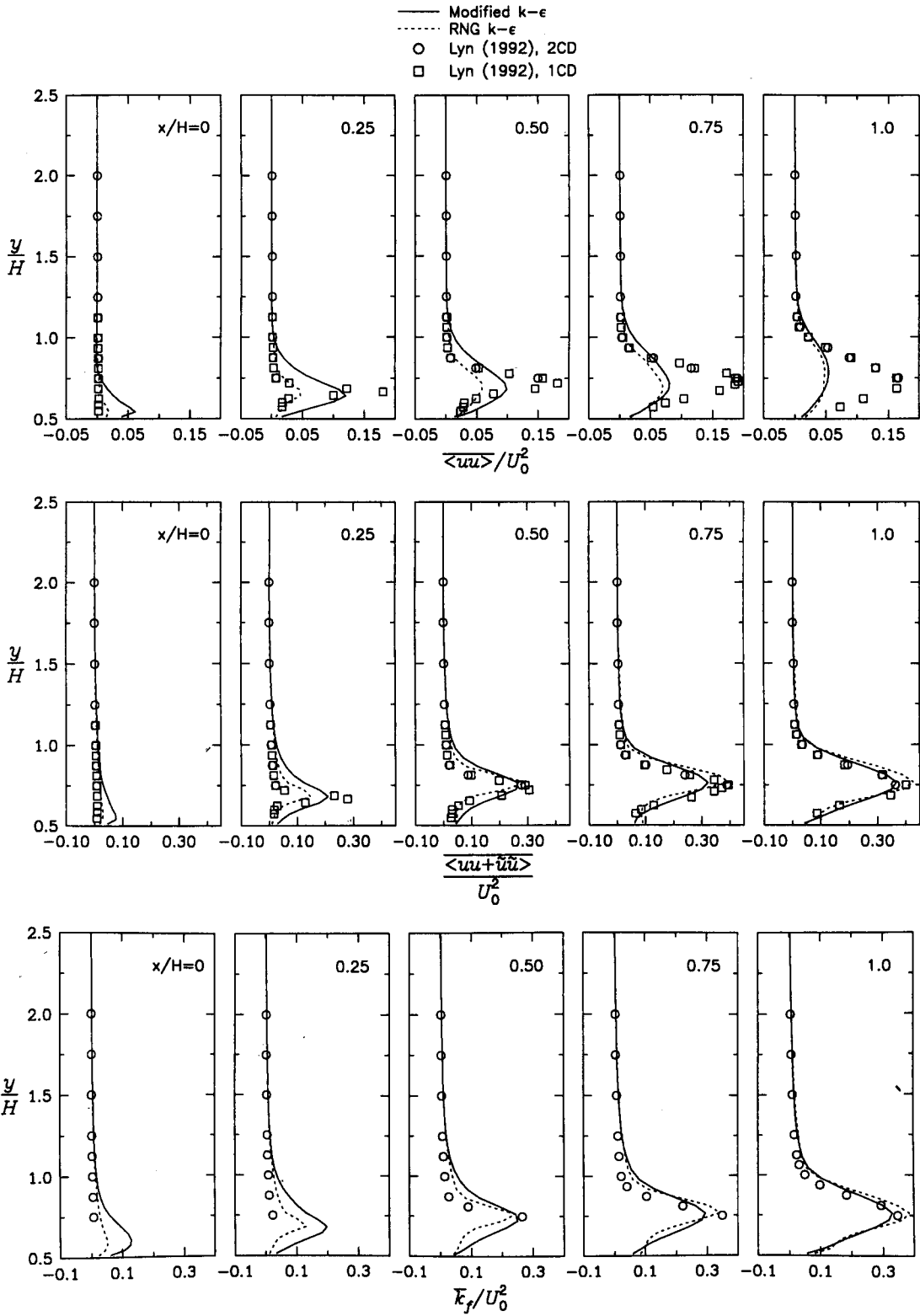
Figure 5.18: The time-averaged profiles of the Reynolds stress component $\langle u^2 \rangle$ (top), apparent component $\langle u'^2 \rangle = \langle u^2 + \tilde{u}^2 \rangle$ (middle) and global fluctuating kinetic energy k_f (bottom) at several lateral cross-sections along the upper side of a square cylinder.

stresses, Figure 5.18(middle), and the total kinetic energy, Figure 5.18(bottom), suggest.

However, more or less good results for the fluctuating energy hide the fundamental problem with current RANS and to some extent with LES methods (if we do not question the ability of experimental studies to separate accurately the stochastic and periodic fluctuations). Turning to the earlier presented Figure 5.6, it is clear that the predictions of k show too low levels of turbulent fluctuations in the near wake region (a factor of 6). Other RANS models also experience the same weakness, Franke and Rodi (1991). This means that tested RANS methods severely overestimate the periodic fluctuations. The LES results of Rodi (1997), displayed also in Figure 5.6, suggest an overall better position of the LES methods.

5.6.3   The phase-averaged results

Lyn (1992) used a pressure signal, taken from a tap at the middle of the top face of a cylinder, to obtain phase information. A typical low-pass filtered pressure signal is given in Figure 5.19(a). The computed signals in a form of the pressure coefficient C_p^M are depicted in Figure 5.19(b) as obtained by using unsteady and RNG models with the reference numerical parameters. Based on the pressure signal, Lyn (1992) defined the

(a)

(b)
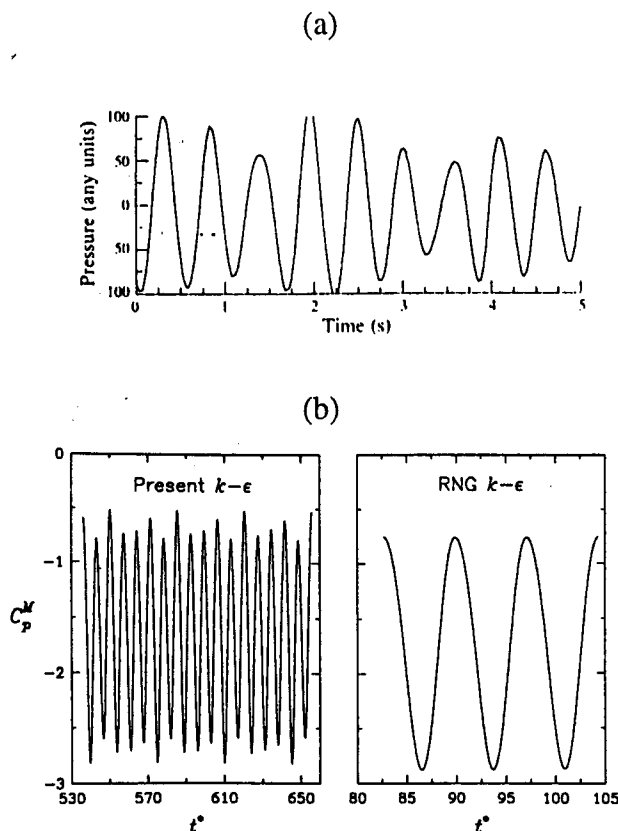
Figure 5.19: Time traces of the pressure signal monitored at the middle of the top face: (a) measurements of Lyn (1992), (b) present computations.

local period for each vortex shedding cycle using a peak-finding algorithm. Then each period was divided into 20 intervals or phase bins and the phase-averaged velocities were calculated as averages of the values sorted into corresponding phase bins. Thus, the phase 0 should correspond to the beginning of the shedding cycle (i.e. to the maximum value of the pressure coefficient C_p^M), phase 1 to $T/20$, etc. Note that in the present computations the maximum pressure coefficient at the middle of the top face is related to the minimum (negative) value of the lift coefficient. The phase-averaging procedure for the present numerical results was designed in a similar way as in the measurements. However, it has appeared that the numerical results for a particular (numerical) phase do not correspond to the measured results for that phase, probably because of the low-pass filtering of the pressure signals in experiments. Franke (1991) and Deng et al. (1993a) preferred to match their numerical and experimental results at a single phase to determine the phase shift for comparisons of the results for other phases. A similar practice is used here so that present numerical results are shifted *three phases backwards* when they are compared with the Lyn's measurements. In the following presentation of the phase-averaged results the phases are those from the measurements. The number of shedding cycles used to calculate the phase-averaged results is shown in Figure 5.19(b) (17 and 3 for the unsteady and RNG model, respectively); for another case with domain D2 seven cycles were used. With these numbers of cycles the uncertainties arising from the phase-averaging procedure are less than 1%.

Figure 5.20 presents predicted and measured distributions of the phase-averaged axial and vertical velocities along the centreline. The present predictions for two phases 1 and 9 are accompanied by the LES results for the phase 1. The comparison of the predicted results for the U-velocity component with experiments in general shows poor agreement. The velocity predicted by all models is overestimated in the far wake region. The present results for two domains D1 and D2 indicate the blockage effect in the near wake region. In this region, the predictions with the smaller domain D2 are closer to the measured values, particularly for the phase 1. For this phase, the LES results over-predict the size of the recirculation zone. By contrast, the vertical velocity profiles predicted by the $k - \epsilon$ models are in fairly good agreement with the measurements, especially in the near wake region. The zero velocity cross–points are close to those found in the experiments which is not the case if the LES results are considered. Similar results for both axial and vertical velocities were obtained by the DSM model (Franke, 1991).

Finally, Figures 5.21 and 5.22 show the phase-averaged results for the axial and vertical velocity components at five lateral cross-sections along the top cylinder's face. Three phases 1, 9 and 17 are considered. At the top of these figures, the time-averaged profiles are displayed. Clearly, both unsteady and RNG models predict the time-averaged velocity distributions fairly well and manage, varying degrees of success, to reproduce most of the
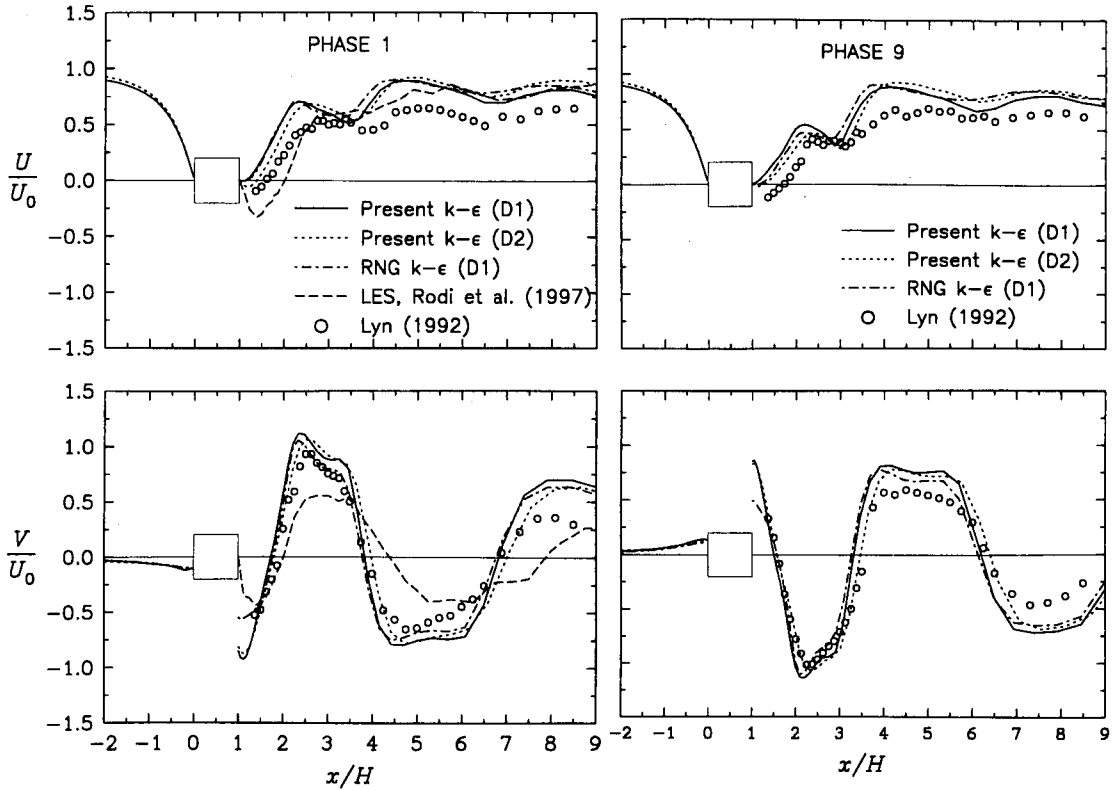
Figure 5.20: Predicted and measured phase-averaged (phases 1, 9) axial (top) and vertical (bottom) velocity profiles along the centreline ($Re = 20000$).

variations observed in the phase-averaged experimental profiles. In general, the values predicted by the RNG model seem to fall closer to the measured data.

5.7   Circular Cylinder: Results and Discussion

The turbulent flow over a circular cylinder was computed at various Reynolds numbers, ranging from 27,400 to 3.5×10^6. In this way, behaviour of the RNG and the unsteady $k - \epsilon$ models can be scrutinized against the measured integral parameters which clearly indicate different flow regimes, Figure 1.2. For each Reynolds number, the flow is computed by employing the grids specified in Table 5.10. Given there are the relative near–wall distances, the number of cells defining the cylinder surface and the total number of cells within the flow domain. Figure 5.23 shows the block–structured grid used to compute the flow at $Re = 1.4 \times 10^5$. For all the grids, the solution domain (defined in Table 5.2 as $D1$) was decomposed into three blocks.

Preliminary tests have shown the vortex shedding results to be very sensitive to the near–wall grid resolution. For this reason, it was appropriate to adopt the smallest practical values for the relative near–wall distances ($\Delta n_c/D$). This, however, would mean that for some near–wall cells the wall units Y^* (Equation (3.101)) may fall below the values for which the logarithmic velocity profile is not justified (i.e. below $Y^* < 11.6$, Sec-
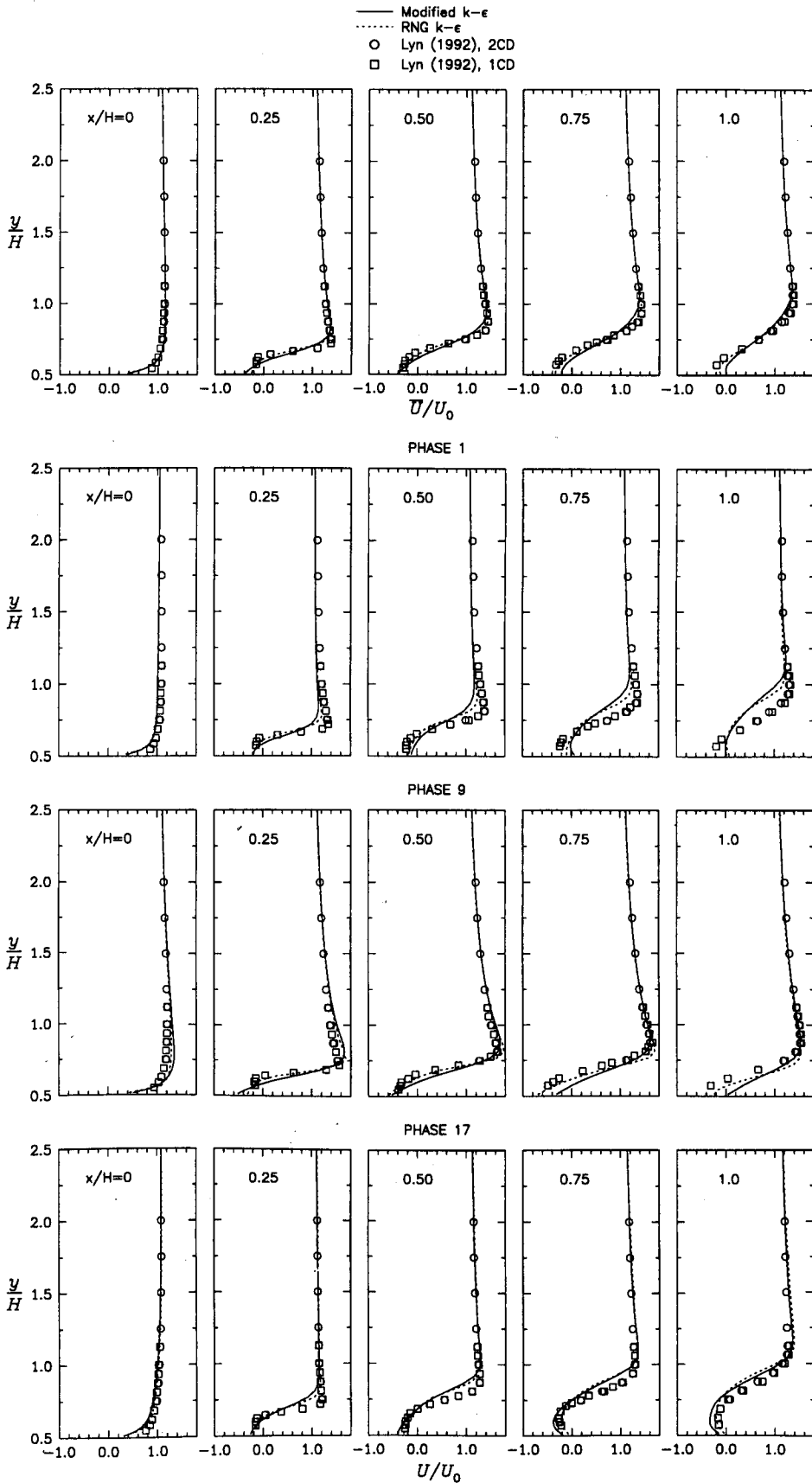
Figure 5.21: Computed and measured time-averaged and phase-averaged (phases 1, 9 and 17) axial velocity profiles at several lateral cross-sections along the top face of a square cylinder.
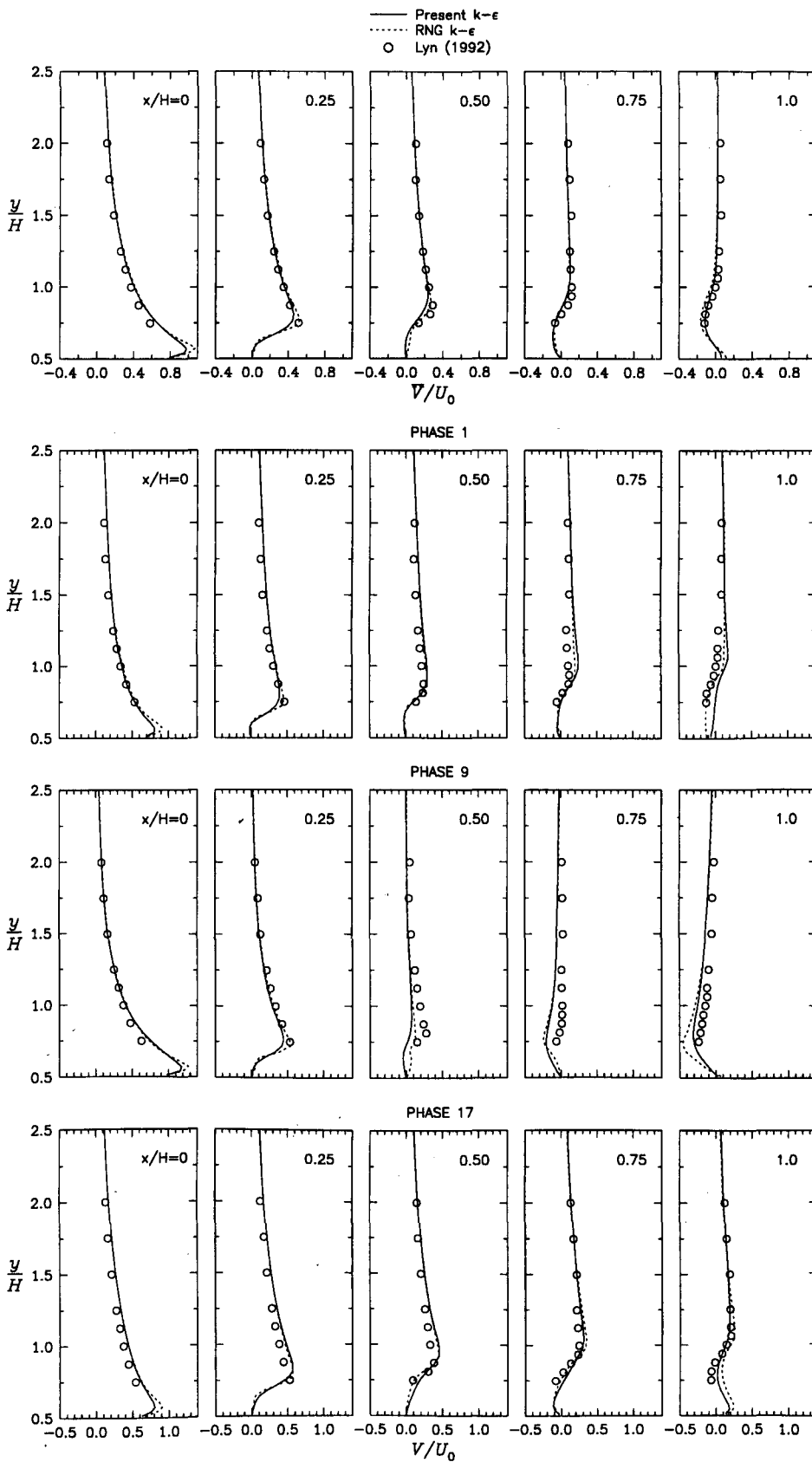
Figure 5.22: Computed and measured time-averaged and phase-averaged (phases 1, 9 and 17) lateral velocity profiles at several lateral cross-sections along the top face of a square cylinder.

tion 2.8). Note that the similar practice was employed by Hanjalic and Jakirlic (1998) in their computations of flows over backward–facing steps.
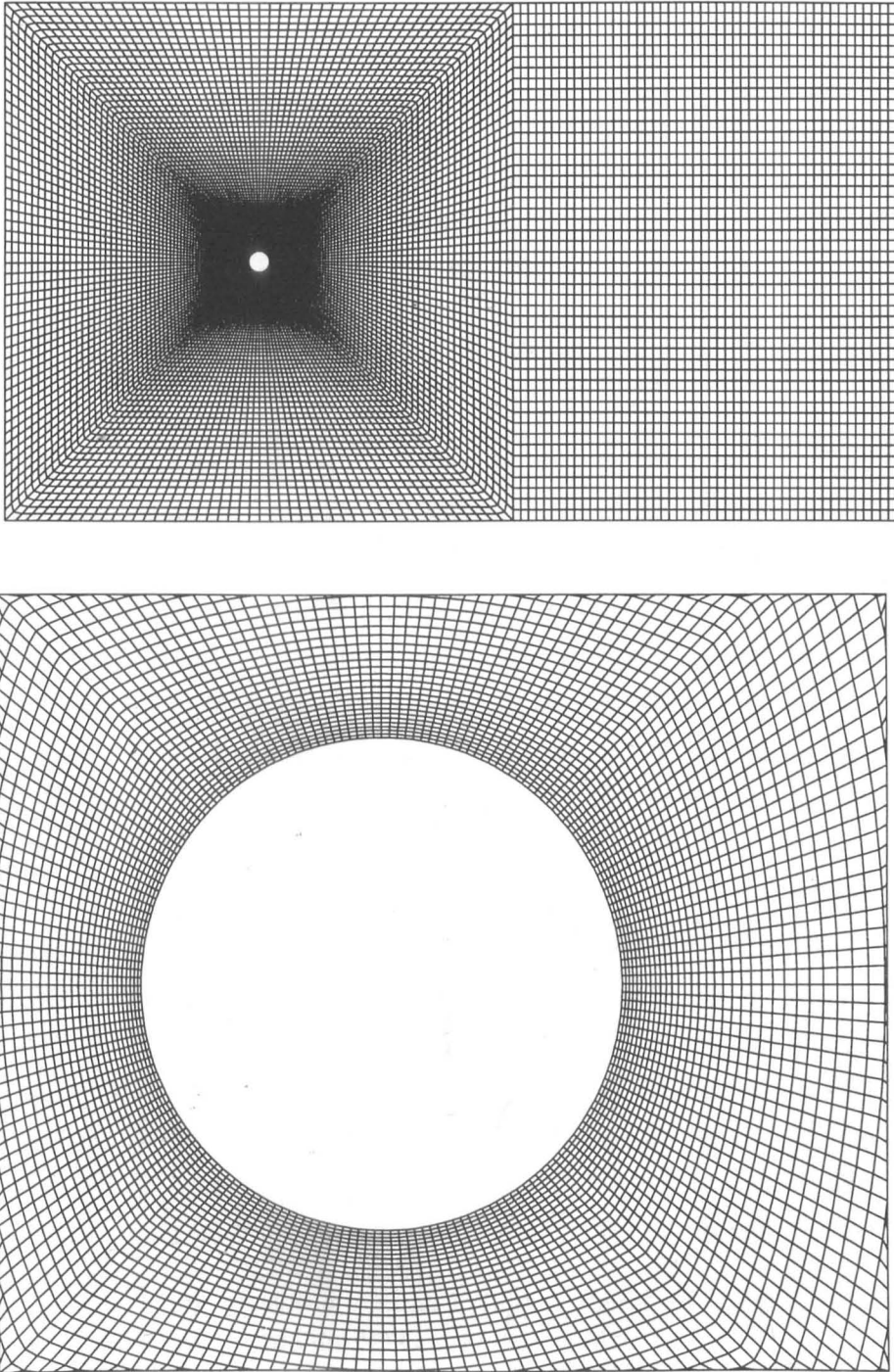
Figure 5.23: Numerical grid $G1$ used for the flow past a circular cylinder at $Re = 1.4 \times 10^5$.

Regarding the inlet conditions, profiles appropriate to 'low' turbulence levels were used. In order to ensure stable solutions when using the high–Reynolds number models,

Grid	$\Delta n_c/D$	Cells/cylinder	Active cells	Computed Re
$G0$	5.75×10^{-3}	160	14000	27400; 45000; 90000
$G1$	3.45×10^{-3}	192	20736	1.4×10^5
$G2$	1.38×10^{-3}	240	31800	5.0×10^5
$G3$	5.75×10^{-4}	288	45936	1.0×10^6; 3.5×10^6

Table 5.10: Parameters of numerical grids used to compute turbulent flows past a circular cylinder.

the following values for T_u and $(\nu_t/\nu)_0$ were chosen, respectively: 0.005 and 1. for $Re \leq 1.4 \times 10^5$, and 0.01 and 10. for $Re \geq 5.0 \times 10^5$.

(a) Unsteady $k - \epsilon$ model

Re	$\Delta t^* \times 10^3$	Y^*	St	$\overline{C}_D$	C'_D	C'_L	$\overline{\theta}_s(°)$
27 400	3.41	2-17	0.290	1.171	0.134	1.016	126.7
45 000	2.80	2-28	0.287	1.117	0.115	0.999	127.7
90 000	2.80	10-50	0.298	1.001	0.099	0.939	130.2
1.4×10^5	2.18	7-42	0.286	1.162	0.178	1.006	124.1
5.0×10^5	3.11	8-66	0.263	0.963	0.262	1.019	117.6
1.0×10^6	1.56	5-52	0.266	0.792	0.120	0.776	115.9
3.5×10^6	2.72	7-176	0.277	0.715	0.103	0.743	119.6

(b) RNG $k - \epsilon$ model

Re	$\Delta t^* \times 10^3$	Y^*	St	$\overline{C}_D$	C'_D	C'_L	$\overline{\theta}_s(°)$
27 400	3.41	2-18	0.297	0.967	0.094	0.926	125.1
45 000	2.80	2-30	0.305	0.887	0.089	0.888	127.4
90 000	2.80	3-46	0.322	0.738	0.076	0.795	131.6
1.4×10^5	1.52	3-52	0.301	0.926	0.101	0.932	125.1
5.0×10^5	3.11	5-68	0.294	0.753	0.071	0.740	116.6
1.0×10^6	0.78	5-52	0.270	0.650	0.058	0.687	119.6
3.5×10^6	1.36	3-169	0.281	0.557	0.048	0.603	122.3

Table 5.11: Turbulent flow around a circular cylinder. Predicted integral parameters as obtained with the unsteady (a) and the RNG (b) $k - \epsilon$ model.

Table 5.11 summarizes the results for the integral parameters calculated by the present and the RNG $k - \epsilon$ models. It also specifies the time–step size and the range of Y^*–values encountered in these computations. In comparison to the RNG model, the unsteady model produces consistently higher values for the force coefficients and lower values for the

Strouhal number.

The time histories of the force coefficients and the angle of separation are shown in Figure 5.24 for three values of Re: 27,400; 1.4×10^5 and 1.0×10^6.
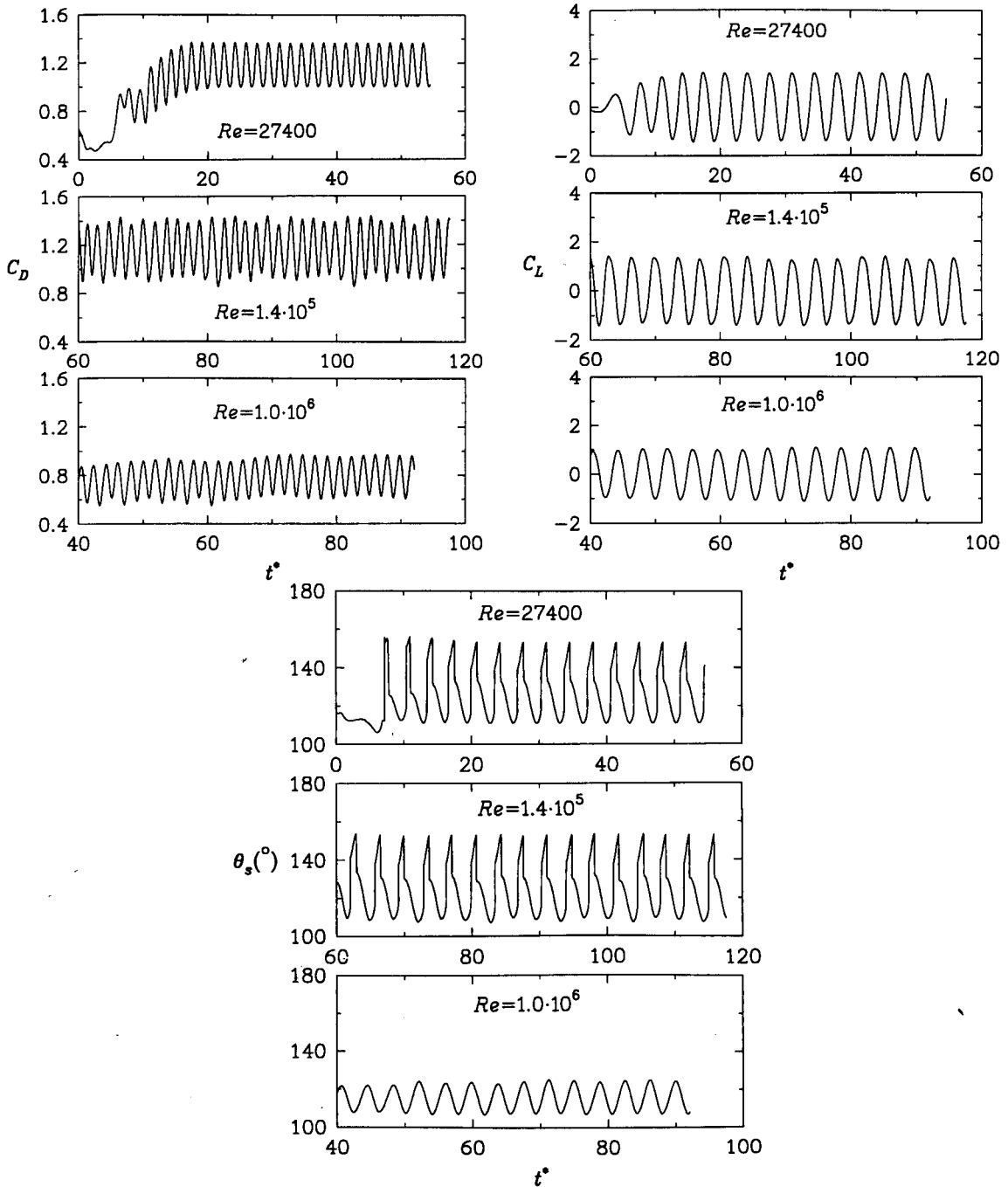
Figure 5.24: Circular cylinder. Time histories of the drag coefficient (right), the lift coefficient (left) and the separation angle (bottom) as calculated by the present $k - \epsilon$ model.

These histories illustrate that the periodic vortex shedding process is in strong evidence. In the case of subcritical regime ($Re \leq (3 - 4) \times 10^5$), the angle of separation varies

160

significantly, with maximum values up to 155°. Having in mind the experimental values of the flow separation points, the separation is delayed by up to 45° for the subcritical regime. It is fairly well predicted for the postcritical regime ($Re \geq 1.0 \times 10^6$), where data suggest $\overline{\theta}_s \approx 115 - 122°$ (Achenbach, 1968).
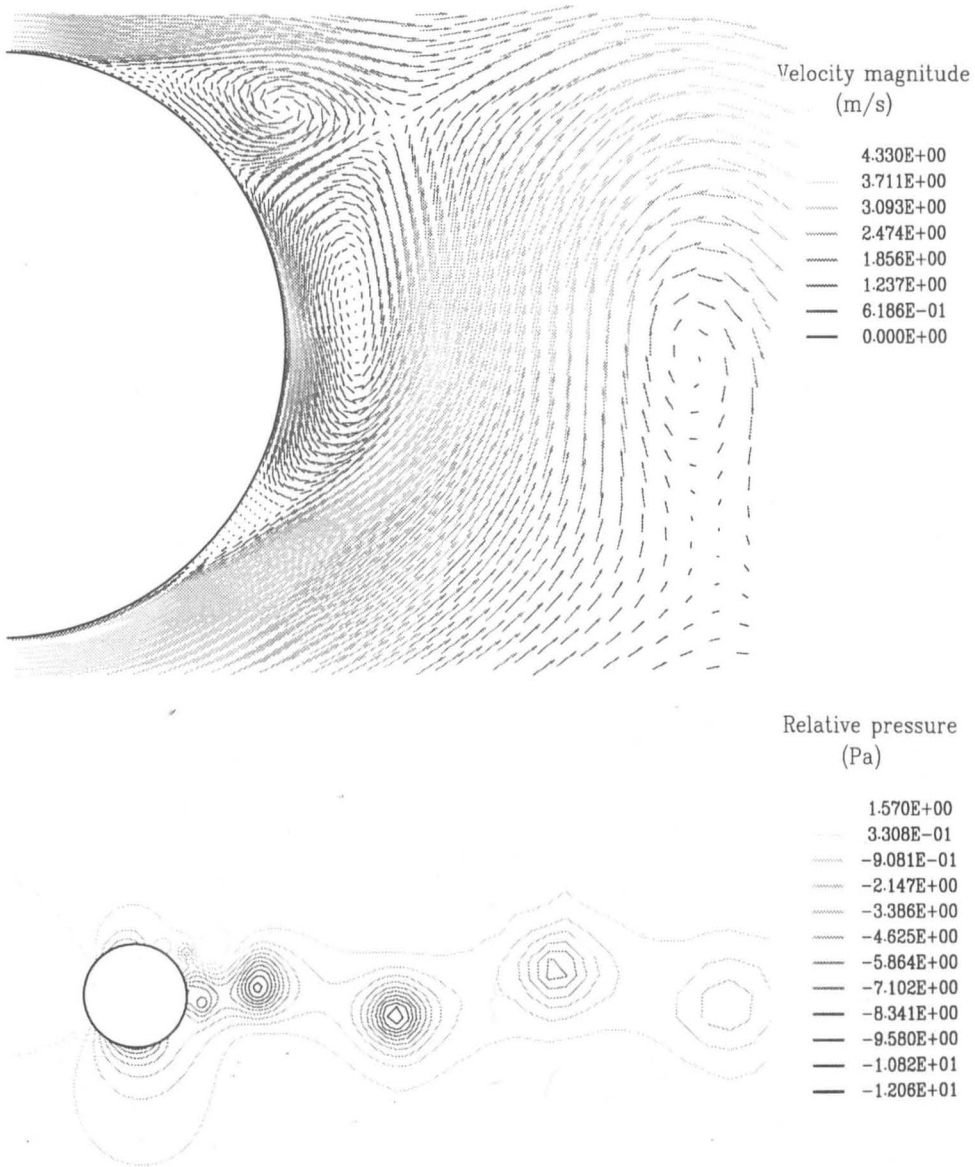
Figure 5.25: Flow past a circular cylinder at $Re = 1.4 \times 10^5$. Velocity vectors (top) and pressure contours (bottom) as computed by the unsteady $k - \epsilon$ model at $t^* = 117.6$ (minimum C_L).

Figure 5.25 gives some insight into the instantaneous near–wake flow field, which was computed at $Re = 1.4 \times 10^5$. The velocity vectors show delayed separation and the quite narrow wake. The pressure contours form a typical pattern that characterizes the vortex shedding process.
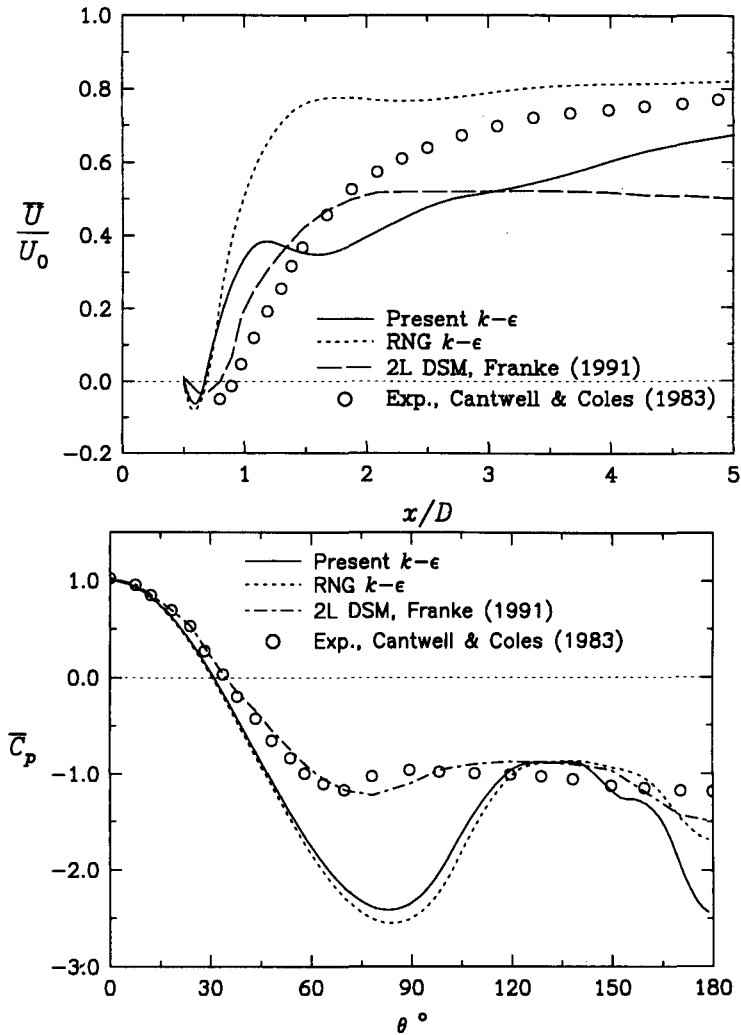
Figure 5.26: The predicted and measured time–averaged centreline velocity (top) and the wall pressure coefficient (bottom) for a circular cylinder ($Re = 1.4 \times 10^5$).

The consequences of the erroneous prediction of the flow separation for the subcritical regime are well illustrated in Figure 5.26. The figure depicts the predicted and the measured time–averaged velocities along the centreline and the wall pressure coefficients, all obtained at $Re = 1.4 \times 10^5$. The tested $k - \epsilon$ models produce much shorter time–averaged recirculation zones than the experiments suggest. Distributions of the pressure coefficient also indicate failure of these models to match the measured data. Much better results were obtained by Franke (1991) who employed the differential Reynolds stress transport equation model with the two–layer near-wall treatment. However, Franke improved the prediction of the flow separation by switching off the turbulence model upstream of the experimental separation point. It is interesting that the present pressure distributions give reasonable values for the mean drag coefficient, Figure 5.28. Obviously, details of the pressure distributions are such that 'cancellation of the errors' takes place.

The principal assumptions behind high–Reynolds number models are more likely to
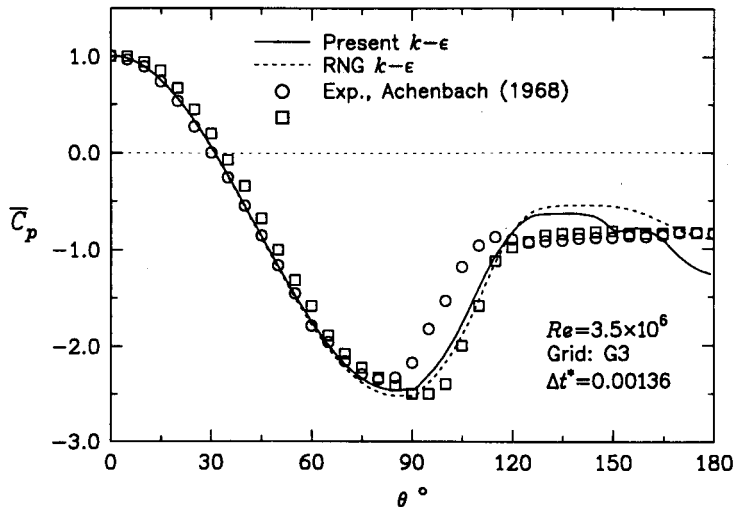
Figure 5.27: Predicted and measured time–averaged wall pressure coefficient for a circular cylinder ($Re = 3.5 \times 10^6$).

be valid for the postcritical flow regime. This is illustrated by Figure 5.27 which displays the time–averaged wall pressure coefficient computed by the UKE and RNG models at $Re = 3.5 \times 10^6$. There is satisfactory agreement with experiments of Achenbach (1968) obtained at $Re = 3.6 \times 10^6$.

In Figure 5.28, the present results for the mean drag coefficient and the Strouhal number are compared with the measured data and with data from other numerical studies. In the subcritical regime, the drag coefficient is underpredicted by the tested $k - \epsilon$ models as well as by the Baldwin–Lomax model employed by Deng et al. (1993b). The same models over-predict the drag in the critical regime so that the drag crisis is not reproduced. The Strouhal number does not exhibit large changes and it varies between 0.25 and 0.30. The two–layer DSM model used by Franke (1991) at $Re = 1.4 \times 10^5$ predicts fairly well the Strouhal number but overpredicts the drag. The two–dimensional LES predictions of Song and Yuan (1990) agree well with the measurements. Note that they introduced many ad hoc assumptions, see Section 1.3.2. In that section, the computations of Tamura et al. (1990) are also reviewed. Their three-dimensional quasi–LES results (i.e. without a turbulence model being used) seem to reproduce the drag behaviour quite well. Unfortunately, the Strouhal number values were not reported.

5.8 Closure

In this chapter, the $k - \epsilon$ eddy–viscosity models described in Chapter 2, were applied to vortex shedding flows from single square and circular cylinders.

The inability of most of the tested models (the standard, RNG and PDM modification) to reproduce the proper levels of the normal Reynolds stresses in the stagnation flow
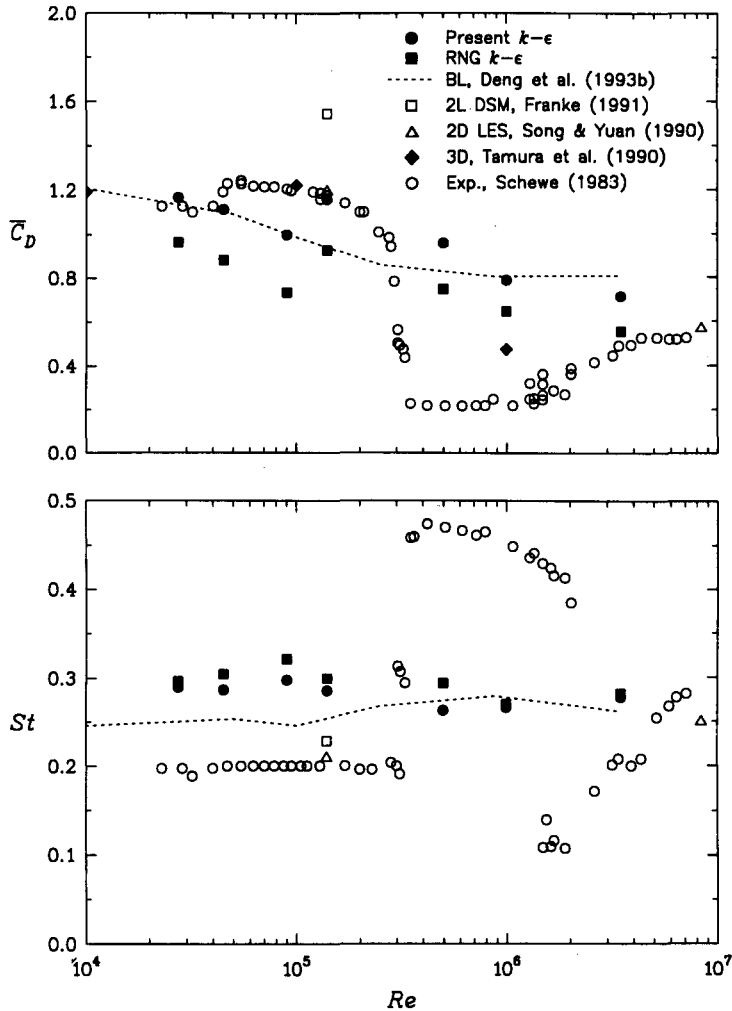
Figure 5.28: Turbulent flow around a circular cylinder. Comparison of the computed mean drag coefficient (top) and the Strouhal number (bottom) with others.

region was demonstrated. For this, experimental data for the flow approaching a circular cylinder at $Re = 27,400$ were used as a benchmark. Only the $k - \epsilon$ model with a new definition of the turbulent time scale (T_ω, Equation (2.50)) predicted the normal stresses in agreement with measurements. This definition was specifically devised for the stagnation flow region, where the normal stresses govern the production of the turbulent kinetic energy. Although encouraging vortex shedding results were obtained, it needs first further improvements and testing in other steady flow regions.

In spite of the incorrect behaviour in the stagnation region, the $k - \epsilon$ models were able to capture the vortex shedding process itself. This was evident after preliminary tests for the case of a square cylinder at $Re = 20,000$. While predictions by the RNG, PDM and unsteady model were satisfactory, the standard model produced much higher levels of k and the turbulent eddy–viscosity, which adversely affected the strength of the vortex shedding process. As a result, the mean drag coefficient was predicted too low and the amplitudes of both the lift and drag coefficients were grossly underestimated. This

renders the standard model inapplicable to flows past square and circular cylinders. The preferential dissipation modification (PDM) to the standard model was quite sensitive to its model constants. Thus, subsequent computations were done by using the RNG and the present unsteady $k - \epsilon$ model.

Before detailed verification of the selected models, the numerical uncertainties for the present computations have been specifically addressed for the vortex shedding from a square cylinder at $Re = 20,000$. The unsteady $k - \epsilon$ model was employed for most computed cases. Grid and time–step refinement tests were carried out in conjunction with the SMART convective scheme. The effects of alternative schemes, as well as of the blockage, were also assessed. In summary, the Strouhal number, the mean drag coefficient and its root–mean–square value increased with better spatial and time resolutions, while the length of the recirculation zone behind the cylinder was reduced. A similar trend was experienced when the blockage effect increased, with the exception that now the recirculation zone became longer. Regarding the r.m.s. lift coefficient, its values were reduced for smaller time-step sizes and for higher blockages. The opposite situation appeared when fine grids were used. The numerical uncertainties for the integral parameters were quantified for the reference numerical parameters and presented in Table 5.7. With regard to the near–wall grid resolution, the unsteady model was not too sensitive to the relative near–wall distances $\Delta n_c/H$, i.e. to the non–dimensional wall units Y^*. The opposite behaviour has characterized the RNG model and this model can severely underestimate the drag coefficient if the near–wall zone is not resolved well in terms of Y^*.

The well–documented measurements (Lyn, 1992; Bearman and Obasaju, 1982; Lee, 1975) were used to validate the present unsteady modification and RNG model for the flow over a square cylinder at $Re = 20,000$. It was found that these models produce *acceptable* results for integral parameters and for most of the time–averaged and phase–averaged flow quantities. However, there is a fundamental problem with the RANS methods, particularly in the wake region. This was first recognized by Franke and Rodi (1991) after using the Reynolds stress transport model. That model, and the $k - \epsilon$ models employed in this study, simulate the total fluctuations correctly but at the expense of considerably overestimated periodic fluctuations and underestimated turbulent fluctuations. In this respect, the LES results of Rodi (1997) and Rodi et al. (1997) indicate more realistic predictions of the turbulent kinetic energy (Figure 5.6) although the total fluctuating energy is still underpredicted (Figure 5.16).

The principal shortcomings of the $k - \epsilon$ models (and other Reynolds stress models) are exposed by the results for the flow past a circular cylinder. These high Reynolds–number models, used in conjunction with the wall functions, fail to predict correctly the boundary layer separation from a smooth surface such as a circular cylinder. This failure can be

expected for $Re < 1.0 \times 10^6$, i.e. for the subcritical, critical and supercritical regimes, where the boundary layers are still laminar before separation. The use of high Reynolds number models implies the turbulent boundary layers and strong mixing, which shifts the separation point considerably downstream. Thus, the wrong prediction of the separation points leads to erroneous vortex shedding results. In the postcritical regime, the boundary layers before separation are fully turbulent, and the separation is predicted fairly well. Consequently, the mean drag coefficient and the Strouhal number show better agreement with the experimental data.

Chapter 6

CLOSURE

The present study was intended to determine what can and cannot be achieved in the numerical modelling of vortex shedding flows from two–dimensional square and circular cylinders by using the two–dimensional finite volume method. Both laminar and turbulent flows were considered, the latter simulated by the $k - \epsilon$ models used in conjunction with the wall function approach. The outcome of this work has been already described in concluding sections of each chapter. This chapter summarizes the present study and its achievements in the light of the initial objectives and outlines suggestions for future work.

6.1 Summary and Achievements

1) The finite volume method for unsteady flows

The first objective was to develop the second order accurate finite volume flow solver for incompressible, steady and unsteady flows. In the present solver, the vector and tensor quantities in the governing equations are defined in terms of Cartesian components. These equations are solved on non–orthogonal curvilinear grids, arranged in a structured or block–structured fashion. Temporal discretisation is the implicit, first–order accurate Euler. Spatial discretisation is by choice of first– (UDS) and higher–order accurate unbounded (CDS, LUDS and QUICK) and bounded schemes (MINMOD, SMART). The high Reynolds–number $k - \epsilon$ models are implemented; the assumption being that the flow under consideration is everywhere turbulent. Thus, no laminar–turbulence transition is allowed and the wall function approach is used to bridge the near–wall region.

2) Numerical uncertainties

For both laminar and turbulent simulations, attention was focused on the numerical uncertainties arising from spatial and temporal discretisation and from the size of the solution

domain (the blockage effect). These uncertainties were quantified for some cases, i.e. for laminar and turbulent vortex shedding from a square cylinder (see Table 4.10 and Table 5.7). It emerged, particularly in laminar flow situations, that the blockage effect very often cancels errors due to space and time discretisation. Several alternative schemes for convection were evaluated for their performance in laminar vortex shedding conditions. With regard to their accuracy and boundedness, the bounded and formally third–order accurate SMART scheme was used for the majority of the present predictions.

3) Validation for unsteady laminar flows

The present finite-volume method has been validated against experimental and other numerical data for vortex shedding encountered in various (laminar) flow configurations. The principal comparisons were with integral vortex shedding parameters such as the Strouhal number, averaged and root-mean-square drag and lift coefficients, and other force coefficients specific to some investigated flow cases. Careful literature review was carried out to identify suitable experimental and numerical results which were all then included in the comparisons. The outcome of comparisons were in all cases either on par or better than those obtained with alternative CFD methods. This conclusion is supported by the following figures related to:

1. Uniform flow around a square cylinder: Figure 4.26;

2. Uniform flow around a circular cylinder: Figures 4.28, 4.29, and 4.30;

3. Uniform flow past two circular cylinders in tandem: Figure 4.33;

4. Pure oscillatory flow around a circular cylinder: Figure 4.36;

5. Combined oscillatory flow with steady current past a circular cylinder: Figure 4.38.

In addition, Table 4.13 (related to the computation of vortex shedding from a circular cylinder) proves the capability of the present method to produce very accurate results, in this case for truly laminar vortex shedding.

4) Physical aspects of laminar vortex shedding

Some physical aspects of the periodic vortex shedding process were analysed for the case of a circular cylinder at $Re = 105$. The overall process was divided into three stages: (i) initiation, (ii) development, and (iii) developed stage. For the present method, there is no need to perturb the initial (uniform) velocity field. It was concluded that the magnitudes of vortex shedding quantities for the established (periodic) vortex shedding should not

depend on the nature of initial disturbances. When a fully periodic vortex shedding flow is established, all the flow parameters fluctuate periodically around their mean values, while the mean lift coefficient becomes zero. The period of oscillation of the drag coefficient is exactly one half that of the lift coefficient. The vortex formation process was analysed in terms of streamlines and separatrices, Figure 4.10.

For single cylinders, submerged in a uniform stream, the flow features depend on the Reynolds number. This dependence, expressed through the mean drag and Strouhal number, was accurately reproduced in the present simulations for Re–numbers below $Re_c^{3d} \approx 200$. Above this number, the three–dimensionality occurs in experimental flows. In regard to this, the limitations and reliability of the two–dimensional simulations were discussed (see Figure 4.30). In other flow configurations, the effects of Reynolds number and additional factors (i.e. the cylinders' spacing ratio for two cylinders in tandem and Kc–number and the velocity ratio U_r for oscillatory flows) were also reproduced in accordance with other numerical studies and/or experimental data.

5) Development of a turbulence model

The important issue of how to model the turbulence in the presence of organized mean–flow periodicity was addressed and a modification to the standard $k - \epsilon$ model was proposed. This modification is based on Younis' idea (Younis, 1988). It was also influenced by Lumley's proposal (Lumley, 1992) who introduced a transport equation for the inverse time scale which was used to calculate the production term of the dissipation rate ϵ. Instead of solving such an equation, the present work introduces the time scale of periodic motion and formulates an overall inverse time scale as a linear combination of the inverse values of the turbulent time scale (k/ϵ) and the periodic time scale. In addition, the modifications that can improve on the predictions of conventional $k - \epsilon$ models, in particular in the stagnation flow region, were considered. After preliminary tests, none of these modifications performed better than the RNG $k - \epsilon$ model, if the latter is used with a sufficiently fine mesh.

6) Validation of the $k - \epsilon$ models

The new, unsteady, model and the RNG model were validated against data for the vortex shedding flows from a square and circular cylinders. In the case of a square cylinder, both models produced acceptable results. In many aspects, the unsteady flow features were reproduced either on par or better than those obtained by other models or with LES methods. The support for this is given in the following table and figures which present:

- Integral vortex shedding parameters: Table 5.9;

- Time–averaged and r.m.s. pressure coefficient distribution along the wall: Figure 5.15;

- Time–averaged centreline velocity and total fluctuating kinetic energy: Figure 5.16;

- Phase–averaged centreline velocity components: Figure 5.20.

Generally successful simulations in the case of a square cylinder can be attributed to the fact that the flow is turbulent before separation, which is , in addition, imposed by the geometry itself, i.e. by the upstream corners. For a circular cylinder, the high Reynolds–number turbulence models cannot cope with transition from laminar to turbulent conditions. This inability adversely leads to wrong predictions of the flow separation points for a wide range of Reynolds numbers ($Re < 10^6$) and the overall results are consequently not satisfactory. Realistic predictions characterize the postcritical flow regime ($Re \geq 10^6$) where the flow is turbulent before separation.

6.2 Future Research

This study has shown that CFD is a powerful and reliable tool for understanding the nature of vortex shedding flows. In order to improve the accuracy of vortex shedding results, fruitful research may be conducted in the following areas:

- Provision of the second–order accurate time discretisation scheme (eg. a three time level implicit scheme).

- Use of 3D simulations since 3D effects cannot be reproduced in 2D calculations.

- Assessment of the $k - \epsilon$ models with the non–linear stress–strain relationship and Reynolds–stress transport closures.

- Alternative treatment of the near-wall region. This may be done by employing some existing low-Reynolds number models (eg. Hanjalic et al., 1997) or by relaxing the 'fully–turbulent flow' assumption and the logarithmic law of the wall invoked in wall functions. The latter should allow for the slope and intercept of the log–law to adjust according to the local state of the flow (Younis, 1998).

- New modelling practices for unsteady flows dominated by organized (periodic) flow structures.

Appendix A

Previous Numerical Studies

Author(s) & year	Reynolds numbers	Numerical method and formulation	Remarks
Davis and Moore (1982)	100–2800	2D–FV–PV	The QUICKEST scheme was used for the spatial and temporal discretisation.
Younis (1988)	250–2800	2D–FV–PV	Good results for laminar flows (Linear-Upwind scheme was used).
Pereira and Durst (1988)	250, 500	2D–FV–PV	Among various convective schemes only the QUICK yielded the reliable results.
Franke (1991)	40–300	2D–FV–PV	Satisfactory results for St and $\overline{C}_D$; a second vortex shedding frequency was found at $Re \geq 250$.
Arnal et al. (1991)	100, 500, 1000	2D–FV–PV	Additional frequencies at $Re \geq 500$.
Carey et al. (1992)	500	2D–FV–PV	A new skew-upwind corner convective scheme was able to sustain vortex shedding.
Kim and Benson (1992)	190	2D–FV–PV	SMAC, PISO and ITA temporal schemes produced similar results.
Kelkar and Patankar (1992)	40–100	2D–FV–PV	Unsteady flow was risen by the linear stability analysis of a steady flow.
Ramaswamy and Jue (1992)	250	2D–FE–PV	The time history of C_D shows cycle-to-cycle variations (additional frequencies).
Okajima et al. (1992)	1000, 4000, 7000	2D–FV–PV	Laminar flow results compare well with experiments.
Mukhopadhyay et al. (1992)	60-800	2D-FV-PV	The St-number was computed for a cylinder in a channel (blockage 12.5%).
Suzuki et al. (1993)	70–250	2D–FD–PV	The St-number results are close to Okajima's data (1982) for $Re \leq 150$.
Nakamura et al. (1993)	100	2D–FD–PV	The effects of four outflow boundary conditions were investigated.
Hwang and Yao (1997)	500, 1000, 1500	2D-FV-PV	Ground effects for a cylinder in a laminar boundary layer were analysed.
Sohankar et al. (1997)	45-250	2D-FV-PV	Strong influence of numerical parameters on the results was found.

Table A.1: Summary of two-dimensional numerical simulations of nominally laminar flows around a square cylinder (FD-finite difference, FE-finite element, FV-finite volume, PV-pressure-velocity).

Author(s) & year	Reynolds numbers	Numerical method and formulation	Remarks
Gresho et al. (1984)	25 – 400	2D–FE–PV	St and $\overline{C}_D$ were higher than experimental data.
Borthwick (1986)	40 – 400	2D–FD– ω, ψ	Two differencing schemes were compared.
Braza et al. (1986)	100, 200, 1000	2D–FV–PV	Secondary vortices were identified and analyzed.
Eaton (1987)	110	2D–FE–PV	Analysis of streamlines and streaklines.
Lecointe and Piquet (1984, 1989)	140 – 2000	2D–FD– ω, ψ	St-numbers were slightly overpredicted for $Re > 200$.
Karniadakis and Triantafyllou (1989)	40 – 250	2D–SE–PV	A continuous variation of St with Re.
Franke (1991)	50 – 5000	2D–FV–PV	St and $\overline{C}_D$ agree well with the experiments for $Re < 1000$.
Engelman and Jamnia (1990)	100	2D–FE–PV	The grid-converged results were obtained.
Sa and Chang (1991)	50–200	2D–FD– ω, ψ	St and $\overline{C}_D$ are lower than experimental data.
Li et al. (1991)	< 500	2D–FE–PV	Large time steps were used ($\Delta t^* = 0.1 - 0.3$) with the Crank-Nicolson temporal scheme.
Behr et al. (1991)	100	2D–FE– ω, ψ	The effect of the outflow boundary location was examined.
Ji and Wang (1991)	40, 70	3D–FD–PV	3–D simulations were done using the QUICK convective scheme.
Wang and Dalton (1991a)	102, 140, 200	2D–FD– ω, ψ	Impulsively started and decelerated flows were computed.
Karniadakis and Triantafyllou (1992)	up to 500	3D–SE–PV	The wake velocity fluctuations indicate a transition to turbulence at $Re = 500$.
Rosenfeld (1994)	200	2D–FV–PV	A grid refinement study was conducted on four meshes up to 513×513 points.
Behr et al. (1995)	100	2D–FE–PV	The influence of the placement of lateral boundaries on the vortex shedding results was investigated.
Henderson (1995)	25–1000	2D–SE	The drag and base pressure coefficients were presented emphasizing the distinct change from a steady to unsteady wake.
Mittal and Balachandar (1995)	525	2D & 3D–SE	The effect of three-dimensionality on the lift and drag was investigated.
Zhang et al. (1995)	40–300	2D & 3D–FD–PV	In 3D, four different instabilities were found for $Re = 160 - 230$, each leading to different transition scenarios.

Table A.2: Summary of numerical simulations of the nominally laminar flows around a circular cylinder (FD-finite difference, FE-finite element, FV-finite volume, SE-spectral element, PV-pressure-velocity).

Author(s) & year	Reynolds numbers	Numerical method	Turbulence modelling & comments
Majumdar and Rodi (1985)	10^5, 1.4×10^5, 3.6×10^6	2D–FV–PV	Standard $k - \epsilon$+WF & Steady flow; at $Re \leq 1.4 \times 10^5$, μ_t was effective only in the separated flow region.
Stansby and Smith (1989)	3.6×10^6	2D–RV–ω, ψ	Algebraic Baldwin–Lomax & Artificial vortex decay was used to improve the results.
Tamura et al. (1990)	10^3, 10^4, 10^5, 10^6	2D&3D–FD–PV	None. & The 'drag crisis' was successfully simulated by 3D simulations.
Song and Yuan (1990)	1.4×10^5, 8.4×10^6	2D–FV–PV	Pseudo LES, Smagorinsky subgrid model & The use of several ad hoc assumptions produced satisfactory results.
Braza et al. (1990, 1992)	$2 \times 10^3 -$ 3×10^4	2D–FV–PV	None. & Frequencies of transition waves in the separated shear layers were in good agreement with experiments.
Franke (1991)	1.4×10^5	2D–FV–PV	Two-layer $k - \epsilon$ and Reynolds-stress transport models & Generally poor results; the turbulence models were switched on after the separation point.
Dawes (1992)	4000	2D–FV–PV	Low–Re Lam–Bremhorst $k - \epsilon$ & Simulations on both fixed and adapted unstructured grids yielded the correct St–number (0.20).
Kondo (1993)	10^5, 10^6	2D–FE–PV	None. & Similar values of $\overline{C}_D$ as obtained by Tamura et al. (1990) in 2D calculations.
Kakuda and Tosaka (1993)	10^4, 10^5, 5×10^5, 10^6, 10^7	2D–FE– PV	None. & The results for $\overline{C}_D$ agree well with similar calculations of other authors (Tamura et al., 1990, Kondo, 1993).
Deng et al. (1993b)	$6 \times 10^3 -$ 3.6×10^6	2D–FV–PV	Algebraic Baldwin-Lomax and Low–Re $k - \epsilon$ models. & None of the turbulence models produced satisfactory results.
Orszag et al. (1993)	$14{,}500$	2D–PV	Low–Re RNG $k - \epsilon$ & At this Re–number, the model was capable to predict vortex shedding correctly ($St = 0.185$ is close to the experimental value of 0.19).

Table A.3: Summary of previous numerical simulations of turbulent flows past a circular cylinder (FD-finite difference, FE-finite element, FV-finite volume, RV-random vortex, PV-pressure-velocity).

Author(s) & year	Reynolds numbers	Numerical method	Turbulence modelling & comments
Sarpkaya and Ihrig (1986)	20,000	2D–RV	None. & Amplitudes of C_D and C_L were too high but the St-number was correctly predicted.
Younis (1988)	3×10^3, 8×10^3, 1.4×10^4	2D–FV–PV	$k - \epsilon$+WF. & An unsteady modification of the dissipation rate source was proposed.
Tamura and Kuwahara (1990)	10,000	2D&3D–FD–PV	None. & The 3D-results for the drag and lift and St-number are closer to the experimental values than 2D-results.
Hadid et al. (1991)	14,000	2D–FV–PV	Nonlinear $k - \epsilon$+WF. & Slightly improved predictions when compared to the standard $k - \epsilon$ model.
Franke (1991)	22,000	2D-FV-PV	Standard $k - \epsilon$ and Reynolds-stress transport models with the WF or two-layer approach. & The Reynolds-stress transport model yielded relatively good results; the periodic fluctuating motion was overpredicted.
Deng et al. (1993a,b)	22,000	2D-FV–PV	Algebraic Baldwin–Lomax. & Successful results have been obtained with this simple model.
Kato and Launder (1993)	22,000	2D–FV–PV	Standard $k - \epsilon$+WF, modified production of k. & The proposed modification gives predictions similar to that obtained by the Reynolds-stress transport model, Franke (1991).
Frank and Mauch (1993)	40,000	3D–FV–PV	LES. & A bit higher St-number than the experimental one was obtained.
Sakamoto et al. (1993) (also Murakami and Mochida, 1995)	10^5	2D&3D–FV–PV	LES, Smagorinsky subgrid model. & Truly LES predictions are in good agreement with experiments. The differences between 2D and 3D simulations are clarified.
Murakami and Mochida (1995)	22,000	3D–FV–PV	LES, Smagorinsky subgrid model. & The results on the grid with $104 \times 69 \times 10$ nodes show good agreement with experiments of Lyn (1992).
Benodekar et al. (1994)	14,000	2D–FV–PV (STAR–CD)	Standard and RNG $k - \epsilon$ + WF. & Only the RNG model produced closer agreement with data of Durao et al. (1988).
Bosch and Rodi (1996)	22,000	2D–FV–PV	$k - \epsilon$+WF, Kato and Launder (1993) modification. & Reasonable good predictions were obtained for a cylinder in the presence of an adjacent wall, including the case without the wall.

Table A.4: Summary of previous numerical simulations of turbulent flows past a square cylinder (FD-finite difference, FV-finite volume, RV-random vortex, PV-pressure-velocity).

Appendix B

Richardson Error Estimator

For the exact solution Φ_0, one can assume series expansion around the approximate discrete solution Φ_1 as (Roache, 1994):

$$\Phi_0 = \Phi_1 + a_1 h + a_2 h^2 + a_3 h^3 + \cdots , \tag{B.1}$$

where h is a characteristic discretisation parameter, and $a_1, a_2, a_3, \ldots$ are functions that do not depend on the parameter h. Then Richardson extrapolation for the ϖ–th order accurate discretisation method is based on a calculation of two numerical solutions Φ_1 and Φ_2 with different discretisation parameters h_1 and h_2. Elimination of the coefficient a_ϖ of the leading order terms leads to the generalized Richardson extrapolation:

$$\Phi_0 \approx \Phi_1 + \frac{\Phi_1 - \Phi_2}{r^\varpi - 1} , \tag{B.2}$$

$$r = \frac{h_2}{h_1}. \tag{B.3}$$

The Actual Fractional Error of the fine solution Φ_1 is defined as:

$$A_1 = \frac{\Phi_1 - \Phi_0}{\Phi_0} . \tag{B.4}$$

It can be shown (Roache, 1994) that an Estimated Fractional Error for the fine solution, derived from Equation (B.2) as:

$$E_1 = \chi \frac{1}{r^\varpi - 1} , \tag{B.5}$$

$$\chi = \frac{\Phi_2 - \Phi_1}{\Phi_1} , \tag{B.6}$$

is an *Error estimator* for the actual error A_1 as long as $E_1 \ll 1$. Note that the quantity χ in the above equation, which is often reported in refinement studies, is not always a good

estimate for the actual error. Equation (B.5) is valid in all space and time directions if the same refinement ratio r and order ϖ are applied. For independent coordinate refinements in time and space (for example $r_t \neq r_x \neq r_y \neq r_z$, and uniform ϖ in each coordinate direction) the resulting estimated error is obtained as the sum of the individual coordinate estimates:

$$E_1 = E_{1t} + E_{1x} + E_{1y} + E_{1z}. \tag{B.7}$$

However, we often perform just two calculations (on the coarse and fine grid) with different r used in different coordinate directions, and in the case of time-dependent computations, with mixed-order methods. For this situation, Roache (1994) suggests a calculation of the conservative estimated error based on the smallest directional refinement ratio r and the smallest order ϖ. When the grid stretching is not analytical the effective grid refinement ratio:

$$r = \left(\frac{(NI * NJ)_1}{(NI * NJ)_2} \right)^{1/2} \tag{B.8}$$

can be used. For a combination of the higher order convective scheme and the second order scheme for the diffusion the formal order of the method is $\varpi = 2$. Similarly, if we have two time-dependent numerical solutions on the fine and coarse grid, obtained with different time-step sizes, a conservative approach would be to calculate E_1 with $\varpi = 1$. Very often we need the estimated fractional error for the coarse grid solution. Denoting as before the solution with the smallest parameter h_1 as Φ_1 and other "coarser" solutions with $h_2 = rh_1$, $h_3 = r^2 h_1, \ldots, h_m = r^{m-1} h_1$ as $\Phi_2, \Phi_3, \ldots, \Phi_m$ respectively, an error estimator for the solution Φ_m is given as:

$$E_m = \frac{\Phi_m - \Phi_1}{\Phi_1} \frac{r^{(m-1)\varpi}}{r^{(m-1)\varpi} - 1}. \tag{B.9}$$

Finally, Roache (1994) discussed the advantages and disadvantages of using Richardson extrapolation and derived Error estimator E_1. In some cases, the conditions behind this theory simply do not hold and one might be concerned over the actual order of the method. Further, Roache proposed uniform reporting of grid refinement studies based on a Grid Convergence Index (GCI) which has been defined as:

$$GCI = 3|E_1| = 3|\chi| \frac{1}{r^\varpi - 1}. \tag{B.10}$$

The idea is to relate the results (more precisely the χ) from any grid refinement study to the expected results from a grid doubling ($r = 2$) using a second-order accurate method ($\varpi = 2$). In this study, only the Richardson Error estimates for the fine (E_1) or coarse (E_m) grid and time refinement tests are reported.

REFERENCES

Abarbanel, S.S., Don, W.S., Gottlieb, D., Rudy, D.H., and Townsend, J.C., 1991, "Secondary Frequencies in the Wake of a Circular Cylinder with Vortex Shedding," Journal of Fluid Mechanics, Vol. 225, pp. 557-574.

Achenbach, E., 1968, "Distribution of Local Pressure and Skin Friction Around a Circular Cylinder in Cross-Flow up to Re=5x106," Journal of Fluid Mechanics, Vol. 34, Part 4, pp. 625-639.

Amano, R., 1985, "Development of a Turbulence Near–Wall Model and Its Application to Separated and Reattached Flows," Numerical Heat Transfer, Vol. 7, pp. 59-75.

Anderson, J.D., 1995, Computational Fluid Dynamics: Basics with Applications, McGraw–Hill, Inc.

Arnal, M.P., Goering, D.J., and Humphrey, J.A.C., 1991, "Vortex Shedding From a Bluff Body Adjacent to a Plane Sliding Wall," ASME Journal of Fluids Engineering, Vol. 113, pp. 384-398.

Baba, N., and Miyata, H., 1987, "Higher–Order Accurate Difference Solutions of Vortex Generation from a Circular Cylinder in an Oscillatory Flow," Journal of Computational Physics, Vol. 69, pp. 362-396.

Baldwin, B.S, and Lomax, H., 1978, "Thin-Layer Approximation and Algebraic Modelfor Separated Turbulent Flows," AIAA Paper 78-257, Huntsville, AL.

Basu, R.I., 1985, "Aerodynamic Forces on Structures of Circular Cross-Section. Part 1. Model-Scale Data Obtained under Two-Dimensional Conditions in Low- Turbulence Streams," Journal of Wind Engineering and Industrial Aerodynamics, Vol. 21, pp. 273-294.

Basu, R.I., 1986, "Aerodynamic Forces on Structures of Circular Cross-Section. Part 2. The Influence of Turbulence and Three-Dimensional Effects," Journal of Wind Engineering and Industrial Aerodynamics, Vol. 24, pp. 33-59.

Batchelor, G.K., 1967, An Introduction to Fluid Dynamics, Cambridge University Press.

Bearman, P.W., and Trueman, D.M., 1972, "An Investigation of the Flow around Rectangular Cylinders," Aeronautical Quarterly, Vol. 23, pp. 229-237.

Bearman, P.W., and Obasaju, E.D., 1982, "An Experimental Study of Pressure Fluctuations on Fixed and Oscillating Square - Section Cylinders," Journal of Fluid Mechanics, Vol. 119, pp. 297-321.

Bearman, P.W., and Morel, T., 1983, "Effect of Free Stream Turbulence on the Flow Around Bluff Bodies," Prog. Aerospace Sci., Vol. 20, pp. 97-123.

Bearman, P.W., 1984, "Vortex Shedding from Oscillating Bluff Bodies," Annual Review of Fluid Mechanics, Vol. 16, pp. 195-222.

Bearman, P.W., Downie, M.J., Graham, J.M.R., and Obasaju, E.D., 1985, "Forces on Cylinders

REFERENCES

in Viscous Oscillatory Flow at Low Keulegan-Carpenter Numbers," Journal of Fluid Mechanics, Vol. 154, pp. 337-356.

Bearman, P.W., and Obasaju, E.D., 1989, "Transverse Forces on a Circular Cylinder Oscillating In-Line with a Steady Current," Proc. 8th International Conference on Offshore Mechanics and Arctic Engineering, Hague, March 19-23, pp. 253-258.

Behr, M., Liou, J., Shih, R., and Tezduyar, T.E., 1991, "Vorticity-Streamfunction Formulation of Unsteady Incompressible Flow Past a Circular Cylinder: Sensitivity of the Computed Flow Field to the Location of the Outflow Boundary,"International Journal for Numerical Methods in Fluids, Vol. 12, pp. 323-342.

Behr, M., Hastreiter, D., Mittal, S., and Tezduyar, T.E., 1995, "Incompressible Flow Past a Circular Cylinder: Dependence of the Computed Flow Field on the Location of the Lateral Boundaries," Computer Methods in Applied Mechanics and Engineering, Vol. 123, pp. 309-316.

Bell, W.H., 1986, "Free Stream Turbulence and Bluff Body Drag," in Encyclopedia of Fluid Mechanics, N.P. Cheremisinoff ed., Gulf Publ. Comp., Vol. 2, pp. 453-475.

Benodekar, R., Issa, R., Sanatian, R., and Uslu, S., 1994, "CFD Biathlon: Two Turbulent Flow Simulations by the STAR-CD Code," ASME FED, Lake Tahoe, June 19-24.

Berger, E., and Wille R., 1972, "Periodic Flow Phenomena," Ann. Rev. of Fluid Mechanics, Vol. 4, pp. 313-340.

Borisenko, A.I., and Tarapov, I.E., 1968, Vector and Tensor Analysis with Applications, Prentice–Hall, Inc., Englewood Cliffs, N.J., USA.

Borthwick, A., 1986, "Comparison Between Two Finite-Difference Schemes for Computing the Flow Around a Cylinder," International Journal for Numerical Methods in Fluids, Vol. 6, pp. 275-290.

Bosch, G., Rodi, W., 1996, "Simulation of Vortex Shedding Past a Square Cylinder Near a Wall," Int. J. Heat and Fluid Flow, Vol. 17, pp. 267-275.

Bradshaw, P., 1994, "Turbulence: The Chief Outstanding Difficulty of Our Subject," Experiments in Fluids, Vol. 16, pp. 203-216.

Bradshaw, P., 1996, "Turbulence Modeling with Application to Turbomachinery," Prog. Aerospace Sci., Vol. 32, pp. 575-624.

Braza, M., Chassaing, P., and Ha Minh, H., 1986, "Numerical Study and Physical Analysis of the Pressure and Velocity Fields in the Near Wake of a Circular Cylinder," Journal of Fluid Mechanics, Vol. 165, pp. 79-130.

Braza, M., Chassaing, P., and Ha Minh, H., 1990, "Prediction of Large-Scale Transition Features in the Wake of a Circular Cylinder," Physics of Fluids A, Vol. 2, pp. 1461-1471.

Braza, M., Nogues, P., and Persillon, H., 1992, "Prediction of Self-Induced Vibrations in Incompressible Turbulent Flows Around Cylinders," Proc. 2nd Int. Offshore and Polar Engineering Conference, San Francisco, USA, 14-19 June, Vol. 3, pp. 284-292.

Breuer, M., Hanel, D., Kloker, J., and Meinke, M., 1993, "Computations of Unsteady Vortical Flows," Computers and Fluids, Vol. 22, pp. 229-237.

Britter, R.E., Hunt, J.C.R., and Mumford, J.C., 1979, "The Distortion of Turbulence by a Circular Cylinder," Journal of Fluid Mechanics, Vol. 92, pt. 2, pp. 269-301.

Cantwell, B., and Coles, D., 1983, "An Experimental Study of Entrainment and Transport in the Turbulent Near-Wake of a Circular Cylinder, Journal of Fluid Mechanics, Vol. 136, pp. 321-374.

Carey, C., Scanlon, T.J., and Fraser, S.M., 1992, "The Reduction of False Diffusion in the Simulation of Vortex Shedding," IMechE Journal of Mechanical Engineering Science, Vol. 206, pp. 399-406.

Cheng, C.M., Lu, P.C., and Chen, R.H., 1992, "Wind Loads on Square Cylinder in Homogeneous Turbulent Flows," Journal of Wind Engineering and Industrial Aerodynamics, Vol. 41, pp. 739-749.

Chieng, C.C., and Launder, B.E., 1980, "On the Calculation of Turbulent Heat Transport Downstream From an Abrupt Pipe Expansion," Numerical Heat Transfer, Vol. 3, pp. 189-207.

Ciofalo, M., Collins, M.W., 1989, "$k - \epsilon$ Predictions of Heat Transfer in Turbulent Recirculating Flows Using an Improved Wall Treatment," Numerical Heat Transfer B, Vol. 15, pp. 21-47.

Coutanceau, M., and Defaye, J-R., 1991, "Circular Cylinder Wake Configurations: A Flow Visualization Survey," Applied Mechanics Review, Vol. 44, pp. 255-305.

Craft, T.J., Graham, L.J.W., and Launder, B.E., 1993, "Impinging Jet Studies for Turbulence Model Assessment - II. An Examination of the Performance of Four Turbulence Models," International Journal of Heat and Mass Transfer, Vol. 36, pp. 2685-2697.

Darwish, M.S., 1993, "A New High Resolution Scheme Based on the Normalized Variable Formulation," Numerical Heat Transfer, Part B, Vol. 24, pp. 353-371.

Davidson, L., 1996, "A Pressure Correction Method for Unstructured Meshes with Arbitrary Control Volumes," International Journal for Numerical Methods in Fluids, Vol. 22, pp. 265-281.

Davis, R.W., and Moore, E.F., 1982, "A Numerical Study of Vortex Shedding from Rectangles," Journal of Fluid Mechanics, Vol. 116, pp. 475-506.

Davydov, B.I., 1961, "On Statistical Dynamics of an Incompressible Turbulent Fluid," Soviet Physics - Doklady, Fluid Mechanics, Vol. 6, No. 1, pp. 10-12.

Dawes, W.N., 1992, "The Practical Application of Solution–Adaption to the Numerical Simulation of Complex Turbomachinery Problems," Prog. Aerospace Sci., Vol. 29, pp. 221-269.

Delany, N.K., and Sorensen, N.E., 1953, "Low-Speed Drag of Cylinders of Various Shapes," NACA TN-3038, Nov. (Referred to by Ericsson (1980)).

Demirdžć, I., and Perić, M., 1990, "Finite Volume Method for Prediction of Fluid Flow in Arbitrarily Shaped Domains with Moving Boundaries," International Journal for Numerical Methods in Fluids, Vol. 10, pp. 771-790.

Demirdžić, I., and Muzaferija, S., 1995, "Numerical Method for Coupled Fluid Flow, Heat Transfer and Stress Analysis Using Unstructured Moving Meshes with Cells of Arbitrary Topology", Comp. Methods Appl. Mech. Eng., Vol. 125, pp. 235-255.

Demirdžić, I., Muzaferija, S., and Perić, M., 1997, "Advances in Computation of Heat Transfer, Fluid Flow, and Solid Body Deformation Using Finite Volume Approaches," Advances in Numerical Heat Transfer, Eds. Minkowycz, W. and Sparrow, E.M., Vol. 1, pp. 59-96.

Deng, G.B., Piquet, J., Queutey, P., and Visonneau, M., 1993a, "Flow Past a Square Cylinder. Predictions with an Eddy-Viscosity Model," 9th Symposium on Turbulent Shear Flows, Kyoto, Japan, August 16-18, pp. 10.2.1-10.2.6.

Deng, G.B., Piquet, J., Queutey, P., and Visonneau, M., 1993b, "Vortex-Shedding Flow Predictions with Eddy-Viscosity Models," Engineering Turbulence Modelling and Experiments 2, W. Rodi & F. Martelli, Eds., Elsevier Science Publishers, pp. 143-152.

Durao, D., Heitor, M., and Pereira, J., 1988, "Measurements of Turbulent and Periodic Flows

Around a Square Cross-Section Cylinder," Experiments in Fluids, Vol. 6, pp. 298-304.

Durbin, P.A., 1991, "Near–Wall Turbulence Closure Modeling Without 'Dumping Functions'," Theoretical and Computational Fluid Dynamics, Vol. 3, pp. 1-13.

Durbin, P.A., 1996, "On the k-3 Stagnation Point Anomaly," Int. J. Heat and Fluid Flow, Vol. 17, pp. 89-90.

Eaton, B.E., 1987, "Analysis of Laminar Vortex Shedding Behind a Circular Cylinder by Computer–Aided Flow Visualization," Journal of Fluid Mechanics, Vol. 180, pp. 117-145.

Engelman, M.S., and Jamnia, M-A., 1990, "Transient Flow Past a Circular Cylinder: A Benchmark Solution," International Journal for Numerical Methods in Fluids, Vol. 11, pp. 985-1000.

Ericsson, L.E., 1980, "Karman Vortex Shedding and the Effect of Body Motion," AIAA Journal, Vol. 18, pp. 935-944.

Ferziger, J., 1993, "Simulation of Complex Turbulent Flows: Recent Advances and Prospects in Wind Engineering," Journal of Wind Engineering and Industrial Aerodynamics, Vol. 46 & 47, pp. 195-212.

Ferziger, J., and Perić, M., 1996, Computational Methods for Fluid Dynamics, Springer, Berlin.

Frank, W., and Mauch, H., 1993, "Large-Eddy-Simulation of the Flow Around Building Models," Journal of Wind Engineering and Industrial Aerodynamics, Vol. 46 & 47, pp. 213- 218.

Franke, R., 1991, "Numerische Berechnung der instationaren Wirbelablosung hinter zylindrischen Korpern," Ph.D. Thesis, University of Karlsruhe, Germany.

Franke, R., and Rodi, W., 1991, "Calculation of Vortex Shedding past a Square Cylinder with Various Turbulence Models," Eight Symp. on Turbulent Shear Flows, Technical University of Munich, Sept. 9-11, pp. 20-1-1 to 20-1-6.

Franke, R., Rodi, W., and Schonung, B., 1990, "Numerical Calculation of Laminar Vortex Shedding Flow Past Cylinders," Journal of Wind Engineering and Industrial Aerodynamics, Vol. 35, pp. 237-257.

Fromm, J.E., and Harlow, F.H., 1963, "Numerical Solution of the Problem of Vortex Street Development," The Physics of Fluids, Vol. 6, pp. 975-982.

Gartshore, I.S., 1984, "Some Effects of Upstream Turbulence on the Unsteady Lift Forces Imposed on Prismatic Two Dimensional Bodies," ASME Journal of Fluids Engineering, Vol. 106, pp. 419-424.

Gaskell, P.H., and Lau, A.K.C., 1988, "Curvature Compensated Convective Transport: SMART, A New Boundedness Preserving Transport Algorithm," International Journal for Numerical Methods in Fluids, Vol. 8, pp. 617-641.

Gerrard, J.H., 1978, "The Wakes of Cylindrical Bluff Bodies at Low Reynolds Number," Philosophical Transaction of Royal Society London, Vol. 288 (1354), pp. 351-382.

Graham, J.M.R., and Djahansouzi, B., 1989, "Hydrodynamic Damping of Structural Elements," Proc. 8th Int. Conf. on Offshore Mechanics and Arctic Engineering, The Hague, March 19-23, pp. 289-293.

Graham, J.M.R., Arkell, R.H., and Zhou, C-Y., 1993, "The Effect of Combinations of Mean Current and Oscillatory Flow on the Forces on a Bluff Body," Journal of Wind Engineering and Industrial Aerodynamics, Vol. 50, pp. 85-96.

Gresho, P.M., Chan, S.T., Lee, R.L., and Upson, C.D., 1984, "A Modified Finite Element method

for Solving the Time-Dependent, Incompressible Navier-Stokes Equations. Part 2: Applications," International Journal for Numerical Methods in Fluids, Vol. 4, pp. 619-640.

Hadid, A.H., Sindir, M.M., and Issa, R.I., 1991, "A Numerical Study of Two–Dimensional Vortex Shedding from Rectangular Cylinders," Proc. 4th Int. Symp. on Computational Fluid Dynamics, Davis, CA, pp. 473-478.

Hanjalić, K., 1970, "Two-Dimensional Flow in an Axisymmetric Channel," Ph.D. Thesis, University of London.

Hanjalić, K., 1994, "Advanced Turbulence Closure Models: A View on the Current Status and Future Prospects," Int. J. Heat & Fluid Flow, Vol. 15, pp. 178-203.

Hanjalić, K., and Jakirlić, S., 1998, "Contribution Towards the Second– Moment Closure Modelling of Separating Turbulent Flows," Computers & Fluids, Vol. 27, No. 2, pp. 137-156.

Hanjalić, K., Hadžić, I, Jakirlić, S., and Basara, B., 1997, "Modelling the Turbulent Wall Flows Subjected to Strong Pressure Variations," ICASE/LaRC/AFOSR Symp. on Modeling Complex Turbulent Flows, NASA-Langley, Virginia, August 11-13.

Hanjalić, K., and Launder, B.E., 1972, "A Reynolds Stress Model of Turbulence and Its Application to Thin Shear Flows," Journal of Fluid Mechanics, Vol. 52, pp. 609-638.

Hanjalić, K., and Launder, B.E., 1980, "Sensitizing the Dissipation Equation to Irrotational Strains," ASME Journal of Fluids Engineering, Vol. 102, pp. 34-40.

Harlow, F.H., and Nakayama, P.I., 1967, "Turbulence Transport Equations," Physics of Fluids, Vol. 10, pp. 2323-2332.

Harten, A., 1983, "High Resolution Schemes for Hyperbolic Conservation Laws," Journal of Computational Physics, Vol. 49, pp. 357-393.

Henderson, R.D., 1995, "Details of the Drag Curve Near the Onset of Vortex Shedding," Physics of Fluids, Vol. 7, pp. 2102-2104.

Hestenes, M.R., and Stiefel, E., 1952, "Methods of Conjugate Gradients for Solving Linear Systems," Journal of Research of the National Bureau of Standards, Vol. 49, pp. 409-436.

Hinze, J.O., 1975, Turbulence, 2nd Edition, McGraw-Hill, New York.

Honji, H., 1981, "Streaked Flow Around an Oscillating Circular Cylinder," Journal of Fluid Mechanics, Vol. 107, pp. 509-520.

Hwang, R.R., and Yao, C-C., 1997, "A Numerical Study of Vortex Shedding From a Square Cylinder With Ground Effect," ASME Journal of Fluids Engineering, Vol. 119, pp. 512-517.

Igarashi, T., 1987, "Fluid Flow and Heat Transfer Around Rectangular Cylinders (The Case of a Width/Height Ratio of a Section of 0.33-1.5)," Int. J. Heat Mass Transfer, Vol. 30, pp. 893-901.

Ishigai, S., Nishikawa, E., Nishimura, K., and Cho, K., 1972, "Experimental Study on Structure of Gas Flow in Tube Banks with Tube Axes Normal to Flow (Part 1. Karman Vortex Flow around Two Tubes at Various Spacings)," Bull. JSME, Vol. 15, No. 86, pp. 949- 956.

James, W.D., Paris, S.W., and Malcolm, G.N., 1980, "Study of Viscous Crossflow Effects on Circular Cylinders at High reynolds Numbers," AIAA Journal, Vol. 18, pp. 1066-1072.

Ji, W., and Wang, P.K., 1991, "Numerical Simulation of Three-Dimensional Unsteady Viscous Flow Past Finite Cylinders in an Unbounded Fluid at Low Intermediate Reynolds Numbers," Theoret. Comput. Fluid Dynamics, Vol. 3, pp. 43-59.

Jin, G., and Braza, M., 1994, Two-Equation Turbulence Model for Unsteady Separated Flows

REFERENCES

Around Airfoils," AIAA Journal, Vol. 32, pp. 2316-2320.

Jones, G.W., Cincotta, J.J., and Walker, R.W., 1969, "Aerodynamic Forces on a Stationary and Oscillating Circular Cylinder at High Reynolds Numbers," NASA Tech. Rep. R-300, pp. 1-62.

Jones, W.P., and Launder, B.E., 1972, "The Prediction of Laminarization with a Two- Equation Model of Turbulence," International Journal of Heat and Mass Transfer, Vol. 15, pp. 301-314.

Jovanović, J., Ye, Q.-Y., and Durst, F., 1995, "Statistical Interpretation of the Turbulent Dissipation Rate in Wall-Bounded Flows," Journal of Fluid Mechanics, Vol. 293, pp. 321- 347.

Justesen, P., 1991, "A Numerical Study of Oscillating Flow Around a Circular Cylinder," Journal of Fluid Mechanics, Vol. 222, pp. 157-196.

Kakuda, K., and Tosaka, N., 1993, "Numerical Simulation of High Reynolds Number Flows by petrov-Galerkin Finite Eleement Method," Journal of Wind Engineering and Industrial Aerodynamics, Vol. 46 & 47, pp. 339-347.

Karniadakis, G.E., and Triantafyllou, G.S., 1989, "Frequency Selection and Asymptotic States in Laminar Wakes," Journal of Fluid Mechanics, Vol. 199, pp. 441-469.

Karniadakis, G., and Triantafyllou, S., 1992, "Three-Dimensional Dynamics and Transition to Turbulence in the Wake of Bluff Objects," Journal of Fluid Mechanics, Vol. 238, pp. 1-30.

Karniadakis, G., Brown, G., 1995, "Vorticity Transport in Modeling Three-Dimensional Unsteady Shear Flows," Physics of Fluids, Vol. 7, pp. 688-690.

Kato, M., and Launder, B.E., 1993, "The Modelling of Turbulent Flow Around Stationary and Vibrating Square Cylinders," Ninth Symp. on Turbulent Shear Flows, Kyoto, Japan, August 16-18, pp. 10-4-1 to 10-4-6.

Kelkar, K.M., and Patankar, S.V., 1992, "Numerical Prediction of Vortex Shedding Behind a Square Cylinder," International Journal for Numerical Methods in Fluids, Vol. 14, pp. 327- 341.

Khosla, P.K., and Rubin, S.G., 1974, "A Diagonally Dominant Second–Order Accurate Implicit Scheme," Computers & Fluids, Vol. 2, pp. 207-209.

Kim, S.-W., and Benson, T.J., 1992, "Comparison of the SMAC, PISO and Iterative Time- Advancing Schemes for Unsteady Flows," Computers and Fluids, Vol. 21, No. 3, pp. 435- 454.

Kim, S-E., and Choudhury, D., 1995, "A near–Wall Treatment Using Wall Functions Sensitized to Pressure Gradient," ASME Symp. Separated and Complex Flows, FED-Vol. 217, pp. 273-280.

Kondo, N., 1993, "Direct Third–Order Upwind Finite Element Simulation of High Reynolds Number Flows around a Circular Cylinder," Journal of Wind Engineering and Industrial Aerodynamics, Vol. 46 & 47, pp. 349-356.

Lamb, H., 1932, Hydrodynamics, 6th Edition, University Press, Cambridge.

Lam, C.K.G., and Bremhorst, K., 1981, "A Modified Form of the $k - \epsilon$ Model for Predicting Wall Turbulence," ASME Journal of Fluids Engineering, Vol. 103, pp. 456-460.

Landahl, M.T., and Mollo-Christensen, E., 1986, Turbulence and Random Processes in Fluid Mechanics, Cambridge University Press, New York.

Launder, B.E., 1988, "On the Computation of Convective Heat Transfer in Complex Turbulent Flows," ASME Journal of Fluids Engineering, Vol. 110, pp. 112-128.

Launder, B.E., 1991, "Current Capabilities for Modelling Turbulence in Industrial Flows," Applied Scientific Research, Vol. 48, pp. 247-269.

REFERENCES

Launder, B.E., and Spalding, D.B., 1974, "The Numerical Computation of Turbulent Flows," Computer Methods in Applied Mechanics and Engineering, Vol. 3, pp. 269-289.

Launder, B.E., Reece, G.J., and Rodi, W., 1975, "Progress in the Develpoment of a Reynolds-Stress Turbulence Closure," Journal of Fluid Mechanics, Vol. 68, pp. 537-566.

Lecointe, Y., and Piquet, J., 1984, "On the Use of Several Compact Methods for the Study of Unsteady Incompressible Viscous Flow Around Circular Cylinders," Computers and Fluids, Vol. 12, No. 4, pp. 255-280.

Lecointe, Y., and Piquet, J., 1989, "Flow Structure in the Wake of an Oscillating Cylinder," ASME Journal of Fluids Engineering, Vol. 111, pp. 139-148.

Lee, B.E., 1975, "The Effect of Turbulence on the Surface Pressure Field of Square Prism," Journal of Fluid Mechanics, Vol. 69, pp. 263-282.

Lee, M.J., Kim, J., and Moin, P., 1990, "Structure of Turbulence at High Shear Rate," Journal of Fluid Mechanics, Vol. 216, pp. 561-583.

Leonard, B.P., 1979, "A Stable and Accurate Convective Modelling Procedure Based on Quadratic Upstream Interpolation," Comp. Meth. Appl. Mech. Eng., Vol. 19, pp. 59-98.

Leonard, B.P., 1988, "Simple High–Accuracy Resolution Program for Convective Modelling of Discontinuities," International Journal for Numerical Methods in Fluids, Vol. 8, pp. 1291-1318.

Leschziner, M.A., and Rodi, W., 1981, "Calculation of Annular and Twin Parallel Jets Using Various Discretization Schemes and Turbulence-Model Variations," ASME Journal of Fluids Engineering, Vol. 103, pp. 352-360.

Lesieur, M., 1987, Turbulence in Fluids, Martinus Nijhoff Publishers, Dordrecht, The Netherlands.

Li, J., Chambarel, A., Donneaud, M., and Martin, R., 1991, "Numerical Study of laminar Flow Past One and Two Circular Cylinders," Computers and Fluids, Vol. 19, No. 2, pp. 155- 170.

Li, G., and Humphrey, J.A.C., 1995, "Numerical Modelling of Confined Flow Past a Cylinder of Square Cross–Section at Various Orientations," International Journal for Numerical Methods in Fluids, Vol. 20, pp. 1215-1236.

Li, J., Sun, J., and Roux, B., 1992, "Numerical Study of an Oscillating Cylinder in Uniform Flow and in the Wake of an Upstream Cylinder," Journal of Fluid Mechanics, Vol. 237, pp. 457-478.

Lien, F.S., and Leschziner, M.A., 1994, "Upstream Monotonic Interpolation for Scalar Transport with Application to Complex Turbulent Flows," International Journal for Numerical Methods in Fluids, Vol. 19, pp. 527-548.

Lien, F.S., and Leschziner, M.A., 1994, "Assessment of Turbulence-Transport Models Including Non-Linear RNG Eddy-Viscosity Formulation and Second-Moment Closure for Flow Over a Backward-Facing Step," Computers and Fluids, Vol. 23, pp. 983-1004.

Lienhard, J.H., 1966, "Synopsis of Lift, Drag, and Vortex Frequency Data for Rigid Circular Cylinders," Washington State Univ., College of Engineering, Research Division Bulletin 300 (Cited by Franke (1991)).

Lin, C-H., and Lin, C.A., 1997, "Simple High–Order Bounded Convection Scheme to Model Discontinuities," AIAA Journal, Vol. 35, pp. 563-565.

Lin, H., and Chieng, C-C., 1991, "Characteristic–Based Flux Limiters of an Essentially Third–Order Flux–Splitting Method for Hyperbolic Conservation Laws," International Journal for Numerical Methods in Fluids, Vol. 13, pp. 287-307.

REFERENCES

Lin, X.W., 1991, Numerical Study of Unsteady Heat Transfer and Fluid Flow over a Bluff Body," PhD Thesis, University of London.

Lugt, H.J., 1983, Vortex Flow in Nature and Technology, John Wiley & Sons, Inc., New York.

Lumley, J.L., 1992, "Some Comments on Turbulence," Physics of Fluids A, Vol. 4, pp. 203-211.

Lyn, D.A., 1992, "Ensemble-Averaged Measurements in the Turbulent Near Wake of a Square Cylinder: A Guide to the Data," Report CE–HSE–92–6, School of Civil Engineering, Purdue University, U.S.A..

Lyn, D.A., and Rodi, W., 1994, "The Flapping Shear Layer Formed by Flow Separation from the Forward Corner of a Square Cylinder," Journal of Fluid Mechanics, Vol. 267, pp. 353-376.

Lyn, D.A., Einav, S., Rodi, W., and Park, J-H., 1995, "A Laser–Doppler Velocimetry Study of Ensemble–Averaged Characteristics of the Turbulent Near Wake of a Square Cylinder," Journal of Fluid Mechanics, Vol. 304, pp. 285-319.

MacCurdy, E., 1954, The Notebooks of Leonardo da Vinci, The reprint society, London.

Majumdar, S., and Rodi, W., 1985, "Numerical Calculations of Turbulent Flow Past Circular Cylinders," 3rd Symp. Numerical and Physical Aspects of Aerodynamic Flows, Long Beach, CA (USA), 21-24 Jan., pp. 1-13.

Mansour, N.N., Kim, J., and Moin, P., 1988, "Reynolds Stress and Dissipation Rate Budgets in Turbulent Channel Flow," Journal of Fluid Mechanics, Vol. 194, pp. 15-44.

Mathur, S.R., and Murthy, J.Y., 1997, "A Pressure–Based Method for Unstructured Meshes," Numerical Heat Transfer, Part B, Vol. 31, pp. 195-215.

Matsumura, M., and Antonia, R.A., 1993, "Momentum and Heat Transfer in the Turbulent Intermediate Wake of a Circular Cylinder," Journal of Fluid Mechanics, Vol. 250, pp. 651-668.

Maull, D.J., and Milliner, M.C., 1978, "Sinusoidal Flow Past a Circular Cylinder," Coastal Engrg., Vol. 2, pp. 149-168 (Cited by Justesen, 1991).

McCroskey, W.J., 1977, "Some Current Research in Unsteady Fluid Dynamics ," ASME Journal of Fluid Mechanics, Vol. 99, pp. 8-39.

Meijerink, J.A., and Van Der Vorst, H.A., 1981, "Guidelines for the Usage of Incomplete Decompositions in Solving Sets of Linear Equations as They Occur in Practical problems," Journal of Computational Physics, Vol. 44, pp. 134-155.

Minh, H.H., and Kourta, A., 1993, "Semi-Deterministic Turbulence Modelling for Flows Dominated by Strong Organized Structures," 9th Symposium on Turbulent Shear Flows, Kyoto, Japan, August 16-18, pp. 10.5.1-10.5.6.

Mittal, R., and Balachandar, S., 1995, "Effect of Three-Dimensionality on the Lift and Drag of Nominally Two-Dimensional Cylinders," Physics of Fluids, Vol. 7, pp. 1841-1865.

Monin, A.S, and Yaglom, A.M., 1971, Statistical Fluid Mechanics: Mechanics of Turbulence, 2 Vols., MIT Press, Cambridge, Massachusetts.

Mukhopadhyay, A., Biswas, G., and Sundararajan, T., 1992, "Numerical Investigation of Confined Wakes Behind a Square Cylinder in a Channel," International Journal for Numerical Methods in Fluids, Vol. 14, pp. 1473-1484.

Murakami, S., Mochida, A., Hayashi, Y., and Sakamoto, S., 1992, "Numerical Study on Velocity–Pressure Field and Wind Forces for Bluff Bodies by $k - \epsilon$ ASM and LES," Journal of Wind Engineering and Industrial Aerodynamics, Vol. 41-44, pp. 2841-2852.

Murakami, S., and Mochida, A., 1995, On Turbulent Vortex Shedding Flow Past 2D Square Cylinder predicted by CFD," Journal of Wind Engineering and Industrial Aerodynamics, Vol. 54/55, pp. 191-211.

Murashige, S., Kinoshita, T., and Hinatsu, M., 1989, "Direct Calculations of the Navier Stokes Equations for Forces Acting on a Cylinder in Oscillatory Flow," 8th Int. Conf. Offshore Mech. and Arctic Engineering, Hague, pp. 19-23.

Nagano, Y., and Tagawa, M., 1990, "An Improved $k-\epsilon$ Model for Boundary–Layer Flows,"ASME Journal of Fluids Engineering, Vol. 112, pp. 33-39.

Najjar, F.M., and Vanka, S.P., 1995, "Effects of Intrinsic Three-Dimensionality on the Drag Characteristics of a Normal Flat Plate," Physics of Fluids, Vol. 7, pp. 2516-2518.

Nakamura, I., Watanabe, T., and Yoshida, T., 1993, "On the Numerical Outflow Boundary Condition of the Viscous Flow Around a Square Cylinder", Memoirs of the School of Engineering, Nagoya University, Vol. 45, No. 1, pp. 105-117.

Norberg, C., 1993, "Flow Around Rectangular Cylinders: Pressure Forces and Wake Frequencies," Journal of Wind Engineering and Industrial Aerodynamics, Vol. 49, pp. 187-196.

Norberg, C., 1996, Unpublished Strouhal number data referred to by Sohankar et al. (1997).

Norris, H.L., and Reynolds, W.C., 1975, "Turbulent Channel Flow with a Moving Wavy Bundary," Dept. Mech. Eng. Rept. FM-10, Stanford University, USA.

Obasaju, E.D., 1983, "An Investigation of the Effects of Incidence on the Flow Around a Square Section Cylinder," Aeronautical Quarterly, November, pp. 243-259.

Obasaju, E.D., Bearman, P.W., and Graham, J.M.R., 1988, "A Study of Forces, Circulation and Vortex Patterns Around a Circular Cylinder in Oscillating Flow," Journal of Fluid Mechanics, Vol. 196, pp. 467-494.

Ohya, Y., Okajima, A., and Hayashi, M., 1989, "Wake Interference and Vortex Shedding," in Encyclopedia of Fluid Mechanics, Vol. 8, N.P. Cheremisinoff, ed., Gulf Publ. Comp., pp. 323-389.

Okajima, A., 1982, "Strouhal Numbers of Rectangular Cylinders," Journal of Fluid Mechanics, Vol. 123, pp. 379-398.

Okajima, A., 1995, Proc. 6th Int. Conf. Flow Induced Vibration, London, 10-12 April, pp. 1-7.

Orszag, S.A., Yakhot, V., Flannery, W.S., Boysan, F., Choudhury, D., Maruzewski, J., and Patel, B., 1993, "Renormalization Group Modeling and Turbulence Simulations," in Near-Wall Turbulent Flows, R.M.C. So, C.G. Speziale & B.E. Launder, Eds., Elsevier Science Publishers B.V., pp. 1031-1046.

Ota, T., Okamoto, Y., and Yoshikawa, H., 1994, "A Correction Formula for Wall Effects on Unsteady Forces of Two-Dimensional Bluff Bodies," ASME Journal of Fluids Engineering, Vol. 116, pp. 414-418.

Owen, F.K., and Johnson, D.A., 1980, "Measurements of Unsteady Vortex Fields," AIAA Journal, Vol. 18, pp. 1173-1179.

Patankar, S.V., 1980, Numerical Heat Transfer and Fluid Flow, McGraw Hill, London.

Patankar, S.V., and Spalding, D.B., 1972, "A Calculation Procedure for Heat, Mass and Momentum Transfer in Three–Dimensional Parabolic Flows," Int. J. Heat Mass Transfer, Vol. 15, pp. 1787-1806.

Patel, V.C., Rodi, W., and Scheuerer, G., 1985, "Turbulence Models for Near–Wall and Low Reynolds Number Flows: A Review," AIAA Journal, Vol. 23, pp. 1308-1319.

Pereira, J.C.F., and Durst, F., 1988, "Finite Difference Methods in Recirculating Flows," in Validation of Computational Fluid Dynamics, AGARD Conference Proceedings No.437, Vol. 2, pp. P4.1-P4.13.

Perić, M., 1985, "A Finite Volume Method for the Prediction of Three–Dimensional Fluid Flow in Complex Ducts," PhD Thesis, University of London.

Perry, A.E., Chong, M.S., and Lim, T.T., 1982, "The Vortex Shedding Process Behind Two- Dimensional Bluff Bodies," Journal of Fluid Mechanics, Vol. 116, pp. 77-90

Pocha, J.J., 1971, "On Unsteady Flow Past Cylinders of Square Cross-Section," Ph.D. thesis, Department of Aeronautics, Queen Mary College, London.

Press, W.H., Flannery, B.P., Teukolski, S.A., and Vetterling, 1988, Numerical Recipes, Cambridge University Press.

Rahman, M.M., Siikonen, T., and Miettinen, A., 1997, "A Pressure–Correction Method for Solving Fluid Flow Problems on a Collocated Grid," Numerical Heat Transfer, Part B, Vol. 32, pp. 63-84.

Ramaswamy, B., and Jue, T.C., 1992, "Some Recent Trends and Developments in Finite Element Analysis for Incompressible Thermal Flows," International Journal for Numerical Methods in Fluids, Vol. 35, pp. 671-707.

Reynolds, O., 1895, "On the Dynamical Theory of Incompressible Viscous Fluids and the Determination of the Criterion," Philosophical Transactions of the Royal Society of London, Vol. 186, Part I, pp. 123-164.

Rhie, C.M., and Chow, W.L., 1983, "Numerical Study of the Turbulent Flow Past an Airfoil with Trailing Edge Separation," AIAA Journal, Vol. 21, pp. 1525-1532.

Roache, P.J., 1994, "Perspective: A Method for Uniform Reporting of Grid Refinement Studies," ASME Journal of Fluids Engineering, Vol. 116, pp. 405-413.

Rodi, W., 1991, "Experience with Two-Layer Models Combining the k- Model with a One-Equation Model Near the Wall," 29th Aerospace Sciences Meeting, Reno, January 7-10, Nevada. (AIAA Paper 91-0216.)

Rodi, W., 1992, "On the Simulation of Turbulent Flow Past Bluff Bodies," 1st Int. Symp. on Computational Wind Eng., Tokyo, 1992.

Rodi, W., 1997, "Comparison of LES and RANS Calculations of the Flow Around Bluff Bodies," Journal of Wind Engineering and Industrial Aerodynamics, Vol. 69-71, pp. 55-75.

Rodi, W., and Mansour, N.N, 1993, "Low Reynolds Number k- Modelling with the Aid of Direct Simulation Data," Journal of Fluid Mechanics, Vol. 250, pp. 509-529.

Rodi, W., Mansour, N.N., and Michelassi, V., 1993, "One-Equation Near-Wall Turbulence Modeling With the Aid of Direct Simulation Data," ASME Journal of Fluids Engineering, Vol. 115, pp. 196-205.

Rodi, W., Ferziger, J.H., Breuer, M., and Pourquie, M., 1997, "Status of Large Eddy Simulation: Results of a Workshop," ASME Journal of Fluids Engineering, Vol. 119, pp. 248-262.

Rosenfeld, M., 1994, "Grid Refinement Test of Time-Periodic Flows Over Bluff Bodies," Computers and Fluids, Vol. 23, pp. 693-709.

REFERENCES

Roshko, A., 1961, "Experiments on the Flow Past a Circular Cylinder at Very High Reynolds Numbers," Journal of Fluid Mechanics, Vol. 10, pp. 345-356.

Sa, J-Y., and Chang, K-S., 1991, "Shedding Patterns of the Near-Wake Vortices Behind a Circular Cylinder," International Journal for Numerical Methods in Fluids, Vol. 12, pp. 463- 474.

Sakamoto, S., Murakami, S., and Mochida, A., 1993, "Numerical Study on Flow Past 2D Square Cylinder by Large Eddy Simulation: Comparison between 2D and 3D Computations," Journal of Wind Engineering and Industrial Aerodynamics, Vol. 50, pp. 61-68.

Sani, R.L., and Gresho, P.M., 1994, "Resume and Remarks on the Open Boundary Condition Minisymposium," International Journal for Numerical Methods in Fluids, Vol. 18, pp. 983-1008.

Sarpkaya, T., 1979, "Vortex-Induced Ocillations," Journal of Applied Mechanics, Vol. 46, p. 241.

Sarpkaya, T., 1986, "Force on a Circular Cylinder in Viscous Oscillatory Flow at Low Keulegan-Carpenter Numbers," Journal of Fluid Mechanics, Vol. 165, pp. 61-71.

Sarpkaya, T., 1992, "Brief Reviews of Some Time-Dependent Flows," ASME Journal of Fluids Engineering, Vol. 114, pp. 283-298.

Sarpkaya, T., and Dalton, C., 1992, "Analysis of Wave Plus Current-Induced Forces on Cylinders," Proc. 24th Annual Offshore Technology Conference, Houston, Texas, May 4-7, pp. 87-93.

Sarpkaya, T., and Ihrig, C.J., 1986, "Impulsively Started Steady Flow About Rectangular Prisms: Experiments and Discrete Vortex Analysis," ASME Journal of Fluids Engineering, Vol. 108, pp. 47-54.

Sarpkaya, T., and Isaacson, M., 1981, Mechanics of Wave Forces on Offshore Structures, Litton Ed. Publ., London.

Sarpkaya, T., and Storm, M., 1985, "In-Line Force on a Cylinder Translating in Oscillatory Flow," Applied Ocean Research, Vol. 7, pp. 188-196.

Schewe, G., 1983, "On the Force Fluctuations Acting on a Circular Cylinder in Crossflow from Subcritical up to Transcritical Reynolds Nymbers," Journal of Fluid Mechanics, Vol. 133, pp. 265-285.

Schlichting, H., 1968, Boundary-Layer Theory, 6th Edition, McGraw-Hill.

Shih, T.H., and Mansour, N.N., 1990, "Modeling of Near–Wall Turbulence," In Engineering Turbulence Modelling and Experiments (ed. W. Rodi & N. Ganic), Elsevier, pp. 13-19.

Skomedal, N.G., Vada, T., and Sortland, B., 1989, "Viscous Forces on One and Two Circular Cylinders in Planar Oscillatory Flow," Applied Ocean Research, Vol. 11, pp. 114-134.

Smagorinsky, J., 1963, "General Circulation Experiments with the Primitive Equations. I. The Basic Experiment," Mon. Weather Rev., Vol. 91, pp. 99-164. (Referred to by Speziale, 1991.)

Sohankar, A., Norberg, C., and Davidson, L., 1997, "Numerical Simulations of Unsteady Low-Reynolds Number Flow Around Rectangular Cylinders at Incidence," Journal of Wind Engineering and Industrial Aerodynamics, Vol. 69-71, pp. 189-201.

Song, C.C.S., and Yuan, M., 1990, "Simulation of Vortex-Shedding Flow About a Circular Cylinder at High Reynolds Numbers," ASME Journal of Fluids Engineering, Vol. 112, pp. 155-161.

Spalding, D.B., 1991, "Kolmogorov's Two-Equation Model of Turbulence," Proc. Roy. Soc. London A, Vol. 434, pp. 211-216.

Speziale, C.G., 1991, "Analytical Methods for the Development of Reynolds-Stress Closures in Turbulence," Annual Review of Fluid Mechanics, Vol. 23, pp. 107-157.

Speziale, C.G., Sarkar, S., and Gatski, T.B., 1991, "Modeling the Pressure– Strain Correlation of Turbulence," Journal of Fluid Mechanics, Vol. 227, pp. 245-272.

Stansby, P., and Slaouti, A., 1991, "Flow Around Multiple Cylinders by the Random Vortex Method," Proc. 1st Int. Offshore and Polar Engineering Conf., Vol. 3, pp. 228-235.

Stansby, P.K., and Smith, P.A., 1989, "Flow Around a Cylinder by the Random Vortex Method," Proc. 8th Int. Conf. on Offshore Mechanics and Arctic Engineering, The Hague, March 19-23, pp. 419-426.

Stone, H.L., 1968, "Iterative Solution of Implicit Approximations of Multidimensional Partial Differential Equations, SIAM J. Numer. Anal., Vol. 5, pp. 530-558.

Sun, J., Li, J., and Roux, B., 1993, "Flow Regimes and Frequency Selection of a Cylinder Oscillating in an Upstream Cylinder Wake," International Journal for Numerical Methods in Fluids, Vol. 16, pp. 915-929.

Suzuki, H., Inoue, Y., Nishimura, T., Fukutani, K., and Suzuki, K., 1993, "Unsteady Flow in a Channel Obstructed by a Square Rod (Crisscross Motion of Vortex)," Int. J. Heat and Fluid Flow, Vol. 14, No. 1, pp. 2-9.

Sweby, P.K., 1984, "High Resolution Schemes Using Flux Limiters for Hyperbolic Conservation Laws," SIAM Journal Numer. Anal., Vol. 21, pp. 995-1011.

Tamura, T., and Kuwahara, K., 1990, "Numerical Study of Aerodynamic Behaviour of a Square Cylinder," Journal of Wind Engineering and Industrial Aerodynamics, Vol. 33, pp. 161-170.

Tamura, T., Ohta, I., and Kuwahara, K., 1990, "On the Realibity of Two-Dimensional Simulation for Unsteady Flows Around a Cylinder-Type Structure," Journal of Wind Engineering and Industrial Aerodynamics, Vol. 35, pp. 275-298.

Tatsuno, M., and Bearman, P.W., 1990, "A Visual Study of the Flow Around an Oscillating Circular Cylinder at Low Keulegan-Carpenter Numbers and Low Stokes Numbers," Journal of Fluid Mechanics, Vol. 211, pp. 157-182.

Taulbee, D.B., and Tran, L., 1988, "Stagnation Streamline Turbulence," AIAA Journal, Vol. 26, pp. 1011-1013.

Tennekes, H., and Lumley, J.L., 1972, A First Course in Turbulence, MIT Press, Cambridge, MA.

Tritton, D.J., 1959, "Experiments on the Flow past a Circular Cylinder at Low Reynolds Numbers," Journal of Fluid Mechanics, Vol. 6, pp. 547-567.

Van Der Vorst, H.A., 1992, "Bi–CGSTAB: A Fast and Smoothly Converging Variant of Bi–CG for the Solution of Nonsymmetric Linear Systems," SIAM J. Scientific Computing, Vol. 13, pp. 631-644.

Van Dyke, M., 1982, An Album of Fluid Motion, Parabolic Press, Stanford, CA, p. 57.

Van Leer, B., 1974, "Towards the Ultimate Conservative Differencing Scheme. II Monotonicity and Conservation Combined in a Second–Order Scheme," Journal of Computational Physics, Vol. 14, pp. 361-370.

Verley, R.L.P., 1979, "The Forces on a Cylinder Oscillating in a Current," Report No. 608018, River and Harbor Lab., NIT, Trondheim, Norway (cited by Sarpkaya and Dalton, 1992).

Wang, X., and Dalton, C., 1991a, "Numerical Solution for Impulsively Started and Decelerated Viscous Flow Past a Circular Cylinder," International Journal for Numerical Methods in Fluids, Vol. 12, pp. 383-400.

Wang, X., and Dalton, C., 1991b, "Oscillating Flow Past a Rigid Circular Cylinder: A Finite-Difference Calculation," ASME Journal of Fluids Engineering, Vol. 113, pp. 377-383.

Warming, R.F., and Beam, R.M., 1976, "Upwind Second Order Difference Schemes and Applications in Aerodynamic Flows," AIAA Journal, Vol. 14, pp. 1241-1249.

West, G.S, and Apelt, C.J., 1993, "Measurements of Fluctuating Pressures and Forces on a Circular Cylinder in the Reynolds Number Range 104 to 2.5105," Journal of Fluids and Structures, Vol. 7, pp. 227-244.

Wieselsberger, C., 1923, "Versuche uber den Luftwiderstand gerundeter und kantiger Korper," Ergebnisse Aerodyn. Versuchsanstalt Gottingen, (ed. L. Prandtl), II, Lieferung, pp.23. (Cited by Schewe (1983)).

Wilcox, D.C., 1993a, "Comparison of Two-Equation Turbulence Models for Boundary Layers with Pressure Gradient," AIAA Journal, Vol. 31, pp. 1414-1421.

Wilcox, D.C., 1993b, Turbulence Modeling for CFD, DCW Industries, Inc., La Canada, California.

Williamson, C.H.K., 1985, "Sinusoidal Flow Relative to Circular Cylinders," Journal of Fluid Mechanics, Vol. 155, pp. 141-174.

Williamson, C.H.K., 1988, "The Existence of Two Stages in the Transition to Three–Dimensionality of a Cylinder Wake," Physics of Fluids, Vol. 31, p. 3165.

Williamson, C.H.K., 1989, "Oblique and Parallel Modes of Vortex Shedding in the Wake of a Circular Cylinder at Low Reynolds Numbers," Journal of Fluid Mechanics, Vol. 206, p.579.

Williamson, C.H.K., 1996, "Vortex Dynamics in the Cylinder Wake," Annual Review of Fluid Mechanics, Vol. 28, pp.477-539.

Yakhot, V., and Orszag, S.A., 1986, "Renormalization Group Analysis of Turbulence. I. Basic Theory," Journal of Scientific Computing, Vol. 1, pp. 3-50.

Yakhot, V., and Smith, L.M., 1992, "The Renormalization Group, the ϵ–Expansion and Derivation of Turbulence Models," Journal of Scientific Computing, Vol. 3, p. 35

Yakhot, V., Orszag, S.A., Thangam, S., Gatski, T.B., and Speziale, C.G., 1992, "Development of Turbulence Models for Shear Flows by a Double Expansion Technique," Physics of Fluids A, Vol. 4, pp. 1510-1520.

Yeung, R.W., Sphaier, S.H., and Vaidhyanathan, M., 1992, "Unsteady Separated Flow Around Blunt Bodies," Proceedings of the Second International Offshore and Polar Engineering Conference, San Francisco, USA, 14-19 June, pp. 194-202.

Younis, B.A., 1988, "On Modeling the Vortex Shedding from Bluff Bodies in Laminar and Turbulent Streams," Proc. 7th Int. Conf. on Offshore Mechanics and Arctic Eng., Houston, Texas, Feb. 7-12, pp. 223-228.

Younis, B.A., 1998, Private communication.

Zdravkovich, M.M., 1977, "Review of Flow Interference Between Two Circular Cylinders in Various Arrangements," ASME Journal of Fluids Engineering, Vol. 99, pp. 618-633.

Zhang, H-Q., Fey, U., Noack, B.R., Konig, M., and Eckelmann, H., 1995, "On the Transition of the Cylinder Wake," Physics of Fluids, Vol. 7, pp.779-794.

Zhu, J., 1992, "On the Higher–Order Bounded Discretization Schemes for Finite Volume Computations of Incompressible Flows," Computer Methods in Applied Mechanics and Engineering,

Vol. 98., pp. 345-360.

Zhu, J., and Rodi, W., 1991, "A Low Dispersion and Bounded Convection Scheme," Computer Methods in Applied Mechanics and Engineering, Vol. 92, pp. 87-96.

Zhu, J., and Shih, T.-H., 1994, "Computation of Confined Coflow Jets with Three Turbulence Models," International Journal for Numerical Methods in Fluids, Vol. 19, pp. 939-956.

Zijlema, M., 1996, "On the Construction of a Third–Order Accurate Monotone Convection Scheme with Application to Turbulent Flows in General Domains," International Journal for Numerical Methods in Fluids, Vol. 22, pp. 619-641.